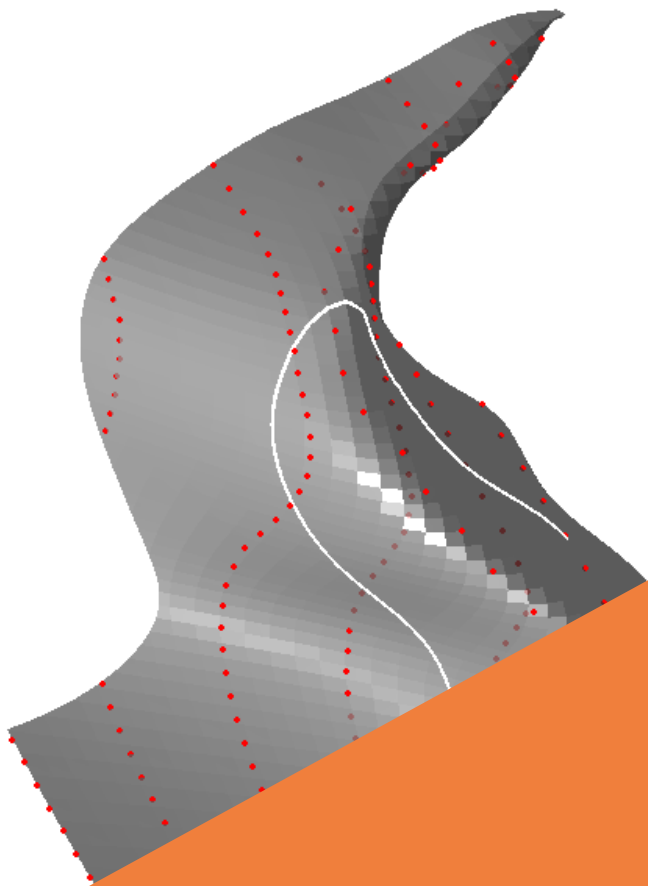


# Control-based methods for the identification of nonlinear structures

A thesis submitted in partial fulfillment of the requirements  
for the degree of Doctor of Philosophy (Phd) in Engineering Science

by

Gaëtan ABELOOS



Supervisor: Gaëtan KERSCHEN

Co-supervisor: Christophe COLLETTE

DOCTORAL COLLEGE IN AEROSPACE AND MECHANICS

OCTOBER 2022

# **Control-based methods for the identification of nonlinear structures**

A thesis submitted in partial fulfillment of the requirements  
for the degree of Doctor of Philosophy (Phd) in Engineering Science

by

**Gaëtan ABELOOS**

Supervisor: Gaëtan KERSCHEN

Co-supervisor: Christophe COLLETTE

**DOCTORAL COLLEGE IN AEROSPACE AND MECHANICS**

**OCTOBER 2022**

---

## **Doctoral Jury**

by alphabetical order

### **President**

Prof. Olivier BRULS  
University of Liège

### **Supervisor**

Prof. Gaëtan KERSCHEN  
University of Liège

### **Co-supervisor**

Prof. Christophe COLLETTE  
University of Liège

### **Members**

Prof. Guillaume DRION  
University of Liège

Prof. Malte KRACK  
Universität Stuttgart

Prof. Jean-Philippe NOËL  
KU Leuven

Dr. Ludovic RENSON  
Imperial College London

---



## Abstract

One of the key roles of structural engineering is to describe how a structure vibrates, or “responds”, when a dynamic load, or “excitation”, is applied to it. Often, the assumption of linear behavior is adopted, meaning that the response to a combination of excitation signals is the combination of the responses to the signals taken individually. When this assumption does not hold, complex dynamical phenomena can arise, including the coexistence of multiple responses for the same excitation, the sudden transition from one such response to another, or responses that are not stable. They render the experimental interrogation of engineering structures particularly challenging. An emerging family of testing methods, termed control-based methods, uses feedback loops and controllers to make the interrogation exhaustive and predictable. In this context, this thesis investigates carefully two recently-introduced methods, namely control-based continuation during which the excitation is corrected or generated by a controller, and phase-locked loop testing which imposes the phase lag between the response and the excitation using feedback control. In the first part of the thesis, we aim to deepen the understanding of control-based methods with the objective to design and tune experiments more systematically, reducing the need for trial and error. In the second part of the thesis, new developments exploiting adaptive filtering are carried out to expand the capabilities of both control-based continuation and phase-locked loop testing, but also to tackle dynamical features that were never identified experimentally before. Finally, this thesis opens the way towards more robust control-based methods and, eventually, to their industrial application.



## Résumé

Un des buts premiers de l'ingénierie des structures est de décrire comment une structure vibre, ou "répond", lorsqu'une charge dynamique, ou "excitation", lui est appliquée. Souvent, l'hypothèse de comportement dynamique linéaire est adoptée : la réponse à une combinaison d'excitations est la combinaison des réponses aux excitations prises individuellement. Quand cette hypothèse n'est pas vérifiée, des phénomènes dynamiques complexes peuvent se produire comme, par exemple, la coexistence de plusieurs réponses à la même excitation, la transition subite d'une de ces réponses à une autre ou des réponses qui ne sont pas stables. Ces phénomènes rendent l'interrogation expérimentale des structures particulièrement difficile. De nouvelles méthodes basées sur le contrôle et utilisant des boucles de rétroaction sont apparues pour rendre l'interrogation exhaustive et prévisible. Dans ce contexte, cette thèse étudie en détail deux méthodes récemment introduites : la continuation basée sur le contrôle durant laquelle l'excitation est corrigée ou générée par un contrôleur et les tests en boucle à verrouillage de phase avec une boucle de rétroaction imposant le retard de phase entre la réponse et l'excitation. La première partie de cette thèse vise à approfondir la compréhension de ces méthodes afin de concevoir les expériences plus efficacement, notamment en diminuant le recours à des essais-erreurs. La seconde partie exploite le filtrage adaptatif pour étendre le champ d'action des méthodes ainsi que pour étudier des phénomènes dynamiques qui n'ont jamais été identifiés expérimentalement de cette manière. Finalement, cette thèse ouvre la voie à des méthodes basées sur le contrôle plus robustes et, un jour, à leur application industrielle.



This thesis was funded by the FRIA grant of the F.R.S.-FNRS.

Cette thèse a été financée par la bourse FRIA du F.R.S.-FNRS.



## Acknowledgements

I would like to express my gratitude to...

... my supervisor, Gaëtan Kerschen. I had the opportunity to lead this research project thanks to him. I feel very grateful and lucky for his enthusiasm, patience, and generosity. I do not think I could have had a better environment to bring this project to fruition.

... my co-supervisor, Christophe Collette. His interest and his questions allowed me to challenge my assumptions and certitudes, and to reach deeper understanding of my subject.

... the rest of my thesis committee, Jean-Philippe Noël and Olivier Bruls. I thank them for the time they invested in following this project.

... all of the above, including Guillaume Drion, Ludovic Renson, and Malte Krack for taking part in my thesis jury. I hope this work will spark their interest.

... Ludovic Renson. He generously invited me for a two-months research stay in his research lab in Bristol. A great deal of my expertise with CBC exists thanks to him.

... Malte Krack, Florian Müller, Maren Scheel, and everyone from their lab. I had a warm welcome for my short research stay in Stuttgart. Another great deal of my expertise in PLL emanated from me working with Maren, Florian, and Malte.

... Florian Müller, Erhan Ferhatoglu, the trainees, and the mentors at the TRC camp. I will keep precious memories of our time together in Houston.

... my lab colleagues and friends, including Jennifer, Ghislain, Nicolas, Martin, Giancarlo, Samuel, Tong, and Thibaut. These years would not have been the same without you.

... Silvia, mes parents, mon frère et ma sœur. Ils ont toujours été présents pour me soutenir et m'écouter me plaindre pendant quatre ans.



# Contents

<b>Contents</b>	<b>xi</b>
<b>Introduction</b>	<b>1</b>
<b>1 Folding in response surfaces</b>	<b>9</b>
1.1 Introduction . . . . .	9
1.2 Open-loop experiment . . . . .	11
1.3 Control-based continuation . . . . .	16
1.4 Phase-locked loop testing . . . . .	21
1.5 Conclusion . . . . .	24
<b>2 Stability of control-based methods</b>	<b>27</b>
2.1 Introduction . . . . .	28
2.2 Open-loop experiment . . . . .	29
2.2.1 Van der Pol transformation . . . . .	30
2.2.2 Phase Van der Pol transformation . . . . .	31
2.3 Control-based continuation . . . . .	34
2.3.1 General controller . . . . .	35
2.3.2 Proportional-differential controller . . . . .	38
2.4 Phase-locked loop testing . . . . .	39
2.4.1 Perfect phase estimation . . . . .	39
2.4.2 Flawed phase estimation . . . . .	42
2.5 Conclusion . . . . .	45
<b>3 Experimental demonstration of control-based continuation and phase-locked loop testing</b>	<b>47</b>
3.1 Introduction . . . . .	48
3.2 Methods . . . . .	49
3.2.1 Phase-locked loop testing . . . . .	49
3.2.2 Control-based continuation . . . . .	50
3.2.3 Identification of backbone curves . . . . .	53

3.2.4	Identification of frequency response curves . . . . .	55
3.2.5	Compensation of the shaker-structure interaction . . . . .	57
3.2.6	Comparison of the methods . . . . .	58
3.3	Experiments . . . . .	60
3.3.1	Experimental setup . . . . .	60
3.3.2	Parameters and gains . . . . .	62
3.3.3	Backbone curves . . . . .	64
3.3.4	Nonlinear modal analysis . . . . .	68
3.3.5	Frequency response curve synthesis . . . . .	70
3.3.6	Frequency response curve identification . . . . .	71
3.4	Conclusion . . . . .	74
<b>4</b>	<b>Online Fourier decomposition for control-based methods</b>	<b>77</b>
4.1	Introduction . . . . .	78
4.2	Fourier decomposition methods . . . . .	78
4.2.1	Discrete Fourier transform . . . . .	78
4.2.2	Synchronous demodulation . . . . .	81
4.2.3	Adaptive notch filter . . . . .	83
4.2.4	Comparison . . . . .	84
4.3	Phase-locked loop . . . . .	86
4.3.1	Virtual experiment . . . . .	87
4.3.2	Physical experiment . . . . .	91
4.4	Control-based continuation . . . . .	95
4.4.1	Online control-based continuation experiment . . . . .	95
4.4.2	Experimental set-up . . . . .	97
4.4.3	Parameters and procedure . . . . .	99
4.4.4	Results . . . . .	101
4.5	Conclusion . . . . .	108
<b>5</b>	<b>Identification of superharmonic resonances</b>	<b>111</b>
5.1	Introduction . . . . .	111
5.2	Resonant phase lags . . . . .	112
5.2.1	Derivation . . . . .	113
5.2.2	Examples . . . . .	116
5.2.3	Discussion . . . . .	123
5.3	Control-based continuation . . . . .	126
5.4	Phase-locked loop testing . . . . .	128
5.5	Experimental demonstration . . . . .	130
5.6	Modal interaction . . . . .	138
5.7	Conclusion . . . . .	140

<b>6</b>	<b>Derivative-free arclength continuation for control-based continuation</b>	<b>141</b>
6.1	Introduction . . . . .	141
6.2	Control-based continuation procedures . . . . .	142
6.2.1	Derivative-based continuation . . . . .	142
6.2.2	Mapping-based approximation . . . . .	144
6.3	Arclength continuation: the basic idea . . . . .	145
6.4	Numerical examples . . . . .	148
6.4.1	Arclength strategy . . . . .	149
6.4.2	Softening-hardening and piecewise linear oscillators .	154
6.5	Experimental demonstration . . . . .	157
6.6	Multi-degree-of-freedom systems . . . . .	158
6.7	Conclusion . . . . .	161
<b>7</b>	<b>Identification of folded backbone curves</b>	<b>163</b>
7.1	Introduction . . . . .	164
7.2	Examples of folded backbone curves . . . . .	164
7.2.1	Isolated frequency response branch . . . . .	164
7.2.2	Modal interaction . . . . .	167
7.3	Backbone identification . . . . .	169
7.3.1	Phase-locked loop experiment . . . . .	169
7.3.2	Control-based continuation experiment . . . . .	170
7.4	Control-based phase-locked loop experiment . . . . .	171
7.5	Experimental demonstration of control-based phase-locked loop . . . . .	175
7.6	Conclusion . . . . .	178
	<b>Conclusions</b>	<b>179</b>
<b>A</b>	<b>Derivation of slowflow dynamics</b>	<b>185</b>
A.1	Van der Pol transformation . . . . .	185
A.1.1	Open-loop experiment . . . . .	186
A.1.2	Control-based continuation . . . . .	187
A.2	Phase Van der Pol transformation . . . . .	189
A.2.1	Open-loop experiment . . . . .	189
A.2.2	Phase-locked loop testing . . . . .	190
<b>B</b>	<b>Dynamics of online Fourier decomposition methods</b>	<b>193</b>
B.1	Synchronous demodulation . . . . .	193
B.2	Adaptive filtering . . . . .	195
B.2.1	Transfer function . . . . .	196

B.2.2	Performance . . . . .	197
B.2.3	Stability . . . . .	201
<b>Bibliography</b>		<b>205</b>

## Abbreviations

CBC	Control-Based Continuation
CBPLL	Control-Based Phase-Locked Loop
FRC	Frequency Response Curve
LP	Low-Pass
NNM	Nonlinear Normal Mode
P	Proportional
PD	Proportional and Differential
PID	Proportional, Integral and Differential
PLL	Phase-Locked Loop
RCT	Response-Controlled stepped-sine Testing
SSI	Shaker-Structure Interaction

## Mathematical symbols

$a_{x,n}$	Sine Fourier coefficient of the response's $n^{\text{th}}$ harmonic
$b_{x,n}$	Cosine Fourier coefficient of the response's $n^{\text{th}}$ harmonic
$c(\Omega)$	Real part of the general controller $C(i\Omega)$ (CBC)
$d(\Omega)$	Imaginary part of the general controller $C(i\Omega)$ (CBC)
$e$	Synthesis error of an adaptive filter
$f$	Excitation (force) applied on the oscillator
$f_{\text{nl}}$	Internal or artificial nonlinear force
$g$	Excitation under Van der Pol transformation
$h$	Excitation under phase Van der Pol transformation
$i$	Imaginary unit
$J$	Jacobian matrix of the open-loop experiment
$J^*$	Jacobian matrix of the control-based experiment
$k_{\text{d}}$	Differential controller gain
$k_{\text{i}}$	Integral controller gain
$k_{\text{p}}$	Proportional controller gain
$n$	Harmonic number
$N$	Total number of harmonics considered
$p$	Amplitude of a fundamental excitation
$r$	Amplitude of a fundamental response
$t$	Time
$u$	Voltage sent to the shaker <b>or</b> cosine coefficient under Van der Pol transformation
$U$	Amplitude of the voltage sent to the shaker
$v$	Sine coefficient under Van der Pol transformation
$w$	Coefficient under complex Van der Pol transformation
$x$	Response (displacement) of the nonlinear oscillator

$x^*$	Reference signal (CBC)
$x_f^*$	Fundamental component of reference signal (CBC)
$x_{nf}^*$	Non-fundamental component of reference signal (CBC)
$X_n$	Amplitude of the response's $n$ th harmonic
$y$	Output of the controller (CBC)
$z$	Internal parameter of the integral controller (PLL)
$\delta$	Linear damping ratio of the oscillator
$\delta^*$	Linear damping ratio of the CBC experiment
$\Delta_\nu$	Phase lag combination of a first-order superharmonic resonance
$\Delta_{\nu,\mu}$	Phase lag combination of a second-order superharmonic resonance
$\Delta^*$	Phase lag combination target for superharmonic resonances (PLL)
$\epsilon$	Settling margin for steady-state
	<b>or</b> factor for small-scale parameters
$\theta$	Instantaneous phase of the excitation (PLL)
$\lambda$	Eigenvalue of the Jacobian
$\mu$	Harmonic entering a second-order superharmonic resonance
$\nu$	Harmonic entering a first-order superharmonic resonance
$\phi$	Phase lag of the response's fundamental harmonic
$\phi_n$	Phase lag of the response's $n$ th harmonic
$\phi^*$	Phase lag target (PLL)
$\omega$	Nonlinear resonance frequency
$\omega_0$	Linear natural frequency
$\omega_0^*$	Linear natural frequency of the CBC experiment
$\Omega$	Excitation frequency

# Introduction

An important part of structural engineering is to predict how a mechanical system will evolve over time under dynamic excitation. The objective can be either to predict the behavior of a system that does not exist yet or to characterize experimentally an existing structure and predict how it will behave under conditions different from the test. Both rely on the creation of mathematical models that, ideally, predict accurately the system's response under any relevant excitation. Then, the model should be validated by submitting the physical structure to experimental characterization [1].

If the structure's behavior is close to linear, the superposition principle ensures that a response to a sum of two excitation signals is itself the sum of the responses resulting from each excitation signal taken individually. The consequence is twofold. On the one hand, the response to a multiharmonic signal is the combination of responses at each component frequency taken individually. Identifying the frequency response function in the frequency range of interest (either by testing each frequency individually during stepped or swept sine testing, or every frequency at once during random testing) allows to predict the response to any periodic excitation [2], a method called modal testing. On the other hand, characterizing the response at an excitation amplitude level allows to predict the response at any other amplitude level. For these reasons, experimental characterization methods for linear systems are now considered mature and well-established [3, 4, 5].

The superposition principle can however not be applied to structures that do not behave linearly, which constitute the norm, not the exception. Nonlinear behavior can emanate from a large number of physical sources. Examples include, but are not limited to, geometric and inertial nonlinearities, nonlinear material behavior (foams, rubber), nonlinear damping (dry friction, hysteretic damping) and boundary conditions (free surfaces, vibro-impacts) [6]. When the nonlinear behavior is weak, linear testing methods

can be applied using, e.g., stepped or swept sine testing [7, 8] or the time-domain Hilbert transform [6]. In general, however, using modal testing to identify the responses at each frequency is neither sufficient to predict the behavior of the structure under multi-harmonic excitation, nor is characterizing the structural behavior at low excitation amplitude to predict high-amplitude behavior.

The absence of superposition principle is a challenge to an exhaustive and general characterization of a nonlinear structure's responses. Usually, a choice is made about which families of responses will be considered. Focusing on responses to harmonic excitation allows for simple, repeatable experiments. Only two input parameters are needed for an open-loop experiment, i.e., the excitation frequency and amplitude, as shown in Fig. 0.1a. We will focus on two types of response branches: backbone curves are a collection of responses at resonance, showing the frequency-amplitude relation of nonlinear normal modes [9]; and frequency response curves (FRC) are collections of responses at constant excitation amplitude, analogous to the frequency response function of linear systems [10]. The nonlinearity triggers complex phenomena in the FRCs, ranging from bifurcations to chaos. Two of them will be the focus of this work:

- The same excitation signal can lead to different responses [10]. We will call this phenomenon “folding”, from the fold bifurcations that appear in response branches. A sister-phenomenon happens when an input parameter is changed toward and across a fold bifurcation, or when a sufficiently large perturbation is applied. The system will experience a “jump”; it will suddenly transition from one branch of responses to another [10, 11].
- Some responses are unstable. In an ideal world with infinite precision and no perturbation, the system would follow responses indiscriminately, stable or not. But the tiniest perturbation or error in the initial conditions makes the system diverge from the response. Another way to understand unstable responses is to say that they correspond to stable solutions when time is reversed. Going back in time, the system converges toward an unstable response just like it would for a stable solution in forward time [12]. Branches of unstable responses cannot be observed in an experimental setting but are very important in the characterization process because they can lead to stable branches that would have been left unidentified otherwise.

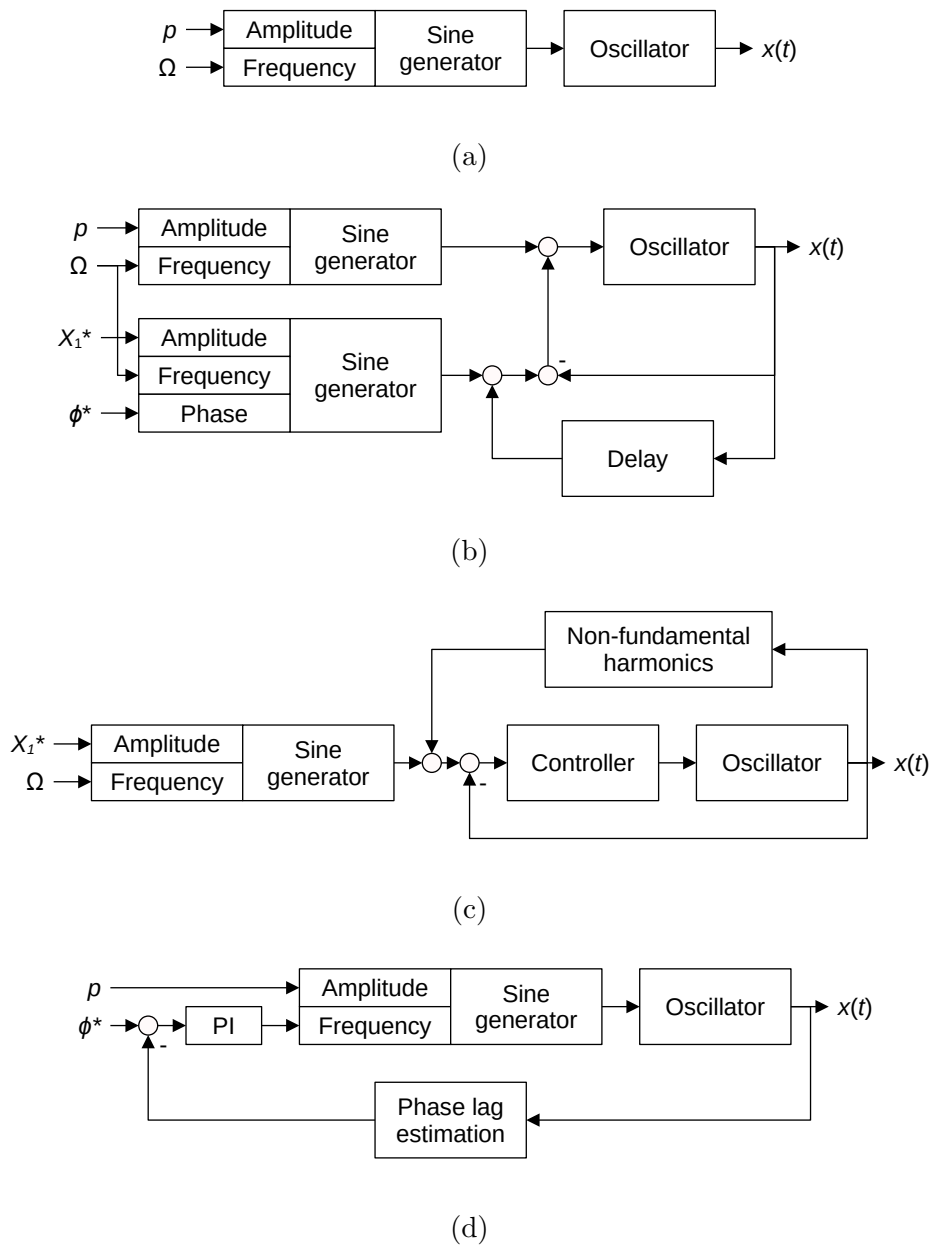


Figure 0.1: Diagrams for the (a) open-loop, (b) action CBC, (c) excitation CBC, and (c) PLL experiments with  $p$  and  $\Omega$  the excitation amplitude and frequency,  $X_1^*$  the fundamental amplitude of the reference signal,  $\phi^*$  a phase lag target, and  $x(t)$  the response

One approach to obtain the FRCs of a nonlinear system without being confronted to folding or unstable responses is to build a model from experiments staying close to the linear regime. Modeling a nonlinear system usually comprises different steps, namely detection and localization of the nonlinearities, approximation of their functional form and estimation of the nonlinear parameters [13, 14, 15]. A model can predict the system's responses to a general excitation, and by extension, responses to harmonic forcing. Branches of responses are identified numerically using continuation techniques that have reached a high degree of maturity [16, 17, 18, 19]. This approach is long and complex; it involves multiple phases from the design of a finite elements model to post-processing experimental data. Furthermore, it can be difficult to build predictive models for certain classes of systems, e.g. frictional systems with uncertainties or bolted joints [20]. A more direct approach to obtain the responses of interest is to measure them directly. We will refer to this as experimental characterization of nonlinear systems. It can be used to identify qualitatively nonlinear behavior, calibrate and validate existing nonlinear models [1, 21], or estimate quantitatively modal parameters [22, 23].

The objective is to design an experiment during which the structure is subjected to a harmonic excitation. The dynamics of the experiment must however be different than the open-loop experiment, such that all of the experiment's responses are stable. The usual way to ensure this is to use feedback control. We will refer to the family of methods discussed below as "control-based methods". Furthermore, the input parameters of the experiment must allow to identify responses across fold bifurcations. In other words, each combination of input parameters must lead to one and only one response. We will say that such an experiment is "unfolded". Furthermore, control-based methods have properties that can be useful during the service life of a structure, such as stabilization [24] or vibration mitigation [25].

One method to design such an experiment is control-based continuation (CBC), proposed in [26] to stabilize a chaotic system, then in [27] to go around a fold bifurcation. It is a general framework whose objective is to apply numerical continuation schemes (e.g. pseudo-arclength continuation [28]) to experiments. In [29, 30, 31], CBC is implemented to stabilize the orbits of a vertically actuated pendulum and go around a fold bifurcation. To that end, the response is compared to a target signal constituted of the response delayed by a number of periods with an arbitrary constant term. The difference between response and target is fed to a PD controller that acts on the pendulum in addition to the excitation. Feedback con-

control allows to stabilize the pendulum’s responses and the arbitrary constant term in the target is an additional parameter needed to go around the fold bifurcation. The constant term in the target is corrected until the response exactly matches the delayed target, at which point the controller action is zero and the CBC experiment responds like the open-loop experiment. It is said that the control is “non-invasive”.

An implementation of a CBC experiment to identify the responses of an oscillator under harmonic forcing was proposed in [32] and is schematized in Fig. 0.1b. The target signal is still a time-delayed response, but the arbitrary parameter allowing to go around the fold bifurcation is the target’s first harmonic. A PD controller is still used. A discussion about practical implementation and resilience to noise was proposed in [33, 34]. We will refer to this implementation of CBC as “action CBC” because the controller provides an invasive action in parallel to the excitation. The target is modified until the action is canceled, in which case only the excitation is applied to the structure. It is important to note that action CBC does not exactly correspond to what is commonly called feedback control. Although the objective is for the response and target to converge towards each other, the controller does not modify the response until it reaches the target. Rather, it is the target that is modified by the experimenter or an algorithm until it reaches the response.

A simpler implementation of CBC was proposed in [35], in which the response is compared to a completely arbitrary reference signal instead of a target signal. The output of the controller is directly the excitation applied on the structure. We will therefore refer to this implementation of CBC as “excitation CBC”. The objective of the experiment is to identify responses of the system under harmonic excitation. One way to ensure that the controller’s output is a harmonic signal is to ensure that the non-fundamental harmonics of the reference signal are identical to the ones of the response, as shown in Fig. 0.1c. Once again, excitation CBC should not be understood as what is commonly called feedback control. The objective of the controller is not to make the response converge towards the reference. Rather, the reference signal is modified until a specific controller output is reached, exciting the structure as desired. Follow-up studies on excitation CBC include a study on the effects of the PD controller gains [34], response stability estimation [36, 37], continuation procedures to identify different features of nonlinear oscillators [38, 39, 40, 41], and applications to friction systems [42] or even biochemical systems [43, 44] and pedestrian flow [45].

Another method to observe unstable responses of nonlinear oscillators uses a phase-locked loop (PLL) and was proposed in [46, 47]. During a PLL experiment, the excitation frequency is driven by a PI controller until the phase lag between the response and the excitation reaches a target value, as shown in Fig. 0.1d. The PLL corresponds to what is commonly thought as feedback control. The objective of the controller is to cancel the phase lag error between the measurement and the target. The phase lag target as an input parameter allows the experiment to go around fold bifurcations of FRCs [48]. The method was applied to different nonlinear structures such as beams and plates with nonlinear stiffness or damping [23, 49, 50, 51]. A stability analysis on the PI controller gains was performed in [49].

Response-controlled testing (RCT) was proposed in [52] to characterize nonlinear oscillators by imposing the response amplitude. Although the control law is proprietary, and therefore unknown, RCT is similar in principle to excitation CBC in the sense that the oscillator is excited by the controller and the input parameters are the frequency and amplitude of a reference signal. The difference resides mainly in the continuation procedure. Section 6.2.2 details the so-called mapping-based continuation procedures. The method has been applied on various engineering structures such as a satellite [52], a T-beam and a guided missile [53, 54].

Finally, there are some other methods that use feedback control or a feedback loop to explore the responses of nonlinear oscillators. In [55], a Hopf bifurcation is created by a positive feedback of the velocity. A maximum response amplitude is imposed by the negative feedback of a Van der Pol oscillator. A similar idea for velocity feedback is proposed in [56]. In this case, the velocity feedback amplitude is arbitrarily chosen.

This work will focus on excitation CBC, hereafter only referred to by “CBC”, and PLL. It is separated in two parts. In the first one, we will focus on understanding how these methods work. Chapter 1 focuses on why and in which case CBC and PLL experiments are unfolded: how can these control-based methods ensure that every input parameter combination corresponds to one and only one response? Chapter 2 develops analytical tools to explain how unstable responses of the open-loop experiment can be stable during a CBC or PLL experiment: can we always tune the control gains to ensure stability? Chapter 3 proposes implementations of the control-based experiments in finer details. It then demonstrates experimentally how they compare to each other, what features they can identify, and how.

The second part of this work focuses on improvements to the CBC and

PLL experiments. Chapter 4 proposes an online Fourier decomposition that improves the performance of both control-based methods. Chapter 5 shows how the PLL method can be modified and applied to characterize superharmonic resonances. Chapter 6 makes a summary of the different CBC continuation procedures and proposes a simple and fast arclength continuation scheme tailored for nonlinear oscillators. Chapter 7 presents a specific case in which the PLL experiment is folded and proposes to combine PLL and CBC into a single unfolded experiment.



# Chapter 1

## Folding in response surfaces

### Abstract

Although control-based methods are increasingly popular in the engineering community, the motivation behind their design is often left unexplained. This Chapter aims to show how control-based continuation and phase-locked loop testing allow to solve one of the two main problems in characterizing nonlinear oscillators in open-loop, i.e., the folding phenomenon. Specifically, how does each method ensure that one set of input parameters leads to one and only one response. The input parameters of each method are described. During an open-loop experiment, the amplitude and frequency of the excitation are chosen. On the one hand, control-based continuation exploits monotonous fundamental S-curves by replacing the excitation amplitude by the fundamental amplitude of the response as an input parameter. On the other hand, phase-locked loop testing exploits the monotonous drop in phase lag across a fundamental resonance peak by replacing the frequency by the phase lag as an input parameter.

### 1.1 Introduction

In this work, an experiment is defined as the interrogation of a system and the measurement of its response. The experimenter, who can be a person when the experiment is manually driven or a computer when it is automated, defines a series of input parameters that drive the experiment. The collection of responses corresponding to each input parameter combination

is called a response space. We will mostly consider experiments with two input parameters, thus we will mostly write about response surfaces.

It is important to distinguish between three types of parameters in an experiment. The parameters governing the dynamics of the interrogated system are called the system parameters and do not vary with time. They can be internal if they correspond to the dynamics of the interrogated structure, in which case they are considered unknown by the experimenter, or user-defined if they are specific to the method. Any parameter describing the response is called a measured parameter. They are known to the experimenter, but their value cannot be directly imposed. The driver of the experiment are the input parameters that are freely chosen by the experimenter.

One of the challenges when characterizing a nonlinear system experimentally is the so-called folding phenomenon, i.e, the same input parameter set can lead to distinct responses. It is therefore often difficult to explore all the responses of a nonlinear experiment in a single test run [10]. Furthermore, fold bifurcations lead to the jump phenomenon during which the experiment suddenly changes its response, leading to potentially unidentified response branches, damage to itself, the testing equipment, or the experimenter [10].

Three experiments are schematized in Figs. 0.1a, 0.1c, and 0.1d. Each of the experiment drives the same nonlinear oscillator. The objective of this Chapter is to show that, even though each experiment has different inputs, they can lead to the same response. Section 1.2 shows that the open-loop experiment has a folded response surface. However, control-based methods allow to define experiments with unfolded response surfaces.

Two facts about nonlinear oscillators are exploited to define unfolded experiments. Firstly, different responses rarely share the same amplitude at constant frequency. In Section 1.3, the response amplitude is indirectly imposed through a feedback loop during control-based continuation (CBC) [31, 32, 57]. The input parameter space is composed of the amplitude and frequency of a reference signal. Secondly, responses around a resonance rarely share the same phase lag at constant excitation amplitude. In Section 1.4, the phase lag is directly imposed through feedback control during phase-locked loop (PLL) testing [58]. The parameter space is composed of the excitation amplitude and a phase lag target.

## 1.2 Open-loop experiment

Let us consider a general single-degree-of-freedom nonlinear oscillator governed by the equation of motion

$$m\ddot{x} + c\dot{x} + kx + f_{\text{nl}}(x, \dot{x}) = f(t). \quad (1.1)$$

In this work, we will focus on the responses of the system to a harmonic excitation  $f(t) = p \sin(\Omega t)$ . The oscillator's linear parameters are its mass  $m$ , damping  $c$  and stiffness  $k$ . The internal nonlinear force  $f_{\text{nl}}(x, \dot{x})$  can be any continuous nonlinear function involving the displacement  $x(t)$  (nonlinear stiffness) or velocity  $\dot{x}(t)$  (nonlinear damping) or both (Van der Pol-type nonlinearity). The right-hand side of the equation defines the excitation. As it comprises a single harmonic, it is called monoharmonic or fundamental.

The response  $x(t)$  can follow any number of trajectories depending on the excitation, internal parameters, nonlinear force, and initial state  $(x, \dot{x})$  of the oscillator. In this work, we will restrict ourselves to the steady-state case where  $x(t)$  is periodic with frequency  $\Omega$ , i.e.  $x(t + 2\pi/\Omega) = x(t)$ . In the rest of this work, we will refer to  $\Omega$  as the frequency in rad/s, sometimes called pulsation to distinguish it from the frequency in Hz. In general, the presence of a nonlinear force causes  $x(t)$  to be multiharmonic. Although the response possesses an infinite number of harmonics in reality, only a limited number is considered in practice: The Fourier series is truncated to  $N$  terms

$$x(t) = b_{x,0} + \sum_{n=1}^N a_{x,n} \sin(n\Omega t) + b_{x,n} \cos(n\Omega t). \quad (1.2)$$

The amplitude and phase of the  $n$ th harmonic are expressed as

$$X_n = \sqrt{a_{x,n}^2 + b_{x,n}^2} \quad (1.3)$$

$$\phi_n = \text{atan2}(b_{x,n}, a_{x,n}) \quad (1.4)$$

respectively, such that

$$a_{x,n} \sin(n\Omega t) + b_{x,n} \cos(n\Omega t) = X_n \sin(n\Omega t + \phi_n). \quad (1.5)$$

The parameters  $m$ ,  $c$ , and  $k$  are internal. The nonlinear force  $f_{\text{nl}}(x, \dot{x})$  is an unknown relationship that does not vary through time and thus can be grouped with the internal parameters. The response trajectory  $x(t)$  is measured by the experimenter and can be described by the amplitude  $X_1$  or phase  $\phi_1$  of its first harmonic; they are measured parameters. The driver

Table 1.1: Set of parameters and laws for single-degree-of-freedom nonlinear systems used as examples in this Chapter

Set	$m$	$c$	$k$	$f_{\text{nl}}(x, \dot{x})$
1	1	0.1	1	$x^3$
2	20	0.5	20	$10x^2 + 2x^3$

of the open-loop experiment is the excitation that is freely chosen by the experimenter. The input parameters are the excitation amplitude  $p$  and frequency  $\Omega$ .

The response surface of a hardening nonlinear oscillator is shown in Fig. 1.1. Different responses can correspond to the same input parameters, i.e., to the same excitation signal. This so-called folding phenomenon emanates from the nonlinearity, in this case a strongly nonlinear stiffness. Fig. 1.1c shows that for some  $(\Omega, p)$ , there exist up to three different responses. Such an instance is shown in Fig. 1.1d. This is far from the worst case scenario. The response surface of a softening-hardening oscillator is shown in Fig. 1.2 where Figs. 1.2c and Fig. 1.2d demonstrate that one set of input parameters can respond to up to five different responses.

Usually, an experimental campaign does not seek to identify the full response surface but only a portion of it. The experimenter keeps one input parameter constant and seeks to characterize the response of the system when varying the other. In most cases, the excitation amplitude  $p$  is kept constant and the frequency  $\Omega$  is changed, leading to a so-called frequency response curve (FRC). They are often sought because they parallel the frequency response function, an essential tool of linear modal analysis [4]. Examples of FRCs are shown in Figs. 1.3a and 1.4a. When keeping  $\Omega$  constant and varying  $p$ , the experimenter identifies a so-called S-curve [57]. Some examples are shown in Figs. 1.3b and 1.4b.

Regardless of the curve that the experimenter aims to identify, Figs. 1.3 and 1.4 evidence that  $\Omega$  and  $p$  are not ideal parameters to conduct the experiment. When increasing (or decreasing) one input parameter continuously, a point at which the curve goes vertical and makes a “half-turn”, called a fold or saddle-node bifurcation [61, 62], is encountered. If the experiment continues to increase (or decrease) the input parameter, the system will make a so-called jump toward another co-existing response, a phenomenon that can leave some responses unidentified [10].

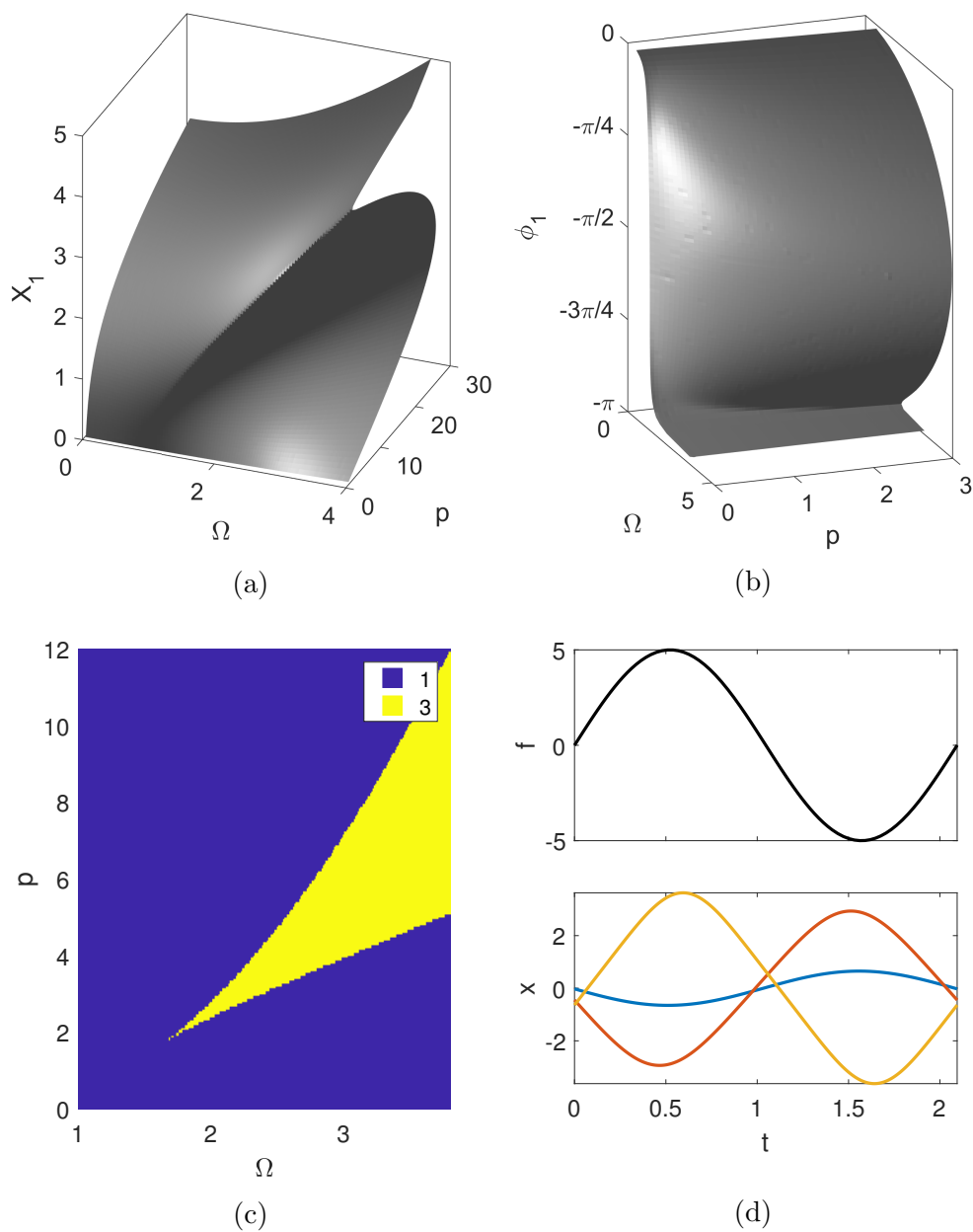


Figure 1.1: (a,b) Response surface of Eq. (1.1) with parameter set 1 from Table 1.1 computed using the harmonic balance method [59] with 1 harmonic; (c) number of different responses in the response surface; (d) every response for  $\Omega = 3$  and  $p = 5$  computed using the shooting method [60]

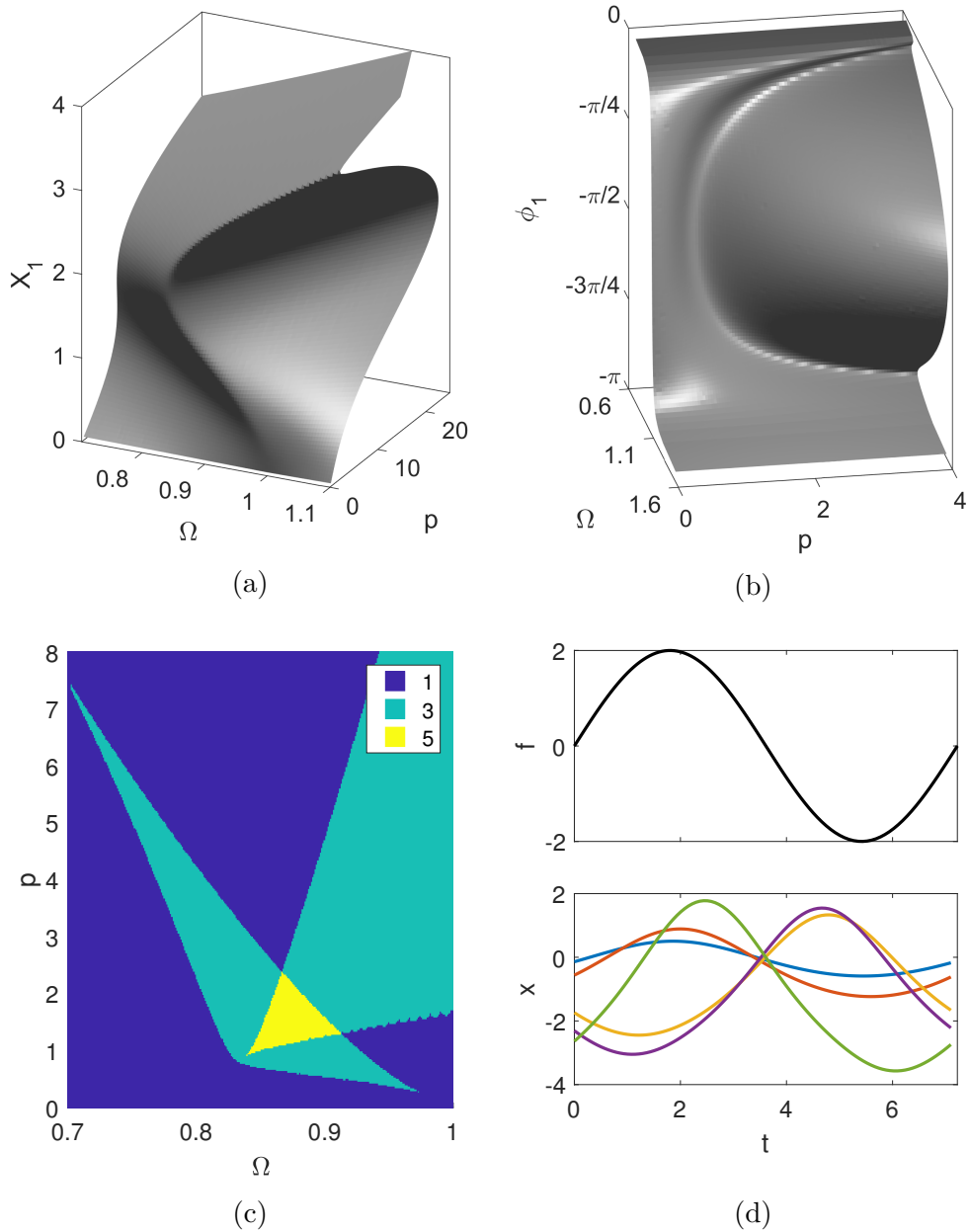


Figure 1.2: (a,b) Response surface of Eq. (1.1) with parameter set 2 from Table 1.1 computed using the harmonic balance method [59] with 1 harmonic; (c) number of different responses in the response surface; (d) every response for  $\Omega = 0.885$  and  $p = 2$  computed using the shooting method [60]

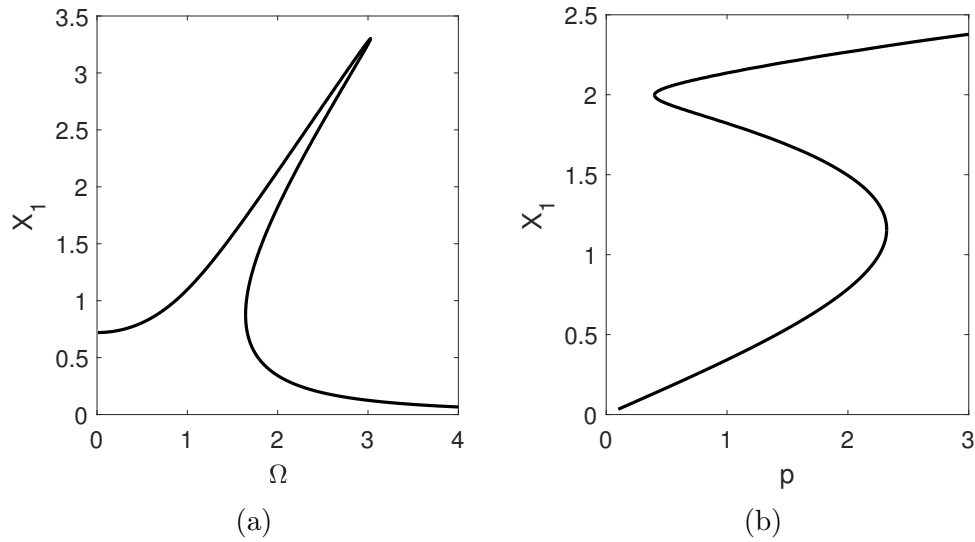


Figure 1.3: (a) FRC at  $p = 1$  and (b) S-curve at  $\Omega = 2$  of Eq. (1.1) with parameter set 1 from Table 1.1 computed using the harmonic balance method[59] with 1 harmonic

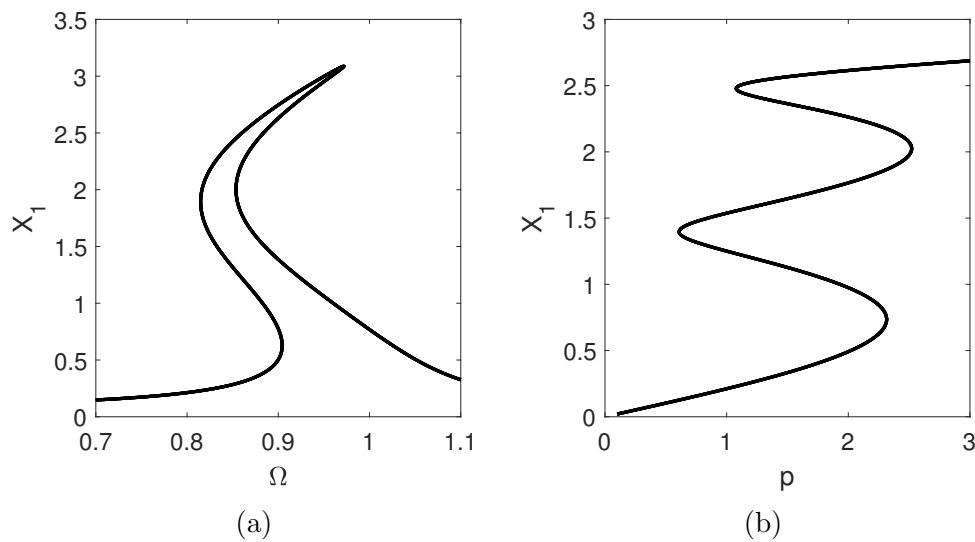


Figure 1.4: (a) FRC at  $p = 1.5$  and (b) S-curve at  $\Omega = 0.87$  of Eq. (1.1) with parameter set 2 from Table 1.1 computed using the harmonic balance method[59] with 1 harmonic

### 1.3 Control-based continuation

Under control-based continuation (CBC), a controller excites the nonlinear oscillator through its action  $y$ . CBC is a general method that can define the action  $y$  in many ways. We will consider an implementation of CBC from [57] that exploits the fact that different responses rarely share the same first harmonic amplitude  $X_1$  at constant frequency. Imposing  $X_1$  would lead to one and only one response, to the condition that fundamental S-curves are monotonous (see Figs. 1.3b and 1.4b), i.e., none of the system's fundamental FRCs intersect. Unfortunately, one cannot directly impose  $X_1$  because it is a measured parameter and not an input parameter. CBC uses a feedback loop to impose  $X_1$  indirectly through the definition of a new input parameter, the amplitude of a reference signal  $x^*$ .

The controller provides the excitation through its action signal  $y(x^* - x)$  [57]:

$$m\ddot{x} + c\dot{x} + kx + f_{\text{nl}}(x, \dot{x}) = y(x^* - x). \quad (1.6)$$

The reference signal  $x^*(t)$ , chosen by the user, can be decomposed in its Fourier coefficients

$$x^*(t) = b_{x^*,0} + \sum_{n=1}^N a_{x^*,n} \sin(n\Omega t) + b_{x^*,n} \cos(n\Omega t). \quad (1.7)$$

We assume that the reference signal has the same number of harmonics  $N$  than the truncated Fourier series of  $x(t)$ . In Section 2.3.1, we explore the effect of a general LTI controller on the dynamics of the oscillator. In the meantime and for the sake of simplicity, we consider here a differential controller (whose performance is also discussed in Section 2.3.1) of gain  $k_d$ :

$$y(x^* - x) = k_d(\dot{x}^* - \dot{x}). \quad (1.8)$$

The gain is user-defined but determines the dynamics of the CBC experiment; it is therefore a system parameter.

The CBC experiment in Eq. (1.6) is only useful when it allows to identify the same responses as the open-loop experiment in Eq. (1.1). For the same response to verify both equations of motion, we need to ensure that their right-hand sides—the excitations—are equal:  $y(x^* - x) = p \sin(\Omega t)$ . In other words, the controller must excite the oscillator with a single harmonic. This condition is verified for the reference signal

$$x^* = x - \frac{p}{\Omega k_d} \cos(\Omega t) + \text{const.} \quad (1.9)$$

The constant term is filtered out by the differential controller and will be omitted from now on.

A necessary condition to Eq. (1.9) is that the non-fundamental Fourier coefficients are identical:

$$\begin{cases} a_{x^*,n} = a_{x,n} \\ b_{x^*,n} = b_{x,n} \end{cases} \quad \forall n \in \{2, \dots, N\}. \quad (1.10)$$

When this condition is respected, the control is sometimes called non-invasive because the response corresponds to an open-loop experiment [35]. We will see how to achieve this in practice in Chapters 3 and 4. This step is represented in Fig. 0.1c by the block “Non-fundamental harmonics”.

For now, we can consider that Eq. (1.10) is always verified because  $x^*$  is chosen freely by the experimenter. The coefficients of the fundamental harmonic verify

$$\begin{cases} a_{x^*,1} = a_{x,1} \\ b_{x^*,1} = b_{x,1} - \frac{p}{\Omega k_d} \end{cases} \quad (1.11)$$

for the excitation to be a sine wave of amplitude  $p$  and frequency  $\Omega$ . We deduce that there is one and only one reference signal corresponding to a specific response.

We can note that the fundamental phase of the reference has no effect on the response. Indeed, the oscillator being time-invariant, a phase difference can always be removed by some time shift. Hence, the controlled experiment in Eq. (1.6) has only two input parameters: the reference frequency  $\Omega$  and amplitude  $X_1^* = \sqrt{a_{x^*,1}^2 + b_{x^*,1}^2}$ . Effectively, the parameter  $p$  has been replaced by  $X_1^*$  with the relation in Eq. (1.11). The control gain  $k_d$  is a system parameter, considered constant during the experiment.

Let us consider an open-loop experiment such that each response at constant  $\Omega$  has a different fundamental amplitude  $X_1$  (see the S-curves in Figs 1.3b or 1.4b). This fact stays true for the corresponding CBC experiment. Eq. (1.11) shows that increasing the control gain  $k_d$  makes  $X_1$  and  $X_1^*$  converge. The  $(X_1, X_1^*)$  relation approaches linearity for high enough  $k_d$ , as shown in Fig. 1.5. Although the open-loop S-curve is folded because multiple responses correspond to the same  $p$ , the CBC S-curve is not folded for high enough  $k_d$  because each response corresponds to one and only one  $X_1^*$ .

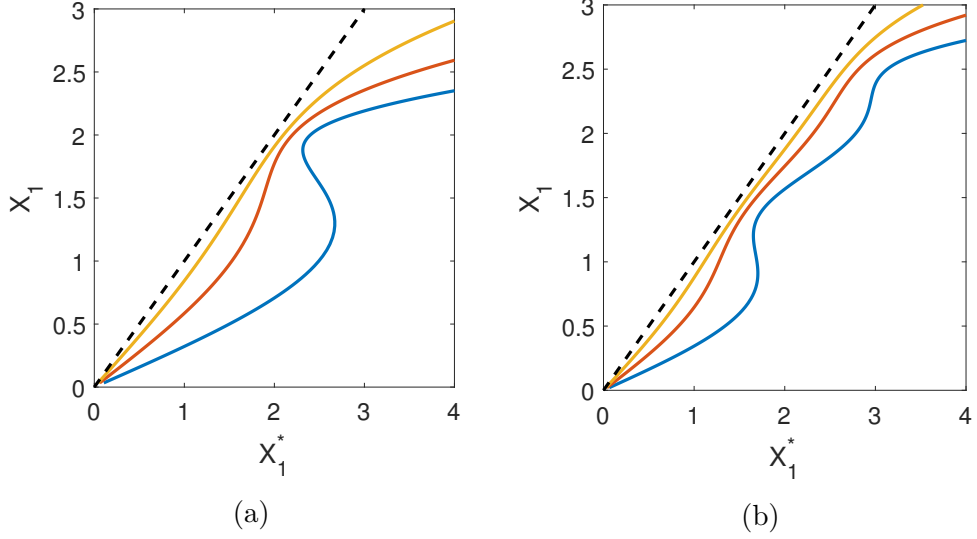


Figure 1.5: S-curves of Eq. (1.6) with (a) parameter set 1 from Table 1.1,  $k_d = 0.5$  (blue), 1 (orange), and 2 (yellow); (b) parameter set 2 from Table 1.1,  $k_d = 2$  (blue), 4 (orange), and 8 (yellow)

Fig. 1.6 shows the response surface of a CBC experiment performed on an oscillator with cubic stiffness. As  $k_d$  increases, the surface approaches  $X_1 = X_1^*$  independently from  $\Omega$ . For high enough  $k_d$ , each response corresponds to one and only one pair of user-parameters  $(\Omega, X_1^*)$ , i.e., there is no folding in the experiment. The same can be said when considering a softening-hardening oscillator, as shown in Fig. 1.7.

The observations made for a differential controller in this Chapter can be generalized easily. Let us consider a general LTI controller  $C$  such that, in the Laplace domain,

$$Y(s) = C(s)(X^*(s) - X(s)). \quad (1.12)$$

To ensure that  $y(t) = p \sin(\Omega t)$ , Eq. (1.9) becomes

$$X^*(s) = X(s) + \frac{1}{C(s)} \frac{p\Omega}{s^2 + \Omega^2}. \quad (1.13)$$

Developing  $X^*$  and  $X$  into their Fourier coefficients leads directly to Eq. (1.10). Increasing the modulus of  $C(s)$  makes  $X_1$  converge towards  $X_1^*$ . From there, we reach the same conclusions as with a differential controller.

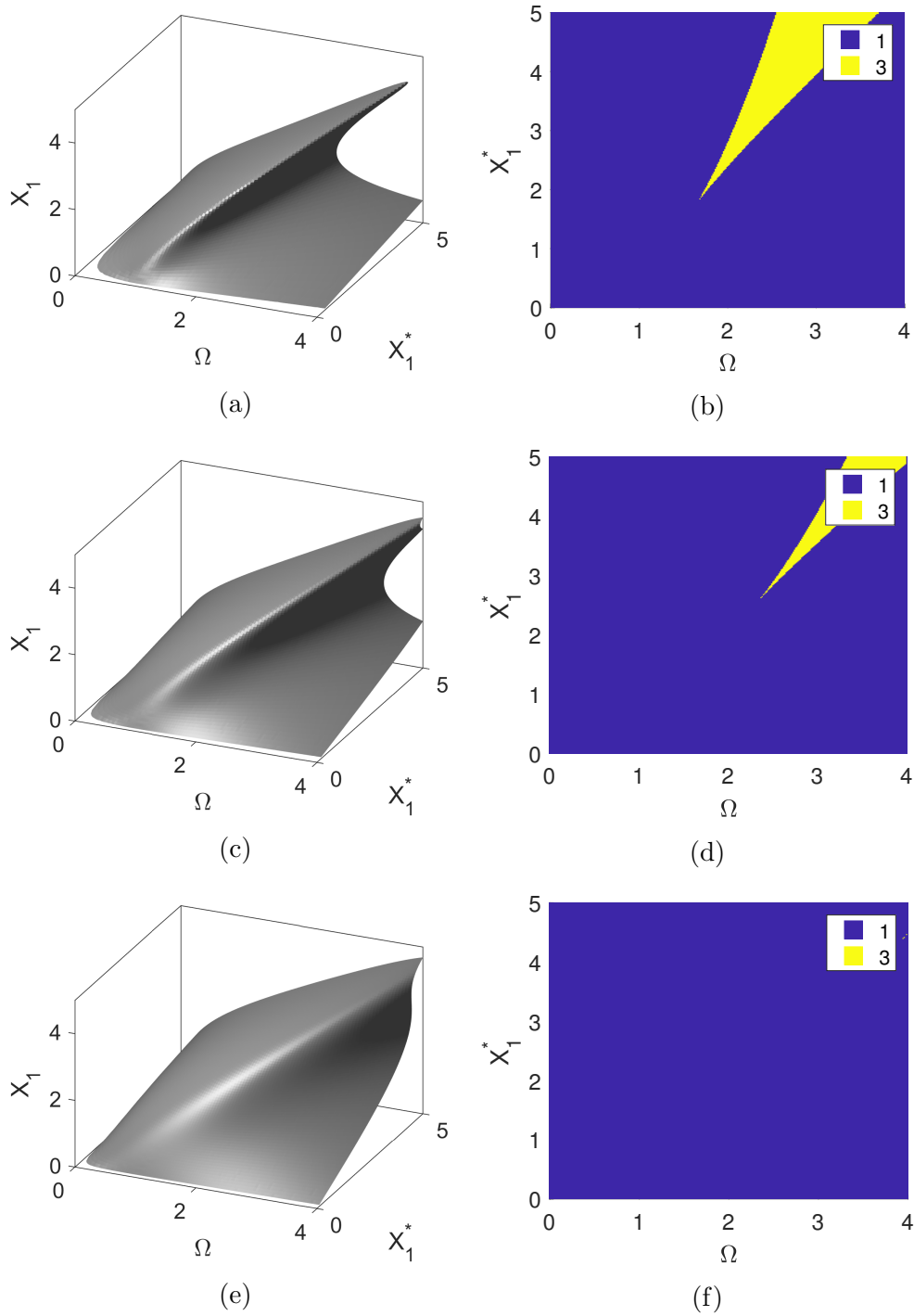


Figure 1.6: (a,c,e) Response surface of Eq. (1.6) with parameter set 1 from Table 1.1 computed using the harmonic balance method[59] with 1 harmonic and (b,d,f) number of responses corresponding to a couple  $(\Omega, X_1^*)$  for varying gains (a,b)  $k_d = 0.5$ , (c,d)  $k_d = 1$ , (e,f)  $k_d = 2$

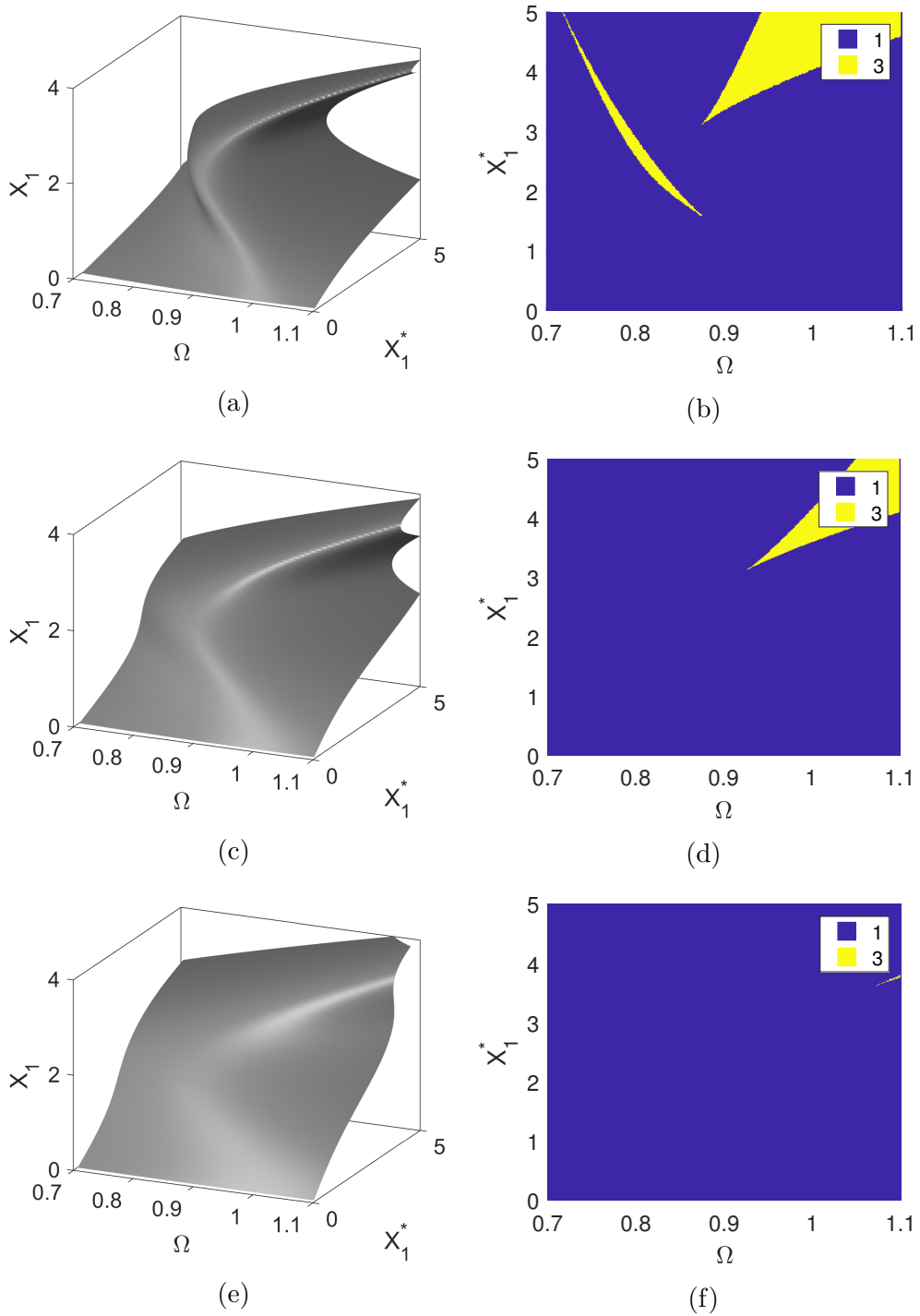


Figure 1.7: (a,c,e) Response surface of Eq. (1.6) with parameter set 2 from Table 1.1 computed using the harmonic balance method[59] with 1 harmonic and (b,d,f) number of responses corresponding to a couple  $(\Omega, X_1^*)$  for varying gains (a,b)  $k_d = 2$ , (c,d)  $k_d = 4$ , (e,f)  $k_d = 8$

## 1.4 Phase-locked loop testing

Phase-locked loop (PLL) testing aims to define an experiment without folding. It exploits the fact that different responses rarely share the same fundamental phase lag  $\phi_1$  at constant excitation amplitude  $p$  (see phase lag FRCs in Figs. 1.8a and 1.8b). Unfortunately,  $\phi_1$  is a measured parameter and cannot be imposed directly. During PLL testing, classical feedback control makes  $\phi_1$  converge towards a target by acting on the excitation frequency  $\Omega$ . The target therefore replaces  $\Omega$  as a input parameter.

For the phase lag  $\phi_1$  of the response to be controlled, it must be measured continuously through time. In this work, the phase lag is derived by continuously estimating the Fourier coefficients of the response and excitation. Methods to make this estimation in practice are presented in Chapters 3 and 4.

During PLL testing, the excitation frequency  $\Omega$  varies through time:

$$m\ddot{x} + c\dot{x} + kx + f_{nl}(x, \dot{x}) = p \sin \left( \int_0^t \Omega(\tau) d\tau \right). \quad (1.14)$$

Although  $p$  is a input parameter,  $\Omega$  is not. It is the control function of a

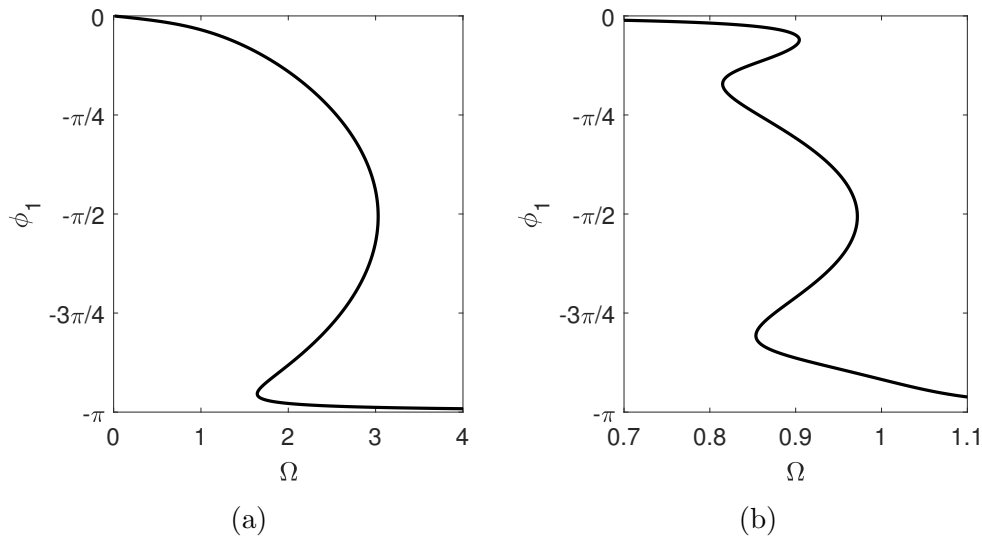


Figure 1.8: FRCs parametrized by the first harmonic phase lag of Eq. (1.1) with (a) parameter set 1 from Table 1.1 at  $p = 1$  and (b) parameter set 2 from Table 1.1 at  $p = 1.5$ ; both computed using the harmonic balance method [59] with 1 harmonic

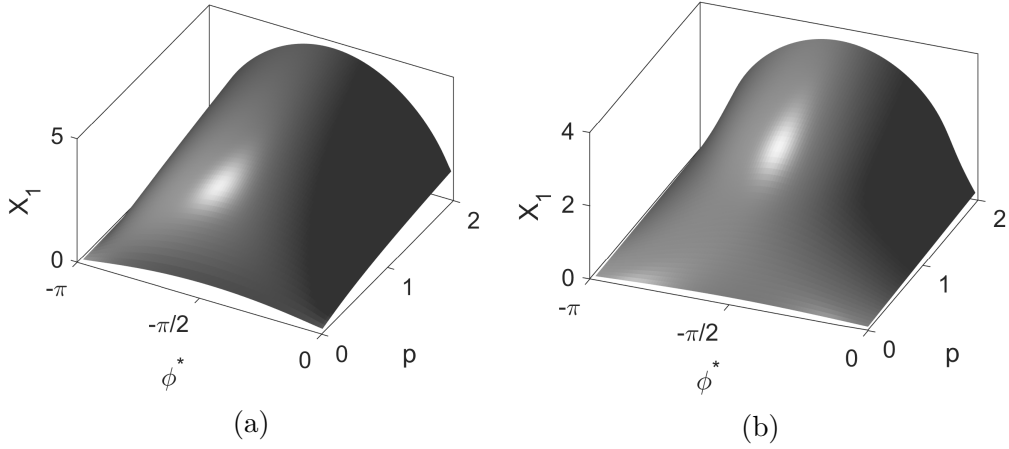


Figure 1.9: Response surface of experiment (1.14) with parameter set (a) 1 and (b) 2 from Table 1.1 computed with the harmonic balance method[59] with 1 harmonic; along with the FRCs from Figs. 1.3a and 1.4a respectively (black curve)

PI controller targeting a input phase lag  $\phi^*$ :

$$\Omega(t) = \omega_0 + k_p(\phi_1 - \phi^*) + k_i \int_0^t (\phi_1 - \phi^*) d\tau. \quad (1.15)$$

This makes  $(\phi^*, p)$  the only two input parameters of the experiment defined in Eq. (1.14). The control gains  $k_p$  and  $k_i$  are user-defined system parameters considered constant during the experiment.

It is important to note that the slopes  $d\phi_1/d\Omega$  in Fig. 1.8 do not always have the same sign. When the slope is positive and the phase lag  $\phi_1$  is larger than targeted, one must decrease  $\Omega$  to reach the phase lag target. However, if the slope is negative, one must increase  $\Omega$  to apply the same correction. With this, it is apparent that a PLL is more complicated than a linear feedback control loop. In general, the same control gains cannot identify every response because they would need to change sign depending on the slope  $d\phi_1/d\Omega$ . We will see in Chapter 2 that it is possible for a PLL experiment to identify every response with constant control gains if they have specific values such that the controller dynamics interact with the oscillator.

Fig. 1.9 shows the response surfaces of PLL testing experiments. Each response corresponds to one and only one pair  $(\phi^*, p)$ . Thanks to the integral part of the controller  $k_i > 0$ , the experiment is only at equilibrium

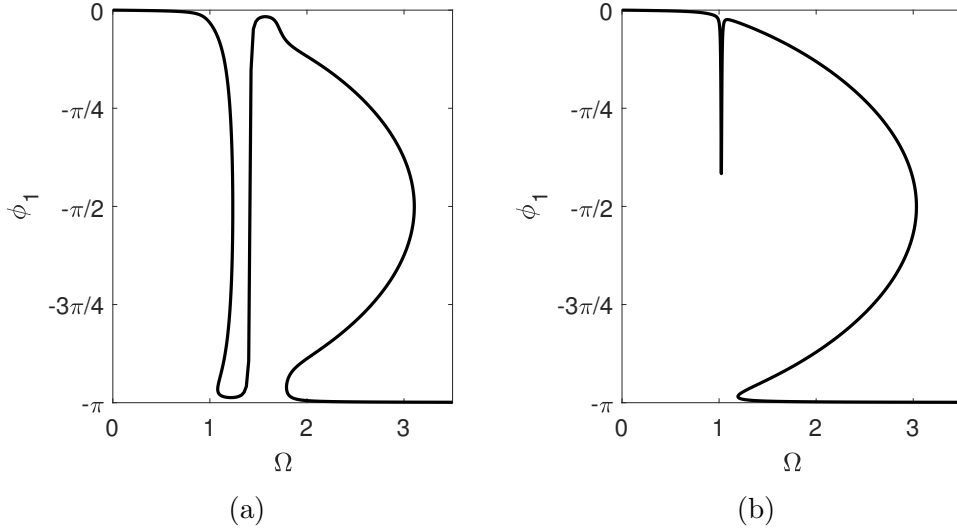


Figure 1.10: FRC of experiment (1.16) parameterized by the fundamental phase lag of the first degree-of-freedom with (a) parameter set 3 from Table 1.2 at  $\mathbf{p} = [0.1 \ 0]^T$  and (b) parameter set 4 from Table 1.2 at  $\mathbf{p} = [0.1 \ 0]^T$

when  $\phi_1 = \phi^*$ . Contrarily to CBC in the previous section, the control gains only modify the transient response of the experiment and not the steady-state. Thus, the geometry of the response surface is independent from  $k_p$  and  $k_i$ . This can be understood with Fig. 0.1d showing that the open-loop experiment is fully comprised into the PLL experiment.

At frequencies far below (resp. above) a fundamental resonance, the phase lag approaches zero (resp.  $-\pi$ ) with a very steep slope  $d\Omega/d\phi_1$ , as shown for instance in Figs. 1.8a and 1.8b: a small phase lag difference implies a large frequency difference. This renders the control loop very sensitive to an error in phase lag estimation far away from a resonance. In practice, PLL testing can only be applied near a resonance.

To highlight some more limitations of PLL testing, let us briefly consider a  $n_{\text{dof}}$  degrees of freedom (DOF) oscillator governed by the equation of motion

$$\mathbf{M}\ddot{\mathbf{x}} + \mathbf{C}\dot{\mathbf{x}} + \mathbf{K}\mathbf{x} + \mathbf{f}_{\text{nl}}(\mathbf{x}, \dot{\mathbf{x}}) = \mathbf{p} \sin(\Omega t) \quad (1.16)$$

with  $\mathbf{M}$ ,  $\mathbf{C}$ ,  $\mathbf{K}$   $n_{\text{dof}} \times n_{\text{dof}}$  matrices and  $\mathbf{x}$ ,  $\mathbf{p}$ ,  $\mathbf{f}_{\text{nl}}$   $n_{\text{dof}} \times 1$  vectors. Fig. 1.10a shows that across different modes of vibration, multiple responses can have the same phase lag. As a result, the response surface of a PLL experiment

Table 1.2: Set of parameters for multiple-degree-of-freedom nonlinear systems used as examples in this Chapter

Set	$\mathbf{M}$	$\mathbf{C}$	$\mathbf{K}$	$\mathbf{f}_{\text{nl}}(\mathbf{x}, \dot{\mathbf{x}})$
3	$\begin{bmatrix} 1 & 0 \\ 0 & 1 \end{bmatrix}$	$\begin{bmatrix} .01 & 0 \\ 0 & .01 \end{bmatrix}$	$\begin{bmatrix} 2 & -1 \\ -1 & 2 \end{bmatrix}$	$\begin{bmatrix} x_1^3 \\ 0 \end{bmatrix}$
4	$\begin{bmatrix} 1 & 0 \\ 0 & 1 \end{bmatrix}$	$\begin{bmatrix} .01 & 0 \\ 0 & .01 \end{bmatrix}$	$\begin{bmatrix} 1.05 & -0.05 \\ -0.05 & 1.05 \end{bmatrix}$	$\begin{bmatrix} x_1^3 \\ 0 \end{bmatrix}$

with multiple DOF always exhibits folding across its multiple modes. This issue is exacerbated for multiple DOF oscillators whose resonant modes are not well separated. Fig. 1.10b shows that every phase lag value between  $-\pi$  and 0 does not exist for all modes. This can lead to jumps in frequency e.g. during phase lag sweeps. A method capable of handling multiple-degrees-of-freedom systems is presented in Chapter 6.

## 1.5 Conclusion

In this Chapter, we considered experiments possessing different types of parameters. Internal parameters do not vary during the experiment and are unknown to the experimenter. Measured parameters characterize the response of the experiment. They are known but cannot be defined by the experimenter. User-defined parameters drive the experiment and can be defined arbitrarily by the experimenter. A response surface is the collection of every response in relation with the corresponding input parameters. The folding phenomenon arises when the same set of input parameters corresponds to multiple responses.

The open-loop experiment in which a nonlinear oscillator is excited by a harmonic excitation possesses two input parameters: the frequency and amplitude of the excitation. An FRC (resp. S-curve) is a subset of the response surface at constant excitation amplitude (resp. frequency). In general, the open-loop experiment exhibits folding, i.e. it can follow different responses to the same input parameters.

During a CBC experiment, the oscillator is excited by a controller. Its input parameters are the frequency and amplitude of a reference signal. For

high enough controller gains, each response corresponds to one and only one reference amplitude and the folding disappears. The limiting requirement is that each response must correspond to one and only one fundamental amplitude at constant frequency, i.e., the fundamental S-curves must be monotonous in fundamental response amplitude, or equivalently, different fundamental FRCs must not cross each other.

During PLL testing, the excitation frequency is driven by a controller until the fundamental phase lag reaches a target. Thus, the input parameters are the excitation amplitude and the phase lag target. Thanks to the integral part of the controller, the system is only at equilibrium when the target has been reached. Unlike CBC, the controller gains do not modify the geometry of the response surface. PLL testing is limited to the vicinity of resonances otherwise the controller becomes very sensitive to phase estimation errors. PLL testing experiments with multiple degrees of freedom are always folded across multiple resonant modes.



## Chapter 2

# Stability of control-based methods

### Abstract

The second problem encountered during experimental characterization of nonlinear oscillators in open-loop is the stability of the responses: some are unstable and cannot be observed. Control-based methods exploit feedback loops that allow to modify the experiment's dynamics. In this Chapter, a class of nonlinear oscillators weakly excited and possessing weak nonlinearity and damping are studied analytically. Their advantage resides in the separation of their slow-flow and fast-flow dynamics. Two transformations are proposed to study their slow-flow stability: one is easily applicable to control-based continuation experiments and the other to phase-locked loop testing. On the one hand, we conclude that a control-based continuation experiment behaves like an oscillator with its own stiffness and damping influenced by its controller. A PD controller allows to modify its stiffness and damping regardless of the excitation frequency. Increasing the damping has an unconditional stabilizing effect, i.e., every response can theoretically be stabilized using a differential controller. On the other hand, the stability of a phase-locked loop experiment resides in the interaction between the oscillator's and the controller's dynamics. The experiment's stability is conditional: there exist optimal controller gains beyond which the performance cannot be improved. The speed of the phase lag estimation is critical in the sense that a slow estimator is detrimental to stability.

## 2.1 Introduction

In the introductory Chapter, we have defined a series of experiments illustrated in Fig. 0.1. Although each experiment has a different input parameter set, we have shown in Chapter 1 that they could all share the same steady-state responses. However, each experiment follows its own dynamics: the transient before reaching the steady-state response differs, and more importantly, so does the stability of the response. Depending on the control gains, unstable responses of the open-loop experiment can be stable in the control-based experiments.

In this Chapter, we will derive simplified dynamic systems for each of the three experiments: open-loop, control-based continuation (CBC) and phase-locked loop (PLL) testing. We will consider assumptions uncoupling the dynamics of the oscillations from the evolution of the oscillation envelope. This will allow us to study the working limitations of the control-based methods and the influence of the control gains. We will show that, although the limit points of the dynamic systems are identical, their Jacobians are influenced by the control gains.

The dynamics and stability of the open-loop experiment are developed in Section 2.2. Under the same set of assumptions, Sections 2.2.1 and 2.2.2 propose two equivalent transformations to separate the fast- and slow-flow dynamics of weakly nonlinear oscillators. One of the transformations separates the slow-flow dynamics in sine and cosine components and is called the Van der Pol (VdP) transformation applied, e.g., in [63]. The other is an adaptation of the VdP transformation, parametrizing the slowflow dynamics with a sine component and its phase lag, called the phase VdP transformation.

For the first time, the effects of CBC on the experiment's stability are analyzed in Section 2.3, first including a general LTI controller in Section 2.3.1, then including a simpler PD controller in Section 2.3.2. The derivation of the PLL experiment dynamics in Section 2.4 expand to general nonlinearities the analyses proposed in [49, 64, 65], focused on specific systems. Perfect and flawed phase lag estimations are considered in Sections 2.4.1 and 2.4.2 respectively.

$\omega_0$	$\delta$	$f_{\text{nl}}(x, \dot{x})$
100	0.01	$x^3$

Table 2.1: Set of parameters for a nonlinear oscillator used as an example in this Chapter

## 2.2 Open-loop experiment

During the open-loop experiment, a general nonlinear oscillator is excited by a harmonic force of amplitude  $p$  and frequency  $\Omega$ . Its response  $x$  follows the equation of motion

$$\ddot{x} + \delta\dot{x} + \omega_0^2 x + f_{\text{nl}}(x, \dot{x}) = p \sin(\Omega t), \quad (2.1)$$

with  $\omega_0$  the natural frequency,  $\delta$  the damping ratio, and  $f_{\text{nl}}$  the nonlinear restoring force of the oscillator.

The closed and repeating trajectories followed by the experiment in the phase space  $(x, \dot{x})$  are called periodic orbits. The stability of periodic orbits is difficult to study. By making the right assumptions, the response in phase space  $(x, \dot{x})$  can be transformed, changing the periodic orbits into limit points. This will help us describe the stability of the open-loop experiment. An oscillator whose parameters are given in Table 2.1 is used to illustrate this Chapter.

In the rest of the Chapter, we will assume that

- the nonlinear internal force  $f_{\text{nl}}(x, \dot{x})$ ,
- the damping  $\delta$ ,
- the excitation amplitude  $p$ , and
- the difference between excitation and natural frequency  $\Omega - \omega_0$

are an order of magnitude smaller than any other parameter. The assumptions allow us to separate two time scales, namely the fast-flow dynamics which drive the oscillations and the slow-flow dynamics which govern the time evolution of the envelope of the oscillations.

### 2.2.1 Van der Pol transformation

The VdP transformation [63] redefines the phase space  $(x, \dot{x})$  by coefficients  $(u, v)$ :

$$\begin{cases} x = u \cos(\Omega t) - v \sin(\Omega t) \\ \dot{x} = -\Omega[u \sin(\Omega t) + v \cos(\Omega t)]. \end{cases} \quad (2.2)$$

It is shown in Appendix A.1.1 that, under the assumptions, the open-loop experiment in Eq. (2.1) is transformed into the slow-flow dynamic system

$$\begin{cases} \dot{u} = \frac{1}{2\Omega} (\psi v - \Omega \delta u + g_s(u, v) - p) \\ \dot{v} = \frac{1}{2\Omega} (-\psi u - \Omega \delta v + g_c(u, v)) \end{cases} \quad (2.3)$$

with  $\psi = \Omega^2 - \omega_0^2$ , the reparametrized nonlinear force

$$g(u, v, \Omega t) = f_{nl}(u \cos(\Omega t) - v \sin(\Omega t), -\Omega[u \sin(\Omega t) + v \cos(\Omega t)]), \quad (2.4)$$

and its projections onto harmonic signals

$$g_s(u, v) = \frac{\Omega}{\pi} \int_t^{t+\frac{2\pi}{\Omega}} g(u, v, \Omega \tau) \sin(\Omega \tau) d\tau, \quad (2.5)$$

$$g_c(u, v) = \frac{\Omega}{\pi} \int_t^{t+\frac{2\pi}{\Omega}} g(u, v, \Omega \tau) \cos(\Omega \tau) d\tau. \quad (2.6)$$

The limit points  $(\hat{u}, \hat{v})$  of system (2.3) are constant through time, i.e. they are defined by  $\dot{u}(\hat{u}, \hat{v}) = \dot{v}(\hat{u}, \hat{v}) = 0$ . They solve

$$\begin{cases} \psi \hat{v} - \delta \Omega \hat{u} + g_s(\hat{u}, \hat{v}) - p = 0 \\ -\psi \hat{u} - \delta \Omega \hat{v} + g_c(\hat{u}, \hat{v}) = 0. \end{cases} \quad (2.7)$$

It is in general difficult if not impossible to obtain the solutions to such a nonlinear system of equations in closed form. Rather, numerical methods must be used.

The stability of a limit point is determined by the eigenvalues  $\lambda$  of its Jacobian

$$J(\hat{u}, \hat{v}) = \begin{bmatrix} \frac{\partial \dot{u}}{\partial u} & \frac{\partial \dot{u}}{\partial v} \\ \frac{\partial \dot{v}}{\partial u} & \frac{\partial \dot{v}}{\partial v} \end{bmatrix}_{(\hat{u}, \hat{v})}. \quad (2.8)$$

$$= \frac{1}{2\Omega} \begin{bmatrix} -\Omega \delta + \frac{\partial g_s}{\partial u} & \psi + \frac{\partial g_s}{\partial v} \\ -\psi + \frac{\partial g_c}{\partial u} & -\Omega \delta + \frac{\partial g_c}{\partial v} \end{bmatrix}_{(\hat{u}, \hat{v})} \quad (2.9)$$

When each of its eigenvalues has a negative real part, the limit point is stable, i.e., the system goes back to the limit point when slightly perturbed. The Routh-Hurwitz stability criterion on the characteristic polynomial of  $J$  is

$$2\Omega\delta > \frac{\partial g_s}{\partial u} + \frac{\partial g_c}{\partial v}, \quad (2.10)$$

$$\left(\frac{\partial g_s}{\partial u} - \Omega\delta\right) \left(\frac{\partial g_c}{\partial v} - \Omega\delta\right) > \left(\frac{\partial g_s}{\partial v} + \psi\right) \left(\frac{\partial g_c}{\partial u} - \psi\right) \quad (2.11)$$

at the limit point  $(\hat{u}, \hat{v})$ ; it allows to determine which limit points are unstable depending on the parameters  $\omega_0$ ,  $\delta$ , and nonlinearity  $g$  of the system.

Let us take a Duffing oscillator as an example:

$$\ddot{x} + \delta\dot{x} + \omega_0^2 x + x^3 = p \sin(\Omega t). \quad (2.12)$$

In this case,  $f_{nl}(x, \dot{x}) = x^3$ , therefore

$$g(u, v, \Omega t) = (u \cos(\Omega t) - v \sin(\Omega t))^3, \quad (2.13)$$

$$g_s(u, v) = -\frac{3}{4}v(u^2 + v^2), \quad (2.14)$$

$$g_c(u, v) = \frac{3}{4}u(u^2 + v^2), \quad (2.15)$$

$$\frac{\partial g_s}{\partial u} = -\frac{3}{2}uv, \quad \frac{\partial g_s}{\partial v} = -\frac{3}{4}(u^2 + 3v^2), \quad (2.16)$$

$$\frac{\partial g_c}{\partial u} = \frac{3}{4}(3u^2 + v^2), \quad \text{and} \quad \frac{\partial g_c}{\partial v} = \frac{3}{2}uv. \quad (2.17)$$

Fig. 2.1 shows the  $(u, v)$  coordinates of the open-loop experiment diverging from an unstable limit point  $(\hat{u}, \hat{v})$ .

### 2.2.2 Phase Van der Pol transformation

An alternative to the VdP transformation is to transform the phase space  $(x, \dot{x})$  into the instantaneous amplitude  $r$  and phase  $\phi$  of the response. This leads to the phase VdP transformation:

$$\begin{cases} x = r \sin(\Omega t + \phi) \\ \dot{x} = r\Omega \cos(\Omega t + \phi). \end{cases} \quad (2.18)$$

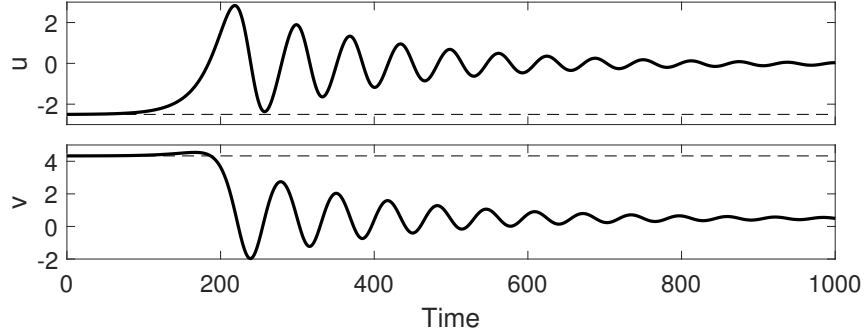


Figure 2.1: Evolution of system (2.3) with initial state  $(u_0, v_0) = (-2.50, 4.33)$  and with parameter set from Table 2.1,  $p = 10$ ,  $\Omega = 100.102$ ; unstable limit point  $(\hat{u}, \hat{v}) = (-2.50, 4.33)$  in dashed lines

It is shown in Appendix A.2.1 that, under the assumptions, the open-loop experiment in Eq. (2.1) is transformed into the slow-flow dynamic system

$$\begin{cases} \dot{r} = -\frac{1}{2} \left( \delta r + \frac{1}{\Omega} (h_c(r) + p \sin \phi) \right) \\ \dot{\phi} = -\frac{1}{2} \left( \frac{\psi}{\Omega} - \frac{1}{\Omega r} (h_s(r) - p \cos \phi) \right), \end{cases} \quad (2.19)$$

with once again  $\psi = \Omega^2 - \omega_0^2$ , the reparametrized nonlinear force

$$h(r, \Omega t + \phi) = f_{\text{nl}}(r \sin(\Omega t + \phi), r \Omega \cos(\Omega t + \phi)), \quad (2.20)$$

and its projections onto harmonic signals

$$h_s(r) = \frac{\Omega}{\pi} \int_t^{t+\frac{2\pi}{\Omega}} h(r, \Omega\tau + \phi) \sin(\Omega\tau + \phi) d\tau \quad (2.21)$$

$$h_c(r) = \frac{\Omega}{\pi} \int_t^{t+\frac{2\pi}{\Omega}} h(r, \Omega\tau + \phi) \cos(\Omega\tau + \phi) d\tau, \quad (2.22)$$

independent of  $\phi$  because  $f_{\text{nl}}$  is assumed periodic with frequency  $\Omega$ . The term  $h_s$  corresponds to the component of the nonlinear force with the same phase as the displacement, i.e. to a nonlinear stiffness, and the term  $h_c$  corresponds to the component of the nonlinear force with the same phase as the velocity, i.e. to a nonlinear damping.

The limit points  $(\hat{r}, \hat{\phi})$  of system (2.19) are defined for  $\dot{r}(\hat{r}, \hat{\phi}) = \dot{\phi}(\hat{r}, \hat{\phi}) = 0$ . They correspond to periodic orbits of system (2.1). The limit points are the solutions to

$$\begin{cases} \delta\Omega\hat{r} + h_c(\hat{r}) + p \sin \hat{\phi} = 0 \\ \psi\hat{r} - h_s(\hat{r}) + p \cos \hat{\phi} = 0. \end{cases} \quad (2.23)$$

If we consider the phase lag  $\phi$  as a known parameter and the excitation frequency  $\hat{\Omega}$  as an unknown, system (2.23) can be rewritten

$$h_c(\hat{r}) + \delta\sqrt{\hat{r}(h_s(\hat{r}) - p\cos\phi + \omega_0^2\hat{r})} + p\sin\phi = 0. \quad (2.24)$$

Using phase VdP, it is only required to solve a single nonlinear equation in  $\hat{r}$ . The frequency

$$\hat{\Omega} = \sqrt{\frac{1}{\hat{r}}(h_s(\hat{r}) - p\cos\phi) + \omega_0^2} \quad (2.25)$$

is derived directly. Under the assumptions made in Section 2.2, Eq. (2.24) is further simplified

$$h_c(\hat{r}) + \delta\omega_0\hat{r} + p\sin\phi \approx 0. \quad (2.26)$$

The stability of a limit point  $(\hat{r}, \hat{\phi})$  is determined by the eigenvalues of its Jacobian

$$J(\hat{r}, \hat{\phi}) = \begin{bmatrix} J_{11} & J_{12} \\ J_{21} & J_{22} \end{bmatrix} = \begin{bmatrix} \frac{\partial \dot{r}}{\partial r} & \frac{\partial \dot{r}}{\partial \phi} \\ \frac{\partial \dot{\phi}}{\partial r} & \frac{\partial \dot{\phi}}{\partial \phi} \end{bmatrix}_{(\hat{r}, \hat{\phi})} \quad (2.27)$$

$$= \frac{1}{2} \begin{bmatrix} -\delta - \frac{1}{\Omega} \frac{dh_c}{dr}(\hat{r}) & -\frac{p}{\Omega} \cos \hat{\phi} \\ \frac{1}{\hat{r}\Omega} \left( -\frac{1}{\hat{r}} h_s(\hat{r}) + \frac{dh_s}{dr}(\hat{r}) + \frac{p}{\hat{r}} \cos \hat{\phi} \right) & \frac{p}{\hat{r}\Omega} \sin \hat{\phi} \end{bmatrix}. \quad (2.28)$$

Its characteristic polynomial is

$$P(\lambda) = \lambda^2 - (J_{11} + J_{22})\lambda + J_{11}J_{22} - J_{12}J_{21}. \quad (2.29)$$

The Routh-Hurwitz stability criterion states that the Jacobian has stable eigenvalues if

$$\delta\Omega + \frac{dh_c}{dr}(\hat{r}) > \frac{p}{\hat{r}} \sin \hat{\phi}, \quad (2.30)$$

$$\delta\Omega + \frac{dh_c}{dr}(\hat{r}) > \left( -\frac{1}{\hat{r}} h_s(\hat{r}) + \frac{dh_s}{dr}(\hat{r}) + \frac{p}{\hat{r}} \cos \hat{\phi} \right) \cot \hat{\phi}. \quad (2.31)$$

Let us once again take the Duffing oscillator as an example. The nonlinear force is  $f(x, \dot{x}) = x^3$ , therefore

$$h(r, \Omega t + \phi) = r^3 \sin^3(\Omega t + \phi), \quad (2.32)$$

$$h_s(r) = \frac{3}{4}r^3, \quad h_c(r) = 0, \quad (2.33)$$

$$\frac{\partial h_s}{\partial r}(r) = \frac{9}{4}r^2, \quad \frac{\partial h_c}{\partial r}(r) = 0. \quad (2.34)$$

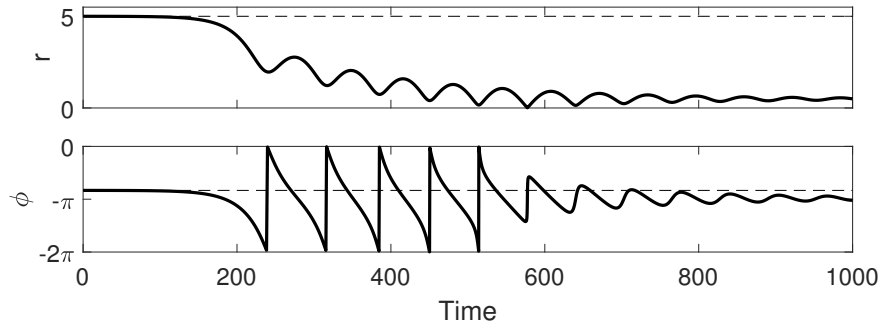


Figure 2.2: Evolution of system (2.19) with initial state  $(r_0, \phi_0, y_0) = (5, -2.62, 0.102)$  and with parameter set from Table 2.1,  $p = 10$ ,  $\Omega = 100.102$ ,  $\phi^* = -2.62$ ,  $k_i = 0$ ,  $k_p = 0$ ; unstable limit point  $(\hat{r}, \hat{\phi}, \hat{y}) = (5, -2.62, 0.102)$  in dashed lines

Fig. 2.2 shows the evolution of the system with an initial state very close to the limit point  $(\hat{r}, \hat{\phi})$  corresponding to the one in Fig. 2.1. After some time, the system diverges towards another limit point at the same frequency but lower amplitude.

## 2.3 Control-based continuation

Control-based continuation (CBC) was introduced as a control-based experiment controlling indirectly the response amplitude by a feedback loop. During the CBC experiment, the response  $x(t)$  follows the equation of motion

$$\ddot{x} + \delta\dot{x} + \omega_0^2 x + f_{nl}(x, \dot{x}) = y(x^* - x). \quad (2.35)$$

The control action  $y(x^* - x)$  excites the same nonlinear oscillator as in the open-loop experiment. It is the output of a controller that takes the difference  $x^* - x$  as an input. The experimenter can define the reference signal  $x^*$  freely; its fundamental frequency  $\Omega$  and fundamental amplitude  $X_1^*$  are the input parameters of the CBC experiment (see Chapter 1).

Although the feedback loop contained inside the experiment modifies the dynamics governing the response  $x(t)$ , we showed in Chapter 1 that each steady-state response of the open-loop experiment could be reached, rendering the CBC experiment useful to characterize the nonlinear oscillator. In this Section, we will show that the CBC experiment responds itself like a nonlinear oscillator with its own modal parameters influenced by the controller. A judicious choice of controller can make every response of the

CBC experiment stable, including responses identical to unstable responses of the open-loop experiment.

### 2.3.1 General controller

At first, let us consider that the excitation  $y$  is the output of a general LTI controller  $C$ . In the Laplace domain,

$$Y(s) = C(s)(X^*(s) - X(s)), \quad (2.36)$$

with  $C(i\Omega) = c(\Omega) + id(\Omega)$ . Under the VdP transformation (Eq. (2.2)) and the assumptions from Section 2.2, Appendix A.1.2 shows that the excitation is expressed

$$y = [c(\Omega)(u^* - u) - d(\Omega)(v^* - v)] \cos(\Omega t) - [d(\Omega)(u^* - u) + c(\Omega)(v^* - v)] \sin(\Omega t), \quad (2.37)$$

with the reference target  $x^* = u^* \cos(\Omega t) - v^* \sin(\Omega t)$ . The slow-flow dynamics of a CBC experiment is

$$\begin{cases} \dot{u} = \frac{1}{2\Omega}((\psi - c)v - (\Omega\delta + d)u + g_s(u, v) + du^* + cv^*) \\ \dot{v} = \frac{1}{2\Omega}(-(\psi - c)u - (\Omega\delta + d)v + g_c(u, v) - cu^* + dv^*). \end{cases} \quad (2.38)$$

Substituting  $y = p \sin(\Omega t)$  into Eq. (2.37) and defining the complex coefficients  $w(t) = (u + iv)/2$  and  $w^* = (u^* + iv^*)/2$ , we obtain

$$p = 2iC(i\Omega)(w^* - w). \quad (2.39)$$

When targeting a known response  $w$ , there is only one reference  $w^*$  leading to  $y = p \sin(\Omega t)$ :

$$w^* = w - \frac{i}{2}C^{-1}(i\Omega)p. \quad (2.40)$$

In practice, the response  $w$  is not known in advance. To target a specific excitation amplitude  $p$ , the experimenter must find the appropriate  $w^*$ , a procedure developed in Chapters 3 and 4. Substituting Eq. (2.40) into Eq. (2.38) and computing the limit points ( $\dot{u} = \dot{v} = 0$ ) lead to Eq. (2.7), i.e., the CBC experiment with an adequate reference signal has a response identical to the open-loop experiment consistently with the conclusions of Chapter 1.

An interpretation of the effects of the controller  $C(s)$  is now apparent. In steady-state, the CBC experiment (Eq. (2.38)) responds itself as a nonlinear

oscillator whose restoring nonlinear force is  $f_{nl}(x, \dot{x})$ , and whose natural frequency and damping are

$$\omega_0^*(\Omega) = \sqrt{\omega_0^2 + c(\Omega)} \quad \text{and} \quad \delta^*(\Omega) = \delta + \frac{d(\Omega)}{\Omega}, \quad (2.41)$$

excited by the signal  $y^*$  obtained when applying  $C(s)$  to  $x^*(t)$ , i.e.,

$$y^*(t) = -(c(\Omega)u^* - d(\Omega)v^*) \cos(\Omega t) + (d(\Omega)u^* + c(\Omega)v^*) \sin(\Omega t). \quad (2.42)$$

The Jacobian of the CBC experiment is expressed in relation to  $J$ , the Jacobian of the open-loop experiment (Eq. (2.9)):

$$J^*(\hat{u}, \hat{v}) = J(\hat{u}, \hat{v}) + \frac{1}{2\Omega} \left( c \begin{bmatrix} 0 & -1 \\ 1 & 0 \end{bmatrix} - d \begin{bmatrix} 1 & 0 \\ 0 & 1 \end{bmatrix} \right). \quad (2.43)$$

Although the CBC experiment's responses are identical to the open-loop experiment, the controller components  $c$  and  $d$  modify the Jacobian. As  $d(\Omega)$  increases, so does the damping  $\delta^*$  (Eq. (2.41)). The result is a shift of the eigenvalues of  $J^*$  towards negative real values, i.e., towards stability. Here lies the crucial strength of a CBC experiment: any response of the nonlinear oscillator can be stabilized by ensuring that the CBC experiment has a large enough damping  $\delta^*$ .

An example of a proper controller leading to an increased damping around the natural frequency  $\omega_0$  is

$$C(s) = \frac{-\omega_0^2 \delta_C k_C}{s^2 + \delta_C s + \omega_0^2}. \quad (2.44)$$

The parameter  $\delta_C$  determines how broad the stabilization is, while the gain  $k_C$  determines the strength of the stabilization, specifically the value of an equivalent differential gain at frequency  $\omega_0$ . Fig. 2.3 shows how this kind of controller locally increases the damping and modifies the natural frequency. The transfer function of controller  $C(s)$  is shown in Fig. 2.4. Its phase lag bounded between 0 and  $\pi$  rad ensures an unconditionally stable closed loop with an oscillator whose phase lag is bounded between  $-\pi$  and 0 rad.

The plain curve in Fig 2.5 shows the  $(u, v)$  coordinates of a CBC experiment using the controller in Eq. (2.44) converging towards the unstable limit point from Fig. 2.1, showing that the CBC experiment is able to identify an unstable response of the open-loop experiment by ensuring a high enough damping  $\delta^*$ .

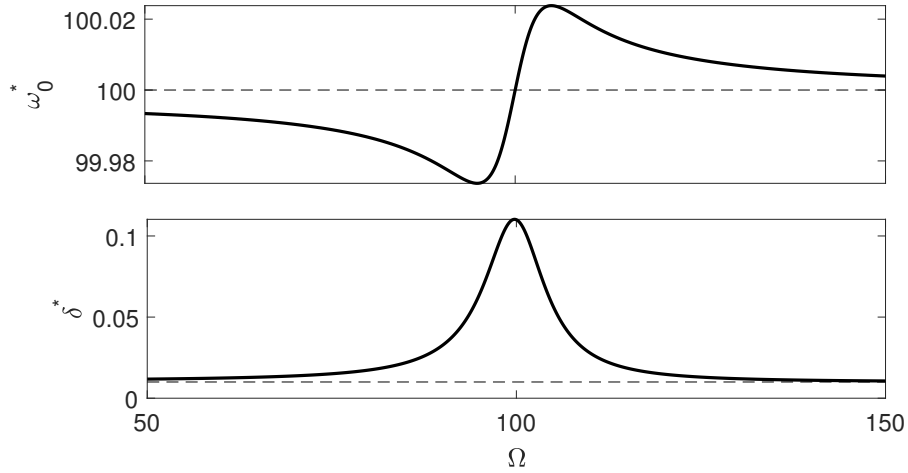


Figure 2.3: Natural frequency and damping of the CBC experiment (2.35) with parameter set from Table 1.1, controller from Eq. (2.44),  $k_C = 0.1$  and  $\delta_C = 10$ ; internal modal parameters  $\omega_0$  and  $\delta$  in dashed lines

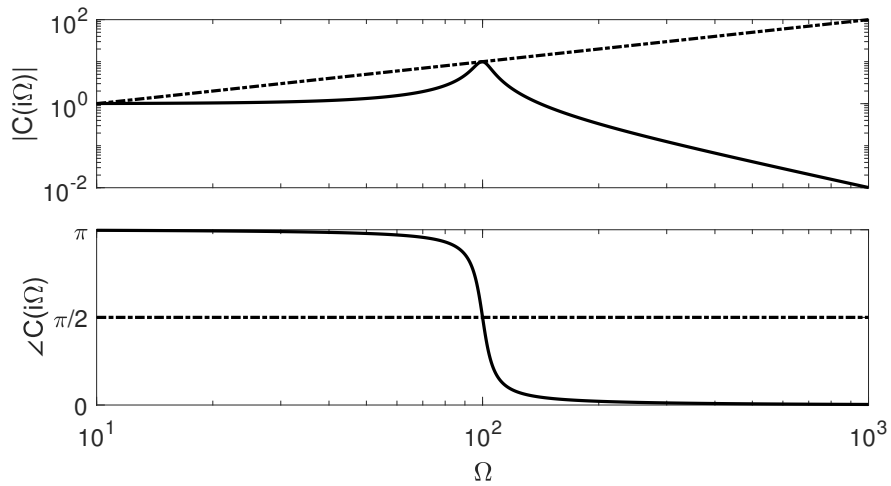


Figure 2.4: Transfer function of the proper controller from Eq. (2.44) with  $\omega_0 = 100$ ,  $k_C = 0.1$  and  $\delta_C = 10$  in plain curve and differential controller with  $k_d = 0.1$  in dashed-dotted curve

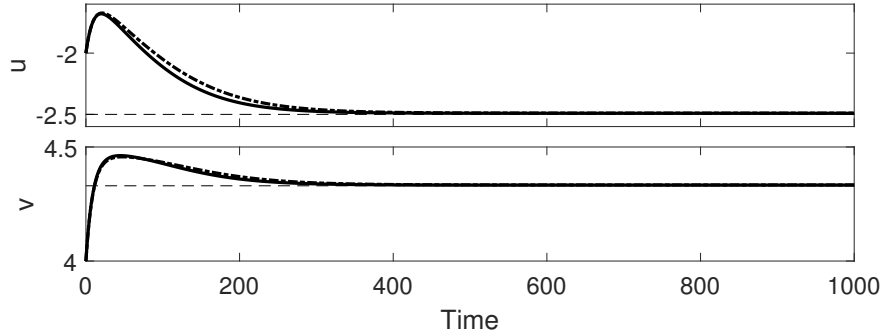


Figure 2.5: Evolution of system (2.38) with initial state  $(u_0, v_0) = (-2, 4)$  and with parameter set from Table 2.1,  $p = 10$ ,  $\Omega = 100.102$ ; driven by the proper controller from Eq. (2.44) with  $k_C = 0.1$  and  $\delta_C = 10$  in plain curve; driven by a differential controller with  $k_d = 0.1$  in dashed-dotted curve; unstable limit point  $(\hat{u}, \hat{v}) = (-2.50, 4.33)$  in dashed lines

### 2.3.2 Proportional-differential controller

A proportional-differential (PD) controller is the special case where  $C(s) = k_p + k_d s$  with a proportional gain  $k_p$  and a differential gain  $k_d$ . The excitation signal becomes

$$y = k_p(x^* - x) + k_d \frac{d}{dt}(x^* - x), \quad (2.45)$$

the modal parameters from Eq. (2.41) become

$$\omega_0^* = \sqrt{\omega_0^2 + k_p} \quad \text{and} \quad \delta^* = \delta + k_d. \quad (2.46)$$

A PD controller therefore allows to set the stiffness and damping of the CBC experiment independently from the excitation frequency.

Increasing the differential gain in theory always has a stabilizing effect. Increasing (resp. decreasing) the proportional gain increases (resp. decreases) the stiffness of the CBC experiment, making the resonance peak shift to a higher (resp. lower) frequency. Usually, fold bifurcations and unstable branches are present around the resonance peak. By shifting the peak, the CBC experiment can exhibit stable branches away from the peak. In this way, a proportional controller can stabilize a CBC experiment, in a more indirect way than the differential controller. These conclusions are in good agreement with what is studied experimentally [34].

Despite the simplicity of a PD controller, it has one main drawback: its transfer function is improper as the degree of its numerator is larger than

the one of its denominator. Hence, high frequency noise is amplified and a discontinuous signal  $x^* - x$  results in an unbounded excitation, as shown by its transfer function in Fig. 2.4.

The dashed curve in Fig 2.5 shows the  $(u, v)$  coordinates of a CBC experiment using a differential controller. The proper controller from Eq. (2.44) and the differential controller have comparable performance, but the effect of the proper controller is localized to the targeted frequency  $\omega_0$ .

## 2.4 Phase-locked loop testing

Let us consider a PLL experiment whose response  $x(t)$  follows the equation of motion

$$\ddot{x} + \delta\dot{x} + \omega_0^2 x + f_{\text{nl}}(x, \dot{x}) = p \sin \theta. \quad (2.47)$$

The instantaneous excitation phase  $\theta(t)$  indicates that the excitation frequency  $\dot{\theta}(t)$  varies through time. In the PLL, a PI controller compares the estimation of the instantaneous phase lag  $\tilde{\phi}$  to a phase lag target  $\phi^*$ :

$$\dot{\theta} = \omega_0 + z + k_p(\tilde{\phi} - \phi^*), \quad (2.48)$$

$$\dot{z} = k_i(\tilde{\phi} - \phi^*). \quad (2.49)$$

The internal parameter  $z$  of the integral controller modifies the excitation frequency along with the proportional controller.

### 2.4.1 Perfect phase estimation

At first and for simplicity, let us assume that the estimation of the phase lag is immediate and without error, i.e.,  $\tilde{\phi} = \phi$ . Under the phase VdP transformation and the assumptions made in Section 2.2, Appendix A.2.2 shows that the slow-flow dynamics of a PLL experiment is

$$\begin{cases} \dot{r} = -\frac{1}{2} \left( \delta r + \frac{1}{\Omega} (h_c(r) + p \sin \phi) \right) \\ \dot{\phi} = -\frac{1}{2} \left( \omega_0 \left( 1 - \frac{\omega_0}{\Omega} \right) + z + k_p(\phi - \phi^*) - \frac{1}{r\Omega} (h_s(r) - p \cos \phi) \right) \\ \dot{z} = k_i(\phi - \phi^*). \end{cases} \quad (2.50)$$

The PLL experiment is therefore completely described by the parameters  $r$ ,  $\phi$ , and  $z$ .

The limit points  $(\hat{r}, \hat{\phi}, \hat{z})$  of system (2.50) are defined for  $\dot{r} = \dot{\phi} = \dot{z} = 0$ . They correspond to orbits of system (2.47). From Eq. (2.48), we deduce that  $\dot{\theta} = 0$  at the limit point, i.e., the excitation frequency is constant.

We therefore can define the constant parameter  $\Omega = \dot{\theta}(\hat{r}, \hat{\phi}, \hat{z})$ . We deduce from Eq. (2.50) that  $k_i \neq 0 \Rightarrow \dot{\phi} = \phi^*$ . Eq. (2.48) therefore implies that  $\Omega = \omega_0 + \hat{z}$ . As per the assumptions made,  $\Omega - \omega_0$  has a small order of magnitude. We conclude that  $\hat{z}^2$  is negligible. The limit points are finally derived

$$\begin{cases} \hat{r} = -\frac{1}{\delta\Omega}(h_c(\hat{r}) + p \sin \phi^*) \\ \hat{\phi} = \phi^* \\ \hat{z} = \frac{1}{2\hat{r}\omega_0}(h_s(\hat{r}) - p \cos \phi^*). \end{cases} \quad (2.51)$$

The system is equivalent to Eq. (2.23) because  $\psi = \Omega^2 - \omega_0^2 \approx 2\omega_0\hat{z}$  neglecting  $\hat{z}^2$ , i.e., the PLL experiment has always a response identical to the open-loop experiment consistently with the conclusions of Chapter 1.

The stability of a limit point is determined by the eigenvalues of its Jacobian

$$\mathbf{J}^*(\hat{r}, \hat{\phi}, \hat{z}) = \begin{bmatrix} \frac{\partial \dot{r}}{\partial r} & \frac{\partial \dot{r}}{\partial \phi} & \frac{\partial \dot{r}}{\partial z} \\ \frac{\partial \dot{\phi}}{\partial r} & \frac{\partial \dot{\phi}}{\partial \phi} & \frac{\partial \dot{\phi}}{\partial z} \\ \frac{\partial \dot{z}}{\partial r} & \frac{\partial \dot{z}}{\partial \phi} & \frac{\partial \dot{z}}{\partial z} \end{bmatrix}_{(\hat{r}, \hat{\phi}, \hat{z})} \quad (2.52)$$

$$= \begin{bmatrix} \mathbf{J}_{11} & \mathbf{J}_{12} & 0 \\ \mathbf{J}_{21} & \mathbf{J}_{22} - k_p & -1 \\ 0 & k_i & 0 \end{bmatrix}. \quad (2.53)$$

The upper-left  $2 \times 2$  matrix contains the Jacobian of the open-loop experiment from Eq. (2.28). Although the PLL experiment's responses are identical to the open-loop experiment, the control gains  $k_p$  and  $k_i$  modify the Jacobian. The characteristic polynomial of  $\mathbf{J}^*$  is

$$P^*(\lambda) = (\lambda k_p + k_i)(\lambda - \mathbf{J}_{11}) + \lambda P(\lambda). \quad (2.54)$$

The control gains  $k_i$  and  $k_p$  have a direct influence on the eigenvalues of the PLL experiment. For illustration, Fig. 2.6 shows the response's longest time constant when targeting the unstable response of the open-loop experiment in Fig. 2.2.

**Low gains** At low gains, the term  $(\lambda k_p + k_i)(\lambda - \mathbf{J}_{11})$  is negligible compared to  $\lambda P(\lambda)$  in Eq. (2.54). The eigenvalues of the PLL experiment are therefore close to the one of the open-loop experiment with an additional root  $\lambda_y \approx 0$  corresponding to a state parameter  $y$  that varies very little when  $k_i$  is small. An unstable response of the open-loop experiment would therefore remain unstable in the PLL experiment, as shown in the lower left corner of Fig. 2.6.

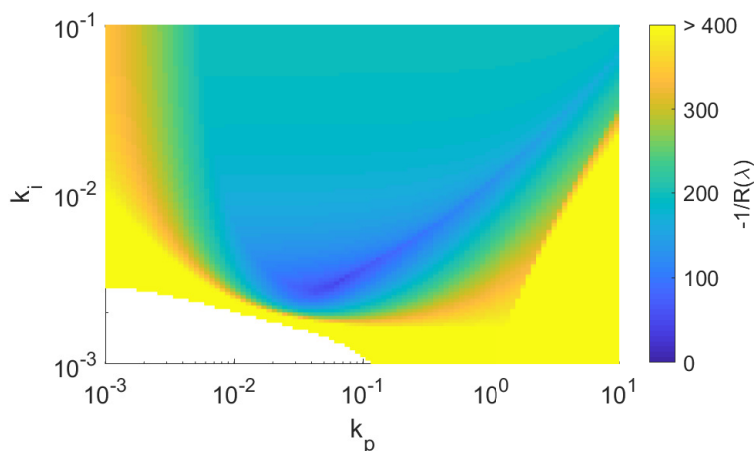


Figure 2.6: Highest time constant for the unstable limit point  $(\hat{r}, \hat{\phi}, \hat{z}) = (5, -2.62, 0.102)$  of system (2.50) depending on the PI controller gains, with parameter set from Table 2.1,  $p = 10$ ,  $\Omega = 100.102$ ; a white area signifies an unstable response

**High gains** At very high gains  $k_i$  and  $k_p$ , the eigenvalues can be approximated

$$\lambda_1 \approx -\frac{k_i}{k_p}, \quad (2.55)$$

$$\lambda_2 \approx -\frac{1}{2} \left( \delta + \frac{1}{\Omega} \frac{dh_c}{dr} \right), \quad (2.56)$$

$$\lambda_3 \approx -k_p. \quad (2.57)$$

The response is always stable if the damping is positive. Under this condition, a PLL experiment with high gains and perfect phase estimation is always capable of identifying an unstable response of the open-loop experiment. However, Eq. (2.56) does not depend on the control gains, showing that the performance will always be constrained by the oscillator's damping. This is visible in Fig. 2.6: the upper right corner shows a stable response, but increasing the control gains further does not reduce the response's time constant.

To show how a PLL experiment can identify an unstable response of the open-loop experiment, Fig. 2.7 shows the evolution of state  $(r, \phi, z)$  of a PLL experiment with optimal control gains converging towards the same unstable response as in Fig. 2.2.

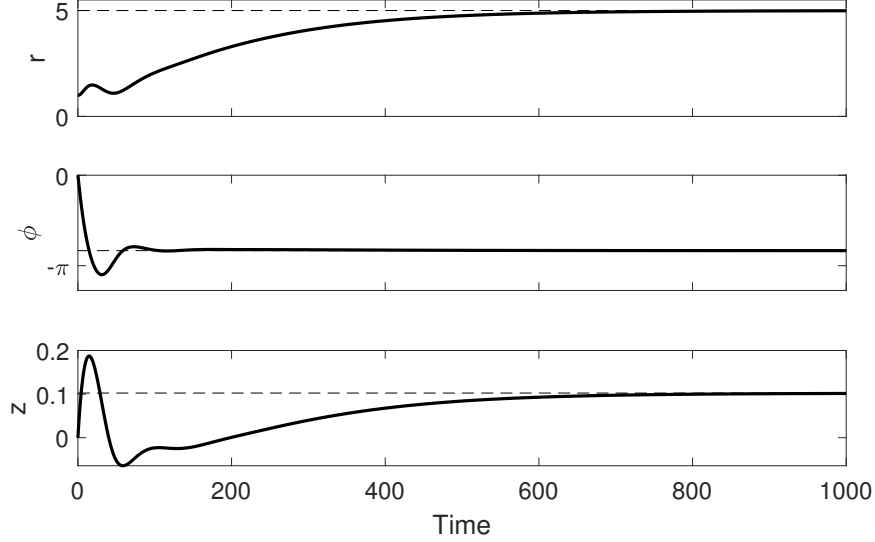


Figure 2.7: Evolution of system (2.50) with initial state  $(r_0, \phi_0, z_0) = (1, 0, 0)$  and with parameter set from Table 2.1,  $p = 10$ ,  $\Omega = 100$ ,  $\phi^* = -2.62$ ,  $k_i = 0.0115$ ,  $k_p = 0.115$ ; unstable limit point  $(\hat{r}, \hat{\phi}, \hat{z}) = (5, -2.62, 0.102)$  in dashed lines

### 2.4.2 Flawed phase estimation

In practice, the estimation of the phase lag  $\tilde{\phi}$  is not immediate. It can be performed in different ways, discussed in Chapter 4. To simplify the analytical expressions, we consider that a low-pass filter with cut-off frequency  $\omega_{lp}$  is applied to the actual phase lag  $\phi$  directly following the analysis proposed in [49]:

$$\dot{\tilde{\phi}} = \omega_{lp}(\phi - \tilde{\phi}). \quad (2.58)$$

Under the assumptions made in Section 2.2, following the development in Appendix A.2.2 leads to the slow-flow dynamic system

$$\begin{cases} \dot{r} = -\frac{1}{2} \left( \delta r + \frac{1}{\Omega} (h_c(r) + p \sin \phi) \right) \\ \dot{\phi} = -\frac{1}{2} \left( \omega_0 \left( 1 - \frac{\omega_0}{\Omega} \right) + z + k_p (\tilde{\phi} - \phi^*) - \frac{1}{r\Omega} (h_s(r) - p \cos \phi) \right) \\ \dot{\tilde{\phi}} = \omega_{lp} (\phi - \tilde{\phi}) \\ \dot{z} = k_i (\tilde{\phi} - \phi^*). \end{cases} \quad (2.59)$$

with an additional state variable  $\tilde{\phi}$  describing the dynamics of the phase lag estimation.

The limit points are now  $(\hat{r}, \hat{\phi}, \hat{z})$ . We deduce from Eq. (2.59) that

$$\dot{z} = 0 \Rightarrow \hat{z} = \phi^*, \quad (2.60)$$

$$\dot{\hat{\phi}} = 0 \Rightarrow \hat{\phi} = \phi^*. \quad (2.61)$$

The limit points solve the nonlinear system of equations

$$\begin{cases} \hat{r} = -\frac{1}{\delta\Omega}(h_c(\hat{r}) + p \sin \phi^*) \\ \hat{\phi} = \phi^* \\ \hat{\phi} = \phi^* \\ \hat{z} = \frac{1}{2\hat{r}\omega_0}(h_s(\hat{r}) - p \cos \phi^*). \end{cases} \quad (2.62)$$

The system is identical to Eq. (2.51) and therefore Eq. (2.23), i.e. the phase lag estimation does not modify the limit points that stay identical to those of the open-loop system. The Jacobian is at the limit point

$$\begin{aligned} \mathbf{J}^*(\hat{r}, \hat{\phi}, \hat{\phi}, \hat{z}) &= \begin{bmatrix} \frac{\partial \dot{r}}{\partial r} & \frac{\partial \dot{r}}{\partial \phi} & \frac{\partial \dot{r}}{\partial \phi} & \frac{\partial \dot{r}}{\partial z} \\ \frac{\partial \dot{\hat{\phi}}}{\partial r} & \frac{\partial \dot{\hat{\phi}}}{\partial \phi} & \frac{\partial \dot{\hat{\phi}}}{\partial \phi} & \frac{\partial \dot{\hat{\phi}}}{\partial z} \\ \frac{\partial \dot{\hat{\phi}}}{\partial r} & \frac{\partial \dot{\hat{\phi}}}{\partial \phi} & \frac{\partial \dot{\hat{\phi}}}{\partial \phi} & \frac{\partial \dot{\hat{\phi}}}{\partial z} \\ \frac{\partial \dot{z}}{\partial r} & \frac{\partial \dot{z}}{\partial \phi} & \frac{\partial \dot{z}}{\partial \phi} & \frac{\partial \dot{z}}{\partial z} \end{bmatrix}_{(\hat{r}, \hat{\phi}, \hat{\phi}, \hat{z})} \\ &= \begin{bmatrix} \mathbf{J}_{11} & \mathbf{J}_{12} & 0 & 0 \\ \mathbf{J}_{21} & \mathbf{J}_{22} & -k_p & -1 \\ 0 & \omega_{lp} & -\omega_{lp} & 0 \\ 0 & 0 & k_i & 0 \end{bmatrix}. \end{aligned} \quad (2.64)$$

The upper-left  $2 \times 2$  matrix is the open-loop Jacobian (2.28).

The characteristic polynomial of  $\mathbf{J}^*$  is

$$P^*(\lambda) = \omega_{lp}(k_p\lambda + k_i)(\lambda - \mathbf{J}_{11}) + \lambda(\lambda + \omega_{lp})P(\lambda). \quad (2.65)$$

Once again, let us discuss the influence of the control gains  $k_i$  and  $k_p$  on the stability of the PLL experiment. For illustration, Fig. 2.8 shows the response's longest time constant when targeting an unstable response.

**Low gains** At low gains, the term  $\omega_{lp}(k_p\lambda + k_i)(\lambda - \mathbf{J}_{11})$  is negligible compared to  $\lambda(\lambda + \omega_{lp})P(\lambda)$  in Eq. (2.65). The eigenvalues of the PLL

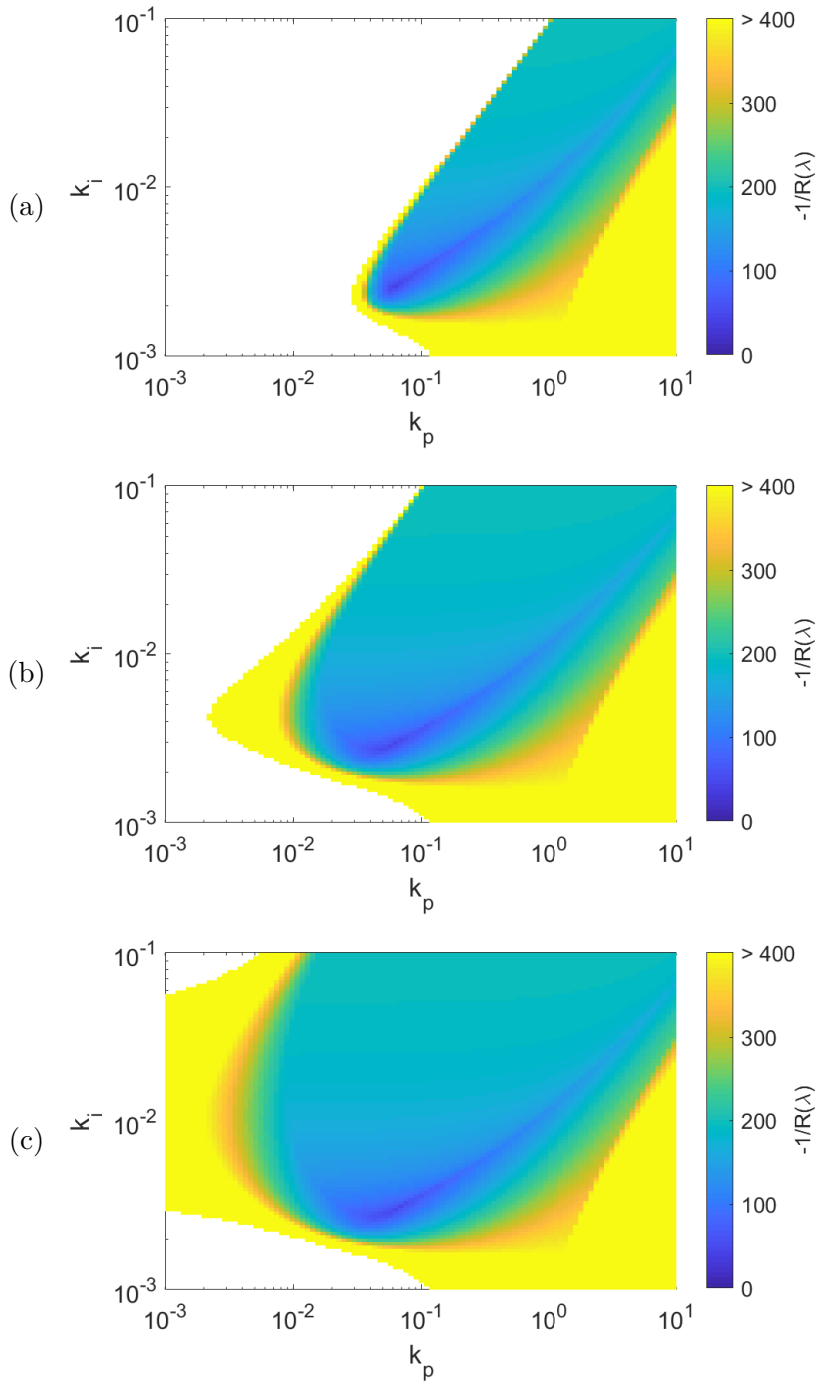


Figure 2.8: Highest time constant for the unstable limit point  $(\hat{r}, \hat{\phi}, \hat{z}) = (5, -2.62, 0.102)$  of system (2.59) depending on the PI controller gains, with (a)  $\omega_{lp} = 0.1$ , (b)  $\omega_{lp} = 1$ , (c)  $\omega_{lp} = 10$ , parameter set from Table 2.1,  $p = 10$ ,  $\Omega = 100.102$ ; a white area indicates that the response is unstable

experiment are therefore close to the one of the open-loop experiment with two additional roots:

$$\lambda_z \approx 0, \quad (2.66)$$

$$\lambda_{\tilde{\phi}} \approx -\omega_{lp}. \quad (2.67)$$

The former corresponds to the state parameter  $z$  varying very little when  $k_i$  is small, and the latter to the dynamics of the low-pass filter when it is uncoupled from the oscillators's dynamics. An unstable response of the open-loop experiment would therefore remain unstable in the PLL experiment, as shown in the lower left corner of Fig. 2.8.

**High gains** At very high gains  $k_i$  and  $k_p$ , the eigenvalues can be approximated by

$$\lambda_1 \approx -\frac{k_i}{k_p}, \quad (2.68)$$

$$\lambda_2 \approx -\frac{1}{2} \left( \delta + \frac{1}{\Omega} \frac{dh_c}{dr} \right), \quad (2.69)$$

$$\lambda_{3,4} \approx \frac{1}{2} \left( \frac{k_i}{k_p} - \omega_{lp} \right) \pm i \sqrt{\omega_{lp} k_p}. \quad (2.70)$$

Unlike the instantaneous phase estimation, increasing both control gains does not necessarily stabilize the system, i.e., the stability is conditioned by the real part of  $\lambda_{3,4}$ . Increasing  $k_i$  has a destabilizing effect that can be compensated by increasing  $k_p$ . The phase estimation must be sufficiently fast, i.e.,  $\omega_{lp}$  must be sufficiently high for responses to be stable, a conclusion shared with [49]. Fig. 2.8 indeed shows that the system is unstable when  $k_i \gg k_p$  (in the upper left corner), and that decreasing  $\omega_{lp}$  shrinks the region in which the response is stable. Similarly to Section 2.4.1, Eq. (2.69) is independent from the control gains, showing that the performance will always be constrained by the damping of the oscillator.

## 2.5 Conclusion

In this Chapter, we have analyzed the stability of experiments during which a nonlinear oscillator is excited. A series of assumptions were made about the experiments: the oscillator is lightly damped and weakly nonlinear, and it is excited at low amplitude close to its natural frequency. The stability analysis of limit points being far easier than for periodic orbits, we have

introduced two transformations allowing to express orbits of the forced oscillator as limit points of a nonlinear dynamic system.

The stability of the open-loop experiment was established by deriving the Jacobian of its slow-flow dynamics. This led to stability conditions depending on the nonlinearity. The same was achieved for the CBC and PLL experiments. We have shown that, although the responses are identical to the open-loop experiment, the controller gains are included in the Jacobian of the corresponding slow-flow dynamics, modifying the experiments' stability conditions. It was shown that an unstable response in the open-loop experiment could always be stable during ideal CBC or PLL experiments.

The CBC experiment responds itself as a nonlinear oscillator whose stiffness and damping depend on the controller, changing the stability conditions of its responses. In particular, when the controller used during the CBC experiment is a PD controller, the proportional and differential gains modify the experiment's stiffness and damping respectively, independently from the excitation frequency. Specifically, the differential gain always shifts the experiment's eigenvalues towards stability. A differential controller alone is therefore capable of stabilizing any orbit under the Chapter's assumptions. However, a differential term in the controller renders the experiment's transfer function improper, amplifying high-frequency noise and giving an unbounded output if its input is discontinuous.

A PLL experiment with instantaneous phase lag estimation can stabilize any orbit if the oscillator's damping is positive. When the estimation of the phase lag is not instantaneous, increasing the control gains asymptotically does not necessarily lead to stability. Specifically, a high integral gain or a slow phase estimation have a destabilizing effect. Whatever the phase estimation, there exists an optimal set of gains above which the performance of the PLL cannot be improved: one of the experiment's time constants is always constrained by the damping of the oscillator independently from the control gains.

## Chapter 3

# Experimental demonstration of control-based continuation and phase-locked loop testing

This Chapter is mainly adapted from the article *A consistency analysis of phase-locked-loop testing and control-based continuation for a geometrically nonlinear frictional system* published in *Mechanical Systems and Signal Processing* Vol. 170, 108820 (2022)

Authors: G. Abeloos, F. Müller, E. Ferhatoglu, M. Scheel, C. Collette, G. Kerschen, M.R.W. Brake, P. Tiso, L. Renson, M. Krack

### Abstract

Two of the most popular vibration testing methods for nonlinear structures are control-based continuation and phase-locked-loop testing. In this Chapter, a detailed implementation is proposed to identify periodic responses at steady-state constituting the phase-resonant backbone curve and nonlinear frequency response curves. The methods are directly compared on the same benchmark system, for the first time, to demonstrate their general capabilities and to discuss practical implementation aspects. The considered system, which is specifically designed for this study, is a slightly arched beam clamped at both ends via bolted joints. It exhibits a pronounced softening-hardening behavior as well as an increasing damping characteristic due to the frictional clamping. To ensure coherent results, the repetition variability is thoroughly assessed via an uncertainty analysis. It is concluded that the results provided by the methods are in excellent agreement.

## 3.1 Introduction

Chapters 1 and 2 were focused on conceptual formulations of control-based experiments. Mathematical models were developed, describing how the experiments would respond in an ideal case. It was assumed that everything was known about the nonlinear oscillator and that we were able to reach any desired state. In actuality, control-based experiments are meant to characterize oscillators of which we know very little. For instance, we do not know in advance what parameters to input or what control gains to choose.

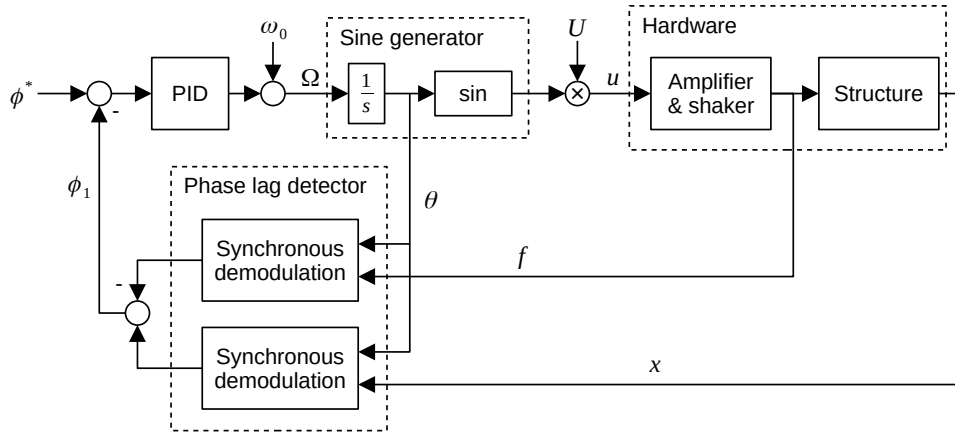
In this Chapter, we define control-based experiments in fine detail. In Section 3.2.1, we present an implementation of the phase-locked loop (PLL) experiment proposed in [47, 58], including the phase lag estimation performed using synchronous demodulation [58]. In Section 3.2.2, we discuss an implementation of the control-based continuation (CBC) experiment proposed in [57], including the necessary operations to ensure that the CBC experiment identifies responses of the open-loop experiment.

The proposed characterization of some nonlinear oscillator is the identification of its backbone curve and frequency response curves (FRCs). The detailed continuation algorithms used to choose adequate input parameters for the identification of backbone curves and FRCs are presented in Sections 3.2.3 and 3.2.4, respectively.

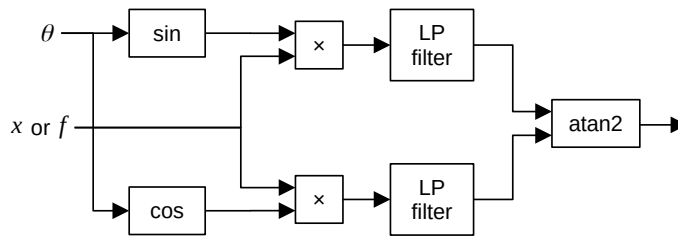
Until now, we assumed that the experimenter was able to apply any force on the oscillator. This is in fact different in practice, i.e., the force is applied by actuators. The experimenter can only choose the signals sent to the actuators. In this Chapter, an electrodynamical shaker applies a force on the oscillator of interest by inputting a voltage signal chosen by the experimenter. Difficulties emanating from this fact are then discussed and practical solutions are proposed. Specifically, the issue of imposing the force amplitude is approached in Section 3.2.4, and some aspects of the shaker-structure interaction (SSI) in Section 3.2.5.

The experimental characterization of a real-life nonlinear structure is presented in Section 3.3. The backbone curve is identified with both methods and compared. The repeatability of the experiments is discussed for each result. FRCs are identified and then compared to FRCs synthesized from the backbone curve data.

After an in-depth conceptual and practical comparison between CBC



(a)



(b)

Figure 3.1: (a) Phase-locked loop and (b) synchronous demodulation [66]

and PLL testing is provided in Section 3.2.6, the choice of adequate control gains without knowledge about the nonlinearity is discussed in Section 3.3.2. Finally, concluding remarks are provided in Section 3.4.

The goal of this Chapter is not to discuss the performance and speed of the methods. To do so would require searching and finding optimal parameters for both methods, something that is out of the scope of this thesis. However, some discussion about performance can be found in Chapter 4.

## 3.2 Methods

### 3.2.1 Phase-locked loop testing

The detailed implementation of PLL testing is illustrated in Fig. 3.1. An electrodynamic shaker excites a nonlinear oscillator through the excitation

force  $f(t)$ . To generate  $f(t)$ , a voltage signal is sent to the shaker:

$$u(t) = U \sin(\theta(t)) = U \sin\left(\int_0^t \Omega(\tau) d\tau\right), \quad (3.1)$$

with instantaneous phase  $\theta(t)$  and time-varying excitation frequency  $\Omega(t)$ . The excitation frequency  $\Omega$  is calculated by a PID control law,

$$\Omega(t) = \omega_0 + k_p(\phi^* - \phi_1(t)) + k_i \int_0^t (\phi^* - \phi_1(\tau)) d\tau - k_d \frac{d\phi_1}{dt}(t). \quad (3.2)$$

The aim is for the phase lag  $\phi_1$  between the fundamental harmonic of the excitation  $f$  and response  $x$  to reach a phase lag target  $\phi^*$  [67]. When the controller has settled, i.e. when the excitation frequency remains constant, the voltage signal is monoharmonic by construction.

A key task within PLL testing is to evaluate the phase lag  $\phi_1$  online, i.e. at each time sample of the experiment. One method to perform this is the synchronous demodulation shown in Fig. 3.1b that consists in an online Fourier decomposition using linear low-pass (LP) filters. It has been successfully applied in other PLL tests [48, 50, 68, 49] and is used in this work. A promising alternative is the use of adaptive filters to perform the online Fourier decomposition (see [69] and Chapter 4).

PLL is capable of stabilizing unstable orbits depending on the gains of its controller (see [49] and Chapter 2). The tuning of the gains is discussed in Section 3.3.2.

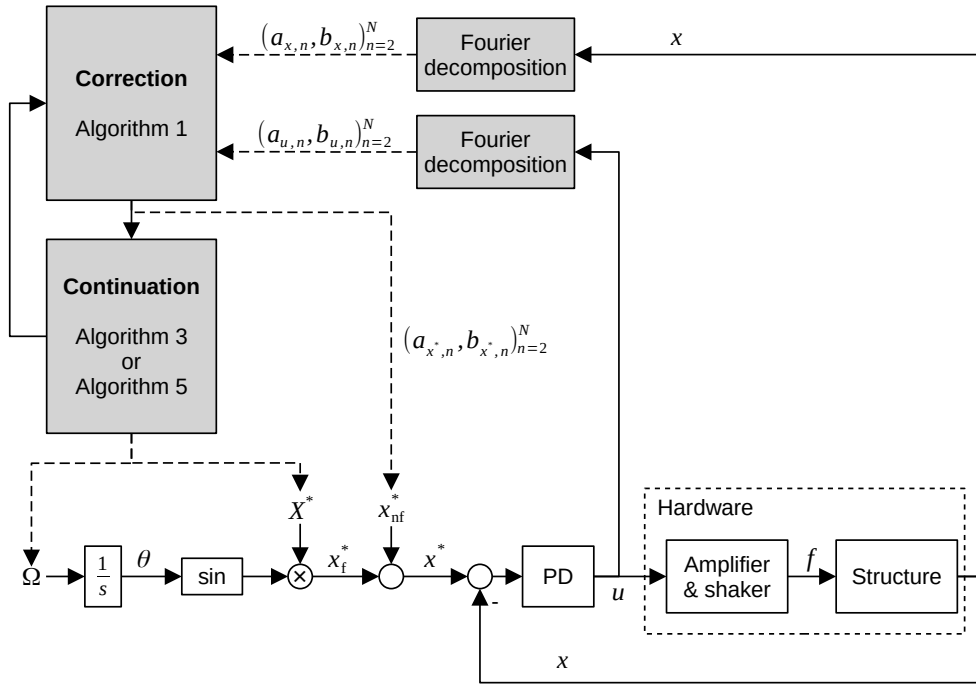
### 3.2.2 Control-based continuation

The general formulation of CBC, as presented in [29], separates the excitation from the control signal that can be applied along the excitation by the same actuator or by a separate actuator. The present Chapter exploits a simplified implementation of CBC [57] shown in Fig. 3.2, in which the excitation is provided by the controller.

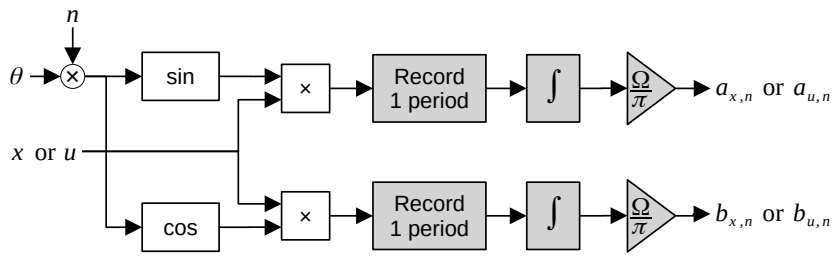
The voltage signal  $u(t)$  is generated by a PD controller whose input is the difference between a reference signal  $x^*$  and the response  $x$  measured on the oscillator:

$$u(t) = k_p(x^*(t) - x(t)) + k_d \frac{d}{dt}(x^*(t) - x(t)). \quad (3.3)$$

The PD controller modifies how the system responds to perturbation and can stabilize unstable orbits (see [34] and Chapter 2). The tuning of the



(a)



(b)

Figure 3.2: (a) Control-based continuation consisting in an online feedback loop and offline correction/continuation algorithms, (b) offline Fourier decomposition for harmonic  $n$ ; offline operations are displayed as grey boxes.

control gains are discussed in Section 3.3.2. Note that CBC does not require a specific type of controller, i.e., another control law could have been used.

The multi-harmonic response of the system generally leads to a multi-harmonic control signal. At steady state, the response  $x$  (see Eq. (1.2)) and the input voltage signal  $u$  can be approximated with truncated Fourier series of  $N$  harmonics:

$$u(t) = \sum_{n=1}^N a_{u,n} \sin(n\Omega t) + b_{u,n} \cos(n\Omega t). \quad (3.4)$$

There exist multiple methods to perform the Fourier decomposition. They are discussed in Chapter 4. In this Chapter, the decomposition is performed offline using the discrete Fourier transform, i.e., by integrating one period of the signal following Fig. 3.2b. The reference signal is constructed to be multi-harmonic with its fundamental component

$$x_f^*(t) = a_{x^*,1} \sin(\Omega t) + b_{x^*,1} \cos(\Omega t) \quad (3.5)$$

and non-fundamental component

$$x_{nf}^*(t) = \sum_{n=2}^N a_{x^*,n} \sin(n\Omega t) + b_{x^*,n} \cos(n\Omega t). \quad (3.6)$$

To compare CBC with PLL testing or even standard open-loop testing methods such as stepped sines, it is necessary to recover a monoharmonic input voltage signal, i.e.  $(a_{u,n}, b_{u,n})_{n=2}^N = 0$ . This can be achieved by adequately choosing the higher-harmonics of the reference signal. Eq. (3.3) shows directly that  $u$  is monoharmonic when

$$(a_{x^*,n}, b_{x^*,n})_{n=2}^N = (a_{x,n}, b_{x,n})_{n=2}^N. \quad (3.7)$$

Eq (3.7) is a zero problem that can be solved using standard root-finding methods while the physical experiment is running. The solver can operate at a frequency that is different or identical to the real-time controller, making iterations offline or online respectively [69]. In this Chapter, the algorithm runs offline and consists in derivative-free Picard-iterations [57]. It is presented in Algorithm 3.1. For the rest of the Chapter, the left arrow operator ( $\leftarrow$ ) signifies a value assignment.

The phase of the reference signal can be constrained by setting  $b_{x^*,1} = 0$ . The only two adjustable parameters of the experiment are the frequency of excitation  $\Omega$  and the fundamental reference amplitude  $X^* = a_{x^*,1}$ . The excitation amplitude  $p$  is not defined by the user but depends on the response  $x$  and reference amplitude  $X^*$ .

---

**Algorithm 3.1** Algorithm to make the voltage monoharmonic during CBC

---

- 1:  $X^*$  defined by user
  - 2:  $(a_{x^*,1}, b_{x^*,1}) \leftarrow (X^*, 0)$
  - 3: **repeat**
  - 4:   Wait a duration  $t_{\text{wait}}$  for steady state
  - 5:   Record time series  $u$  and  $x$  during one period
  - 6:   Perform Fourier decomposition on  $u$  and  $x$
  - 7:    $(a_{x^*,n}, b_{x^*,n})_{n=2}^N \leftarrow (a_{x,n}, b_{x,n})_{n=2}^N$
  - 8: **until**  $\max_n (|a_{u,n}|, |b_{u,n}|)_{n=2}^N < \text{tol}$
- 

---

**Algorithm 3.2** Algorithm to identify backbone curves during PLL testing

---

- 1:  $\phi_{\text{ref}} \leftarrow 0$
  - 2:  $U \leftarrow U_{\text{init}}$
  - 3: **loop**
  - 4:   Wait for convergence of  $\Omega$
  - 5:   Save response
  - 6:    $U \leftarrow U + \Delta U$
  - 7: **end loop**
- 

### 3.2.3 Identification of backbone curves

Phase quadrature is directly imposed by the PLL to identify responses of the backbone curve. A sequential continuation (i.e. a parameter stepping) shown in Algorithm 3.2 is followed to step through different amplitude levels. For the rest of the Chapter, simple loops are used in algorithms to signify that the interruption is decided by the user. For the identification of backbones, it is practical to start at low amplitude and use the corresponding natural frequency  $\omega_0$  of the underlying linear system as initial condition for the excitation frequency  $\Omega$  [23].

Keeping the reference amplitude  $X^*$  constant during CBC and varying the excitation frequency  $\Omega$  allows the continuation of periodic responses with an indirect constraint on the response amplitude under which a single periodic response is in phase resonance (similar to constant-response FRFs identified by the RCT method [53]). CBC therefore enables the identification of backbone curves by performing a sequential continuation on  $X^*$  and solving  $\phi_1(\Omega) = 0$  at every step using the bisection method, as was done in [38]. Both are implemented in Algorithm 3.3.

In summary, the same phase quadrature can be attained by different

---

**Algorithm 3.3** Algorithm to identify backbone curves during CBC

---

```

1:  $X^* \leftarrow X_{\text{init}}^*$ 
2:  $\Omega \leftarrow \omega_0$ 
3: loop
4:    $\Delta\Omega \leftarrow \Delta\Omega_{\text{init}}$ 
5:   Make voltage monoharmonic following Algorithm 3.1
6:   Evaluate  $\phi_1$ 
7:   while  $|\phi_1| > \text{tol}_\phi$  and  $|\Delta\Omega| > \text{tol}_\Omega$  do
8:     if  $\text{sign}(\phi_1 \Delta\Omega) < 0$  then
9:        $\Delta\Omega \leftarrow -\Delta\Omega/2$ 
10:    end if
11:     $\Omega \leftarrow \Omega + \Delta\Omega$ 
12:    Make voltage monoharmonic following Algorithm 3.1
13:    Evaluate  $\phi_1$ 
14:  end while
15:  Save response
16:   $X^* \leftarrow X^* + \Delta X^*$ 
17: end loop

```

---

means during PLL testing and CBC. On the one hand, PLL testing is an online method in that the phase lag converges continuously towards quadrature thanks to the PID controller acting on the excitation frequency. On the other hand, CBC has been implemented as an offline method, i.e. successive periodic responses are identified and an algorithm is used to iterate automatically the excitation frequency until quadrature is found up to tolerance. More operations are made online during PLL testing (numerical integration, synchronous demodulation) while CBC's offline continuation algorithm possesses more steps. The amplitude of the periodic responses is determined by the voltage signal  $U$ , defined directly during PLL testing or indirectly through the reference amplitude  $X^*$  during CBC.

Limitations of the algorithms presented in this section arise when confronted to internal resonance. In such a case, the excitation amplitude could locally decrease along the backbone curve [70]. Given that Algorithm 3.2 increases the excitation amplitude sequentially, such drop would result in a jump in the backbone curve. A solution to this problem is proposed in Chapter 7.

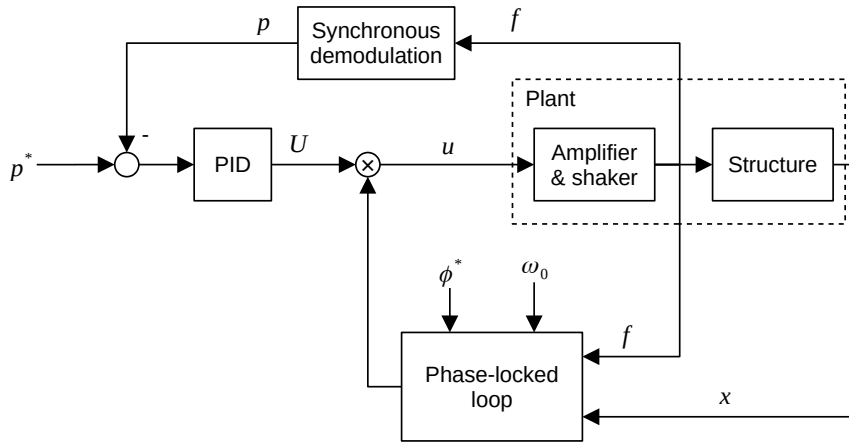


Figure 3.3: Amplitude control of the voltage  $U$  to reach a reference excitation amplitude  $p^*$  for the identification of FRCs during PLL testing

---

**Algorithm 3.4** Algorithm to identify FRCs during PLL testing

---

- 1:  $p^*$  defined by user
  - 2:  $\phi^* \leftarrow \phi_{\text{init}}^*$
  - 3: **loop**
  - 4:   Wait for convergence of  $U$  and  $\Omega$
  - 5:   Save response
  - 6:    $\phi^* \leftarrow \phi^* + \Delta\phi^*$
  - 7: **end loop**
- 

### 3.2.4 Identification of frequency response curves

The identification of FRCs requires a constant-amplitude, single-harmonic excitation. To reach a constant excitation amplitude  $p$  at the fundamental excitation frequency, the feedback loop shown in Fig. 3.3 is introduced on top of the controlled experiment. This loop contains a synchronous demodulation to measure  $p$  online and a PID controller that adjusts the amplitude  $U$  of the voltage signal to reach the forcing amplitude  $p^*$ . The force applied to a nonlinear structure also contains higher harmonics, which typically result from shaker-structure interactions and the lack of linearity between the voltage sent to the shaker's amplifier and the force applied by the shaker. A method to compensate for these higher harmonics and cancel them is presented in Section 3.2.5. The algorithm to identify FRCs using PLL testing is shown in Algorithm 3.4. It performs a sequential continuation on the phase lag in the vicinity of the resonance [68].

---

**Algorithm 3.5** Algorithm to identify a collection of S-curves during CBC in order to approximate FRCs from the dynamic response surface

---

```

1:  $X^* \leftarrow X_{\text{init}}^*$ 
2:  $\Omega \leftarrow \Omega_{\text{init}}$ 
3: loop
4:   loop
5:     Make voltage monoharmonic following Algorithm 3.1
6:     Save response
7:      $X^* \leftarrow X^* + \Delta X^*$ 
8:   end loop
9:    $X^* \leftarrow X_{\text{init}}^*$ 
10:   $\Omega \leftarrow \Omega + \Delta\Omega$ 
11: end loop

```

---

Although CBC can be used for the direct identification of FRCs, more complicated continuation procedures are required to go around fold bifurcations (see [32, 41, 71] and Chapter 6). It is usually easier to identify S-curves and extract FRCs through post-processing as in [38]. Keeping the excitation frequency  $\Omega$  constant and varying  $X^*$  enables the continuation of S-curves following Algorithm 3.5. In the absence of internal resonance, S-curves vary monotonically with  $X^*$  and a sequential continuation procedure is applicable (otherwise, see Chapter 5). Identifying a collection of S-curves at different frequencies and defining a suitable interpolation allows to identify the full (continuous) response surface. Regression techniques can then be exploited to approximate FRCs at constant excitation amplitude  $p$ . This indirect identification removes therefore the need for the feedback loop applied to the fundamental excitation amplitude shown in Fig. 3.3 and used during PLL testing.

In summary, the same periodic responses can be identified during PLL testing and CBC. In the former, a continuation on the phase lag can be made thanks to the PLL. However, it is necessary to add an additional control loop during PLL testing in order to impose the desired FRC's excitation amplitude  $p$ . CBC can identify FRCs directly and would, in that case, also require additional effort to impose  $p$  (e.g. a control loop or iterations). Alternatively, S-curves can be identified sequentially and interpolated into a continuous response surface in post-processing, providing an approximation of the FRCs of interest. As discussed in Section 3.2.5, the two methods can use an additional control loop to cancel higher harmonics present in the applied excitation.

### 3.2.5 Compensation of the shaker-structure interaction

Shaker-structure interaction (SSI) can result in multiple phenomena including resonance force drop, jumps, internal resonance, or subharmonic resonance [72]. Although these phenomena were not observed in the experiments of this Chapter, higher harmonics in the applied force were. As the excitation is directly measured at the application point by an impedance head, it can be directly validated, i.e., if the force signal is close to a sine wave at the desired amplitude, the system's response is accepted.

Without additional control, a monoharmonic voltage  $u$  can lead to a multiharmonic excitation  $f$  [23]. The excitation  $f$  can be approximated by a truncated Fourier series of  $N$  harmonics:

$$f(t) = \sum_{n=1}^N a_{f,n} \sin(n\Omega t) + b_{f,n} \cos(n\Omega t). \quad (3.8)$$

The amplitude and phase of harmonic  $n$  are expressed as  $F_n = \sqrt{a_{f,n}^2 + b_{f,n}^2}$  and  $\phi_{f,n} = \text{atan2}(b_{f,n}, a_{f,n})$ , respectively. Once the voltage  $u$  is monoharmonic during CBC or PLL testing, a correction is computed from its instantaneous voltage phase  $\theta$  by a proportional controller:

$$u_{\text{nf},n} = -k_p F_n \cos(n\theta(t) - \phi_{f,n}) \quad (3.9)$$

shown in Fig. 3.4. In this paper, this correction was done for only  $n = 2$  and 3 as the higher harmonics were not significant in the experiments. The controller gain is discussed in Section 3.3.2.

This method makes the assumption that the shaker is phase-neutral, i.e. the phase-lag between the voltage and the force is zero. At high amplitudes, when the SSI is most significant, the shaker indeed approaches phase-neutrality and the higher harmonics are reduced by the feedback loop. At low amplitudes, the phase-lag added by the shaker approaches  $90^\circ$  between the voltage and the force. The violation of the assumption is considered acceptable due to the low amplitude of higher harmonics in this case. The discussion of the limitations of the method are beyond the scope of this Chapter. Until more analytical work is done, the method is to be considered *ad-hoc* and not generally applicable.

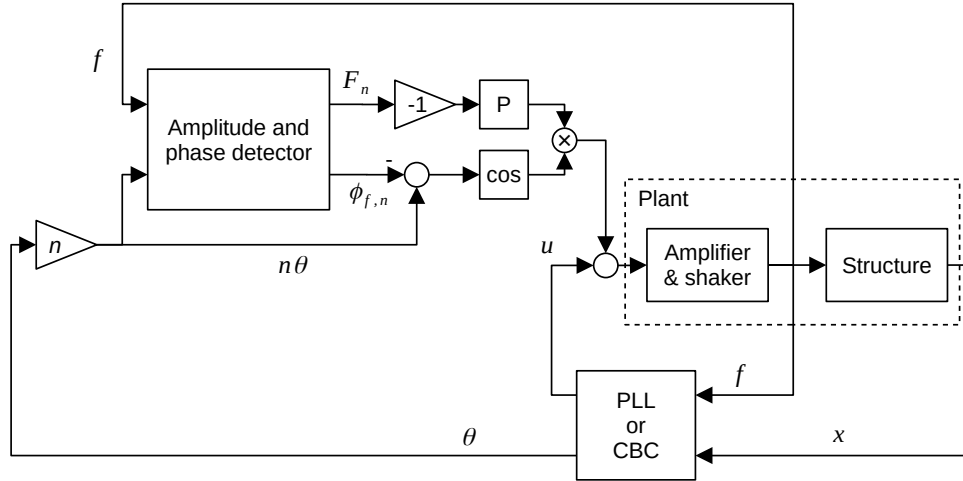


Figure 3.4: Shaker-structure interaction control correcting the  $n^{\text{th}}$  harmonic of the voltage by a proportional controller (P)

### 3.2.6 Comparison of the methods

To summarize the previous sections, a general comparison of the working principles behind phase-locked loop (PLL) testing and control-based continuation (CBC) is summarized below.

Control	<p><b>PLL testing</b> includes a controller designed to reach a phase lag target. It is usually a PI controller [48], the proportional gain providing stability and the integral gain leading to a zero set point error (see Chapter 2). The control and excitation are applied via the same actuator.</p> <p><b>CBC</b> includes a controller designed to stabilize the system's response by comparing it to a reference signal. The actuator used to apply the control can be identical or different to the one used to apply the system excitation. With the simplified CBC method, the controller is not required to reach the reference signal. Examples of controllers include PD controllers [29] and controllers designed by pole-placement techniques [40].</p>
---------	--

Identified features	<p><b>PLL testing</b> controls the phase lag. It is naturally suited to identify backbone curves [48] and FRCs [67, 68]. <b>CBC</b> controls the response signal. It can identify FRCs [32, 57, 41] and backbone curves [38] but can also reach a broader range of responses that might not be well parametrized by the phase [39].</p>
Harmonic excitation	<p><b>PLL testing</b> is designed to send a monoharmonic voltage to the exciter once the PLL has converged, such that measured responses are directly comparable with responses obtained with open-loop methods such as stepped sines.</p> <p>With <b>CBC</b>, the voltage provided to the exciter is a priori multi-harmonic such that a specific reference signal must be found to recover results comparable with open-loop tests.</p> <p><b>Both methods</b> require additional precautions to cancel higher harmonics present in the applied force, due to e.g. shaker-structure interaction.</p>
Online/offline variants	<p><b>PLL testing</b> is an online method, i.e. the method runs in real time. The Fourier decomposition must be online as the phase lag is fed to the controller.</p> <p><b>CBC</b> comprises in general an offline algorithm running in parallel to the experiment and performing the continuation procedure. Online variants are possible [69].</p>

Additionally, here is a comparison of more practical aspects focusing on the continuation algorithms to identify FRCs and backbone curves, the features of interest in this Chapter.

Identification of backbone curves	<p>With <b>PLL testing</b>, backbone curves are identified by keeping the phase lag constantly at quadrature and performing a sequential continuation on the voltage amplitude.</p> <p>With <b>CBC</b>, backbone curves are identified by performing a sequential continuation on the voltage amplitude and finding phase quadrature at each step by iterating on the excitation frequency.</p>
-----------------------------------	---

Identification of FRCs With **PLL testing**, FRCs are identified by keeping the force amplitude constant via an additional control loop and performing a sequential continuation on the phase lag. With **CBC**, FRCs can be identified by implementing a pseudo-arclength continuation [32]. In this Chapter, FRCs are extracted from a collection of S-curves identified by keeping the frequency constant and performing a sequential continuation on the voltage amplitude [57].

### 3.3 Experiments

In this Section, the PLL and CBC experiments as described in this Chapter are applied to characterize a physical structure with nonlinear behavior. It consists of a thin beam slightly curved bolted to a frame to form a doubly clamped beam presented in Section 3.3.1.

The system is subjected to a series of experiments to characterize the first bending mode of the beam. Specifically, a harmonic force  $f = p \sin(\Omega t)$  is applied vertically to the frame. Its acceleration  $\ddot{x}$  is measured by an impedance head while the velocity  $\dot{x}$  of the beam is measured by a laser vibrometer. When periodic, these signals define closed orbits characterizing the system's response to the excitation.

PLL testing and CBC are independently used to identify the periodic responses of the beam at and around the resonance of the first bending mode. The excitation frequency at resonance  $\omega$  depends on the amplitude of the response and is obtained through the identification of backbone curves in Section 3.3.3 following the method presented in Section 3.2.3. The backbone is used for estimating the modal properties of the NNM, presented in Section 3.3.4. These properties define a reduced order model [73] which enables to synthesize FRCs in the vicinity of the mode, presented in Section 3.3.5. Additionally, FRCs are directly identified during experiments in Section 3.3.6 following the method presented in Section 3.2.4.

#### 3.3.1 Experimental setup

The main structure of the experimental campaign is presented in [51, 74] and consists of a thin arched beam whose both ends are clamped via bolted joints to a frame. The slightly curved beam was specifically designed in [75] to observe a softening-hardening behavior in the experiments. The beam's

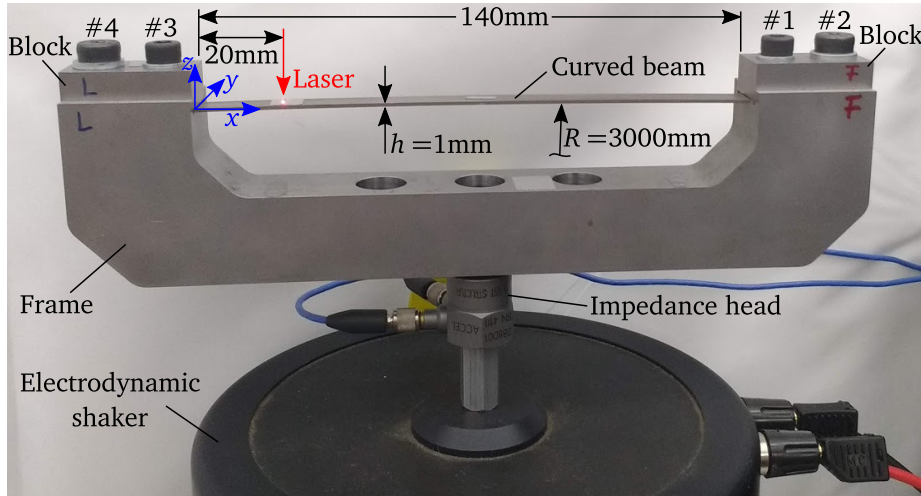


Figure 3.5: Test rig consisting in a thin arched beam with both ends clamped to a frame which is connected to an electrodynamic shaker

shape is defined as a circular arc with radius of curvature  $R$  and constant thickness  $h$ , see Fig. 3.5. The detailed properties of the material, screws and mounting procedure to ensure a proper clamped-clamped boundary condition is available in [51, 74].

The frame supporting the curved beam is connected to an electrodynamic shaker (B&K type 4809 driven by amplifier type 2718). An impedance head (PCB 288D01) is placed between the shaker's armature and the frame to measure both excitation force and acceleration of the frame at the drive point. The beam's response is measured by a laser Doppler vibrometer (Polytec OFV-5000 with OFV-552-2 laser head) 20 mm away from the left clamping. The measurement location was chosen close to clamping to avoid instabilities in feedback loops emanating from the measurement and driving points being non-collocated.

The velocity  $\dot{x}$  measured by the laser vibrometer is transformed into the displacement  $x$  that constitutes the beam's response. The force  $f$  measured by the impedance head constitutes the excitation. When a harmonic voltage of the form  $u(t) = U \sin(\Omega t)$  is sent to the electrodynamic shaker, it generates the force  $f(t)$  as illustrated in Figs. 3.1 and 3.2.

At low forcing amplitudes, the beam is assumed to behave linearly. Therefore, the modal properties corresponding to the lowest frequency bending mode of the underlying linear system were determined using a hardware platform for linear modal analysis (m+p VibRunner). A random voltage

Table 3.1: Parameters for Algorithm 3.1

$t_{\text{wait}}$ in s	tol in V
1	0.05

Table 3.2: Parameters for Algorithm 3.2

$U_{\text{init}}$ in V	$\Delta U$ in V
0.006	0.006

Table 3.3: Parameters for Algorithm 3.3

$X_{\text{init}}^*$ in m/s	$\Delta X^*$ in m/s	$\Delta\Omega_{\text{init}}$ in rad/s	$\text{tol}_\phi$ in rad	$\text{tol}_\Omega$ in rad/s
0.01	0.02	1	0.05	0.01

signal was sent to the shaker's amplifier with an amplitude of 0.03 V and a frequency range between 10 and 3200 Hz. The natural frequency was measured to be  $\omega_0 = 1988$  rad/s, and the damping ratio  $\delta_0 = 0.026\%$ . To realize the control loops of PLL testing and CBC (see Sect. 3.2.1 and 3.2.2 for details), the sensors and the amplifier are connected to a rapid control prototyping system (dSPACE MicroLabBox, sampling frequency: 10,000 Hz).

### 3.3.2 Parameters and gains

This Section presents the value chosen for each parameter introduced in this Chapter. They heavily depend on the application and almost certainly will not be adequate for other experiments. Each parameter was chosen by trial and error, and there could exist parameters leading to a faster or more accurate characterization. Chapter 4 provides some discussion about speed and performance.

The parameters used in Algorithm 3.1 are shown in Tables 3.1. On the one hand, a shorter waiting time  $t_{\text{wait}}$  might introduce error in the Fourier decomposition because of transients that are not fully damped out. On the other hand, waiting time longer than the settling time increases the duration of the experiment without benefit. A higher tolerance might reduce the duration of the experiment, but enhances higher harmonics in the voltage signal. A potential consequence is for the CBC experiment to exhibit responses different from the open-loop experiment.

The parameters used in Algorithms 3.2 and 3.3 are shown in Table 3.2 and 3.3 respectively. The initial amplitudes  $U_{\text{init}}$  and  $X_{\text{init}}^*$  determine the

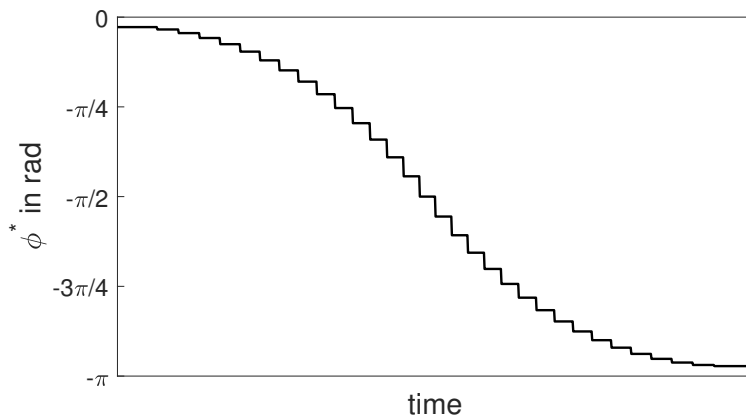
Figure 3.6: Proposed time profile of  $\phi^*$  for Algorithm 3.4

Table 3.4: Parameters for Algorithm 3.5

$X_{\text{init}}^*$ in m/s	$\Omega_{\text{init}}$ in rad/s	$\Delta X^*$ in m/s	$\Delta\Omega$ in rad/s
0.01	1967	0.01	3.14

lowest excitation level of the backbone curve. Small step sizes  $\Delta U$  and  $\Delta X^*$  increase the duration of the experiment but lead to a finer identified curve. The initial frequency step size  $\Delta\Omega_{\text{init}}$  influences the time taken to converge to the resonance frequency  $\omega$  during a CBC experiment. A large phase tolerance  $\text{tol}_\phi$  diminishes the accuracy of the identified backbone curve during the CBC experiment, while the frequency tolerance  $\text{tol}_\Omega$  determines the acceptable accuracy limit.

The parameters in Algorithm 3.4 consist only in the evolution of the phase lag target. For lightly damped structures, the ratio  $\partial\Omega/\partial\phi$  is small at resonance but large away from it. To avoid divergence of the controller after a phase step (e.g. towards another mode) and to obtain reasonably spaced data points in the amplitude frequency plane, smaller steps of the reference phase are chosen away from resonance, shown in Fig. 3.6.

The parameters used during Algorithm 3.5 are shown in Table 3.4. The initial amplitude  $X_{\text{init}}^*$  and frequency  $\Omega_{\text{init}}$  determine the starting point of the sought response surface. The amplitude step  $\Delta X^*$  determines how fine the identified S-curves are going to be. Finer S-curves take longer to identify, but a large  $\Delta X^*$  might lead to jumps in the unstable branches, leaving an S-curve only partially identified. The frequency step  $\Delta\Omega$  determines how close to each other the S-curves will be. Certain regions of the response surface

Table 3.5: Gains of the controllers used in PLL testing and in CBC (\* backbone identification, † FRC identification)

	PLL	Ampl. control (PLL)	CBC	SSI control
$k_p$	150 s <sup>-1</sup>	120 <sup>†</sup>	20 Ns/m	12*,40 <sup>†</sup>
$k_i$	50 s <sup>-2</sup>	40 <sup>†</sup> s <sup>-1</sup>	–	–
$k_d$	40*, 10 <sup>†</sup>	0.04 <sup>†</sup> s	0.4 Ns <sup>2</sup> /m	–

such as the resonance peak of a lightly damped structure might need a fine frequency resolution to be accurately interpolated or approximated.

There is currently no general method to construct a control law for control-based methods to reach their control objectives—e.g. the stabilization of unstable responses—without knowing some characteristics of the system. However, control-based methods are meant to be applicable without the need to identify a model beforehand. There is some promising but very early proposals for such tuning methods, for instance using control Lyapunov-Razumikhin functions [76] or adaptive control design [77, 78]. In the meantime, control gains are tuned heuristically, i.e., by trial and error. The formal derivation of the influence and effect of each control gain on the dynamics of general systems is developed in Chapter 2.

The controller used during PLL testing has a conventional purpose: the phase lag  $\phi_1$  between the beam’s velocity and the force must converge towards the reference phase lag  $\phi^*$ . One can therefore use manual tuning for PID controllers, as proposed for instance in [79]. The PID gains found in this way are shown in the first column in Table 3.5. A similar methodology is followed for tuning the PID controller used to impose a constant force amplitude.

During the CBC experiment, a PD controller is chosen to stabilize the responses, following the conclusions of Chapter 2. To tune the gains in practice, a frequency at which the structure exhibits unstable responses at the force levels of interest is chosen. Successive S-curves are identified following Algorithm 3.5. The proportional and differential gains are increased progressively until all of the S-curve are stabilized.

### 3.3.3 Backbone curves

Figure 3.7a shows backbone curves identified during PLL testing and CBC following Algorithms 3.2 and 3.3. The experiment was repeated six times

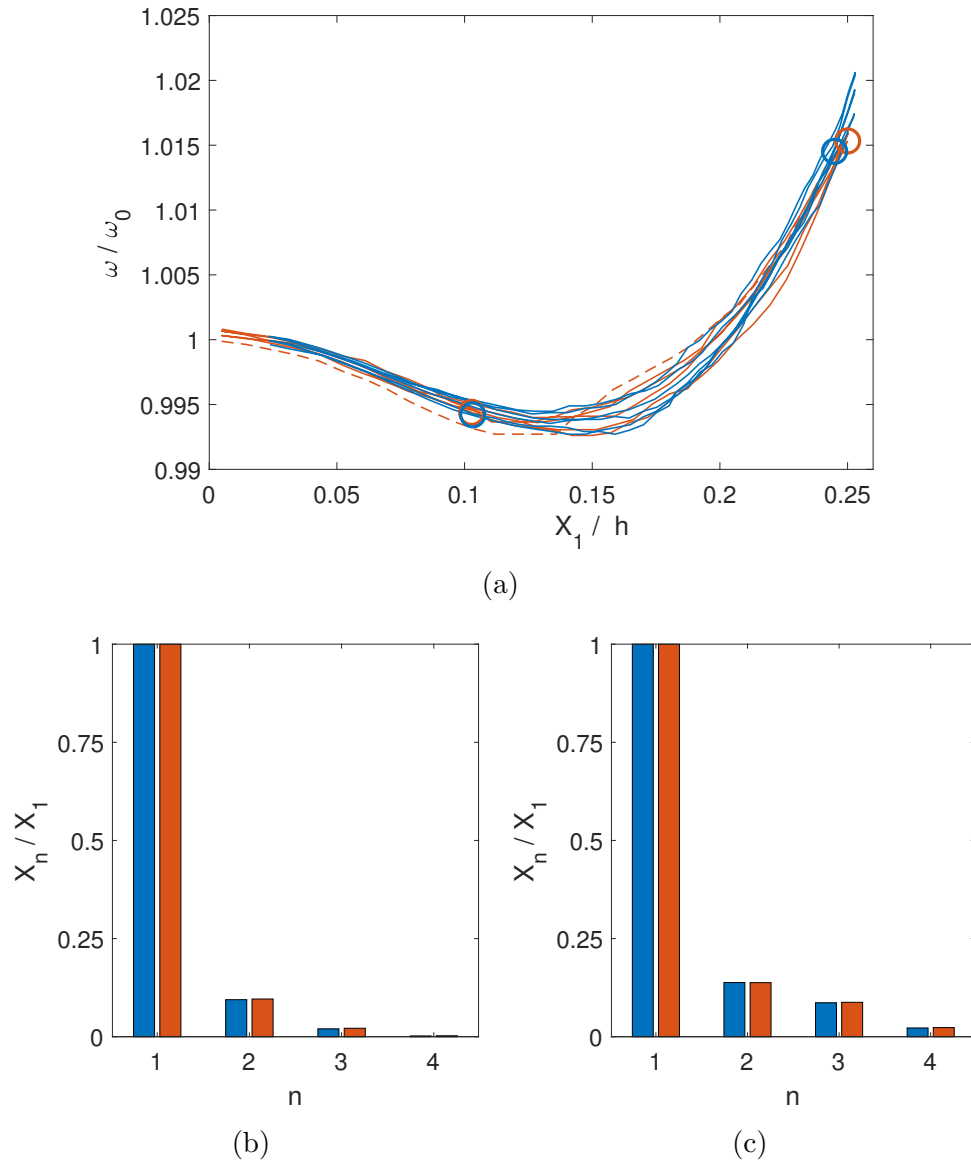


Figure 3.7: (a) Backbone curves identified with PLL testing (blue curve) and CBC (orange curve) from six successive experimental identifications (warm-up in dashed curve); frequency content of periodic responses at resonance and at amplitudes (b)  $X_1/h \approx 0.1$  and (c)  $X_1/h \approx 0.25$  identified during PLL testing (blue) and CBC (orange)

in a row to assess repeatability. The first experiment of the series applied CBC and resulted in a qualitatively different identification (dashed curve). It is suspected that the temperature of the beam increased during the experiment, resulting in a change of modal properties. The curve is therefore discarded while the five subsequent CBC experiments and six PLL testing experiments constitute the results. The frequency content of two periodic responses—one at low amplitude in the softening regime and the other at high amplitude in the hardening regime—is shown in Figs. 3.7b and 3.7c. The low amplitude of higher harmonics relative to the fundamental supports the assumption that a single mode is excited without modal interaction.

The minimum amplitude reachable during the experiments depends on the signal-to-noise ratio. PLL testing requires an online Fourier decomposition for the phase lag to be fed into the PLL controller at each sample time. Low signal-to-noise ratio prevents the PLL from converging and low-amplitude responses are left unidentified. In contrast, the offline Fourier decomposition used during CBC can gather as much data as needed before proceeding with the continuation algorithm. This allows averaging of the signals and better performance at low signal-to-noise ratios.

The nonlinear natural frequency  $\omega$  approaches the linear natural frequency  $\omega_0$  at low amplitudes. The beam exhibits a softening behavior until an amplitude  $X_1/h \approx 0.15$  above which  $\omega$  increases. This turning point corresponds to a displacement amplitude of  $0.67h$  at the beam's center (estimated using the linear mode shape of the FE model). A softening-hardening transition at this amplitude is expected from a slightly curved beam, as demonstrated in [80] showing excellent agreement between the results and theory.

Let the successive backbone curves be described by the functions  $\omega_k(X_1)$  for the  $k^{\text{th}}$  curve. For every value  $X_1$ , the standard deviation  $\sigma(\omega)$  is computed and shown in Fig. 3.8a. The standard deviation increases suddenly when reaching amplitude  $X_1/h = 0.15$ , corresponding to the softening-hardening transition, and stays large at higher amplitudes. The maximum standard deviations

$$\begin{aligned} \max_{X_1} \sigma(\omega_k(X_1)) &= 0.00145\omega_0 && \text{for PLL testing and} \\ &= 0.00137\omega_0 && \text{for CBC,} \end{aligned}$$

are comparable between the methods. These values are small in absolute value but relatively significant in the light of the amplitude-dependent frequency change of about  $-0.5\%$  and  $+2\%$  attributed to the softening and

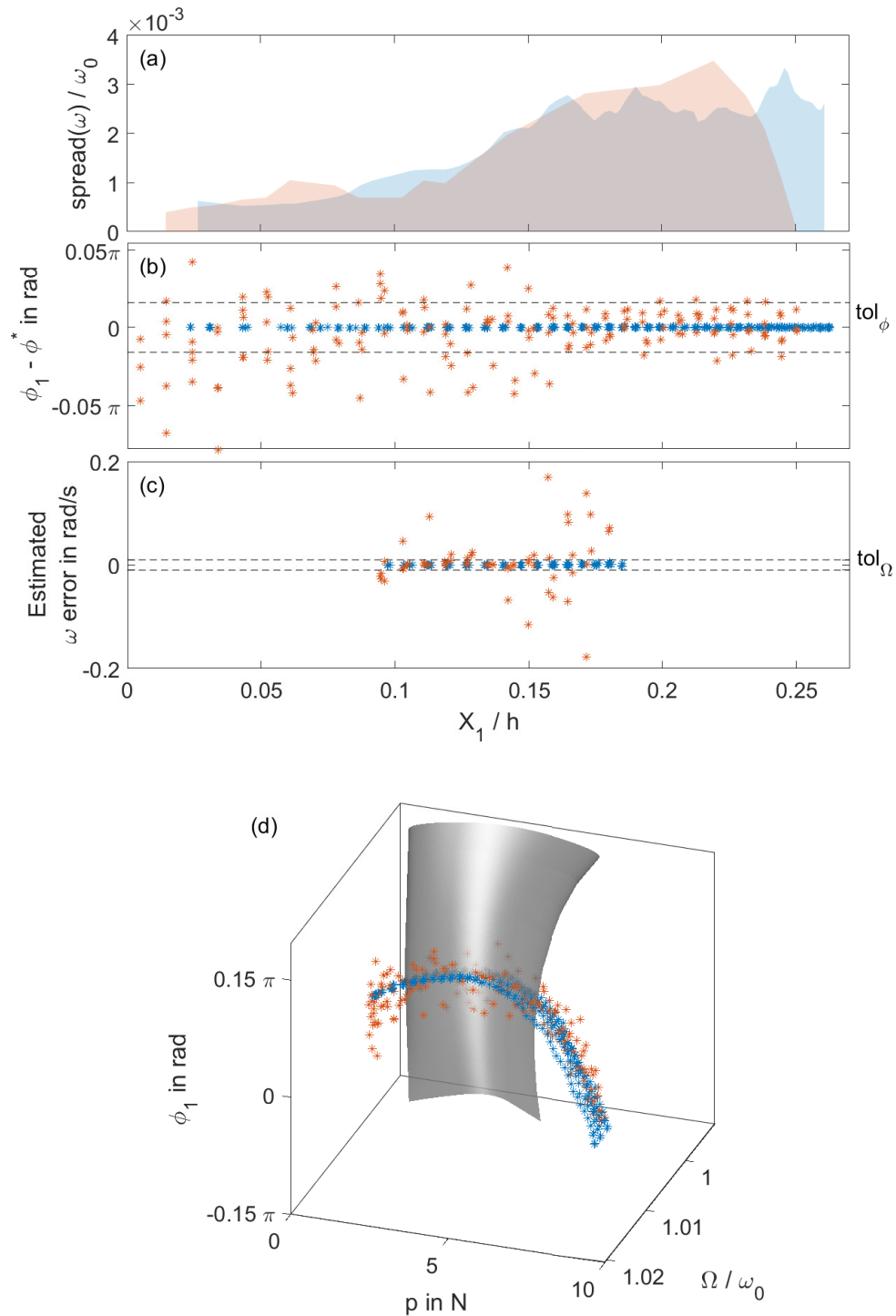


Figure 3.8: (a) Standard deviation of the successive backbone experiments using PLL testing (blue area) and CBC (orange area), (b) measured phase lag error and (c) frequency error in the identified backbone responses during PLL testing (blue curve) and CBC (orange line and squares) estimated from the (d) local response phase surface around the backbone

hardening behavior, respectively. To adequately represent the repeatability variations, the standard deviation is included as colored areas next to the results in the rest of the Chapter.

Fig. 3.8b shows the error in phase lag compared to the quadrature target  $\phi_1 = -\pi/2$  rad. PLL testing is able to reach a phase error almost two orders of magnitude lower than CBC. This is not surprising as CBC can only approach quadrature using prescribed finite steps, presently following Algorithm 3.3. Despite the higher precision achieved by PLL testing, the standard deviation shown in Fig. 3.8a is not reduced compared to CBC. It can be concluded that high phase precision is not needed in this particular application due to high inherent variability.

A frequency error shown in Fig. 3.8c is estimated as the distance from the local response surface shown in Fig. 3.8d. The surface is an interpolation of S-curves identified using CBC and presented later in the Chapter (Fig. 3.12). Fig. 3.8b shows that most periodic responses identified during CBC at high amplitudes ( $X_1/h > 0.15$ ) lie within the phase tolerance, while Fig. 3.8c shows that most periodic responses at low amplitudes ( $X_1/h < 0.15$ ) lie within the frequency tolerance. This can be linked to later results showing that damping increases with amplitude (Fig. 3.9b). Lower damping implies a sharper resonance peak; the phase-lag is sensitive to small variations in frequency. As damping increases, the sensitivity to changes in frequency diminishes while the sensitivity to changes in phase lag increases. The change in damping can be seen visually in Fig. 3.8d as the response surface is flatter on its left-hand boundary (lower amplitude and damping) and more curved on its right-hand boundary (higher amplitude and damping).

### 3.3.4 Nonlinear modal analysis

As established in [23], the amplitude-dependent modal properties can be extracted from the phase-resonant backbone curve, provided that strong modal interactions (e.g. due to closely-spaced or internally resonant natural frequencies) remain absent and damping is light. Here, the definition of a nonlinear mode in accordance with the extended periodic motion concept [81] is used. The modal frequency (or natural frequency)  $\omega$  corresponds to the excitation frequency at phase resonance and is a direct output of the experiments. The nonlinear modal damping ratio  $\delta$  is determined by following the idea that the power supplied by the excitation has to cancel the power dissipated by the system-inherent damping (see [23] for details). The

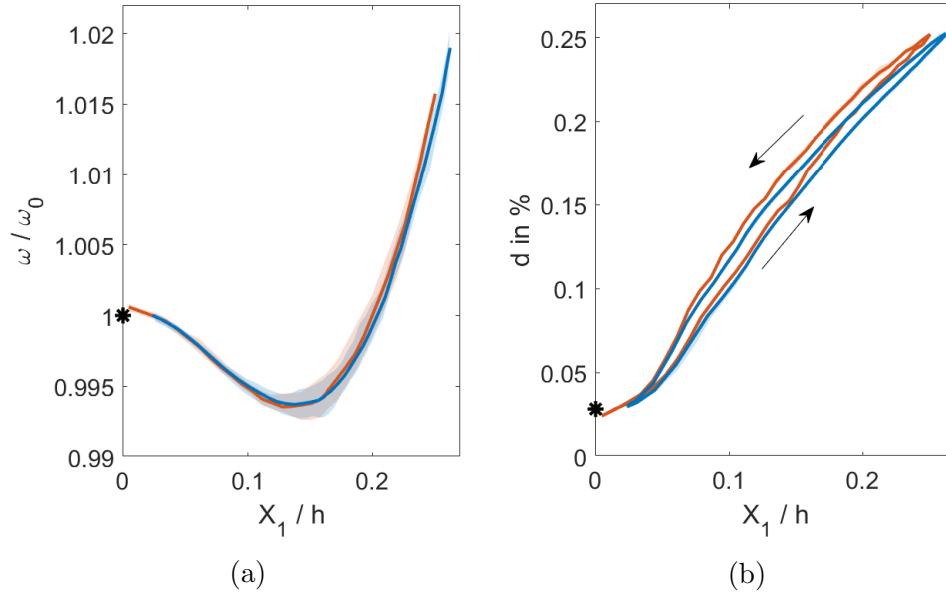


Figure 3.9: (a) average nonlinear natural frequency and (b) nonlinear modal damping depending on the response level, identified with PLL testing (blue curve) and CBC (orange curve); compared to linear parameters identified during the linear modal analysis (\*)

average modal frequency and modal damping ratio are shown in Fig. 3.9a and Fig. 3.9b, respectively. As expected, the values of the parameters at low amplitude are consistent with the linear modal parameters.

Increasing damping ratio with amplitude is typical for micro-slip friction, which may also cause the increase in variability with amplitude shown in Fig. 3.8a. Although the damping has a standard deviation so small that it is barely visible in Fig. 3.9b, it exhibits an interesting hysteresis behavior. It is important to note that it is not a dynamical hysteresis, i.e. each point on the curve corresponds to a steady state periodic response identified during PLL testing or CBC. Rather, the behavior of the structure is different whether the amplitude is sequentially increased or decreased. We do not know the cause of this behavior, but a possible explanation could be linked to thermal effects analogous to the observations in [82].

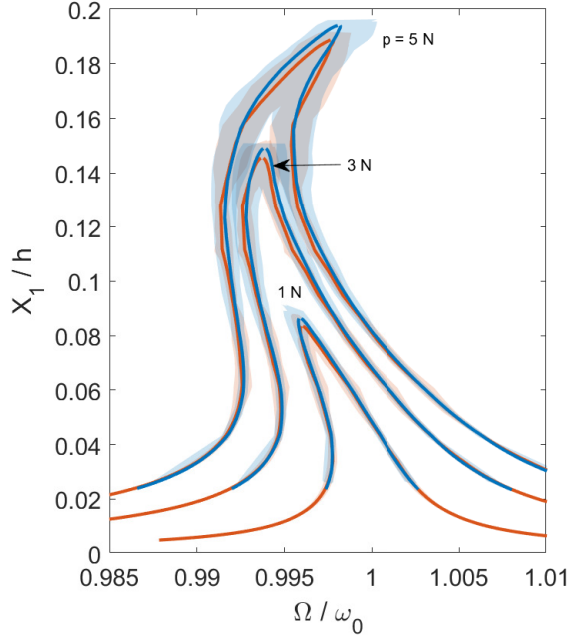


Figure 3.10: FRCs at varying excitation amplitudes synthesized from the average backbone curve identified with PLL testing (blue curve) and CBC (orange curve), and compared to the standard deviation from PLL testing (blue area) and CBC (orange area) data

### 3.3.5 Frequency response curve synthesis

FRCs can be synthesized from the nonlinear modal parameters presented in Section 3.3.4. It can be advantageous to do this as fewer periodic responses need to be measured compared to a direct FRC identification. Identifying FRCs both through synthesis and directly is done here as a cross-validation.

The synthesis relies on the single-nonlinear-mode theory. The frequency  $\Omega$  of the FRC at a specific response amplitude is computed following [83]. The FRCs synthesized from the backbone curves (Fig. 3.7a) are shown in Fig. 3.10. They are parametrized by their phase lag such that there is a one-to-one correspondence between each point of the different curves. The successive FRCs are described by the functions  $\omega_k(\phi_1)$  and  $X_1(\phi_1)$  for the  $k^{\text{th}}$  curve. The standard deviation is computed for each phase lag value both in amplitude and frequency, and is shown as colored areas in Fig. 3.10.

The softening-hardening behavior is apparent in the FRCs. Under a forcing amplitude of 3 N, the FRCs are in the softening regime and are

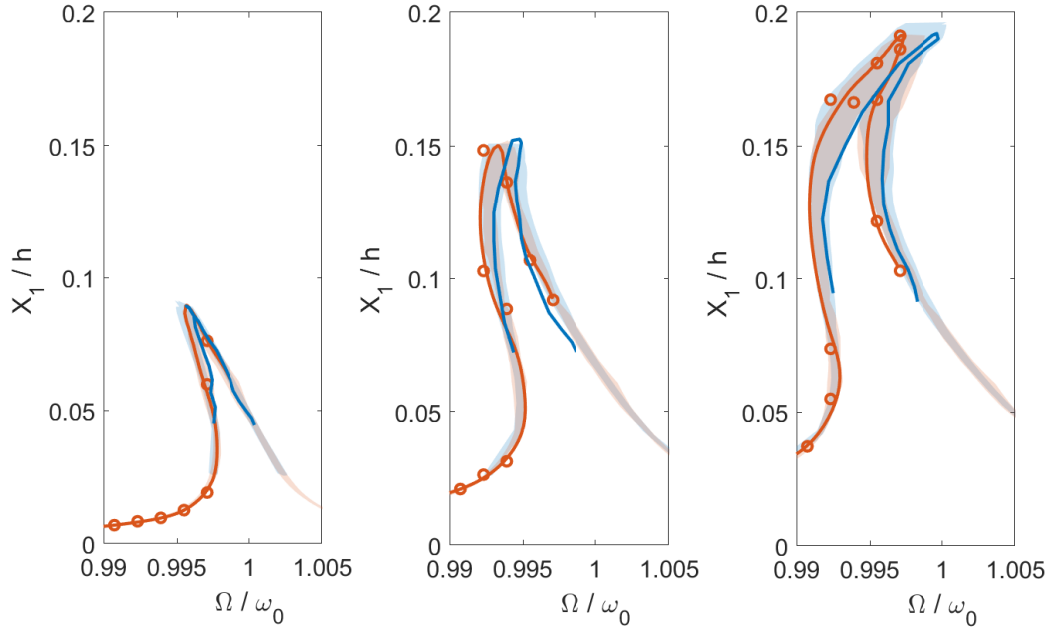


Figure 3.11: FRCs at excitation amplitudes (a)  $F = 1$  N, (b) 3 N, and (c) 5 N identified experimentally with PLL testing (blue curve) and CBC (orange curve), compared to the S-curves identified with CBC (o) and to the standard deviation of the FRCs synthesized from backbone curves identified with PLL testing (blue area) and CBC (orange area)

skewed toward lower frequencies. They include two saddle-node bifurcations. This indicates the existence of a branch of unstable orbits. Increasing the forcing amplitude above 3 N creates two more saddle-node bifurcations as the FRCs begin to be skewed towards higher frequencies. This hardening regime therefore includes two branches of unstable orbits, one due to softening and the other due to hardening. Recall that this leads to as much as four turning point bifurcations and a stable high-level branch which can be unreachable by a conventional frequency response test (stepping or slowly sweeping the frequency and controlling only the excitation level).

### 3.3.6 Frequency response curve identification

FRCs are identified experimentally using PLL testing by following Algorithm 3.4. They are shown in blue in Fig. 3.11. The identification of FRCs is limited around the resonance peak. Further from resonance, a small phase lag variation implies a large frequency variation. Consequently, even

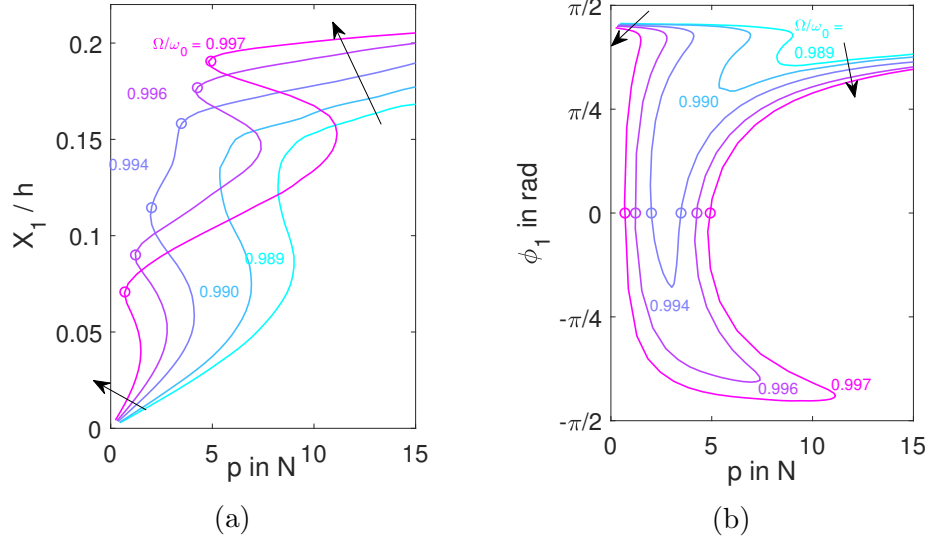


Figure 3.12: (a) Amplitude and (b) phase lag of S-curves identified experimentally during CBC for varying excitation frequencies; with highlighted resonance points at phase quadrature (o)

low phase lag uncertainty prevents the accurate identification of periodic responses. Additionally, periodic responses further from resonance have a low amplitude, leading to low signal-to-noise ratio in the measurement and high phase lag uncertainty, as explained in Section 3.2.3. Such a limitation is nuanced by the fact that interesting behavior is rarely expected far from resonance.

The S-curves identified during CBC by following Algorithm 3.5 are shown in Fig. 3.12. Far away from resonance, the force level increases quickly, constituting a potential limitation of the method when applied to structures or equipment sensitive to high forcing. The phase lag along the S-curves is shown in Fig. 3.12b. The presence of two resonance points where  $\phi_v = 0$  rad and the double-S shape of some S-curves results from the softening-hardening behavior of the system.

Combining the data of multiple S-curves allows to identify a region of the response surface. FRCs can then be extracted in post-processing. For repeatable experiments, an accurate response surface can be obtained by interpolating the points of the S-curves using kriging [84] or other basis functions [85]. In the present work, the experiments are not perfectly repeatable due to the inherent variability of the structure. An approximation

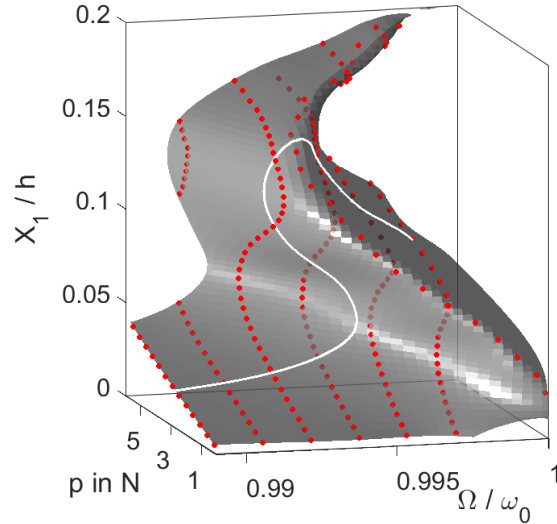


Figure 3.13: Response surface representing the response amplitudes of the system for varying excitation signals, approximated from the S-curves and the backbone identified experimentally with CBC (data points shown in orange and approximated FRC at  $F = 3$  N in white)

of the S-curve data is therefore preferred to an interpolation. The response surface is approximated by a cubic spline surface with 10 equally spaced control points along the frequency dimension and 12 points along the response amplitude dimension. The location of the control points along the fundamental excitation force dimension is determined by minimizing the average distance between the surface and the data points. The data consists in the S-curves and the average backbone, useful to accurately capture the resonance region. The surface and data points are shown in Fig. 3.13.

The FRCs are finally extracted from the response surface as collections of periodic responses at constant excitation amplitudes. They are shown in orange in Fig. 3.11. To highlight the fact that the FRCs are not interpolations but approximations, the intersection of the S-curves with the plane embedding the FRC are shown as orange circles. The resulting FRCs stay close to these intersections, showing an accurate approximation.

Although the identified FRCs—either directly using PLL testing or indirectly using CBC—show a slight difference in frequency, they lie within or very close to the standard deviation of FRCs synthesized from the backbones. In other words, such a difference in frequency is expected from the inherent variability of the system. This gives strong confidence in both

the FRCs and the backbone curves identified using PLL testing and CBC. Finally, both methods successfully stabilize the unstable orbits in the FRCs.

### 3.4 Conclusion

The aim of this Chapter was to present a detailed implementation and to compare two recently-developed methods capable of nonlinear modal characterization on the same structure. Both methods use feedback to control different experimental parameters. During phase-locked loop (PLL) testing, the phase lag between response and excitation signals is imposed by a controller. During control-based continuation (CBC), a controller generates an excitation signal from the difference between a reference signal and the response of the structure.

Both PLL testing and CBC were capable to successfully characterize the amplitude-dependent modal properties of the lowest-frequency bending mode of a thin beam possessing an intrinsic curvature. The structure exhibits complex nonlinear softening-hardening dynamics and nonlinear micro-slip in the bolted joints, accurately characterized by both methods. The backbone identification—and subsequent nonlinear modal parameters and synthesized FRCs—and the FRC identification lead to consistent results obtained by PLL testing or CBC.

It is difficult to compare quantitatively experimental duration using both methods. The tuning of the controllers plays a critical role in the dynamics of the system, e.g., the time needed to reach steady state. The parameters chosen in the continuation algorithms affect greatly the duration of experiments. An in-depth parameter study might be done to assess accurately performance of CBC and PLL testing but it is deemed outside the scope of this Chapter. With these considerations, no significant difference in performance was observed in this study.

This Chapter focused on bringing PLL testing and CBC together and presenting their different approaches in performing the same characterization. An equally relevant approach would set the methods apart by studying special cases where PLL testing or CBC might fail. Such cases are mentioned in this Chapter and result from a difference in parametrization of the response surface exploited by both methods. On the one hand, superharmonic resonance might prevent a parametrization by a single response harmonic [86] and a characterization by CBC might be incomplete. Chapter 5 looks into such a particular situation. On the other hand, modal

interaction might render a parametrization by phase lag challenging [70] and a characterization by PLL testing incomplete. Chapters 6 and 7 look into these issues.

General methods are still lacking regarding the determination of control laws for control-based methods. Unless knowing in advance the nonlinearities of a system—i.e. building a model, defeating the purpose of the methods—controller gains are currently tuned heuristically. Further work looking into robust and general methods for building control laws is needed, possibly building upon the early work done on the subject in [76, 78].



# Chapter 4

## Online Fourier decomposition for control-based methods

This Chapter contains excerpts of the article *Stepped and swept control-based continuation using adaptive filtering* published in *Nonlinear Dynamics* 104, pages 3793–3808 (2021)

Authors: G. Abeloos, L. Renson, C. Collette, G. Kerschen

### Abstract

Both control-based continuation and phase-locked loop testing require that Fourier coefficients are estimated during the experiment. The former has to cancel non-fundamental harmonics in the excitation, and the latter needs to estimate the phase lag. Two existing Fourier decomposition methods are discussed. First, the discrete Fourier transform is applied to recorded time histories. Experiments must therefore be put on hold while it is performed, which makes it offline. Second, synchronous demodulation acts by extracting Fourier coefficients continuously using a low-pass filter. A compromise must be made between accuracy and speed, as an oscillatory error is always present in the output. An alternative method based on adaptive notch filters that output Fourier coefficients as by-product is proposed in this Chapter. Adaptive filtering features accuracy and speed similar to discrete Fourier transform while having an online architecture like synchronous demodulation. It is shown to improve performance of both control-based continuation and phase-locked loop testing during virtual and physical experiments. Specifically, a faster, more accurate phase lag estimation improves the stability of phase-locked loop experiments and a novel online control-based continuation experiment allows for fast characterization.

## 4.1 Introduction

The control-based methods studied in this work require the estimation of some parameters during the experiment to function properly. On the one hand, the non-fundamental harmonics of the response must be identified during the control-based continuation (CBC) experiment to ensure that the force is monoharmonic. On the other hand, the phase lag between the fundamental harmonic of the response and the excitation must be identified during the phase-locked loop (PLL) experiment.

A method to estimate the non-fundamental harmonics of the response during CBC has already been described in Chapter 3 using the offline Fourier decomposition in Fig. 3.2b. Similarly, a method to estimate the phase lag during PLL using synchronous demodulation is illustrated in Fig. 3.1b. This Chapter aims to present the drawbacks of these methods and introduce a new one based on adaptive filtering [87, 88].

In Section 4.2, we will discuss three methods to perform a Fourier decomposition during an experiment, namely the discrete Fourier transform (DFT) in Section 4.2.1, the synchronous demodulation in Section 4.2.2, and the adaptive notch filter in Section 4.2.3. We will then compare the performance of the different methods during PLL and CBC experiments in Sections 4.3 and 4.4, respectively. A conclusion is provided in Section 4.5.

## 4.2 Fourier decomposition methods

### 4.2.1 Discrete Fourier transform

The DFT is used to compute Fourier coefficients of time signals that have already been recorded. Using the coefficients during the experiment requires applying DFTs at regular intervals in parallel to the experiment, a type of method that we will call “offline”. A computer must first record a time series into a buffer memory, then apply the DFT, and finally use the resulting coefficients to drive the experiment. Fig. 4.1a shows the time series of a measured signal. The signal is stored in memory over one period, as symbolized by the arrows. Once the period is fully recorded, the DFT is applied at times marked by dashed lines. The sampling time of the Fourier coefficients (dashed lines) is usually longer than the one of the measurement (dots).

The time series on which the DFT is applied must be periodic for the

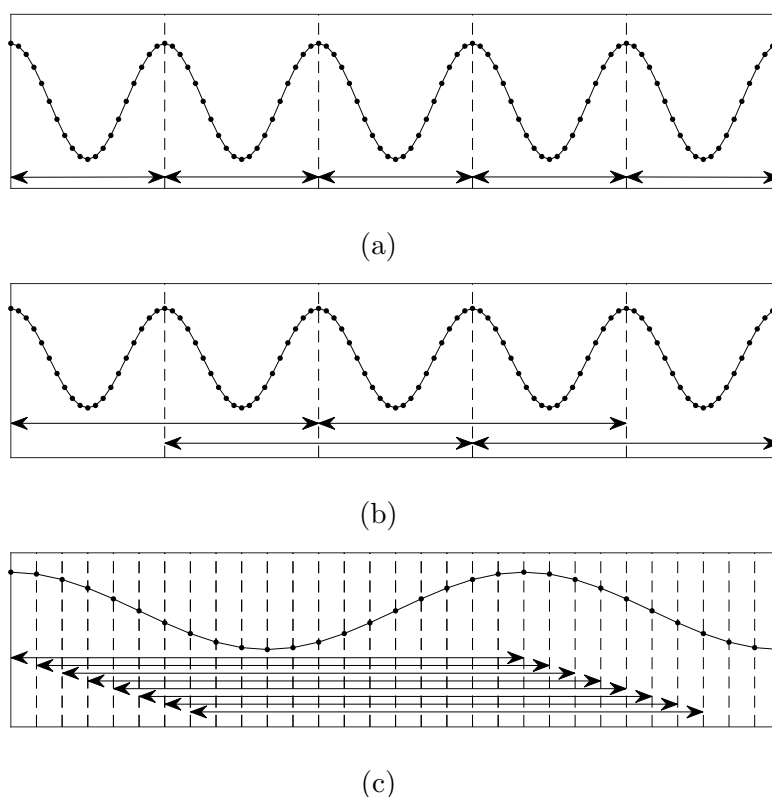


Figure 4.1: Different buffer sizes when applying a DFT during an experiment with (a) one period buffer every period, (b) two periods buffer every period, and (c) one period buffer every sample; an arrow symbolizes the data used for the DFT and a dashed line represents the time steps at which the DFT data is available

estimated Fourier coefficients to be accurate. Fig. 4.2 shows a periodic signal sampled 39 times every two periods. One period therefore lasts 19.5 samples. A naive approach is to round the number of samples per period to constitute the buffer. Consequently, the stored discrete signal is not periodic and the estimation of the Fourier coefficients is erroneous, as shown for the worst case scenario in Fig. 4.3. Increasing the sampling frequency decreases this misalignment error but increases the resources needed by the computer and the measurement hardware. For instance, to ensure that the error is less than 5%, the sampling frequency must be 40 times the frequency of the signal's highest harmonic of interest. A more complex solution is to resample the measured data, ensuring that there are a whole number of samples during a period. The sampling frequency therefore depends on the measured signal's frequency.

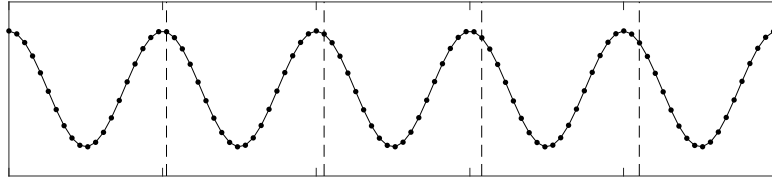


Figure 4.2: Misalignment between the sampling time and the signal's period at 39 samples every two periods; with dashed lines marking the number of samples per period rounded to the nearest integer

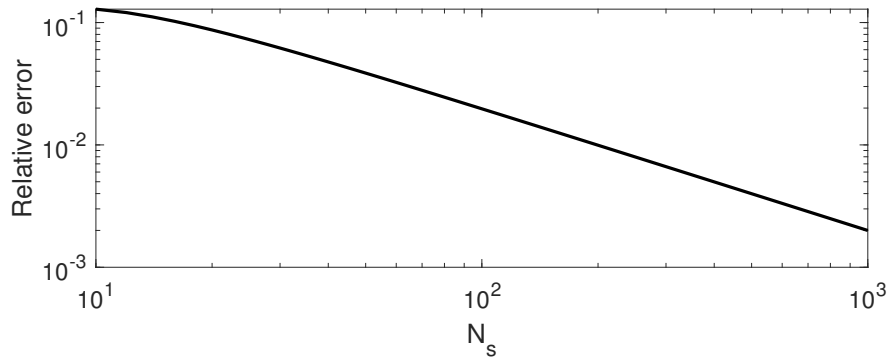


Figure 4.3: Relative error between the Fourier coefficient of a sine wave discretized by  $2N_s + 1$  samples every two periods and the DFT output of a time series whose length is  $(2N_s + 1)/2$  rounded to the nearest integer

Storing multiple periods in the buffer is useful to average out potential noise in the measurement or to compensate for a misalignment between the sampling time and the period. However, the sampling time of the Fourier coefficients is multiplied by the same amount, i.e., the Fourier coefficients are updated less frequently. A solution is to record buffers in parallel. Fig. 4.1b shows an example in which each buffer contains two periods but a new buffer is started every period.

It is possible to update the estimation of the Fourier coefficients at every measurement sample, as shown in Fig. 4.1c. A new buffer is started at every sample and the time series is recorded during a whole number of periods. This method is expensive in operation counts because a DFT must be applied at every measurement sample, and expensive in memory usage because a large number of buffers run in parallel.

An additional challenge to using DFT during experiments are applica-

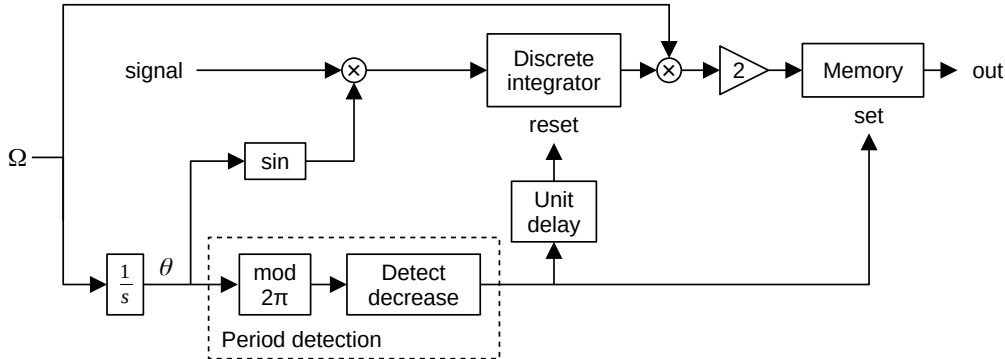


Figure 4.4: Implementation of the DFT for frequency-varying applications (shown: identification of the fundamental sine Fourier coefficient)

tions during which the frequency of the signal changes, e.g., during a PLL experiment. An implementation is proposed in Fig. 4.4. The instantaneous phase  $\theta$  of the DFT basis is computed by integrating the frequency through time. Its value mod  $2\pi$  will increase until reaching  $2\pi$ , at which point it will drop to zero. The end of one period coincides with this drop. In parallel to this, the signal is multiplied by the harmonic basis and integrated through time as per the DFT method. The integrator is a cumulative sum multiplied by the time step. When reaching the end of the period, the integrator value multiplied by twice the frequency is the Fourier coefficient and is stored into memory. The integrator is reset one step after storing the coefficient into memory.

### 4.2.2 Synchronous demodulation

The principle behind a Fourier transform is the orthogonality of sine waves, i.e., the product of two sine waves at identical frequencies has a constant term proportional to the Fourier coefficient. Integrating over one period cancels every periodic term and allows to extract the Fourier coefficient. Synchronous demodulation uses the same principle; the product's constant term is not extracted through integration but by applying a low-pass filter [58].

Contrarily to DFT that consists in performing operations in parallel to the experiment, synchronous demodulation consists in performing operations on the signals directly and continuously through time. We will thus refer to as “online” method. Online methods are interesting because the

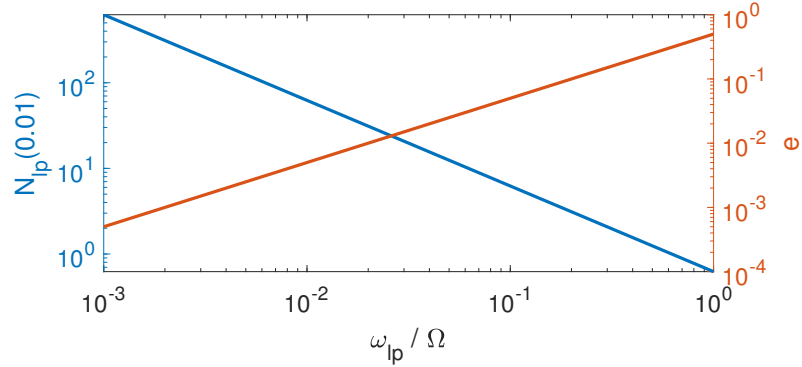


Figure 4.5: Number of periods taken to settle within 1% of the steady-state, and amplitude of the oscillatory error versus the cut-off frequency of the low-pass filter

estimation of the Fourier coefficients is updated continuously or at each measurement sample. The coefficients can then be used in feedback loops directly using measurement data.

The performance of synchronous demodulation using a linear low-pass filter is derived in Appendix B.1. When estimating the Fourier coefficients of a signal at frequency  $\Omega$  using a low-pass cut-off frequency  $\omega_{lp}$ , an oscillation is present at the output. The amplitude of the oscillation relative to the actual Fourier coefficient is

$$e \approx \frac{\omega_{lp}}{2\Omega}. \quad (4.1)$$

The number of periods needed for the estimated Fourier coefficient to settle within a relative margin  $\epsilon$  is

$$N_{lp}(\epsilon) \approx -\frac{\Omega}{2\pi\omega_{lp}} \log(2\epsilon). \quad (4.2)$$

Therefore, a compromise must be made between a precise estimation of the Fourier coefficients (low  $e$ ) or a fast estimation (low  $N_{lp}(\epsilon)$ ). This trade-off is shown in Fig. 4.5. Furthermore, a low-frequency application requires necessarily a slow filter.

Fig. 4.5 shows that a cut-off frequency  $\omega_{lp} = \Omega/50$  for the phase demodulation corresponds to an oscillatory error ratio  $e = 1\%$ , in which case the estimation will take 16 periods to converge within 1% of the actual Fourier coefficient value. Similarly,  $\omega_{lp} = \Omega/10$  and  $\Omega/5$  correspond to oscillatory error ratios of  $e = 5\%$  and  $10\%$ , taking 3 periods and 1.5 periods to converge within 1% of the coefficient value respectively.

### 4.2.3 Adaptive notch filter

The method proposed to perform a high-performance online Fourier decomposition uses the adaptive notch filter introduced in [87]. The primary objective of adaptive notch filters is to isolate or remove a component from the input signal at a specific frequency. However, we will not use the usual outputs of the filter. Rather, the Fourier coefficients of the targeted component, which are internal parameters of the filter, are directly accessed and constitute the output in our application.

An adaptive filter synthesizes the signal  $\hat{x}$  by performing a time-varying linear combination of a basis  $\mathbf{q}$  such that it approximates the input signal  $x$  [88]:

$$\hat{x}(t) = \mathbf{w}^T(t)\mathbf{q}(t) \approx x(t). \quad (4.3)$$

In an adaptive notch filter, the basis  $\mathbf{q}$  is composed of harmonic signals

$$\mathbf{q}(t) = \begin{bmatrix} q_0(t) \\ q_{1s}(t) \\ q_{1c}(t) \\ q_{2s}(t) \\ \vdots \\ q_{N_{\text{Hc}}}(t) \end{bmatrix} = \begin{bmatrix} 1 \\ \sin(\Omega t) \\ \cos(\Omega t) \\ \sin(2\Omega t) \\ \vdots \\ \cos(N_{\text{H}}\Omega t) \end{bmatrix} \quad (4.4)$$

and the weights leading to an accurate synthesis

$$\mathbf{w}(t) = \begin{bmatrix} w_0(t) \\ w_{1s}(t) \\ w_{1c}(t) \\ w_{2s}(t) \\ \vdots \\ w_{N_{\text{Hc}}}(t) \end{bmatrix} \quad (4.5)$$

are determined by an algorithm. One of the simplest and least expensive is the least mean squares (LMS) algorithm [88], which updates  $\mathbf{w}$  discretely through time. At time step  $i$ , the synthesis error is estimated,  $e(t_i) = x(t_i) - \mathbf{w}^T(t_i)\mathbf{q}(t_i)$ , and the weights are updated following

$$\mathbf{w}(t_{i+1}) = \mathbf{w}(t_i) + \mu\mathbf{q}(t_i)e(t_i), \quad (4.6)$$

where  $\mu$  is the step size factor, which is an internal parameter of the LMS algorithm

The performance of an adaptive filter is studied in Appendix B.2. The optimal coefficient  $\mu$  to estimate the Fourier coefficients of a signal at frequency  $\Omega$  is the critical

$$\mu_c = 2 \sin(\Omega t_s) \frac{1 - \sin(\Omega t_s)}{\cos^2(\Omega t_s)}, \quad (4.7)$$

the number of periods necessary for the estimated Fourier coefficient to settle within a relative margin  $\epsilon$  is

$$N_{\text{af}}(\epsilon) \approx -\frac{1}{2\pi} W_{-1}(-\epsilon). \quad (4.8)$$

If multiple harmonics are decomposed using an adaptive filter, a single value of  $\mu$  is only optimal for one of the harmonics. Higher or lower harmonics will be under or over damped, respectively. An alternative would be to define critical values of  $\mu$  for each harmonic. This case has not been studied in this work.

When the synthesis error  $e$  is close to zero and the weights  $\mathbf{w}$  are close to constant, Eq. (4.3) is similar to a Fourier decomposition of  $x$  and the elements of  $\mathbf{w}$  approximate its Fourier coefficients (see Eq. (1.2)):

$$\begin{cases} w_0 \approx b_{x,0} \\ w_{ks} \approx a_{x,k} \\ w_{kc} \approx b_{x,k} \end{cases} \quad \forall k \in \{1, \dots, N_{\text{H}}\}. \quad (4.9)$$

#### 4.2.4 Comparison

The settling time of the adaptive filter is compared to the synchronous demodulation in Fig. 4.6. The estimation by adaptive filtering converges within 1% of the Fourier coefficient value in approximately one period of the input signal. It is faster than synchronous demodulation even when the oscillatory error amplitude is allowed to reach 20% the Fourier coefficient value. Using adaptive filtering is therefore faster and more accurate than synchronous demodulation.

The three methods are used to identify the amplitude and phase of a harmonic signal in Fig. 4.7. The sampling frequency was chosen to maximize the error of the DFT identification due to period misalignment (see Fig. 4.2). The DFT is applied once every period and reaches an acceptable identified amplitude and phase at the first estimation. Due to misalignment between the signal and sampling frequencies, the relative error alternates between

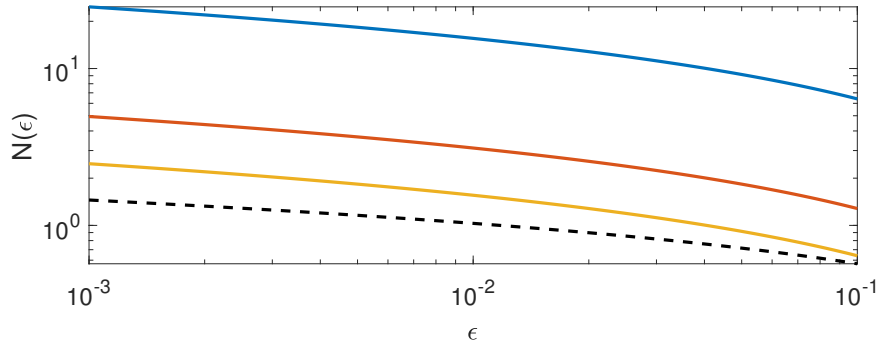


Figure 4.6: Number of periods necessary for the estimation of the Fourier coefficient to converge within an amplitude ratio  $\epsilon$  of the actual Fourier coefficient value using synchronous demodulation with  $\omega_{lp} = \Omega/25$  (blue curve),  $\Omega/5$  (orange curve),  $\Omega/2.5$  (yellow curve) corresponding to oscillatory error ratios of  $e = 2\%$ ,  $10\%$  and  $20\%$  respectively; or adaptive filtering (dashed curve)

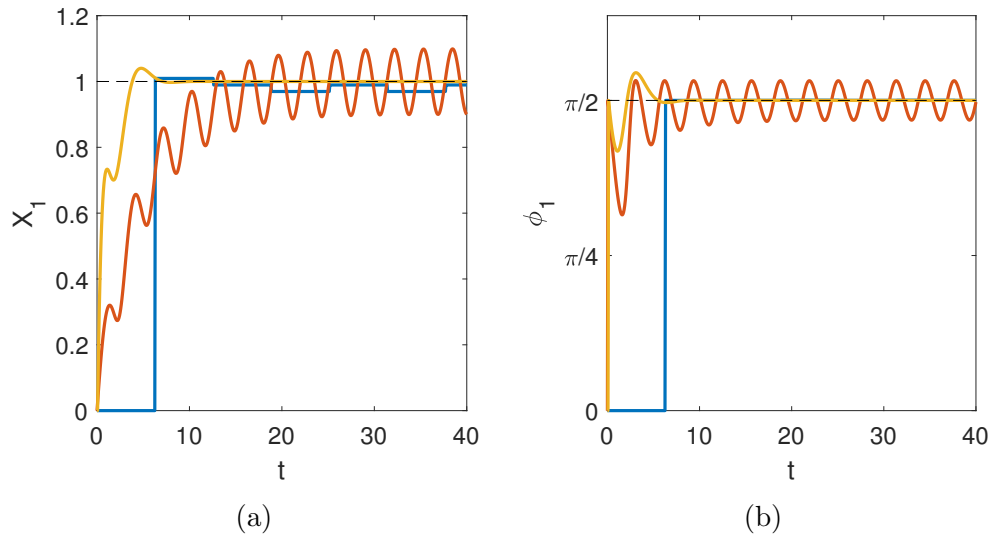


Figure 4.7: Identified amplitude  $X_1$  and phase  $\phi_1$  of input signal  $x = \sin(\Omega t + \pi/2)$  with frequency  $\Omega = 1$  rad/s, sampling frequency  $f_s = 16$  Hz, using one DFT every period (blue), synchronous demodulation with cut-off frequency  $\omega_{lp} = \Omega/5$  (orange), or adaptive filtering with LMS factor  $\mu = \mu_c$  (yellow)

1% and 3%, which is consistent with the predicted 2% value from Fig. 4.3. The misalignment causes however no error in the estimated phase.

Using synchronous demodulation, the low-pass frequency was chosen  $\omega_{lp} = \Omega/5$ , leading to a 10% error in the identified amplitude and 0.2 rad error in the identified phase, consistently with predicted values in Fig. 4.5. The predicted 3 periods necessary for the estimated coefficients to converge within 1% also seem consistent with Fig. 4.7a.

Using adaptive filtering, the coefficients were predicted to converge within 1% of their final value in one period, which is consistent with Fig. 4.7. The amplitude and phase converge quickly to the exact values and the error converges to zero.

### 4.3 Phase-locked loop

If the fundamental harmonic of the response  $x(t)$  and excitation  $f(t)$  are expressed as

$$a_x \sin(\Omega t) + b_x \cos(\Omega t) = X \sin(\Omega t + \phi_x) \text{ and} \quad (4.10)$$

$$a_f \sin(\Omega t) + b_f \cos(\Omega t) = F \sin(\Omega t + \phi_f) \quad (4.11)$$

respectively, the phase lag is simply  $\phi = \phi_x - \phi_f$ . The phase of each signal can be derived from the Fourier coefficients of the fundamental harmonic:

$$\phi_x = \text{atan2}(b_x, a_x), \quad (4.12)$$

$$\phi_f = \text{atan2}(b_f, a_f) \quad (4.13)$$

and used during a PLL experiment.

The particularity of the PLL experiment is that the Fourier estimation is part of a control loop that acts on the excitation frequency  $\Omega$ . Chapter 2 showed that the responses of an experiment with continuous feedback control could all be stable, including the ones that were unstable in the open-loop experiment.

The Fourier coefficients of the response and excitation can be estimated using DFT. At one extreme, the estimation can be performed at every measurement sample, ensuring stability at a large cost in computation power and memory usage. At the other extreme, the Fourier coefficients can take one or more periods to be updated. While the estimated phase lag is kept constant between updates, the experiment can be considered in open loop, preventing any stabilization.

Table 4.1: Set of parameters and laws for the virtual PLL experiment

$m$	$c$	$k$	$f_{nl}$	$p$	$k_i$	$k_p$	$\omega_0$ in rad/s	$f_s$ in Hz
0.05	0.2	57	$2 \times 10^8 x^3$	0.01	1	3	30	$10^4$

Chapter 3 implemented a PLL experiment using synchronous demodulation. The low-pass filter takes a certain time to estimate the Fourier coefficients. In Chapter 2, we showed the importance of a fast phase lag estimation to ensure the stability of the experiment's responses. Therefore, there is a minimal value for the cut-off frequency  $\omega_{lp}$  under which some responses may not be stable for the chosen control gains. Additionally, there is an oscillatory error in the estimated Fourier coefficients that will propagate into the estimated phase lag, reducing the accuracy of the PLL.

With adaptive filtering, these problems are alleviated. The phase lag estimation is online and fast, improving the stability of the experiment's responses. In addition, the estimation error converges to zero, making the PLL accurate when targeting a certain phase lag.

### 4.3.1 Virtual experiment

A PLL experiment is simulated numerically to characterize the Duffing oscillator in Eqs. (1.14) and (1.15). The experiment is integrated in discrete time with sampling frequency  $f_s$ . The internal and user-defined system parameters are shown in Table 4.1, and the corresponding theoretical frequency response curve (FRC) is shown in Fig. 4.8. An unstable response corresponding to a phase lag  $\phi_1 = -2.4$  rad is taken as an example.

Fig. 4.9 shows cases in which the Fourier decomposition method prevents the PLL to stabilize on the targeted response. Applying the DFT every two periods is not fast enough to stabilize the response. After one period, the Fourier coefficients are evaluated and the frequency is suddenly modified by the PI controller. At this new frequency, the response is significantly different and so are the new Fourier coefficients. The phase lag target is overshoot. A new evaluation of the Fourier coefficients leads to frequency correction and the phase lag target is overshoot in the other direction. This process repeats and the system never converges. A similar problem happens in Fig. 4.9 with synchronous demodulation when the filter is too slow, i.e., when the cut-off frequency of the low-pass filter  $\omega_{lp}$  is too small. The phase lag target is overshoot, then the PI controller over-corrects due to inertia in the phase lag evaluation. The system oscillates around the targeted

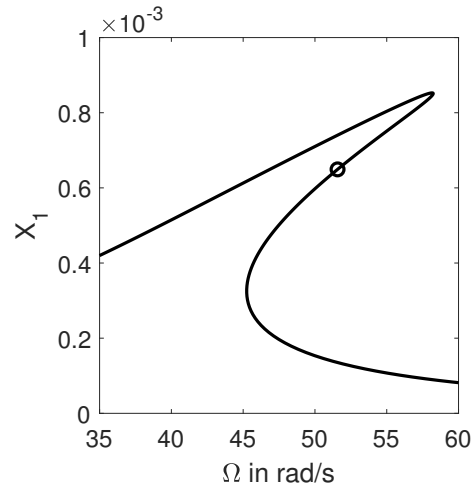


Figure 4.8: FRC of the system whose parameters are in Table 4.1 computed with the HB method and pseudo-arclength continuation [59]; example of unstable response with  $\phi_x = -2.4$  rad highlighted with a circle

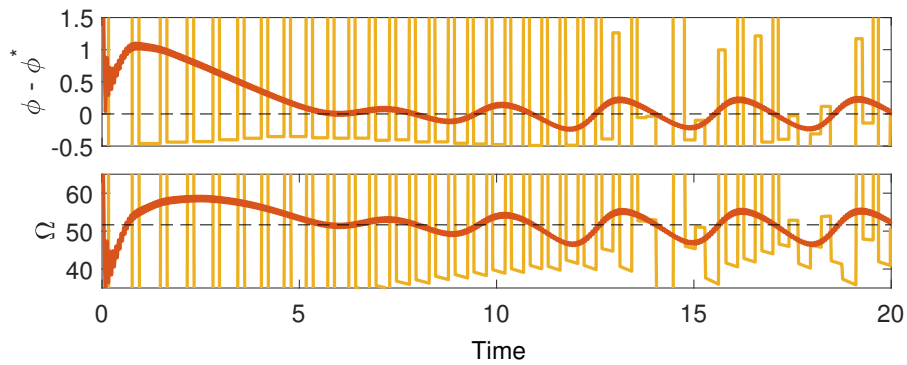


Figure 4.9: Time series of the phase lag error and frequency when stabilizing the system in Table 4.1 at  $\phi^* = -2.4$  rad using synchronous demodulation with a slow low-pass filter  $\omega_{lp} = \omega_0/15$  (orange) and DFT every two periods (yellow)

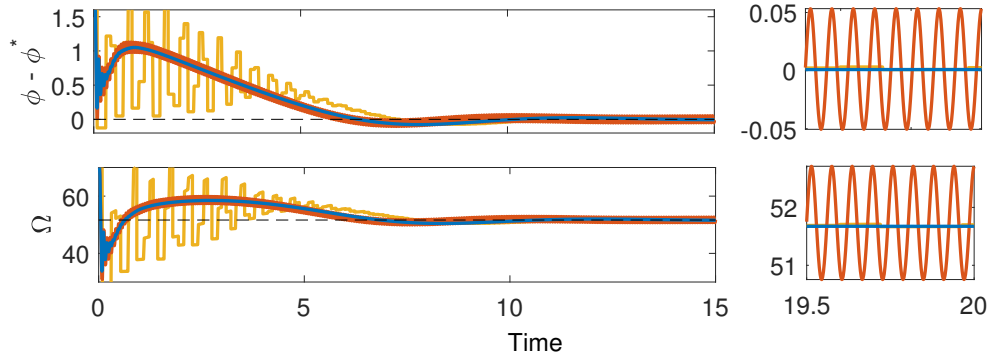


Figure 4.10: Time series of the phase lag error and frequency when stabilizing the system in Table 4.1 at  $\phi^* = -2.4$  rad using adaptive filtering with  $\mu = 0.002$  (blue), synchronous demodulation with a fast low-pass filter  $\omega_{lp} = \omega_0/7.5$  (orange), and DFT every period (yellow)

response.

Fig. 4.10 shows cases in which the PLL successfully converges to the targeted response. A DFT applied at every period is fast enough for the PLL to converge. However, early oscillations show the equilibrium's fragility. Although there is a misalignment between the sampling frequency and the DFT, the frequency error is 0.08% of the targeted  $\Omega$ , an excellent precision. Synchronous demodulation with a fast low-pass filter allows the experiment to converge, but an oscillatory error remains during steady-state. As a result, the phase lag oscillates within 0.05 rad of the target, and the frequency oscillates within 4% of the targeted value. When adaptive filtering is used to estimate the Fourier coefficients, the phase lag converges precisely towards the target. Regardless of the speed of the Fourier decomposition, the PLL converges at a similar rate towards the targeted response. The performance of a PLL experiment is always constrained by the oscillator's damping, as shown in Chapter 2.

The virtual PLL experiment is used to identify the FRC of the system in Table 4.1 by sweeping the phase lag target  $\phi^*$ , following the method described in Section 3.2.4. The target is swept from  $\phi^* = -0.1$  to  $-\pi+0.1$  rad for a duration of 100 time units following a cosine profile, slowing the continuation far away from the resonance peak. The FRC identified using phase demodulation is shown in Fig. 4.11a. The oscillation error is proportional to the response amplitude and causes a thick region of uncertainty. On the one hand, the oscillation in  $X_1$  is an estimation artifact. Averaging over one

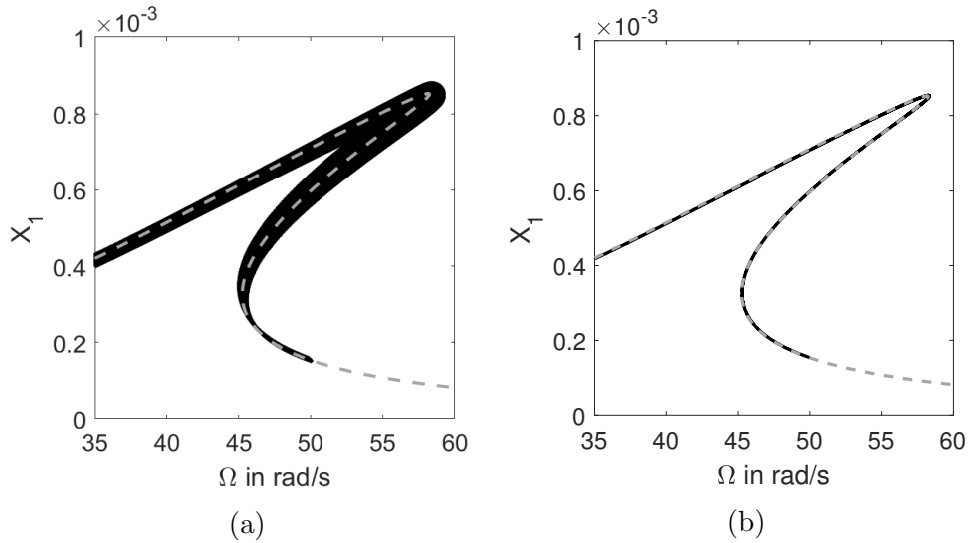


Figure 4.11: FRCs identified during virtual PLL experiments of system whose parameters are in Table 4.1 using (a) phase demodulation with  $\omega_{lp} = \omega_0/7.5$  and (b) adaptive filtering with  $\mu = 0.002$ ; theoretical FRC as a gray dashed curve

or more periods could remove this factor. On the other hand,  $\Omega$  oscillates when the phase lag error is fed into the PLL controller. The oscillation increases with the control gains. Although it can also be averaged in post-processing, it is the actual excitation frequency applied to the oscillator. It therefore affects the accuracy of the identification. Fig. 4.11b shows the FRC identified using adaptive filtering. Its accuracy is excellent.

Section B.2.3 in the Appendix shows that an adaptive filter put in a feedback loop with an oscillator is not always stable. The stability of an adaptive filter put in a PLL has not been derived analytically. However, the conclusions are similar: the loop can lose stability due to the adaptive filter for high values of the parameter  $\mu$ , as shown in blue in Fig. 4.12. Decreasing  $\mu$  has a stabilizing effect on the adaptive filter but slows down the phase lag estimation. The purple curve in Fig. 4.12 shows again that a too slow phase lag estimation prevents stability of the PLL. The choice of  $\mu$  is therefore a compromise between the stability of the adaptive filter and the PLL.

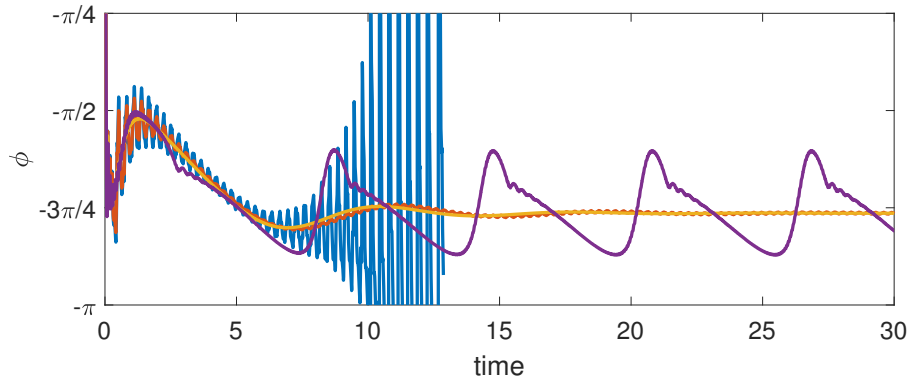


Figure 4.12: Time series of the phase lag when stabilizing the system in Table 4.1 at  $\phi^* = -2.4$  rad using adaptive filtering with  $\mu = 0.009$  (blue), 0.008 (orange), 0.002 (yellow), and 0.0001 (purple)

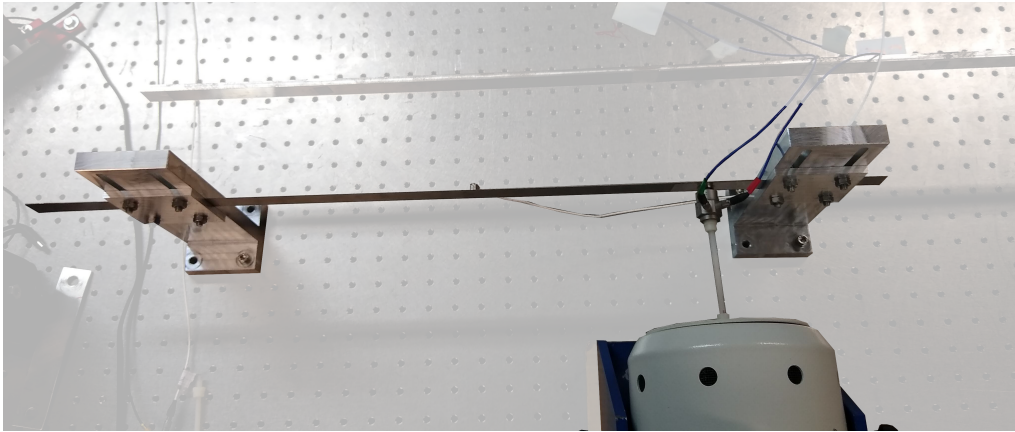


Figure 4.13: Experimental set-up comprising a clamped-clamped thin beam (45.5 cm long, 0.75 mm thick, 20 mm wide) excited near one clamp with mid-length acceleration measurement

### 4.3.2 Physical experiment

A PLL experiment is designed to characterize the first bending mode of a clamped-clamped thin beam shown in Fig. 4.13. The beam is 45.5 cm long, 0.75 mm thick, 20 mm wide and is made of structural steel S235. The beam is excited by an electrodynamic shaker (TIRA TV 51075) attached at 4.5 cm of the beam's clamping. An impedance head (DYTRAN 5860B) is fastened to the shaker's stinger and glued to the beam's side. It measures the force applied to the beam. An accelerometer (DYTRAN 3035BG) is fixed by wax at the middle of the beam. The continuation method is applied

Table 4.2: Set of parameters for the physical PLL experiment

$k_i$ in $\text{rad}^{-1}$ (PLL)	$k_p$ in $(\text{rad s})^{-1}$ (PLL)	$k_i$ in $\text{V}(\text{N s})^{-1}$ (amplitude)
5	3	1
$\omega_0$ in Hz	$f_s$ in kHz	$\mu$
12	10	0.01

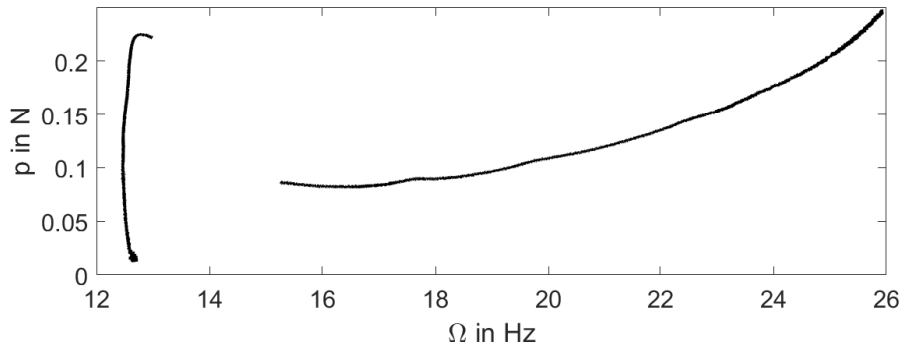


Figure 4.14: Backbone curve of the clamped-clamped thin beam illustrating the presence of an isolated branch of responses

by a digital real-time controller (dSPACE MicroLabBox) and the excitation signal is sent to a power amplifier (TIRA BAA 120) in voltage mode. The displacement amplitude  $X$  is deduced from the acceleration measurement.

In addition to the PLL illustrated in Fig. 3.1a, the force amplitude is imposed through amplitude control as illustrated in Fig. 3.3, implemented with an integral controller. The method to evaluate the force amplitude  $p$  is identical to the one used to evaluate the phase lag, i.e., either using DFT, synchronous demodulation, or adaptive filtering. The parameters are shown in Table 4.2.

Fig. 4.14 shows the backbone of the clamped-clamped beam's first bending mode, identified in a PLL experiment using the method developed in Section 3.2.3. The mode is slightly softening-hardening at low force amplitude  $p$ , i.e., the nonlinear resonance frequency  $\omega$  decreases then increases when the forcing amplitude increases. The force amplitude reaches a maximum  $p \approx 0.25$  N before decreasing. This is typical of an isolated frequency response curve, or isola [89]. A portion of the backbone is left unidentified (dashed line) by a PLL alone, for reasons explained in Chapter 7. The backbone on the isola shows that the structure is hardening, i.e., its resonance

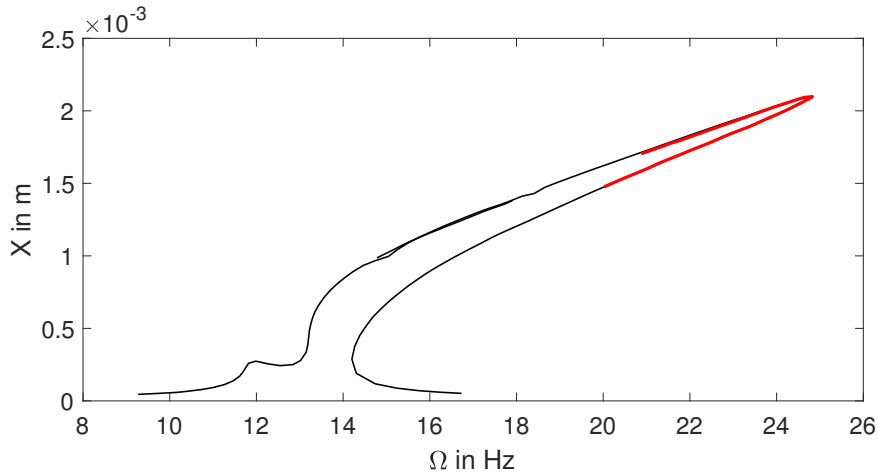


Figure 4.15: Complete FRC of the thin beam setup identified using CBC following the method described in Chapter 6 at  $p = 0.2$  N; branch used as an example in this Chapter shown as a red curve

frequency increases with amplitude.

An FRC of the thin beam possessing an isola is shown in black in Fig. 4.15, identified during a CBC experiment following the method developed in Chapter 6. A PLL alone cannot identify the full FRC of an isola, for reasons explained in Chapter 6. The portion of the isola identifiable during the PLL experiment is shown in red, following the method in Section 3.2.4.

The unstable part of the branch shown in red in Fig. 4.15 is identified using a PLL experiment following the method in Section 3.2.4. First, the beam is stabilized at resonance by fixing  $\phi^* = -\pi/2$  rad. Then,  $\phi^*$  is swept from  $-\pi/2$  rad to  $-2.7$  rad. If stability is lost during the experiment, observing the divergence at constant input parameter can be useful to identify the cause of instability. In such a case, the sweep is manually interrupted.

Using adaptive filtering leads to no issue in the identification, as shown in Fig. 4.16a. Each response of the PLL experiment is stable and the accuracy is high. Using synchronous demodulation with a fast low-pass filter leads to stable responses, as shown in Fig. 4.16b. However, the oscillations in the Fourier decomposition leads to a very broad uncertainty region. Decreasing this oscillation error implies slowing down the phase estimation. Fig. 4.16c shows that slow synchronous demodulation is not capable of stabilizing every response. Fig. 4.16d shows that DFT leads to an accurate estimation

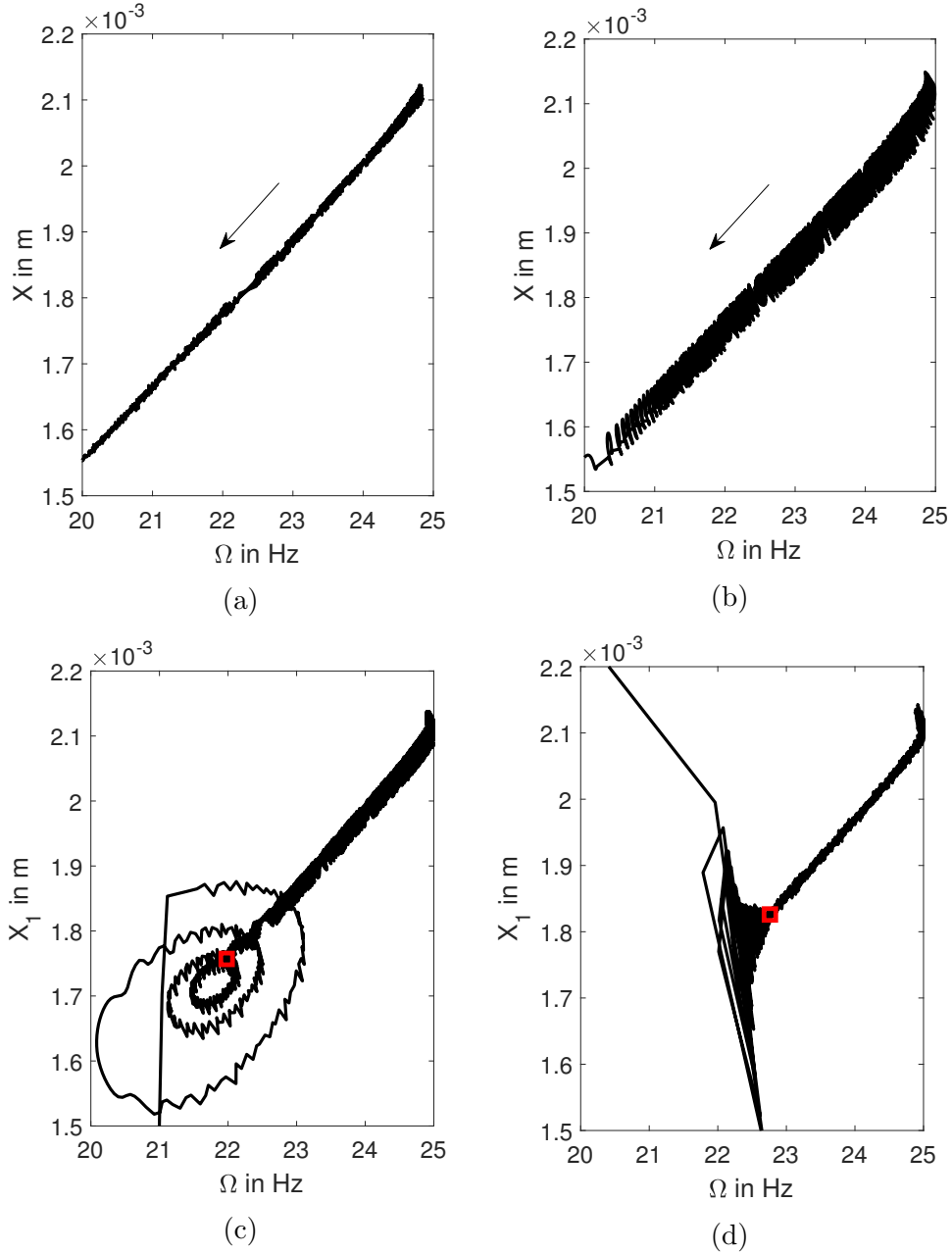


Figure 4.16: Portion of the isolated frequency response's unstable branch at  $p = 0.2 N$  identified by a PLL experiment with different Fourier decomposition methods: (a) adaptive filtering, (b) synchronous demodulation with low-pass cut-off frequency  $\omega_{lp} = 2$  rad/s, (c) same with  $\omega_{lp} = 1$  rad/s, (d) DFT at every period; loss of stability highlighted by a red square

of the Fourier coefficients, but can be too slow for the PLL experiment to be stable. Even though some unstable responses of the oscillator are successfully identified, over-correction by the PI controller after each DFT ultimately leads to divergence.

The duration of each experiment whose result is shown in Fig. 4.16 was independent from the Fourier decomposition method used. It took around 5 min to identify the unstable branch at  $p = 0.2$  N from  $\Omega = 25$  to 20 Hz. The speed of the Fourier decomposition is not the limiting factor in the system's transients that depend on the damping of the beam and the PLL gains. The performance of a PLL experiment is limited by the uncontrolled dynamics of the studied oscillator, as shown in Chapter 2.

## 4.4 Control-based continuation

The CBC experiment includes estimating the non-fundamental harmonics of the response  $x$  to build the reference signal  $x^*$  to ensure that the excitation is monoharmonic. In Chapter 3, we proposed an implementation of the CBC experiment relying on the DFT. We will refer to this implementation as the offline CBC experiment. Algorithm 3.1 requires iterations each time the buffer memory is filled. In this Section, we will see how including adaptive filtering in the CBC experiment removes the need for such iterations, simplifying and accelerating the process.

### 4.4.1 Online control-based continuation experiment

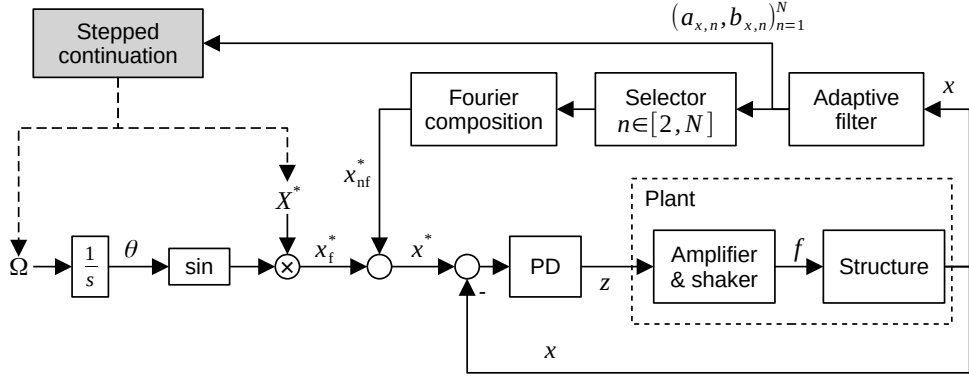
Including adaptive filtering in the CBC experiment allows to perform the Fourier decomposition continuously through time or at each measurement sample. For the input parameters  $(\Omega, X^*)$ , the adaptive filter estimates the Fourier coefficients  $a_{x,n}$  and  $b_{x,n}$  for  $n \in [1, N]$  (see Eq. (1.2)) and the reference signal can be directly defined  $x^*(t) = x_f^*(t) + x_{nf}^*(t)$  with a fundamental component

$$x_f^*(t) = X^* \sin(\Omega t) \quad (4.14)$$

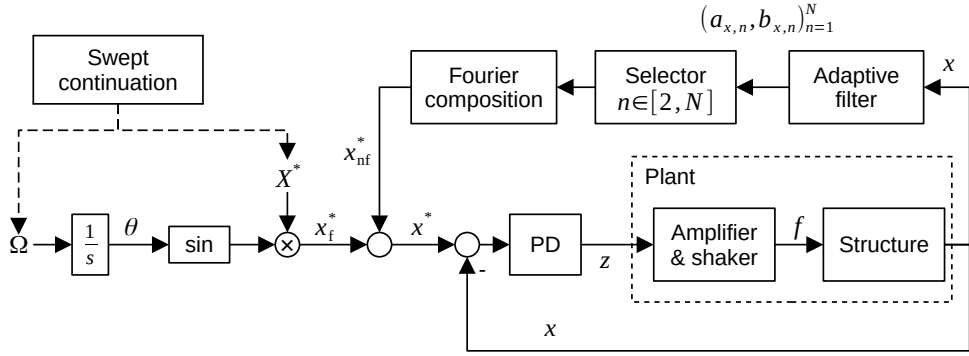
and a non-fundamental component

$$x_{nf}^* = \sum_{n=2}^N a_{x,n} \sin(n\Omega t) + b_{x,n} \cos(n\Omega t). \quad (4.15)$$

The excitation is therefore necessarily monoharmonic once reaching steady-state.



(a)



(b)

Figure 4.17: (a) Stepped CBC experiment with the stepped continuation depending on measured parameters, and (b) Swept CBC experiment with the swept continuation independent of measurement; the gray box represents an offline process

We propose two simple continuation procedures for the input parameter  $X^*$  to identify an S-curve at constant  $\Omega$ . In the first procedure,  $X^*$  is sequentially increased by a step  $h$  once steady-state is reached:  $X^* := X^* + h$ . The steady-state must be detected, e.g., by detecting when the Fourier coefficients  $(a_{x,n}, b_{x,n})_{n=1}^N$  settle. The experiment is called stepped CBC and is illustrated in Fig. 4.17a. In the second procedure,  $X^*$  is increased at a constant rate,  $X^*(t) = \eta t$ . The experiment is called swept CBC and is illustrated in Fig. 4.17b.

Table 4.3: Dimensions of the cantilever steel beam in cm

Length	Width	Height
100	0.6	2

The advantage of swept CBC is that it requires no offline operation. The identification of an S-curve can therefore be significantly sped up. However, a large sweep rate  $\eta$  introduces transients in the response than can alter the accuracy of the characterization, similarly to a swept sine excitation.

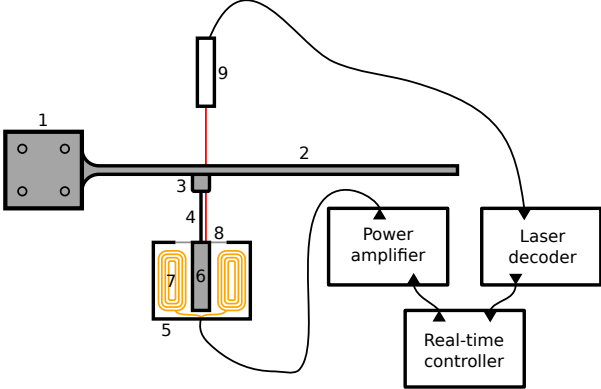
Section B.2.3 shows that an adaptive filter put in feedback with an oscillator can be unstable for large values of  $\mu$ . Stability issues with the adaptive filter can be solved easily in the case of CBC by decreasing  $\mu$ . However, that slows the filter down and the Fourier decomposition takes more time to converge. In consequence, the non-fundamental harmonics take longer to be canceled.

#### 4.4.2 Experimental set-up

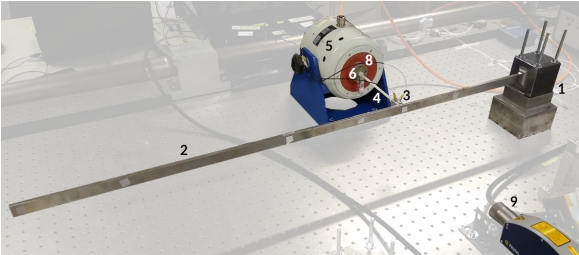
The experimental set-up in Fig. 4.18 comprises a cantilever steel beam excited by an electrodynamic shaker. Its displacement is measured by a laser vibrometer to form a single-input single-output (SISO) system.

The beam and its base in Fig. 4.18b are made from a single block of metal in order to avoid micro-slips in the beam-base connection. The absence of micro-slips renders the physical structure as linear as possible so that nonlinear behavior comes predominantly from the artificial nonlinearity. Furthermore, the absence of bolts between the beam and the base is expected to improve repeatability. The base is bolted to the ground. The dimensions of the beam are listed in Table 4.3. The electrodynamic shaker (TIRA TV 51075) is connected perpendicularly to the beam at 30 cm from the base through a stinger and an impedance head (DYTRAN 5860B) glued to the surface, see Fig. 4.18c.

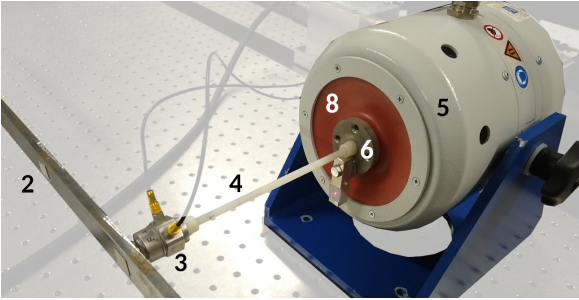
The different nonlinearities are realized using the real-time controller (RTC) dSPACE MicroLabBox. The force applied by the shaker to the structure is  $f_{\text{shaker}}(t) = f(t) - f_{\text{nl}}(x, \dot{x})$  where  $f(t)$  is the external force and  $f_{\text{nl}}$  is the artificial nonlinearity. The RTC sends the excitation signal as a voltage, transformed in current by the power amplifier (TIRA BAA 120). The current then runs through the shaker's coils, generating a force on the magnetic core attached to the casing by a membrane. For the generation



(a)



(b)



(c)

Figure 4.18: Experimental setup composed of: (1) fixed base, (2) cantilever beam, (3) impedance head, (4) stinger, (5) shaker's casing, (6) shaker's magnetic core, (7) shaker's electrical coils, (8) shaker's membrane, (9) laser vibrometer.

Table 4.4: Natural frequencies  $\omega_{0,n}$  and damping ratios  $\xi$  of the physical system's first 6 modes

Mode	$\omega_{0,n}$ in Hz	$\xi$ in %
1	6.2	0.82
2	31.8	0.66
3	78.3	0.35
4	170.9	0.13
5	254.6	1.24
6	303.5	0.56

of the artificial nonlinearities, it is important that the force applied to the physical system corresponds to the signal sent by the RTC. It is non-trivial to impose an exact force signal at the impedance head, whereas the force inside the shaker is proportional to the current running through its coil. For this reason, the physical system includes the impedance head, the stinger, the magnetic core, and the shaker's membrane in addition to the beam. The excitation point is therefore the shaker's magnetic core. The proportionality constant between the force applied to the core and the RTC's output was measured to be 160 N/V for frequencies larger than 20 Hz.

The laser vibrometer (Polytec NLV-2500-5) measures the displacement and velocity of the magnetic core so that the excitation and measurement points are collocated. The displacement and velocity signals are then sent to the RTC for the calculation of the artificial nonlinearities.

A linear model of the beam is created. The beam is excited by sine sweeps at a low amplitude of 0.3 N without artificial nonlinearity in order to obtain its linear frequency response function (FRF). The PolyMAX method [90] identifies the modal parameters of the first six modes, shown in Table 4.4. The FRF was then expressed as a linear combination of six single-pole transfer functions, each corresponding to a mode. The single-pole transfer functions gains were computed such that the amplitude of their sum at resonance corresponds to the measurement. A linear mass-spring-damper model of the beam was also established. The measured and synthesized FRFs are compared in Fig. 4.19.

### 4.4.3 Parameters and procedure

The system is made nonlinear by defining a non-zero nonlinear function  $f_{nl}(x, \dot{x})$ . CBC is used to characterize the system and a differential controller

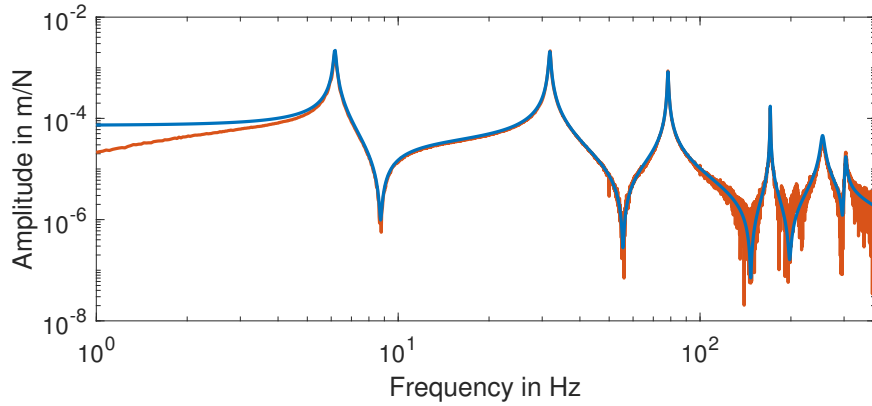


Figure 4.19: FRFs of the linear beam: measured (orange) and synthesized from the mass-spring-damper model (blue)

is used (see Section 2.3.2). Its gain  $k_d$  is chosen by trial and error: it is increased until there are no more jumps during the different continuation runs. A gain  $k_d = 400$  Ns/m was found to be adequate for stabilizing the different nonlinear systems considered in this Section.

The user-defined parameters are listed in Table 4.5. Five harmonics are considered for all CBC strategies and a 10 kHz sampling frequency is sufficient for measuring them properly. The step size  $h$  for the offline and stepped methods is chosen to obtain approximately 50 measurement points on the S-curves, a good compromise between short testing time and sufficient refinement of the S-curves for interpolating the response surface. The sweep rate  $\eta$  for the swept continuation is such that the testing time is significantly shorter than with the other strategies.

The steady-state detection algorithm illustrated in Fig. 4.20 is implemented for the offline and stepped methods. The Fourier coefficients of the displacement signal are estimated after each period. A buffer collects the evolution of the coefficients over 5 periods and computes their standard deviations. The greatest standard deviation among the Fourier coefficients (“max std(X)”) defines the convergence indicator that is compared to an absolute tolerance  $\text{tol}_{\text{conv},a}$ . Because of transients, this indicator is evaluated after each interval of 10 periods. Similarly, the greatest non-fundamental Fourier coefficient of the force signal (“max  $|F_{\text{nf}}|$ ”) defines an invasiveness indicator that is used for the offline method. Because the amplitude of the force varies greatly along an S-curve, this indicator is compared to an absolute tolerance  $\text{tol}_{\text{inv},a}$  and its ratio to the fundamental amplitude is com-

Table 4.5: Parameters of the different CBC strategies: (a) offline, (b) stepped, (c) swept

(a)

$h$ in m	interval in #per	buffer in #per
$1 \times 10^{-5}$	10	5
$\text{tol}_{\text{inv,a}}$ in N	$\text{tol}_{\text{inv,r}}$ in %	$\text{tol}_{\text{conv,a}}$ in m
0.01	1	$2 \times 10^{-7}$

(b)

$h$ in m	interval in #per	buffer in #per
$1 \times 10^{-5}$	10	5
$\text{tol}_{\text{conv,a}}$ in m	$\mu$	
$2 \times 10^{-7}$	$10/f_s$	

(c)

$\eta$ in m/s	$\mu$
$4 \times 10^{-5}$	$10/f_s$

pared to a relative tolerance  $\text{tol}_{\text{inv,r}}$ . For the stepped and swept methods, the internal parameter  $\mu$  of the LMS algorithm depends strongly on the sampling frequency. Its normalized value is listed in Table 4.5.

By collecting S-curves measured at different frequencies, the response surface can be constructed and interpolated by kriging [84], a relatively inexpensive method capable of addressing noise in the data (kriging was used online in [41]).

#### 4.4.4 Results

The first artificial nonlinearity considered to demonstrate the CBC algorithms is a cubic stiffness:

$$f_{\text{nl},1}(x) = k_3 x^3, \quad (4.16)$$

where  $k_3 = 3 \times 10^{11}$  N/m<sup>3</sup>. The offline, stepped and swept strategies are applied to this oscillator. To have a more precise view of the invasiveness of the different schemes, the invasiveness indicator  $\max|F_{\text{nf}}|$  is shown in

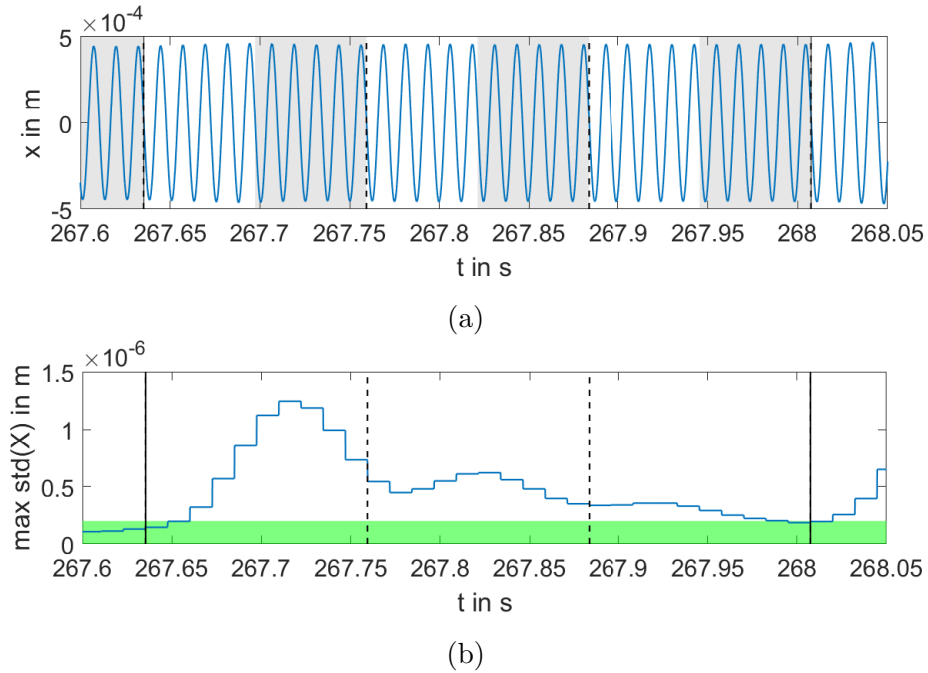


Figure 4.20: Steady-state detection algorithm: (a) time series of the displacement with evaluation of steady-state every 10 periods (dashed line) and with continuation steps (plain line) when the indicator is below the tolerance and (b) convergence indicator computed every period over buffers of 5 periods (gray area) with the tolerance  $\text{tol}_{\text{conv},a}$  (green area)

Fig. 4.21. Without invasiveness cancellation, i.e. if  $x_{\text{nf}} = 0$ ,  $\max|F_{\text{nf}}|$  rises above 1 N. The offline method is able to reduce  $\max|F_{\text{nf}}|$  down to two orders of magnitude by performing corrective iterations. The stepped method cannot reduce  $\max|F_{\text{nf}}|$  below twice what is achieved with the offline method highlighting that there is a limit to the performance of adaptive filtering depending on the parameter  $\mu$ . Due to transient effects, the swept method reaches values of  $\max|F_{\text{nf}}|$  up to twice what is obtained by the stepped method.

After identifying a collection of S-curves, the response surface can be interpolated and sliced at constant excitation amplitudes to extract the FRCs in Fig. 4.22 (see Section 3.2.4 for details). For comparison, this figure also includes the FRCs measured using classical sine sweeps up and down. The FRCs identified using offline and stepped CBC are indistinguishable whereas the FRC identified using swept CBC exhibits a slight discrepancy near the resonance peak. They all correlate very well with the displacement

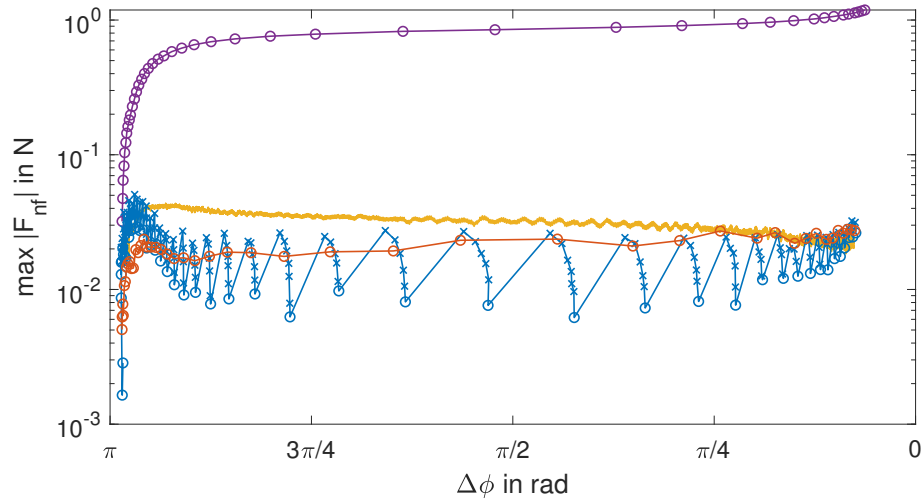


Figure 4.21: Invasiveness indicator at 82 Hz: no corrections (purple), offline (blue), stepped (orange) and swept (yellow); correction and continuation steps marked with  $(\times)$  and  $(\circ)$  respectively; phase lag  $\Delta\phi$  between  $X_f$  and  $F_f$  indicating the progression along the S-curve

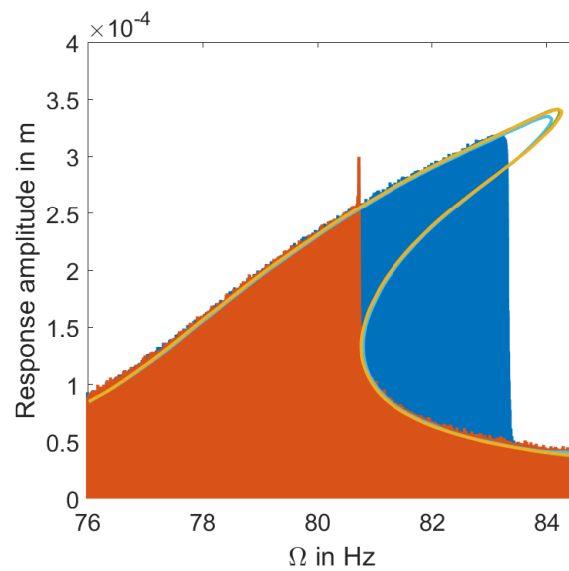


Figure 4.22: Cubic stiffness, FRC at 1N forcing: open-loop sweep up (blue) and down (orange), offline CBC (green), stepped CBC (yellow) and swept CBC (cyan)

Table 4.6: Time in [mm:ss] to identify the S-curve at 82 Hz and manifold of the Duffing oscillator

Algorithm	S-curve	Manifold
Swept	00:13	07:09
No cancellation	00:17	—
Stepped	00:18	10:14
Offline	00:32	14:29

amplitude obtained under open-loop sine sweeps. However, as the sweep up approaches the fold bifurcation near resonance, the system jumps prematurely without identifying the periodic orbits close to resonance. This result nicely evidences the practical relevance of stabilizing responses using control-based methods.

The testing time required for the identification of the S-curve and of the manifold is listed in Table 4.6. It heavily depends on the duration of transients in the system's response, themselves depending on the CBC controller. Because transients last for a certain number of periods, they are expected to be shorter when identifying a mode around 80 Hz than modes at lower frequencies. Consequently, the absolute duration of the experiments should not be directly compared to performance in the literature. Rather, the relative performance of the online CBC and swept CBC can be compared herein to the state-of-the-art offline CBC. As per design, the swept CBC method is the fastest. Interestingly, the stepped method is almost as fast as the algorithm with no corrective action. It stems from the fact that both methods must wait for steady-state before performing the continuation. The offline method is the slowest and requires roughly twice the time needed for the swept method.

The identification of a system with hardening-softening-hardening stiffness

$$f_{nl,2}(x) = k_2 x^2 \operatorname{sgn}(x) + k_3 x^3 + k_4 x^4 \operatorname{sgn}(x) \quad (4.17)$$

with  $k_2 = 10^8 \text{ N/m}^2$ ,  $k_3 = -2 \times 10^{11} \text{ N/m}^3$ , and  $k_4 = 10^{14} \text{ N/m}^4$  is shown in Fig. 4.23. The hardening at low and high displacement amplitudes is implemented to avoid negative stiffness. One can notice the existence of four bifurcation points in the FRC, rendering the open-loop identification much more challenging.

The capability of CBC to characterize a system with non-smooth non-

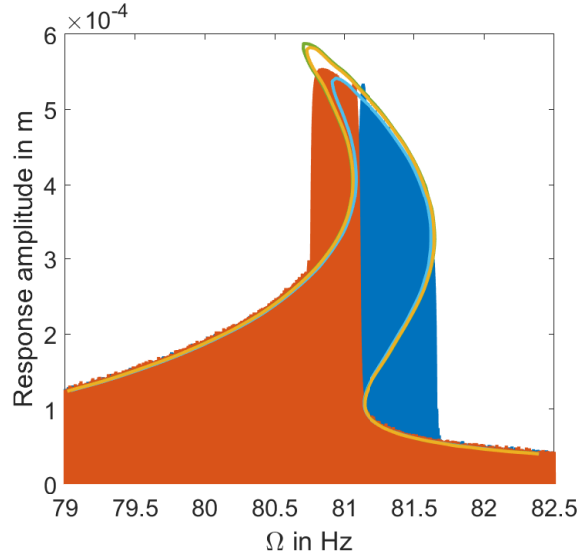


Figure 4.23: Hardening-softening-hardening stiffness, FRC at  $F = 0.6$  N, open-loop sweep up (blue) and down (orange), offline CBC (green), stepped CBC (yellow) and swept CBC (cyan)

linearity is demonstrated by introducing a piece-wise linear stiffness

$$f_{nl,3}(x) = \begin{cases} k_{pwl}(x + x_{lim}) & \text{for } x \leq -x_{lim}, \\ 0 & \text{for } -x_{lim} < x < x_{lim}, \\ k_{pwl}(x - x_{lim}) & \text{for } x \geq x_{lim}, \end{cases} \quad (4.18)$$

with  $x_{lim} = 3 \times 10^{-4}$  m and  $k_{pwl} = 3 \times 10^4$  N/m. The response surface (and thus the FRC) in Fig. 4.24 changes suddenly when reaching the displacement amplitude  $x_{lim}$ .

Fig. 4.25 presents the CBC results when quadratic damping is added to a cubic stiffness:

$$f_{nl,4}(x, \dot{x}) = k_3 x^3 + k_{qd} \dot{x}^2 \operatorname{sgn}(\dot{x}) \quad (4.19)$$

with  $k_3 = 3 \times 10^{11}$  N/m<sup>3</sup> and  $k_{qd} = 20$  Ns<sup>2</sup>/m<sup>2</sup>. The FRCs for a lower excitation level are included to illustrate the change in damping with amplitude.

Finally, friction is added to a cubic stiffness

$$f_{nl,5}(x, \dot{x}) = k_3 x^3 + \begin{cases} -k_{frict} & \text{for } \dot{x} < 0 \\ 0 & \text{for } \dot{x} = 0 \\ k_{frict} & \text{for } \dot{x} > 0 \end{cases} \quad (4.20)$$

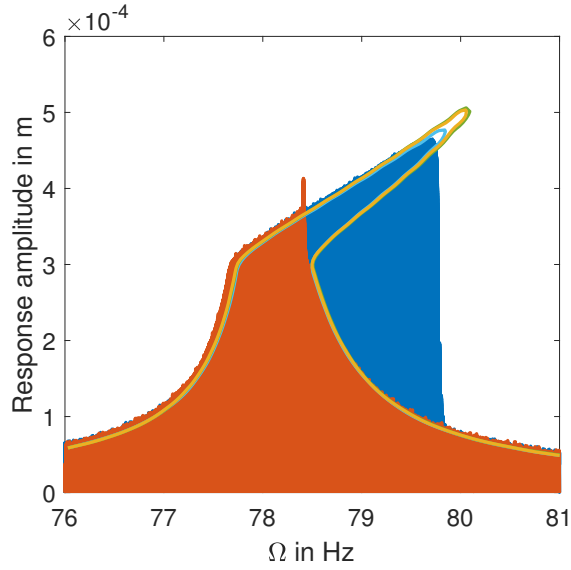


Figure 4.24: Piece-wise linear stiffness, FRC at  $F = 0.6$  N, open-loop sweep up (blue) and down (orange), offline CBC (green), stepped CBC (yellow) and swept CBC (cyan)

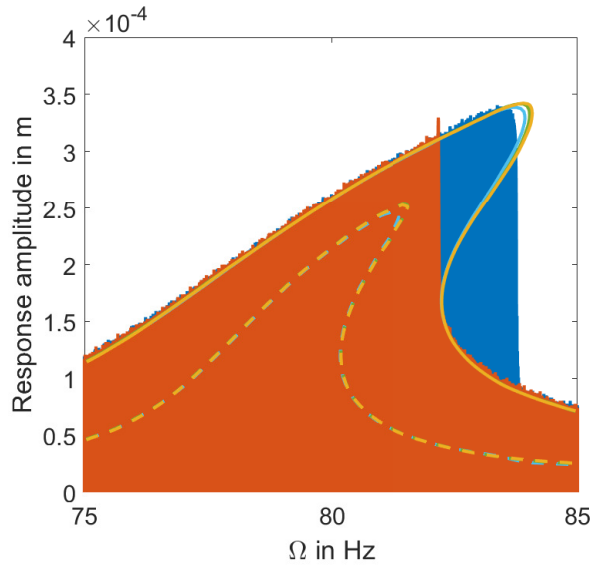


Figure 4.25: Quadratic damping and cubic stiffness, FRC at  $F = 2$  N, open-loop sweep up (blue) and down (orange), offline CBC (green), stepped CBC (yellow) and swept CBC (cyan); FRC at  $F = 0.7$  N (dashed curve) obtained by CBC

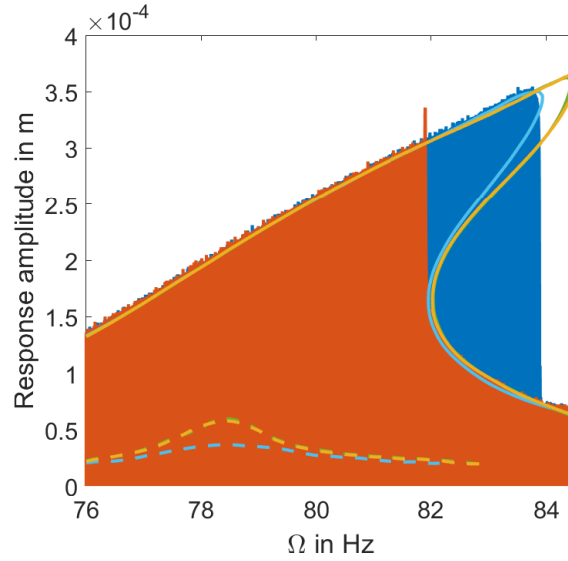


Figure 4.26: Friction and cubic stiffness, FRC at  $F = 2$  N, open-loop sweep up (blue) and down (orange), offline CBC (green), stepped CBC (yellow) and swept CBC (cyan); FRC at  $F = 0.7$  N (dashed curve) obtained by CBC

Table 4.7: Time in [mm:ss] for the identification of the manifold with cubic stiffness (1), hardening-softening-hardening stiffness (2), piece-wise linear stiffness (3), quadratic damping and cubic stiffness (4), and friction and cubic stiffness (5)

Algorithm	System				
	1	2	3	4	5
Swept	07:09	04:22	06:51	05:18	04:38
Stepped	10:14	08:40	10:23	06:19	06:04
Offline	14:29	10:09	11:55	09:18	09:06

with  $k_3 = 3 \times 10^{11}$  n/m<sup>3</sup> and  $k_{\text{frict}} = 0.5$  N. The CBC results are given in Fig. 4.26. The lower amplitude FRCs show that, unlike quadratic damping, the effect of friction is independent of the excitation amplitude.

The testing time to identify the different response surfaces is shown in Table 4.7. Consistent results are observed, namely the swept CBC is the fastest algorithm followed by stepped CBC and then by the offline CBC. It

is also seen that the gain in time depends on the type of nonlinearity. For instance, the softening and piece-wise nonlinearities might increase the duration of the transients, which could explain the greater difference between swept and stepped CBC for those nonlinearities.

## 4.5 Conclusion

In this Chapter, we discussed three methods to perform the Fourier decomposition of a periodic signal during an experiment. An estimation of the phase lag between the response and the force is needed during a PLL experiment, while a monoharmonic excitation is ensured by copying the non-fundamental harmonics of the response into the reference signal during a CBC experiment.

The DFT is the most straightforward method but requires the recording of a whole number of periods. The transformation is done by a real-time controller in parallel to the experiment, making it an offline method. Using multiple buffer memories storing data in parallel allows to update the Fourier coefficients at a rate faster than the signal's frequency, but requires a lot of storage and computing power. Although DFT can be implemented in a CBC experiment, it is incompatible with PLL testing because control would be lost between each coefficient update.

Synchronous demodulation is an online method, i.e., the Fourier coefficients are estimated continuously or at every measurement sample, making it compatible with PLL testing. The drawback of the method is linked to the low-pass filter that is used to isolate constant terms from oscillations. There is a compromise to be made between the filter's speed and the amount of oscillation left in its output. Speed and accuracy are desired for both CBC and PLL experiments. Furthermore, the stability of PLL experiments is directly linked to the speed of the phase lag estimation, as shown in Chapter 2.

Adaptive notch filters, which are usually used to isolate or remove a component at a specific frequency from a signal, perform a very efficient and accurate online Fourier decomposition as an internal process. The Fourier coefficients can be accessed and used directly. We have shown in this Chapter that adaptive filtering provides better performance compared to synchronous demodulation. The speed of the Fourier decomposition is increased by an order of magnitude, improving the stability of PLL experiments. Using an online decomposition during a CBC experiment allows

to simplify and accelerate continuation runs. Fully transient continuation procedures are now possible, without using discrete iterations. However, putting a very fast (high  $\mu$ ) adaptive filter in a feedback loop with an oscillator exposes the system to instabilities. Slowing the filter down to prevent this instability creates a trade-off during PLL experiments because fast phase lag estimation is required to ensure stable responses.



# Chapter 5

## Identification of superharmonic resonances

### Abstract

Superharmonic resonances happen when a nonlinear oscillator resonates at a frequency that is a multiple of the excitation frequency. If fundamental resonances can be defined by a response in phase quadrature with the excitation, this Chapter shows analytically that the phase lag of the dominant harmonic of a superharmonic resonance may be influenced by other harmonics. As a result, it is a combination of phase lags which reaches a specific value at a superharmonic resonance. Phase-locked loops are then exploited to estimate the different phase lags in order to characterize (for the first time) superharmonic resonances using control-based methods. After a numerical demonstration, 3:1 and 5:1 superharmonic resonances of an experiment with an artificial cubic nonlinearity are characterized, with one of them interacting with a fundamental resonance.

### 5.1 Introduction

The previous Chapters focused on the characterization of fundamental resonances of nonlinear oscillators, but nonlinear systems may also exhibit other types of resonance. This Chapter focuses on superharmonic resonances that can be defined as responses with one harmonic reaching a maximum amplitude, whose frequency is a whole multiple of the excitation frequency  $\Omega$  [10]. The superharmonic resonances of a Duffing oscillator were also characterized through their resonant phase lags in [86, 91].

A new result of this Chapter is that superharmonic resonances may not necessarily happen at a specific phase lag between the higher harmonic and the excitation. Instead, they happen when a combination of different harmonic phase lags reaches a specific value. The value of this phase lag combination can be imposed by a phase locked loop (PLL). In practice, the influence of lower harmonics is often negligible, in which case a superharmonic resonance can be identified by imposing the phase lag of the harmonic alone. However, when multiple resonances happen at the same excitation frequency, a phenomenon called modal interaction [10, 92, 93], the influence of lower harmonics must be taken into account.

The relation between superharmonic resonances and the harmonic phase lags is discussed in Section 5.2. Section 5.3 illustrates how control-based continuation (CBC) can be ineffective in characterizing superharmonic resonances. In Section 5.4, a PLL testing procedure is proposed to characterize superharmonic resonances. In Section 5.5, the procedure is applied to an experiment with a virtual cubic nonlinearity to characterize one of the fundamental resonances together with third and fifth superharmonic resonances. The fundamental and fifth superharmonic resonances interact and the consequences on phase lag are developed in Section 5.6. Concluding remarks are provided in Section 5.7.

## 5.2 Resonant phase lags

Periodic responses of a nonlinear oscillator following Eq. (1.1) excited by the force  $f(t) = p \sin(\Omega t)$  have multiple harmonics, as stated in Chapter 1:

$$x(t) = x_0 + \sum_{n=1}^N x_n(t) = r_0 + \sum_{n=1}^N r_n \sin(n\Omega t + \phi_n). \quad (5.1)$$

This work focuses on applications in which subharmonic components of the response, i.e., whose frequencies are rational multiples of the excitation frequency, can be disregarded. The phase lag between the  $n$ th harmonic and the excitation is  $\phi_n$ .

A fundamental resonance can be defined as a response whose amplitude reaches a local maximum. By extension, the  $n$ th superharmonic resonance is a response whose  $n$ th harmonic reaches a maximum [10]. Alternatively, a fundamental resonance can be the response whose phase lag is in quadrature with the excitation. Similarly, the  $n$ th superharmonic resonance can be a response whose  $n$ th harmonic has a well-defined phase lag compared to the

fundamental excitation [86, 91]. This particular phase lag depends on the parity of the harmonic. We will refer to these definitions of resonance as “amplitude resonance” and “phase resonance”, respectively.

In what follows, we propose an improvement of the definition of phase resonance. To this end, we study the phase lag of higher harmonics of the response  $x$  of a weakly nonlinear oscillator:

$$\ddot{x} + \delta\dot{x} + \omega_0^2 x + \epsilon f_{\text{nl}}(x, \dot{x}) = p \sin(\Omega t). \quad (5.2)$$

The coefficient  $\epsilon$  is one order of magnitude smaller than unity. A perturbation series  $x = x_0 + \epsilon x_1 + \epsilon^2 x_2$  is assumed. In essence, this perturbation analysis is the harmonic balance method [94] without correcting the natural frequency of the oscillator [10]. This omission allows for simpler developments focused exclusively on the harmonic phase lags. The results are therefore only valid for small amplitudes. Specifically, the hardening or softening effect of the nonlinearity cannot be studied in this manner [95]. The analytical results will eventually be compared to those given by harmonic balance to assess the validity of the simplification.

### 5.2.1 Derivation

The nonlinear force can be decomposed in a perturbation series as well, using the Taylor series expansion of the function  $f_{\text{nl}}(x, \dot{x})$ :

$$f_{\text{nl}}(x, \dot{x}) = f_{\text{nl}}(x_0, \dot{x}_0) + \epsilon \left( \frac{\partial f_{\text{nl}}}{\partial x}(x_0, \dot{x}_0) x_1 + \frac{\partial f_{\text{nl}}}{\partial \dot{x}}(x_0, \dot{x}_0) \dot{x}_1 \right) + O(\epsilon^2) \quad (5.3)$$

$$= f_{\text{nl}}(x_0, \dot{x}_0) + \epsilon f'_{\text{nl}}(x_0, \dot{x}_0, x_1, \dot{x}_1) + O(\epsilon^2). \quad (5.4)$$

Substituting the perturbations series of the response and nonlinear force into the equation of motion and separating the different orders of magnitude yields a system of linear oscillators:

$$\begin{cases} \ddot{x}_0 + \delta\dot{x}_0 + \omega_0^2 x_0 = p \sin(\Omega t) \\ \ddot{x}_1 + \delta\dot{x}_1 + \omega_0^2 x_1 = -f_{\text{nl}}(x_0, \dot{x}_0) \\ \ddot{x}_2 + \delta\dot{x}_2 + \omega_0^2 x_2 = -f'_{\text{nl}}(x_0, \dot{x}_0, x_1, \dot{x}_1). \end{cases} \quad (5.5)$$

Each of these equations is easy to solve and relies on the solutions at lower orders. The response at order zero is  $x_0 = r_{0,1} \sin(\Omega t + \phi_{0,1})$  with

$$\begin{cases} r_{0,1} = \frac{p}{\sqrt{\delta^2 \Omega^2 + \psi_1^2}} \\ \phi_{0,1} = \text{atan2}(-\delta\Omega, -\psi_1) \end{cases} \quad (5.6)$$

and  $\psi_1 = \Omega^2 - \omega_0^2$ .

### First-order response

The first-order response  $x_1$  corresponds to the response of a linear oscillator excited by the signal  $-f_{nl}(x_0, \dot{x}_0)$  known from order zero. This excitation is a multiharmonic signal that can be decomposed into  $N$  harmonics

$$\begin{aligned} f_{nl}(x_0, \dot{x}_0) &= f_{nl}(r_{0,1} \sin(\Omega t + \phi_{0,1}), r_{0,1} \Omega \cos(\Omega t + \phi_{0,1})) \\ &= h_0(r_{0,1}) + \sum_{n=1}^N g_n(r_{0,1}) \sin(n(\Omega t + \phi_{0,1})) + h_n(r_{0,1}) \cos(n(\Omega t + \phi_{0,1})). \end{aligned} \quad (5.7)$$

Let express the  $N$  harmonics of the first-order response

$$x_1 = x_{1,0} + \sum_{\nu=1}^N x_{1,\nu} = r_{1,0} + \sum_{\nu=1}^N r_{1,\nu} \sin(\nu \Omega t + \phi_{1,\nu}) \quad (5.8)$$

with amplitudes  $r_{1,\nu}$  and phase lag  $\phi_{1,\nu}$ . The subscript  $\nu$  refers to harmonics related to the first-order response. The components of  $f_{nl}(x_0, \dot{x}_0)$  in the basis  $(\sin(\nu \Omega t + \phi_{1,\nu}), \cos(\nu \Omega t + \phi_{1,\nu}))$  are

$$\frac{\Omega}{\pi} \int_t^{t+\frac{2\pi}{\Omega}} f_{nl}(x_0, \dot{x}_0) \sin(\nu \Omega \tau + \phi_{1,\nu}) d\tau = g_\nu(r_{0,1}) \cos \Delta_\nu + h_\nu(r_{0,1}) \sin \Delta_\nu, \quad (5.9)$$

and

$$\frac{\Omega}{\pi} \int_t^{t+\frac{2\pi}{\Omega}} f_{nl}(x_0, \dot{x}_0) \cos(\nu \Omega \tau + \phi_{1,\nu}) d\tau = -g_\nu(r_{0,1}) \sin \Delta_\nu + h_\nu(r_{0,1}) \cos \Delta_\nu \quad (5.10)$$

with  $\Delta_\nu = \phi_{1,\nu} - \nu \phi_{0,1}$ .

Each side of the second equation in (5.5) is multiplied by either  $\sin(\nu \Omega t + \phi_{1,\nu})$  or  $\cos(\nu \Omega t + \phi_{1,\nu})$  and averaged over one period. For each harmonic  $\nu$ , we have a system of two equations:

$$\begin{cases} \nu \Omega \delta r_{1,\nu} - g_\nu(r_{0,1}) \sin \Delta_\nu + h_\nu(r_{0,1}) \cos \Delta_\nu = 0 \\ \psi_\nu r_{1,\nu} - g_\nu(r_{0,1}) \cos \Delta_\nu - h_\nu(r_{0,1}) \sin \Delta_\nu = 0 \end{cases} \quad (5.11)$$

with  $\psi_\nu = \nu^2 \Omega^2 - \omega_0^2$ . The solution is

$$\begin{cases} \Delta_\nu = \text{atan2}(\delta \nu \Omega g_\nu(r_{0,1}) + \psi_\nu h_\nu(r_{0,1}), \psi_\nu g_\nu(r_{0,1}) - \delta \nu \Omega h_\nu(r_{0,1})) \\ r_{1,\nu} = \frac{1}{\delta \nu \Omega} (g_\nu(r_{0,1}) \sin \Delta_\nu - h_\nu(r_{0,1}) \cos \Delta_\nu). \end{cases} \quad (5.12)$$

$x_1$  is thus fully determined.

### Second-order response

The second-order excitation can be decomposed as a sum in which each term corresponds to one harmonic of  $x_1$ :

$$f'_{\text{nl}}(x_0, \dot{x}_0, x_1, \dot{x}_1) = \frac{\partial f_{\text{nl}}}{\partial x}(x_0, \dot{x}_0)x_1 + \frac{\partial f_{\text{nl}}}{\partial \dot{x}}(x_0, \dot{x}_0)\dot{x}_1 \quad (5.13)$$

$$= \sum_{\nu=1}^N \left( \frac{\partial f_{\text{nl}}}{\partial x}(x_0, \dot{x}_0)x_{1,\nu} + \frac{\partial f_{\text{nl}}}{\partial \dot{x}}(x_0, \dot{x}_0)\dot{x}_{1,\nu} \right) \quad (5.14)$$

$$= \sum_{\nu=1}^N f'_{\text{nl},\nu}(x_0, \dot{x}_0, x_{1,\nu}, \dot{x}_{1,\nu}). \quad (5.15)$$

The subscript  $\nu$  refers again to harmonics related to the first-order response. Each term is a multiharmonic signal with the Fourier decomposition:

$$\begin{aligned} f'_{\text{nl},\nu}(x_0, \dot{x}_0, x_{1,\nu}, \dot{x}_{1,\nu}) &= h'_{\nu,0}(r_{0,1}, r_{1,\nu}) \\ &+ \sum_{n=1}^N g'_{\nu,n}(r_{0,1}, r_{1,\nu}) \sin(n\Omega t + \phi_{1,\nu} + (n - \nu)\phi_{0,1}) \\ &+ h'_{\nu,n}(r_{0,1}, r_{1,\nu}) \cos(n\Omega t + \phi_{1,\nu} + (n - \nu)\phi_{0,1}). \end{aligned} \quad (5.16)$$

The second-order response can be written as

$$x_2 = x_{2,0} + \sum_{\mu=1}^N x_{2,\mu} = r_{2,0} + \sum_{\mu=1}^N r_{2,\mu} \sin(\mu\Omega t + \phi_{2,\mu}). \quad (5.17)$$

The subscript  $\mu$  refers to harmonics related to the second-order response. The Fourier coefficients of the second-order excitation  $f'_{\text{nl},\nu}(x_0, \dot{x}_0, x_{1,\nu}, \dot{x}_{1,\nu})$  in the basis  $(\sin(\mu\Omega t + \phi_{2,\mu}), \cos(\mu\Omega t + \phi_{2,\mu}))$  are

$$\begin{aligned} \frac{\Omega}{\pi} \int_t^{t+\frac{2\pi}{\Omega}} f'_{\text{nl},\nu}(x_0, \dot{x}_0, x_{1,\nu}, \dot{x}_{1,\nu}) \sin(\mu\Omega\tau + \phi_{\mu}) d\tau \\ = g'_{\nu,\mu}(r_{0,1}, r_{1,\nu}) \cos \Delta_{\nu,\mu} + h'_{\nu,\mu}(r_{0,1}, r_{1,\nu}) \sin \Delta_{\nu,\mu} \end{aligned} \quad (5.18)$$

and

$$\begin{aligned} \frac{\Omega}{\pi} \int_t^{t+\frac{2\pi}{\Omega}} f'_{\text{nl},\nu}(x_0, \dot{x}_0, x_{1,\nu}, \dot{x}_{1,\nu}) \cos(\mu\Omega\tau + \phi_{\mu}) d\tau \\ = -g'_{\nu,\mu}(r_{0,1}, r_{1,\nu}) \sin \Delta_{\nu,\mu} + h'_{\nu,\mu}(r_{0,1}, r_{1,\nu}) \cos \Delta_{\nu,\mu} \end{aligned} \quad (5.19)$$

with  $\Delta_{\nu,\mu} = \phi_{2,\mu} - \phi_{1,\nu} - (\mu - \nu)\phi_{0,1}$ .

Both sides of the third equation in (5.5) are multiplied by either  $\sin(\mu\Omega t + \phi_{2,\mu})$  or  $\cos(\mu\Omega t + \phi_{2,\mu})$  and averaged over one period. For each harmonic  $\mu$ , we have a system of two equations:

$$\begin{cases} \nu\Omega\delta r_{2,\mu} - \sum_{\nu=1}^N (g'_{\nu,\mu}(r_{0,1}, r_{1,\nu}) \sin \Delta_{\nu,\mu} - h'_{\nu,\mu}(r_{0,1}, r_{1,\nu}) \cos \Delta_{\nu,\mu}) = 0 \\ \psi_\nu r_{2,\mu} - \sum_{\nu=1}^N (g'_{\nu,\mu}(r_{0,1}, r_{1,\nu}) \cos \Delta_{\nu,\mu} + h'_{\nu,\mu}(r_{0,1}, r_{1,\nu}) \sin \Delta_{\nu,\mu}) = 0 \end{cases} \quad (5.20)$$

This system is very difficult to solve because there is a different  $\Delta_{\nu,\mu}$  for each harmonic  $\nu$  of the first-order solution  $x_1$ . In the particular case where the harmonic  $\mu$  of  $x_2$  is generated by a single harmonic  $\nu$  of  $x_1$ , i.e.,

$$g'_{k,\mu}(r_{0,1}, r_{1,k}) = h'_{k,\mu}(r_{0,1}, r_{1,k}) = 0 \quad \forall k \neq \nu, \quad (5.21)$$

the solution is directly

$$\begin{cases} \Delta_{\nu,\mu} = \text{atan2}(\delta\mu\Omega g'_{\nu,\mu} + \psi_\mu h'_{\nu,\mu}, \psi_\mu g'_{\nu,\mu} - \delta\mu\Omega h'_{\nu,\mu}) \\ r_{2,\mu} = \frac{1}{\delta\mu\Omega} (g'_{\nu,\mu} \sin \Delta_{\nu,\mu} - h'_{\nu,\mu} \cos \Delta_{\nu,\mu}) \end{cases} \quad (5.22)$$

with  $\psi_\mu = \mu^2\Omega^2 - \omega_0^2$ . In this case, the harmonic  $x_{2,\mu}$  is fully determined.

### 5.2.2 Examples

To illustrate the previous developments, the first and second-order responses of two nonlinear oscillators are derived. The first (resp. second) example has a cubic (resp. quadratic) stiffness, illustrating an odd (resp. even) nonlinearity.

#### Cubic stiffness

A nonlinear oscillator whose equation of motion is Eq. (5.2) with  $f_{\text{nl}}(x, \dot{x}) = x^3$  is considered. The nonlinear force applied to the response at order zero  $x_0 = r_{0,1} \sin(\Omega t + \phi_{0,1})$  is

$$f_{\text{nl}}(x_0, \dot{x}_0) = \frac{3}{4}r_{0,1}^3 \sin(\Omega t + \phi_{0,1}) - \frac{1}{4}r_{0,1}^3 \sin(3(\Omega t + \phi_{0,1})). \quad (5.23)$$

There are therefore two non-zero harmonics with Fourier coefficients

$$g_1(r_{0,1}) = \frac{3}{4}r_{0,1}^3, \quad h_1(r_{0,1}) = 0, \quad (5.24)$$

$$g_3(r_{0,1}) = -\frac{1}{4}r_{0,1}^3, \quad h_3(r_{0,1}) = 0. \quad (5.25)$$

The first-order excitation is decomposed into the basis of the first-order response:

$$f_{nl}(x_0, \dot{x}_0) = \frac{3}{4}r_{0,1}^3 (\cos \Delta_1 \sin(\Omega t + \phi_{1,1}) - \sin \Delta_1 \cos(\Omega t + \phi_{1,1})) \\ - \frac{1}{4}r_{0,1}^3 (\cos \Delta_3 \sin(3\Omega t + \phi_{1,3}) - \sin \Delta_3 \cos(3\Omega t + \phi_{1,3})) \quad (5.26)$$

with  $\Delta_1 = \phi_{1,1} - \phi_{0,1}$  and  $\Delta_3 = \phi_{1,3} - 3\phi_{0,1}$ .

The first-order response is derived from Eq. (5.12), and its frequency response is shown in Fig. 5.1. The analytical results agree with those of harmonic balance. Two peaks can be observed in  $r_{1,3}$  in Fig. 5.1a. The peak at  $\Omega = \omega_0$  corresponds to the fundamental resonance, i.e., an extremum of  $r_{0,1}$ , leading to an extremum of  $g_3(r_{0,1})$ . There is, however, a second resonance peak at  $\Omega = \omega_0/3$  which does not correspond to an extremum of  $g_3(r_{0,1})$ . It can only correspond to an extremum of  $\sin \Delta_3$ , i.e.,  $\Delta_3 = -\pi/2$ , which is confirmed in Fig. 5.1b. The phase lag  $\phi_{1,3}$  drops by  $\pi$  rad at the third superharmonic resonance and  $3\pi$  rad at the fundamental resonance, shown in Fig. 5.1c.

The second-order excitation generated by harmonic  $\nu = 1$  is

$$f'_{nl,1}(x_0, \dot{x}_0, x_{1,1}, \dot{x}_{1,1}) = \frac{3}{4}r_{0,1}^2 r_{1,1} (2 \sin(\Omega t + \phi_{1,1}) \\ + \sin(\Omega t + 2\phi_{0,1} - \phi_{1,1}) - \sin(3\Omega t + 2\phi_1 + \phi_{1,1})) \quad (5.27)$$

and the one generated by harmonic  $\nu = 3$  is

$$f'_{nl,3}(x_0, \dot{x}_0, x_{1,3}, \dot{x}_{1,3}) = -\frac{3}{4}r_{0,1}^2 r_{1,3} (\sin(\Omega t + \phi_{1,3} - 2\phi_{0,1}) \\ - 2 \sin(3\Omega t + \phi_3) + \sin(5\Omega t + \phi_{1,3} + 2\phi_{0,1})). \quad (5.28)$$

For harmonic  $\nu = 3$  of the first-order response, only three Fourier coefficients are non-zero:

$$g'_{3,1}(r_{0,1}, r_{1,3}) = -\frac{3}{4}r_{0,1}^2 r_{1,3}, \quad h'_{3,1}(r_{0,1}, r_{1,3}) = 0, \quad (5.29)$$

$$g'_{3,3}(r_{0,1}, r_{1,3}) = \frac{3}{2}r_{0,1}^2 r_{1,3}, \quad h'_{3,3}(r_{0,1}, r_{1,3}) = 0, \quad (5.30)$$

$$g'_{3,5}(r_{0,1}, r_{1,3}) = -\frac{3}{4}r_{0,1}^2 r_{1,3}, \quad h'_{3,5}(r_{0,1}, r_{1,3}) = 0. \quad (5.31)$$

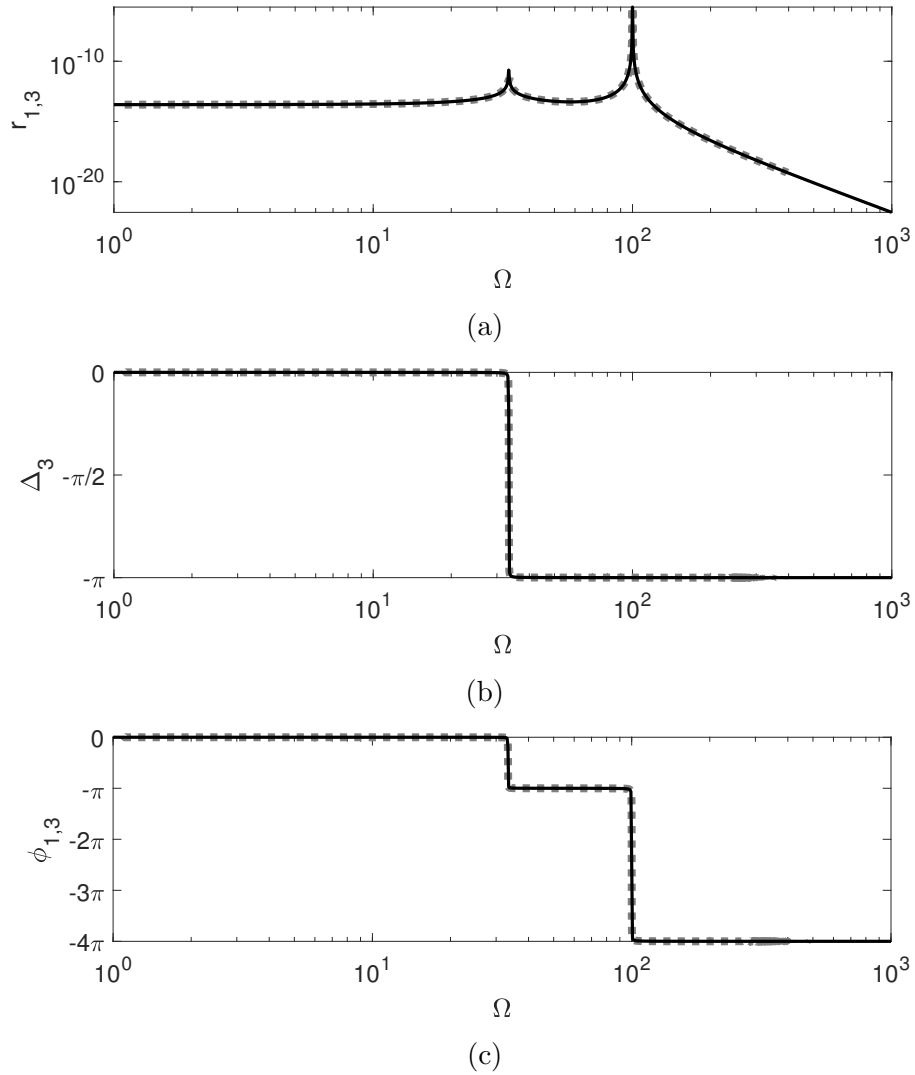


Figure 5.1: Third harmonic parameters of the first-order response; oscillator (5.2) with cubic stiffness,  $\omega_0 = 100$ ,  $\delta = 0.1$ ,  $p = 10$ ; analytical solution (black) and harmonic balance with pseudo-arclength continuation and three harmonics [59] (dashed gray).

The second-order excitation generated by harmonic  $\nu = 3$  of the first-order response is then decomposed into the basis of the second-order response:

$$\begin{aligned} f'_{nl,3} = & -\frac{3}{4}r_{0,1}^2 r_{1,3} (\cos \Delta_{3,1} \sin(\Omega t + \phi_{2,1}) - \sin \Delta_{3,1} \cos(\Omega t + \phi_{2,1})) \\ & + \frac{3}{2}r_{0,1}^2 r_{1,3} (\cos \Delta_{3,3} \sin(3\Omega t + \phi_{2,3}) - \sin \Delta_{3,3} \cos(3\Omega t + \phi_{2,3})) \\ & - \frac{3}{4}r_{0,1}^2 r_{1,3} (\cos \Delta_{3,5} \sin(5\Omega t + \phi_{2,5}) - \sin \Delta_{3,5} \cos(5\Omega t + \phi_{2,5})) \end{aligned} \quad (5.32)$$

with  $\Delta_{3,1} = \phi_{2,1} - \phi_{1,3} + 2\phi_{0,1}$ ,  $\Delta_{3,3} = \phi_{2,3} - \phi_{1,3}$ , and  $\Delta_{3,5} = \phi_{2,5} - \phi_{1,3} - 2\phi_{0,1}$ .

Harmonics  $\mu = 1$  and 3 of the second-order response are both generated from harmonics  $\nu = 1$  and 3 of the first-order response. However, harmonic  $\mu = 5$  is only generated by harmonic  $\nu = 3$ . This means that the second-order term  $x_{2,5}$  is easily derived from Eq. (5.22) and its frequency response function is shown in Fig. 5.2. The forcing amplitude was increased for the harmonic balance method to be above machine precision, due to the very low amplitude of the fifth harmonic. Although the hardening of the fundamental peak is not modeled in the analysis, the analytical results are still consistent with harmonic balance. There are three peaks observed in  $r_{2,5}$  in Fig. 5.2a. The peak at  $\Omega = \omega_0$  is again the fundamental resonance due to an extremum of  $r_{0,1}$  and  $g'_{3,5}(r_{0,1}, r_{1,3})$ . The peak at  $\Omega = \omega_0/3$  is the third superharmonic resonance corresponding to an extremum of  $r_{1,3}$  and  $g'_{3,5}(r_{0,1}, r_{1,3})$ . However, there is a peak at  $\Omega = \omega_0/5$  that does not correspond to an extremum of  $g'_{3,5}(r_{0,1}, r_{1,3})$  but rather of  $\sin \Delta_{3,5}$ , i.e.,  $\Delta_{3,5} = -\pi/2$ , which is confirmed in Fig. 5.2b. The phase lag  $\phi_{2,5}$  drops by  $\pi$  rad at the fifth and third superharmonic resonance and by  $5\pi$  rad at the fundamental resonance, shown in Fig. 5.2c.

In conclusion, the phase lag of the fundamental harmonic has an influence on the third superharmonic resonance. The resonance peak happens at the quadrature of both  $\Delta_3$  and  $\phi_{1,3}$ , consistently with [86]. The phase lags of the fundamental and third harmonics both influence the fifth superharmonic resonance. The resonance peak happens at the quadrature of both  $\Delta_{3,5}$  and  $\phi_{2,5}$ , consistently with [86]. In the particular case of a single-degree-of-freedom system, it is not useful to consider the influence of the fundamental harmonic.

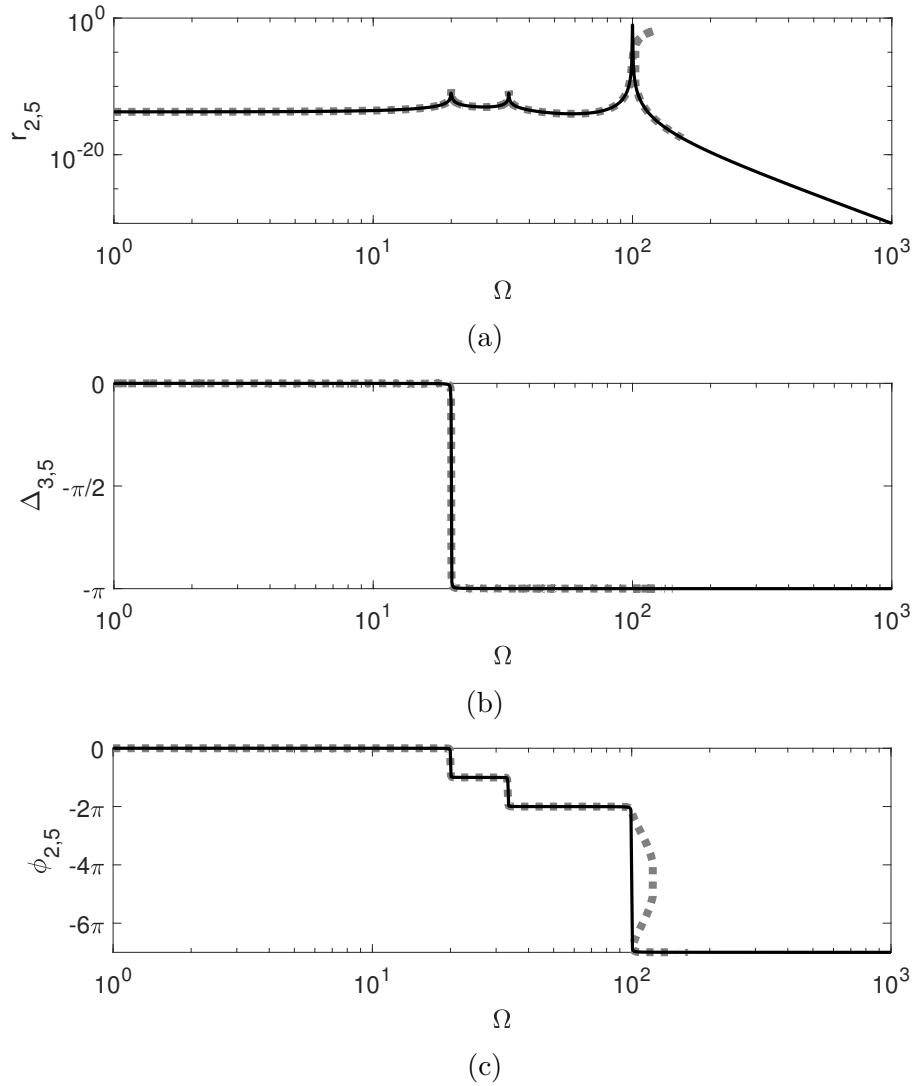


Figure 5.2: Fifth harmonic parameters of the second-order response; oscillator (5.2) with cubic stiffness,  $\omega_0 = 100$ ,  $\delta = 0.1$ ,  $p = 10^3$ ; analytic solution (black) and harmonic balance with pseudo-arclength continuation and five harmonics [59] (dashed gray).

### Quadratic stiffness

For  $f_{\text{nl}}(x, \dot{x}) = x^2$ , the nonlinear force at order zero is

$$f_{\text{nl}}(x_0, \dot{x}_0) = \frac{1}{2}r_{0,1}^2 - \frac{1}{2}r_{0,1}^2 \cos(2(\Omega t + \phi_{0,1})). \quad (5.33)$$

There are therefore two non-zero harmonics with Fourier coefficients

$$h_0(r_{0,1}) = \frac{1}{2}r_{0,1}^2, \quad (5.34)$$

$$g_2(r_{0,1}) = 0, \quad h_2(r_{0,1}) = -\frac{1}{2}r_{0,1}^2. \quad (5.35)$$

It follows that:

$$f_{\text{nl}}(x_0, \dot{x}_0) = \frac{1}{2}r_{0,1}^2 - \frac{1}{2}r_{0,1}^2 (\cos \Delta_2 \sin(2\Omega t + \phi_{1,2}) - \sin \Delta_2 \cos(2\Omega t + \phi_{1,2})) \quad (5.36)$$

with  $\Delta_2 = \phi_{1,2} - 2\phi_{0,1}$ .

The first-order response derived from Eq. (5.12) is shown in Fig. 5.3. The analytical results agree with those of the harmonic balance. Two peaks can be observed in  $r_{1,2}$  in Fig. 5.3a. The peak at  $\Omega = \omega_0$  corresponds to the fundamental resonance, i.e., an extremum of  $r_{0,1}$ , leading to an extremum of  $h_2(r_{0,1})$ . There is a second resonance peak at  $\Omega = \omega_0/2$  corresponding to an extremum of  $\cos \Delta_2$ , i.e.,  $\Delta_2 = 0$ , which is confirmed in Fig. 5.3b. The phase lag  $\phi_{1,2}$  drops by  $\pi$  rad at the second superharmonic resonance and  $2\pi$  rad at the fundamental resonance, as shown in Fig. 5.3c.

The second-order excitation generated by the constant term ( $\nu = 0$ ) of the first-order response is

$$f'_{\text{nl},0}(x_0, \dot{x}_0, x_{1,0}) = 2r_{0,1}r_{1,0} \sin(\Omega t + \phi_{0,1}) \quad (5.37)$$

and the one generated by harmonic  $\nu = 2$  is

$$f'_{\text{nl},2}(x_0, \dot{x}_0, x_{1,2}, \dot{x}_{1,2}) = r_{0,1}r_{1,2}(\cos(\Omega t + \phi_{1,2} - \phi_{0,1}) - \cos(3\Omega t + \phi_{1,2} + \phi_{0,1})). \quad (5.38)$$

For harmonic  $\nu = 2$ , only two Fourier coefficients are non-zero:

$$g'_{2,1}(r_{0,1}, r_{1,2}) = 0, \quad h'_{2,1}(r_{0,1}, r_{1,2}) = r_{0,1}r_{1,2}, \quad (5.39)$$

$$g'_{2,3}(r_{0,1}, r_{1,2}) = 0, \quad h'_{2,3}(r_{0,1}, r_{1,2}) = -r_{0,1}r_{1,2}. \quad (5.40)$$

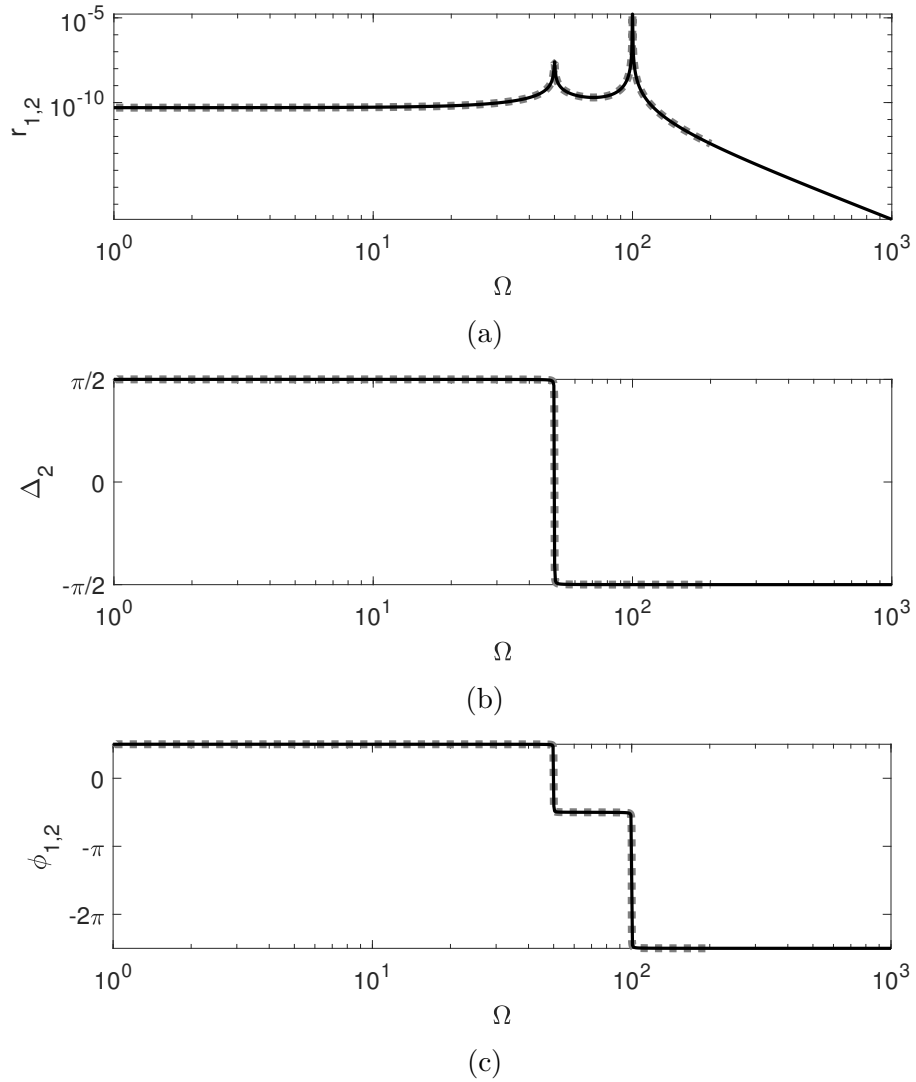


Figure 5.3: Second harmonic parameters of the first-order response; oscillator (5.2) with quadratic stiffness,  $\omega_0 = 100$ ,  $\delta = 0.1$ ,  $p = 10$ ; analytic solution (black) and harmonic balance with pseudo-arclength continuation and five harmonics [59] (dashed gray).

Then,

$$\begin{aligned} f'_{\text{nl},2} = & r_{0,1}r_{1,2} (\cos \Delta_{2,1} \sin(\Omega t + \phi_{2,1}) - \sin \Delta_{2,1} \cos(\Omega t + \phi_{2,1})) \\ & + r_{0,1}r_{1,2} (\cos \Delta_{2,3} \sin(3\Omega t + \phi_{2,3}) - \sin \Delta_{2,3} \cos(3\Omega t + \phi_{2,3})) \end{aligned} \quad (5.41)$$

with  $\Delta_{2,1} = \phi_{2,1} - \phi_{1,2} + \phi_{0,1}$  and  $\Delta_{2,3} = \phi_{2,3} - \phi_{1,3} - \phi_{0,1}$ .

Harmonic  $\mu = 1$  of the second-order response is generated both from the constant term ( $\nu = 0$ ) and harmonic  $\nu = 2$  of the first-order response. However, harmonic  $\mu = 3$  is only generated by harmonic  $\nu = 2$ . The second-order term  $x_{2,3}$  is thus easily derived from Eq. (5.22) and shown in Fig. 5.4. There are three peaks observed in  $r_{2,3}$  in Fig. 5.4a. The peak at  $\Omega = \omega_0$  is once again the fundamental resonance due to an extremum of  $r_{0,1}$  and of  $h'_{2,3}(r_{0,1}, r_{1,2})$ . The peak at  $\Omega = \omega_0/2$  is the second superharmonic resonance corresponding to an extremum of  $r_{1,2}$  and  $h'_{2,3}(r_{0,1}, r_{1,2})$ . The peak at  $\Omega = \omega_0/3$  corresponds to an extremum of  $\cos \Delta_{2,3}$ , i.e.  $\Delta_{2,3} = 0$ , as seen in Fig. 5.4b. The phase lag  $\phi_{2,3}$  drops by  $\pi$  rad at the third and second superharmonic resonance and by  $3\pi$  rad at the fundamental resonance, as shown in Fig. 5.4.

### Conjectures for general odd and even nonlinearities

It is conjectured that an odd (resp. even) nonlinearity  $f_{\text{nl}}$  necessarily leads to  $h_\nu(r_{0,1}) = 0$  ( $g_\nu(r_{0,1}) = 0$ ). The reasoning is that a sine wave—an odd signal—put to an odd (even) function must result in an even (odd) signal. Therefore, we conclude from Eq. (5.12) that first-order superharmonic resonances always happen at  $\Delta_\nu = -\pi/2$  rad ( $\Delta_\nu = 0$  rad) for odd (even) nonlinearities. This is consistent with Eqs. (5.24) and (5.25) (Eqs. (5.34) and (5.35)).

The same reasoning applies to second-order superharmonic resonances. If  $f_{\text{nl}}$  is odd (resp. even), then  $\partial f_{\text{nl}}/\partial x$  and  $\partial f_{\text{nl}}/\partial \dot{x}$  must be even (odd) and therefore  $f'_{\text{nl}}$  must be odd (even). Finally,  $h'_{\nu,\mu}(r_{0,1}, r_{1,\nu}) = 0$  ( $g'_{\nu,\mu}(r_{0,1}, r_{1,\nu}) = 0$ ), which is consistent with Eqs. (5.29) to (5.31) (Eqs. (5.39) and (5.40)). We conclude from Eq. (5.22) that resonance happens at  $\Delta_{\nu,\mu} = -\pi/2$  rad ( $\Delta_{\nu,\mu} = 0$  rad) for harmonics  $\mu$  that are generated by a single harmonic  $\nu$ .

### 5.2.3 Discussion

Let us consider a Fourier decomposition of the response:

$$x(t) = r_0 + \sum_{n=1}^N r_n \sin(n\Omega t + \phi_n). \quad (5.42)$$

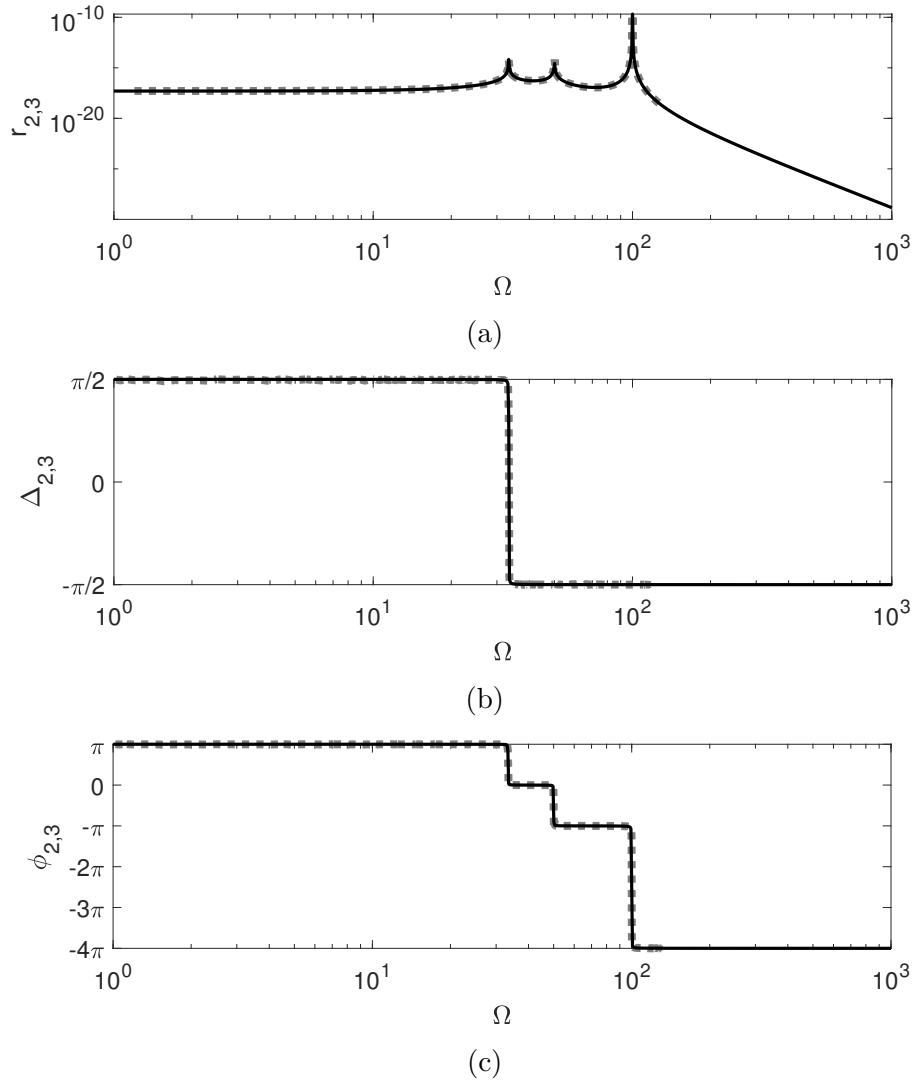


Figure 5.4: Third harmonic parameters of the second-order response; oscillator (5.2) with quadratic stiffness,  $\omega_0 = 100$ ,  $\delta = 0.1$ ,  $p = 10$ ; analytic solution (black) and harmonic balance with pseudo-arclength continuation and five harmonics [59] (dashed gray).

We have shown that the fundamental harmonic of the response is

$$r_1 \sin(\Omega t + \phi_1) = r_{0,1} \sin(\Omega t + \phi_{0,1}) + \epsilon r_{1,1} \sin(\Omega t + \phi_{1,1}) + \epsilon^2 r_{2,1} \sin(\Omega t + \phi_{2,1}) + O(\epsilon^3). \quad (5.43)$$

The component at order zero is at least one order of magnitude higher than those of the higher orders. We can therefore assume that  $r_1 \approx r_{0,1}$  and  $\phi_1 \approx \phi_{0,1}$ . Harmonic  $\nu$  is

$$r_\nu \sin(\nu\Omega t + \phi_\nu) = \epsilon r_{1,\nu} \sin(\nu\Omega t + \phi_{1,\nu}) + \epsilon^2 r_{2,\nu} \sin(\nu\Omega t + \phi_{2,\nu}) + O(\epsilon^3). \quad (5.44)$$

Every superharmonic resonance corresponding to a harmonic  $\nu$  present in the nonlinear force  $f_{\text{nl}}$  is one order of magnitude lower than the fundamental, i.e.,  $r_\nu \approx \epsilon r_{1,\nu}$  and  $\phi_\nu \approx \phi_{1,\nu}$ . For every harmonic  $\mu$  present in  $f'_{\text{nl}}$  but not in  $f_{\text{nl}}$ ,  $r_{1,\mu} = 0$ , and  $r_\mu \approx \epsilon^2 r_{2,\mu}$  and  $\phi_\mu \approx \phi_{2,\mu}$ .

For general nonlinearities, Eqs. (5.12) and (5.22) imply that first-order superharmonic resonances happen when

$$\tan \Delta_\nu = -\frac{g_\nu(r_{0,1})}{h_\nu(r_{0,1})}, \quad (5.45)$$

and second-order superharmonic resonances happen when

$$\tan \Delta_{\nu,\mu} = -\frac{g'_{\nu,\mu}(r_{0,1}, r_{1,\nu})}{h'_{\nu,\mu}(r_{0,1}, r_{1,\nu})}. \quad (5.46)$$

In conclusion, it is in general impossible to know the phase lag value at superharmonic resonance for a system with an unknown nonlinearity. The phase lag is known in advance if and only if the nonlinearity is purely odd or purely even.

The analysis cannot predict the existence of even superharmonic resonances of systems with an odd nonlinearity. However, such superharmonic resonances are known to exist [86]. It appears that even superharmonic resonances of odd systems are created through a different mechanism. This kind of resonance peak does not lie on the main FRC branch, rather, a new branch is created near the resonance by branch-point bifurcations [86].

For single-degree-of-freedom oscillators, superharmonic resonances are always well separated from each other and from the fundamental resonance. At frequencies below the fundamental resonance,  $\phi_1 \approx 0$  rad and  $\Delta_\nu \approx \phi_\nu$ . Similarly, if  $\mu > \nu$ ,  $\phi_1 \approx \phi_\nu \approx 0$  rad and  $\Delta_\mu \approx \phi_\mu$  at low frequencies. In

other words, the influence of lower harmonics on superharmonic resonances can be neglected, in which case superharmonic resonances always happen at the same phase lag, as stated in [86].

For multiple-degrees-of-freedom oscillators, the fundamental phase lag  $\phi_1$  drops by  $\pi$  rad when crossing a resonance and rises by the same amount when crossing an antiresonance. At frequencies in-between,  $\phi_1$  is a multiple of  $\pi$  rad, i.e.,  $\phi_1 \approx k\pi$ . If a first-order  $\nu$ th superharmonic resonance happens in this region, Eq. (5.12) tells us that the phase lag of its  $\nu$ th harmonic is  $\phi_\nu \approx \Delta_\nu + k\nu\phi_1$ . The superharmonic resonance does not always happen at the same phase lag, because it is shifted due to the influence of the fundamental phase lag. This influence is absent from  $\Delta_\nu$ , which can be used to identify the resonance.

A critical case happens when a superharmonic resonance interacts with a fundamental resonance or antiresonance, as shown in Section 5.6. The fundamental phase lag  $\phi_1$  is in the process of dropping or rising by  $\pi$  rad; its influence on  $\phi_\nu$  is therefore greater than  $2\pi$ :  $\phi_\nu$  can have any value at resonance depending on  $\phi_1$ . The influence of  $\phi_1$  can be removed only by considering  $\Delta_\nu$  instead of  $\phi_\nu$ .

The same discussion applies to a second-order superharmonic resonance. This time, however, both  $\phi_1$  and  $\phi_\nu$  influence the phase lag  $\phi_\mu$ . Previous fundamental or  $\nu$ th superharmonic resonance change the phase lag  $\phi_\mu$  at which the  $\mu$ th superharmonic resonance happens. Modal interactions with the fundamental or  $\nu$ th superharmonic resonance can lead to any  $\phi_\mu$  value at resonance. The influence of  $\phi_1$  and  $\phi_\nu$  can be removed only by considering  $\Delta_{\nu,\mu}$  instead of  $\phi_\mu$ .

### 5.3 Control-based continuation

As discussed in Chapter 1, S-curves increasing monotonically in response amplitude allow for the definition of a CBC experiment without folding. However, superharmonic resonances are an example for which the S-curves can exhibit folding, i.e., multiple responses share the same fundamental amplitude  $X_1$ .

For an oscillator with natural frequency  $\omega_0$  under harmonic excitation at  $\Omega = \omega_0/\nu$  for  $\nu \in \mathbb{N}_1$ , part of the oscillator's energy can be transferred from the fundamental harmonic to the  $\nu$ th harmonic, leading to a superharmonic resonance [96]. This energy redistribution causes the amplitude

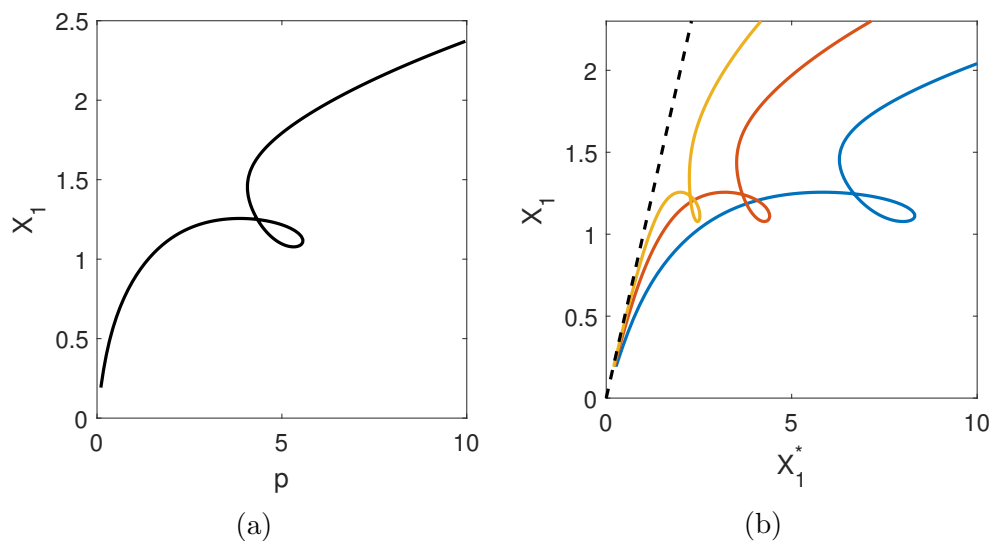


Figure 5.5: S-curve of a third superharmonic resonance of (a) Eq. (1.1) and (b) Eq. (1.6) with  $k_d = 1$  (blue), 2 (orange), and 4 (yellow); all with parameter set 1 from Table 1.1, and  $\Omega = 0.7$ ; computed using the harmonic balance method [59] with 3 harmonics.

of the fundamental harmonic  $X_1$  to decrease locally, as shown in Fig. 5.5a. Fig. 5.5b illustrates that the observed folding persists even if the control gain is increased. Thus, a CBC experiment acting on the fundamental harmonic alone is in general not able to characterize superharmonic resonances without jumps.

It is difficult to extrapolate the conclusions of Chapter 2 to superharmonic resonances because the fundamental harmonic is not dominant; a critical assumption of the analysis. Further work is needed to understand the stability of such orbits. It is not clear whether increasing the damping of a CBC experiment with a differential controller can always stabilize responses such as the ones shown in Fig. 5.5. It is however certain that "excitation CBC" as formulated in this work cannot cross the fold bifurcations shown in Fig. 5.5 because both its input parameters are locally constant at the fold points. Further work is needed to determine whether "action CBC" with the resonating harmonic of the reference signal as an additional input is capable of crossing fold bifurcations at superharmonic resonances during a pseudo-arclength continuation process.

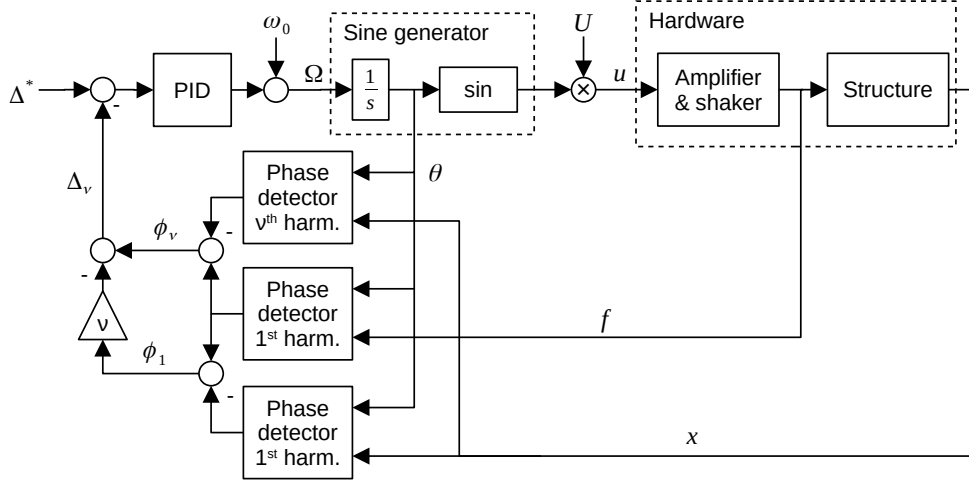


Figure 5.6: PLL controlling the parameter  $\Delta_\nu = \phi_\nu - \nu\phi_1$  for a first-order  $\nu$ th superharmonic resonance

## 5.4 Phase-locked loop testing

Chapter 4 demonstrated that online Fourier decomposition methods are capable of estimating the phase lag of any harmonic. Besides, as discussed in Section 5.2, a first-order superharmonic resonance happens at a specific value of  $\Delta_\nu = \phi_\nu - \nu\phi_1$  (e.g.,  $-\pi/2$  rad for odd nonlinearities and 0 rad for even nonlinearities).  $\Delta_\nu$  can be evaluated by combining estimations of  $\phi_\nu$  and  $\phi_1$ . A PLL can therefore identify a superharmonic resonance following the diagram in Fig. 5.6. For second-order superharmonic resonances, PLL can be used by considering the phase lag  $\Delta_{\nu,\mu} = \phi_\mu - \phi_\nu - (\mu - \nu)\phi_1$  instead. It should be noted that the phase lag  $\Delta$  depends on the nonlinearity. Specifically, if the nonlinearity is purely odd or even, the target phase is known a priori. Otherwise, the nonlinearity must be fully identified prior to PLL testing.

The procedure to identify the backbone curve of a superharmonic resonance is identical to the one proposed in Section 3.2.3. The phase difference target  $\Delta^*$  is set to the desired value, and the voltage amplitude  $U$  is swept (Algorithm 3.2).

Fig. 5.7 depicts the frequency response curve (FRC), calculated using the harmonic balance method, around the first and second-order superharmonic resonances of the cubic oscillator in Table 5.2. As shown earlier,

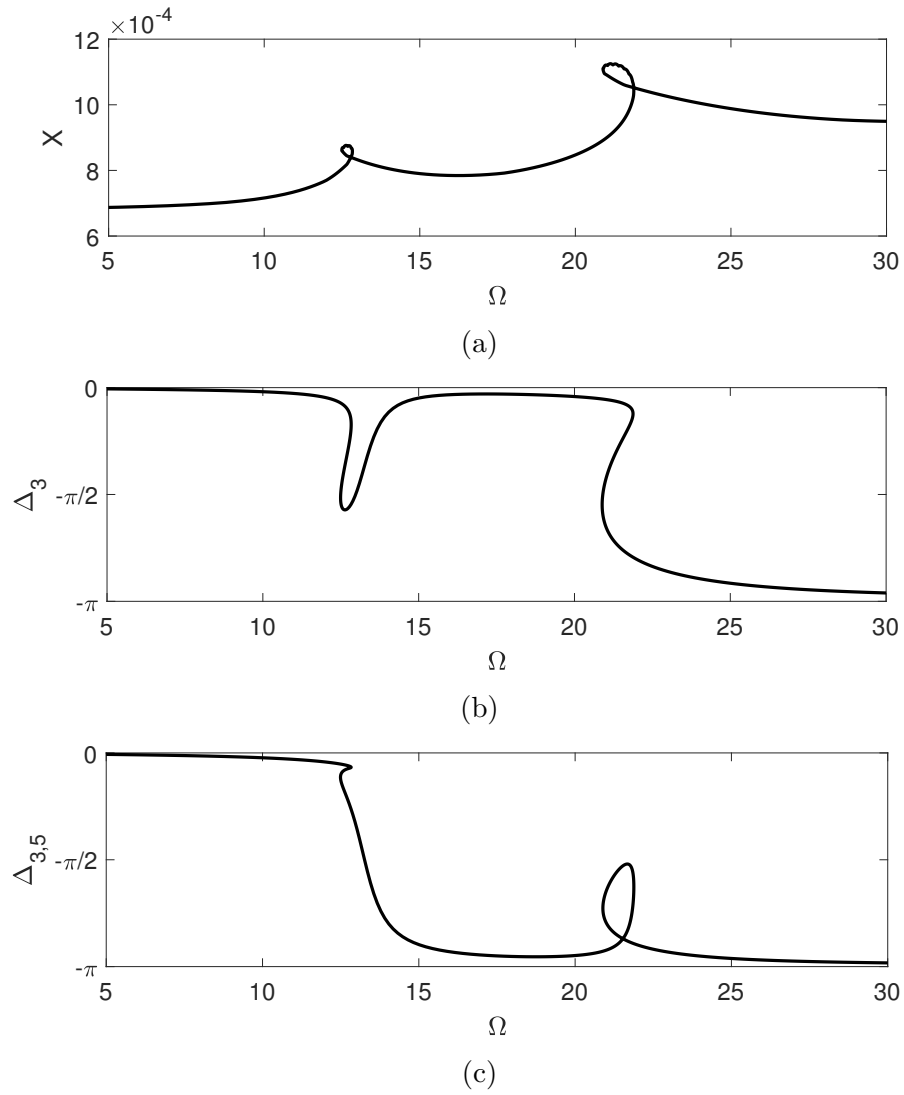


Figure 5.7: FRC around the third and fifth superharmonic resonances of Eq. (1.1) with parameters in Tab. 5.2; computed using the harmonic balance method [59] with 5 harmonics.

Table 5.1: Parameters of the virtual PLL experiment.

$k_i$	$k_p$	$\mu$	$f_s$	$N$
0.2	0.3	$10^{-3}$	$10^4$	11

Table 5.2: Parameters of the cubic oscillator.

$m$	$c$	$k$	$f_{nl}(x, \dot{x})$	$p$
0.05	0.2	57	$2 \times 10^8 x^3$	0.1

the first (resp. second) order resonance happens when  $\Delta_3 = -\pi/2$  rad ( $\Delta_{3,5} = -\pi/2$ ). Fig. 5.7b (5.7c) shows that  $\Delta_3$  ( $\Delta_{3,5}$ ) drops monotonically by approximately  $\pi$  rad across the first (second) order resonance. Therefore, the FRC can be identified using the method in Section 3.2.4, i.e., the force amplitude  $p$  is kept constant by the additional control loop in Fig. 3.3 and the target  $\Delta^*$  is swept from above to below the value at resonance. Similarly to fundamental resonances, the FRC can only be identified in the vicinity of the resonance, because the slope  $d\Omega/d\Delta_3$  ( $d\Omega/d\Delta_{3,5}$ ) becomes very large far from the resonance.

The parameters of the virtual PLL experiment designed to identify the FRC are listed in Table 5.1. The high number of harmonics  $N$  of the Fourier decomposition decreases the noise in the estimated phase lags. The amplitude of the dominant harmonics around the third and fifth superharmonic resonances are presented in Fig. 5.8 along with harmonic balance results. It is clear that the PLL is able to stabilize and accurately identify the resonance peaks for both superharmonic resonances.

## 5.5 Experimental demonstration

The experimental set-up is the nonlinear beam with artificial cubic nonlinearity presented in Section 4.4.2, Fig. 4.18 and Eq. (4.16). The motion was recorded at three additional locations, namely 54, 77, and 100 cm from the clamping, with three accelerometers DYTRAN 3035BG. Except for the mode shapes, every measurement is performed by the laser vibrometer at 30 cm from the clamping. During the PLL experiments, the online Fourier decomposition was performed using adaptive filtering with  $\mu = 10^{-3}$ . The sampling frequency was  $f_s = 10$  kHz, and the number of harmonics was  $N = 10$ . A PI controller with the gains in Table 5.3 was used.

The linear frequency response function is displayed in Fig. 5.9. The (low-

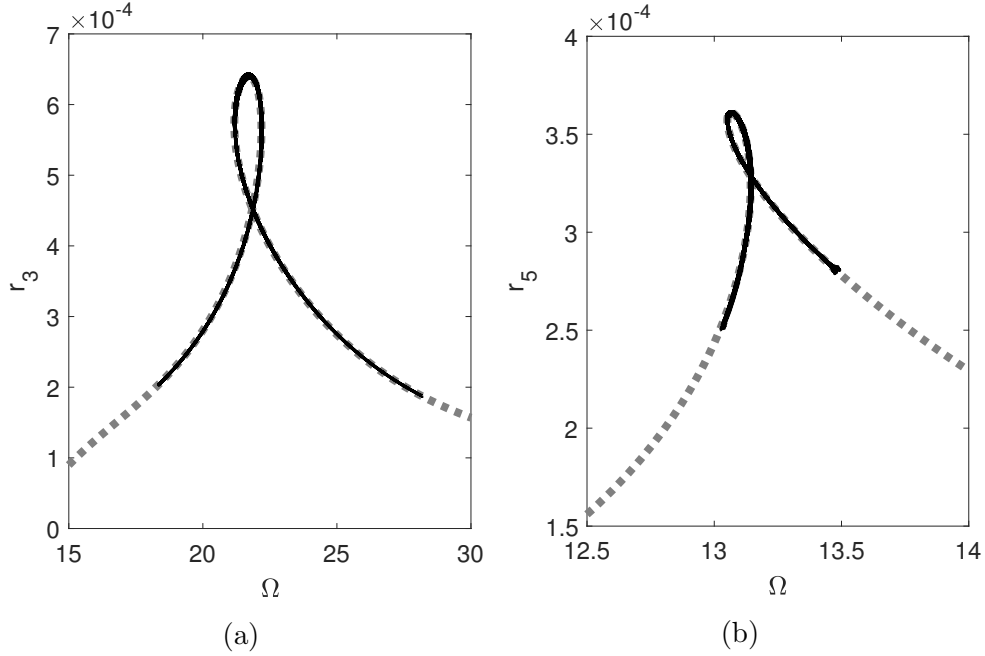


Figure 5.8: (a) Amplitude of the third harmonic around the third superharmonic resonance;  $\Delta_3$  is swept from  $-\pi + 0.1$  rad to  $-0.1$  rad, and (b) amplitude of the fifth harmonic around the fifth superharmonic resonance;  $\Delta_{3,5}$  is swept from  $-\pi + 0.2$  rad to  $-0.2$  rad. Virtual PLL experiment (black) and harmonic balance with 20 harmonics (dashed gray).

Table 5.3: Controller gains of the PLL.

	$k_p$ in $\text{Hz rad}^{-1}$	$k_i$ in $\text{Hz (rad s)}^{-1}$
H1M2	20.0	20.0
H3M3	2.5	2.5
H5M4	0.1	0.5

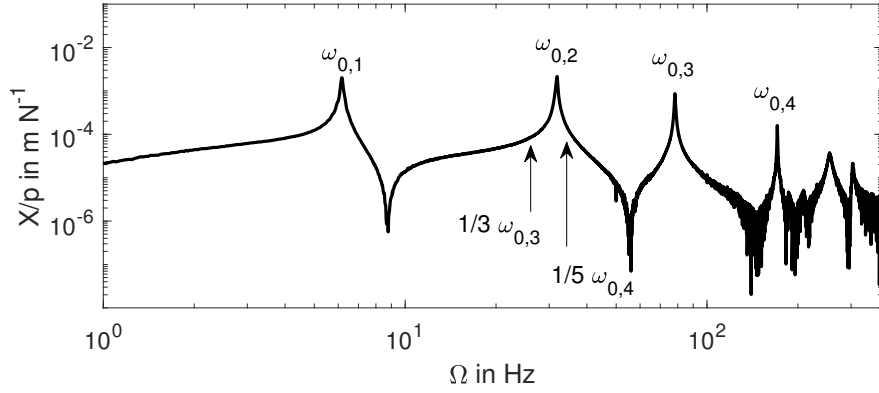


Figure 5.9: Linear frequency response function of the experimental beam.

amplitude) resonance frequencies  $\omega_0$  are listed in Table 4.4. The letter “M” refers to a mode whereas the letter “H” refers to a harmonic. For instance, H1M2 means that the second mode is undergoing fundamental resonance. Fig. 5.9 shows that  $\omega_{0,2}$  is slightly greater than  $\omega_{0,3}/3$  and slightly lower than  $\omega_{0,4}/5$ . We thus expect the third mode to feature a H3M3 superharmonic resonance around  $\Omega = \omega_{0,3}/3$ . Similarly, the fourth mode is expected to exhibit a H5M4 superharmonic resonance around  $\Omega = \omega_{0,4}/5$ .

Fig. 5.10 depicts the frequency response curve around H1M2 identified using an open-loop frequency sweep and PLL testing. The fundamental resonance peak bends toward higher frequencies due to the hardening cubic stiffness. Two additional peaks can be seen around  $\Omega = 26$  Hz and 34 Hz, corresponding to the superharmonic resonances H3M3 and H5M4, respectively. The figure also displays the backbone curves identified thanks to PLL testing. For H1M2, the phase lag  $\phi_1 = -\pi/2$  was targeted in view of the cubic nonlinearity. H3M3 resonance being of first order, the targeted phase lag difference was  $\Delta_3 = -\pi/2$  rad. For the second-order superharmonic resonance H5M4, the PLL targeted  $\Delta_{3,5} = -\pi/2$  rad.

To evaluate the validity of the assumed odd (cubic) nonlinearity, different phase lags along the FRC are represented in Fig. 5.11. Fig. 5.11a confirms that the fundamental phase lag drops from 0 to  $-\pi$  rad across the H1M2 resonance. The phase lag difference  $\Delta_3 = \phi_3 - 3\phi_1$  in Fig. 5.11b also drops from 0 to  $-\pi$  rad across H3M3, as expected from a first-order superharmonic resonance for an odd nonlinearity. Fig. 5.11c shows  $\Delta_{3,5} = \phi_5 - \phi_3 - 2\phi_1$  around the H5M4 resonance. The curve is not displayed away from H5M4 because the noise in  $\phi_5$  becomes larger than  $2\pi$ . Even if

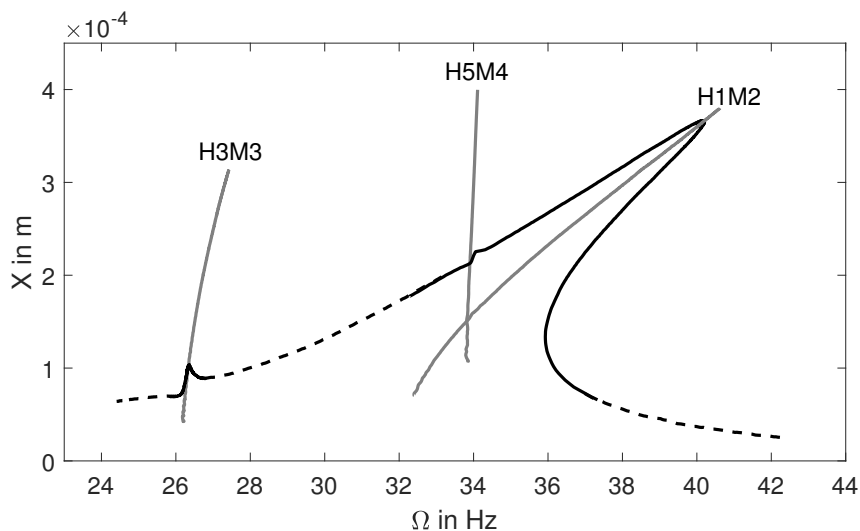


Figure 5.10: Frequency response curve (PLL: solid black, open loop: dashed black) at  $p = 1$  N around the second mode of the beam. The identified backbone curves are pictured in gray.

$\Delta_{3,5}$  drops by  $\pi$  rad, it is close to  $\pi/4$  rad before H5M4, which indicates that the nonlinearity is not purely odd. Nonetheless, the response at which  $\Delta_{3,5} = -\pi/2$  is still near resonance, and such a target is deemed sufficiently close for our application.

Fig. 5.12 presents the time series of the displacement at resonances H1M2, H3M3, and H5M4. It confirms that H1M2 is dominated by the fundamental harmonic. The responses at H3M3 and H5M4 have a high third and fifth harmonic component, indicating a resonance at three and five times the excitation frequency, respectively. However, both responses at H3M3 and H5M4 resonances have a dominant fundamental harmonic, due to the proximity to H1M2.

The  $n$ th harmonic mode shape is defined from the complex Fourier coefficients  $c_{x,n} = (b_{x,n} - ia_{x,n})/2$  of the displacement, localized at the different measurement points on the structure. The sine and cosine Fourier coefficients  $a_{x,n}$  and  $b_{x,n}$  are defined in Eq. (1.2). Just like fundamental mode shapes, the harmonic mode shapes are in general complex but usually closely aligned. The mode shape amplitude is therefore the modulus of  $c_{x,n}$ , and its sign is determined by the direction of the coefficient along the alignment axis, as explained in [1]. The measured harmonic mode shapes are represented in Fig. 5.13. The mode shape of H1M2 has one node, as

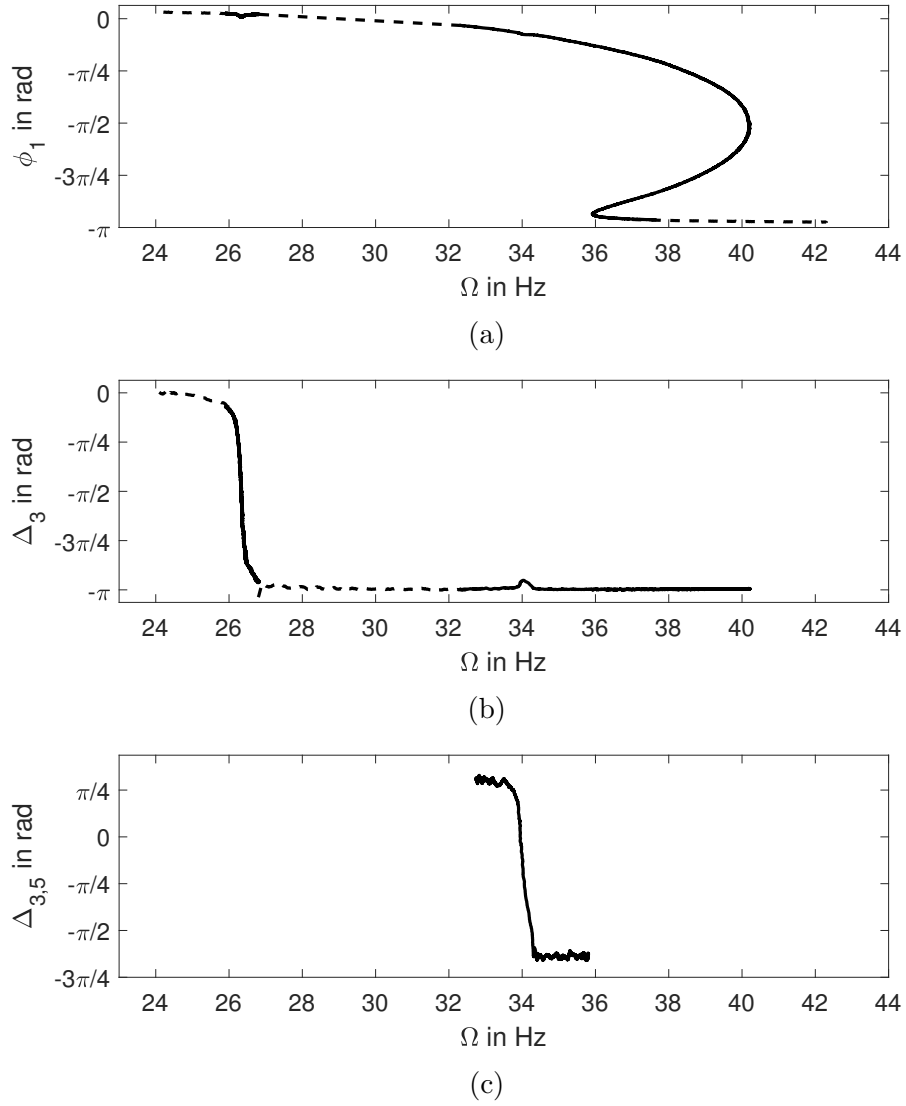


Figure 5.11: (a) Fundamental phase lag, (b)  $\Delta_3$ , and (c)  $\Delta_{3,5}$  across the H1M2 resonance of the beam at  $p = 1$  N (solid: PLL, dashed: open loop).

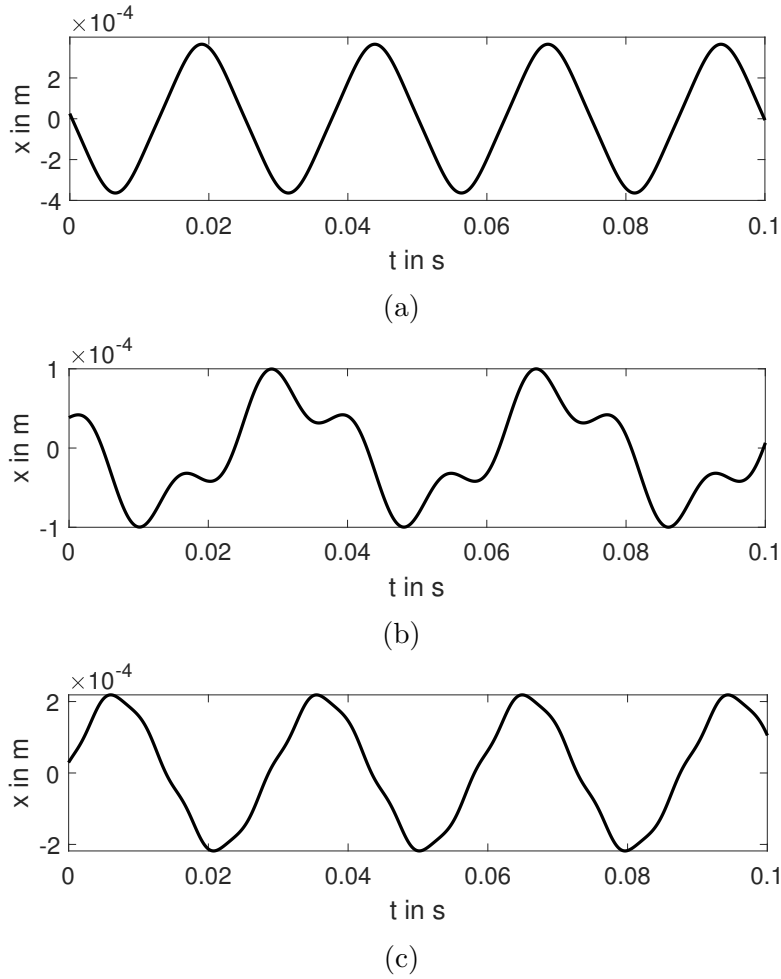
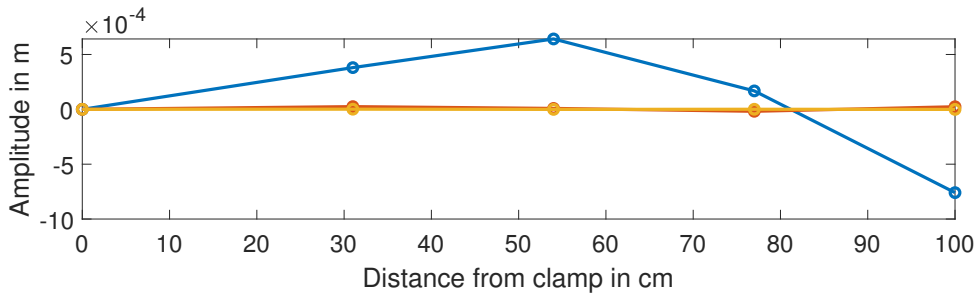


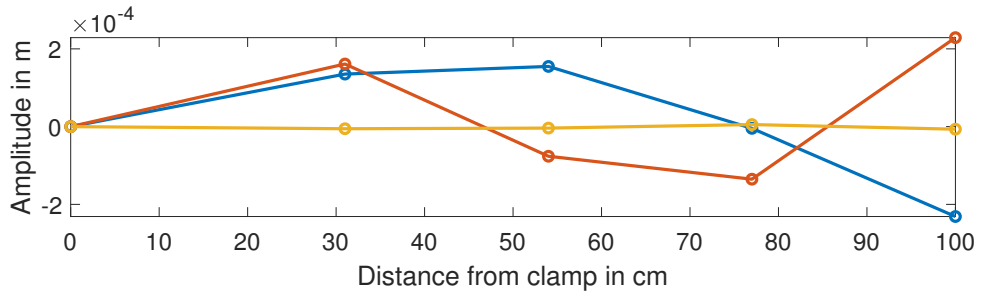
Figure 5.12: Beam displacement measured by a laser vibrometer at  $p = 1$  N and at resonance: (a) H1M2, (b) H3M3, (c) H5M4.

expected from the second bending mode, whereas the third (resp. fifth) harmonic mode shape has two (three) nodes at H3M3 (H5M4), in accordance with the third (fourth) bending mode.

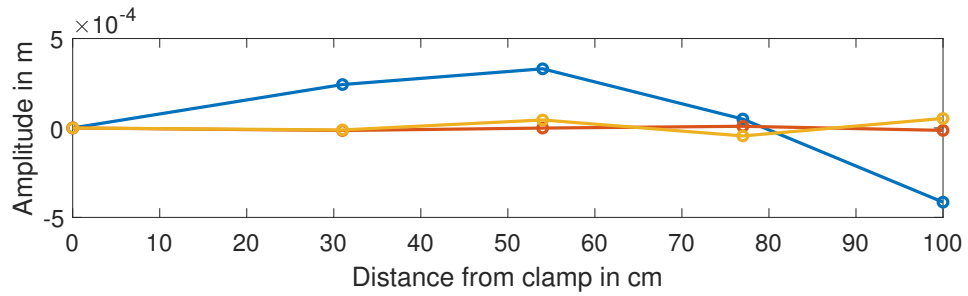
The FRCs around H1M2 at different forcing amplitudes are displayed in Fig. 5.14a. Fig. 5.14b depicts a close-up of H3M3. Complicated dynamics in the form of a loop appears in the frequency response for higher force amplitudes. The backbones resulting from either  $\phi_3 = -\pi/2$  or  $\Delta_3 = \phi_3 - 3\phi_1 = -\pi/2$  rad slightly disagree due to the proximity of H1M2 meaning that  $\phi_1$  has an influence on the superharmonic resonance. H5M4 in Fig. 5.14c happens on the resonance peak of H1M2, leading to a modal in-



(a)



(b)



(c)

Figure 5.13: Measured mode shape of first (blue), third (orange), and fifth (yellow) harmonic of the beam at (a)  $p = 1$  N,  $\Omega = 40.2$  Hz, (b)  $p = 4$  N,  $\Omega = 27.3$  Hz, and (c)  $p = 2$  N,  $\Omega = 34.0$  Hz.

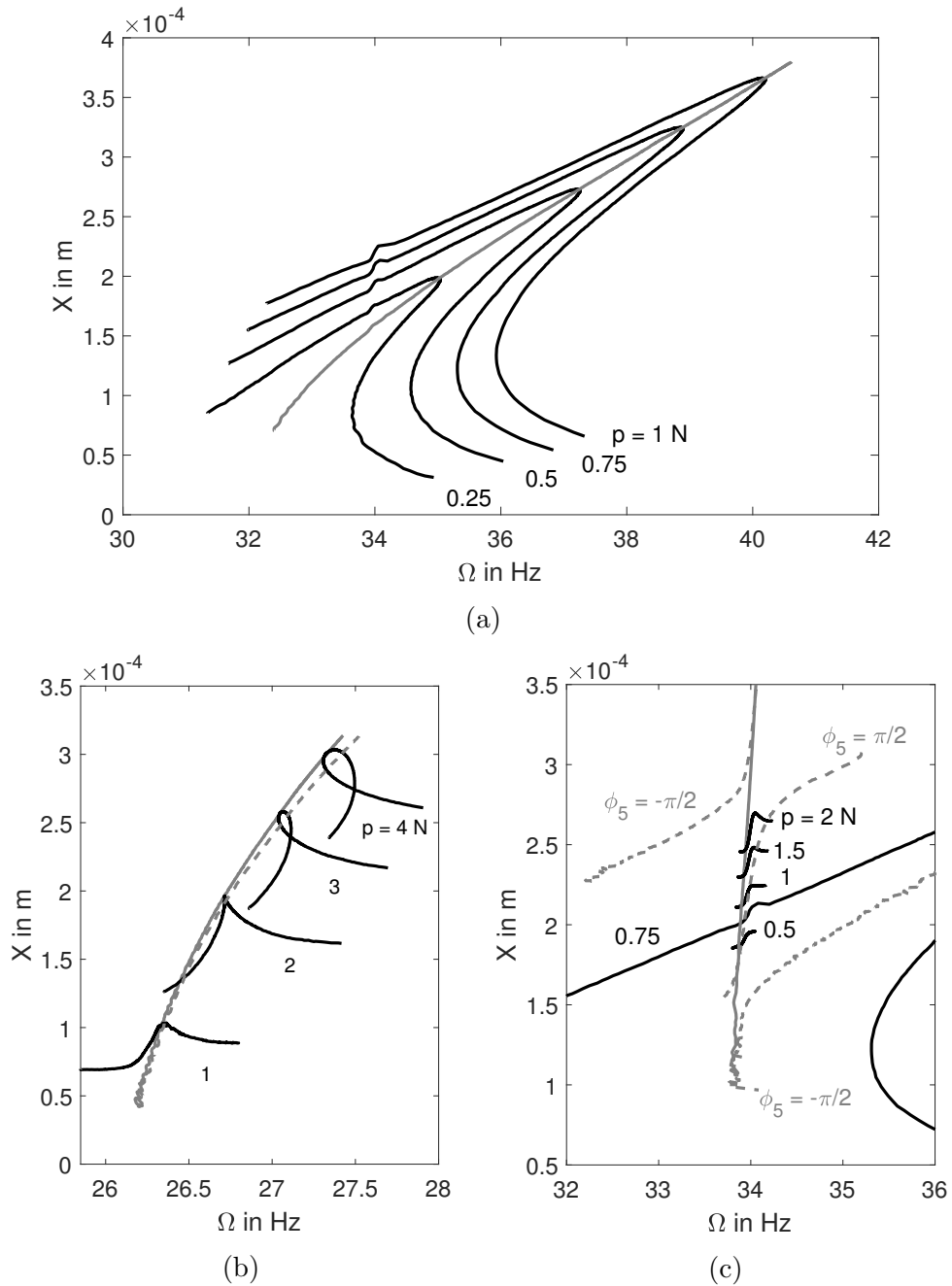


Figure 5.14: Frequency response curves (black) and backbone curves (gray) of (a) H1M2, (b) H3M3, and (c) H5M4 of the beam. The dashed backbones are defined by quadrature of phase lags (a)  $\phi_1$ , (b)  $\phi_3$ , and (c)  $\phi_5$ . The solid backbones are defined by quadrature of phase lag differences (b)  $\Delta_3$  and (c)  $\Delta_{3,5}$ . Everything is identified during PLL experiments, except for the plain gray curve in (b) which is identified during a CBPLL experiment. (Chapter 7)

teraction. On the one hand, when the PLL targets either  $\phi_5 = -\pi/2$  rad or  $\phi_5 = \pi/2$  rad, the measured responses do not always correspond to H5M4. On the other hand, when  $\Delta_{3,5} = -\pi/2$  rad is sought, each measured response is near H5M4. Due to the folding in the backbone, the responses at  $\Delta_{3,5} = -\pi/2$  rad had to be identified during a control-based phase-locked loop (CBPLL) experiment as proposed in Chapter 7.

## 5.6 Modal interaction

It is difficult to understand the behavior of  $\phi_5$  during the H5M4-H1M2 modal interaction because the measured fifth harmonic has a low signal-to-noise ratio. A nonlinear model of the experiment is therefore used in this section. A cubic stiffness identical to the artificial nonlinearity was added to the linear model of the steel beam made in Section 4.4.2. The harmonic balance method was again exploited for FRC computation.

Fig. 5.15a shows the FRCs at relatively low amplitudes. The fifth harmonic phase lag  $\phi_5$  drops by  $5\pi$  rad across the fundamental resonance H1M2, in agreement with the behavior predicted in Section 5.2. Around  $\Omega = 34$  Hz,  $\phi_5$  drops by a value of  $\pi$  rad, highlighting the existence of the superharmonic resonance that cannot yet be seen from the amplitude plot. The fundamental peak has not reached  $\Omega = 34$  Hz; there is no modal interaction. At around  $p = 0.1$  N, the high amplitude fold bifurcation of H1M2 crosses  $\Omega = 34$  Hz in Fig. 5.15b. There are three superharmonic resonances, each on a different branch of the H1M2 peak, namely on the high amplitude stable branch, on the unstable branch, and on the low amplitude stable branch. No peak is seen in the amplitude plot on the lower branch, but the phase  $\phi_5$  of each superharmonic resonance drops by  $\pi$  rad. Simultaneously,  $\phi_5$  gradually drops by  $5\pi$  rad across the fundamental resonance. As a consequence, the exact value of  $\phi_5$  at H5M4 can range anywhere from 0 to  $2\pi$  depending on  $\phi_1$ . The solution is to consider  $\Delta_{3,5}$  instead in Fig. 5.16. It alternates between 0 and  $-\pi$  rad along the FRC, each time a fifth superharmonic resonance is encountered. The experimenter can thus target  $\Delta_{3,5} = -\pi/2$  rad to reach resonance, or sweep  $\Delta_{3,5}$  from 0 to  $-\pi$  rad to identify the local FRC around the fifth superharmonic resonance.

As a final remark, we highlight that the H5M4 backbone has fold bifurcations in forcing amplitude. A PLL imposing the forcing amplitude as an input parameter cannot handle such a case without jumps. Chapter 7 introduces a novel control-based method able to identify such backbones.

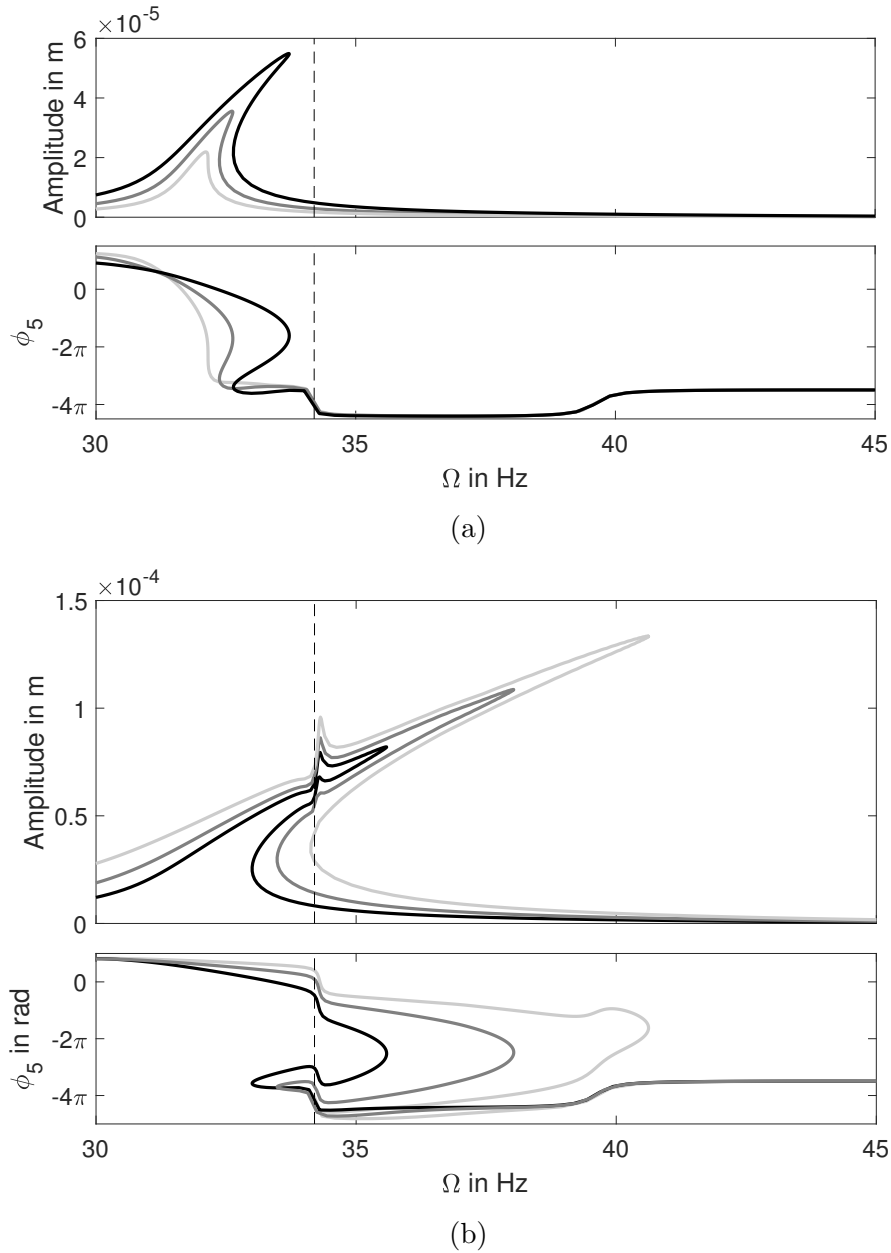


Figure 5.15: Amplitude and fifth harmonic phase lag around H1M2 (numerical model, computed using harmonic balance with 5 harmonics [59]), (a) without modal interaction at  $p = 0.03$  N (light gray), 0.05 N (dark gray), 0.08 N (black) and (b) with modal interaction at  $p = 0.13$  N (black), 0.22 N (dark gray), and 0.36 N (light gray)

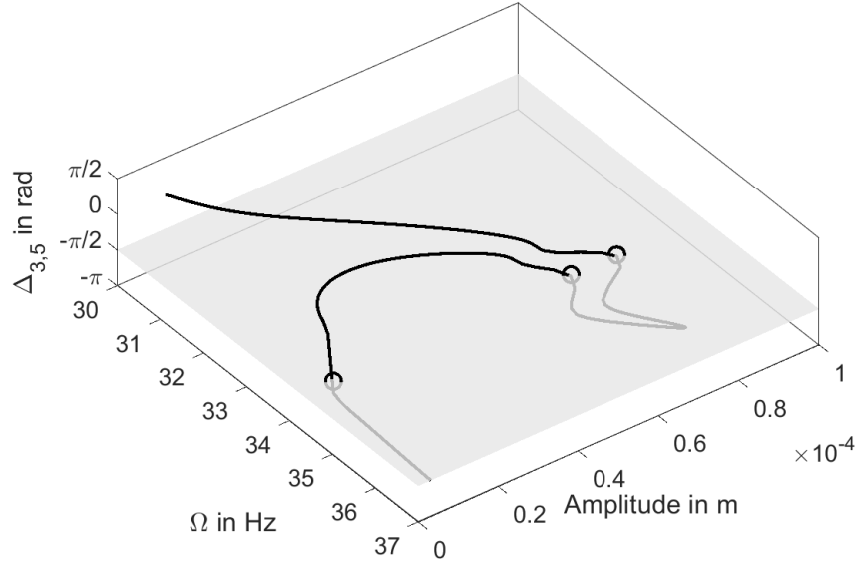


Figure 5.16:  $\Delta_{3,5}$  around H5M4 of the numerical model; the intersection with the plane  $\Delta_{3,5} = -\pi/2$  rad (gray) is highlighted by circles.

## 5.7 Conclusion

This Chapter has proposed a new phase lag-based technique for the identification of superharmonic resonances. The technique was validated both numerically and experimentally. The phase lag of the relevant harmonic drops monotonically through the resonance, making it an ideal input parameter for a PLL-based method. Conversely, CBC cannot identify superharmonic resonances in view of the folding present in the S-curves.

There is an important difference between the identification of fundamental and superharmonic resonances. The former always happens at phase quadrature, whereas the latter may be influenced by multiple harmonics. In the particular case of a single degree-of-freedom oscillator, the influence of additional harmonics can be neglected. In any other case and especially for modal interactions, targeting a single value of the resonant harmonic phase lag can lead to failure. The harmonics involved in the combination and the corresponding resonant value depend on the nonlinearity. Therefore, prior knowledge about the nonlinearity is necessary for a successful identification of superharmonic resonances.

# Chapter 6

## Derivative-free arclength continuation for control-based continuation

### Abstract

This Chapter focuses on the continuation process that is inherent to control-based continuation. Existing continuation procedures can be separated in two families. Similarly to numerical continuation, derivative-based methods find the solution of an objective function, the derivatives of which are estimated using finite differences. In mapping-based methods, the input parameter space is exhaustively or partially explored during the experiment. The features of interest can then be extracted during a post-processing phase or in parallel to the experiment. A novel arclength continuation procedure is developed in this Chapter. It requires neither the estimation of derivatives nor the identification of responses outside the features of interest, thus simplifying and accelerating the continuation process. The method is demonstrated numerically using several examples, then experimentally on a thin curved beam possessing an isolated frequency response branch.

### 6.1 Introduction

Chapter 1 discussed how experiments should be designed such that a set of input parameters always leads to a single response, in which case the

Table 6.1: Parameters of the cubic oscillator.

$m$	$c$	$k$	$f_{\text{nl}}(x)$
0.05	0.2	57	$2 \times 10^8 x^3$

experiment is said to be unfolded. Specifically, a control-based continuation (CBC) experiment can always be unfolded when none of the system's frequency response curves (FRCs) intersect. Then, a continuation procedure takes place during which a trajectory in the input parameter space is followed (see Chapters 3 to 5). In this Chapter, we propose a new, derivative-free continuation scheme to identify FRCs.

Section 6.2 presents the existing continuation schemes for CBC experiments, namely derivative-based methods in Section 6.2.1 and mapping-based methods in Section 6.2.2. The novel continuation procedure is proposed in Section 6.3. This arclength continuation procedure is validated numerically using different oscillators in Section 6.4. It is then demonstrated experimentally in Section 6.5 using the system introduced in Section 4.3.2. This system possesses complicated dynamics including an isola. Concluding remarks are drawn in Section 6.7.

## 6.2 Control-based continuation procedures

To illustrate the concepts in the following Sections, the oscillator in Eq. 1.1 with the parameters in Table 6.1 is studied. As discussed in Chapter 1, each input parameter pair corresponds to one and only one response when the differential gain  $k_d = 2$  is considered (see Fig. 1.6). Fig. 6.1 shows the corresponding excitation amplitude  $p$  for each coordinate in the input parameter space  $(\Omega, X_1^*)$ . An FRC is the collection of responses at a constant  $p$ . For example, the FRC corresponding to  $p = 0.01$  is represented in Fig. 6.1. To identify a FRC, the experimenter must find both the reference frequencies  $\Omega$  and amplitudes  $X_1^*$  leading to the desired  $p$  in the input parameter space.

### 6.2.1 Derivative-based continuation

The pair of input parameters for CBC  $(\Omega, X_1^*)$  defines the fundamental reference signal

$$x_f^* = X_1^* \sin(\Omega t). \quad (6.1)$$

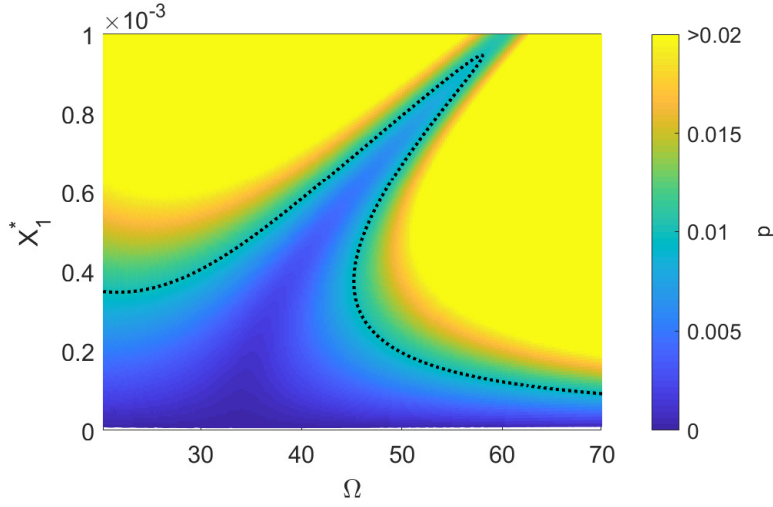


Figure 6.1: Input parameters of a CBC experiment applied to the cubic oscillator with  $k_d = 2$ ; the FRC corresponding to  $p = 0.01$  is represented with a dotted line.

In turn, the non-fundamental harmonics of the reference must equal to ones of the response for the excitation output by a differential controller

$$f = k_d(\dot{x}^* - \dot{x}) \quad (6.2)$$

to be monoharmonic (see Section 3.2.2). The oscillator responds in steady-state with a fundamental harmonic

$$x_1 = X_1 \sin(\Omega t + \phi_1). \quad (6.3)$$

The measured parameters are the response amplitude  $X_1(\Omega, X_1^*)$  and phase lag  $\phi_1(\Omega, X_1^*)$ .

Identifying an FRC during a CBC experiment consists in finding the pair  $(\Omega, X_1^*)$  which leads to a targeted excitation amplitude  $p^*$ , essentially finding the roots of the objective function

$$Y(\Omega, X_1^*) = p - p^* \quad (6.4)$$

$$= \Omega k_d \sqrt{(X_1^* - X_1 \cos \phi_1)^2 + (X_1 \sin \phi_1)^2} - p^*. \quad (6.5)$$

The usual method to solve this equation is Newton's method. This approach works whether the experiment is numerical or physical, as noted in [29, 31]. Because the governing equations of motion are unknown during a physical experiment, the gradient of the objective function must be estimated using

finite differences [32], which requires to interrupt the continuation process. The procedure is therefore adequate for the offline methods presented in this thesis: the Fourier coefficients can be estimated using the DFT (Section 4.2.1) and the non-fundamental harmonics of the excitation can be canceled offline, e.g., using fixed-point iterations (Algorithm 3.1).

An alternative is to consider the multiharmonic reference

$$x^* = \sum_{n=1}^N X_n^* \sin(n\Omega t) \quad (6.6)$$

and to extend to objective function to each harmonic

$$Y(\Omega, X_1^*, \dots, X_N^*) = \Omega k_d \begin{bmatrix} \sqrt{(X_1^* - X_1 \cos \phi_1)^2 + (X_1 \sin \phi_1)^2} \\ 2\sqrt{(X_2^* - X_2 \cos \phi_2)^2 + (X_2 \sin \phi_2)^2} \\ \vdots \\ N\sqrt{(X_N^* - X_N \cos \phi_N)^2 + (X_N \sin \phi_N)^2} \end{bmatrix} - \begin{bmatrix} p^* \\ 0 \\ \vdots \\ 0 \end{bmatrix}. \quad (6.7)$$

Its Jacobian is first estimated by finite differences, then it can be updated using Broyden's method [97], as in [32, 35]. Although it requires the estimation of more derivatives, this method has the advantage of taking care of potential shaker-structure interaction because we can directly solve for the desired force signal, rather than the voltage sent to the shaker.

Once the objective function has been solved, the FRC can be identified point by point using a prediction-correction algorithm such as the pseudo-arclength continuation method [98, 99]. The prediction is made along the tangent to the FRC extracted from the derivatives, whereas the correction is made along the orthogonal direction.

### 6.2.2 Mapping-based approximation

A more straightforward approach to finding the input parameters  $(\Omega, X_1^*)$  is to explore a large portion of the parameter space, leading to a response surface. The desired FRC is simply a two-dimensional section of the resulting surface [40, 53, 57].

Chapter 3 presented a procedure in which a collection of S-curves at constant excitation amplitude was used to build the response surface [57]. The trajectory to be followed in the input parameter space is displayed in Fig. 6.2a. The advantage is that the continuation can be carried out on-

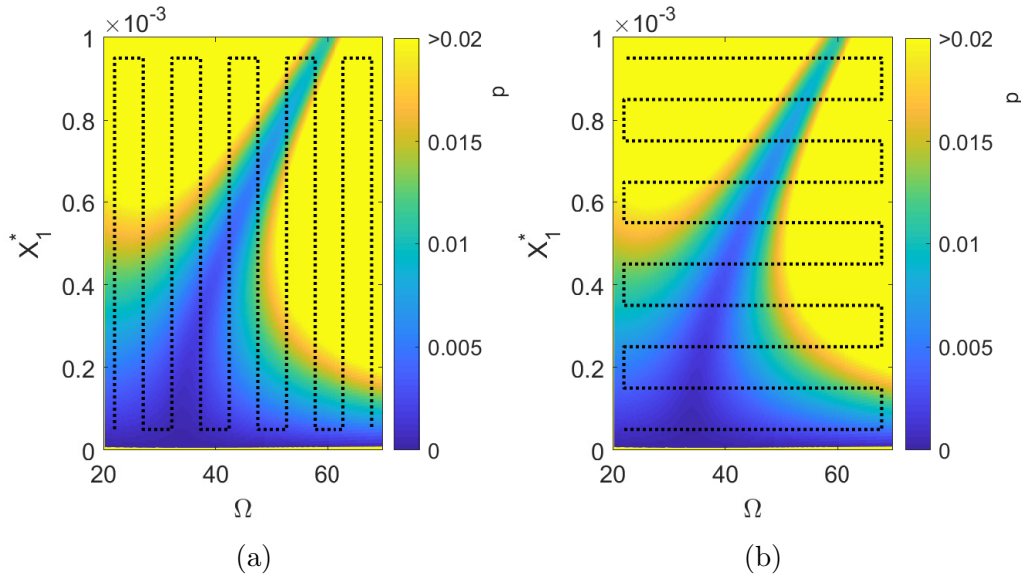


Figure 6.2: Input parameter plane of a CBC experiment for the cubic oscillator ( $k_d = 2$ ). The trajectories to identify the complete response surface are drawn with dotted black lines. (a) S-curve and (b) RCT approaches.

line by sweeping the reference amplitude at constant frequency. An equivalent method, termed response-controlled stepped-sine testing (RCT), is to identify successive responses at varying frequency but constant amplitude [53, 54], shown in Fig. 6.2b. The drawback of both approaches is that the excitation amplitude increases significantly far away from the resonance (see the yellow areas in Fig. 6.2).

The entirety of the parameter space must not necessarily be explored. A local approximation of the response surface can be achieved during the experiment, as in [41, 71]. The CBC experiment stays close to the FRC, and the continuation procedure follows a branch.

### 6.3 Arclength continuation: the basic idea

The objective of this Section is to develop a continuation procedure which is simple to conceptualize and to implement and which avoids the need for post-processing or offline computations. The method is inspired by (i) the numerical arclength continuation procedure [100, 101] during which a control parameter is changed until it reaches the desired equilibrium, and (ii) the adaptive filtering-based online CBC experiment of Chapter 4.

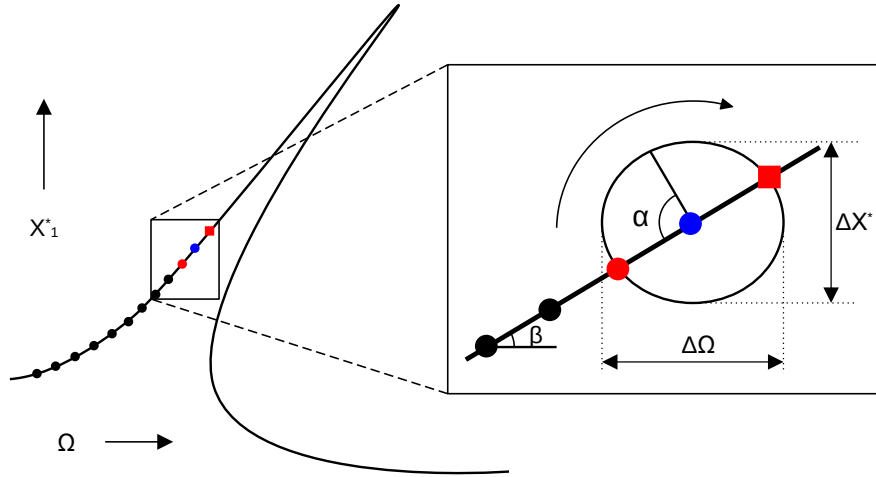


Figure 6.3: The proposed arclength continuation procedure. Previously-identified responses: circles, next response to be identified: square, center of the arc: blue, and responses on the arc: red.

Because the sought FRC is one-dimensional in the input parameter space, a sufficiently small ellipse centered on the branch intersects it twice, as illustrated by the red markers in Fig. 6.3. One intersection is a previously-identified response, and the other one is the next response to be identified. Successive responses on the FRC can thus be identified by increasing the arc angle  $\alpha$  on the ellipse until the system reaches the next intersection. The response lies on the FRC if the excitation amplitude  $p$  given by the CBC controller equals the targeted excitation amplitude  $p^*$ . For illustration, Fig. 6.4 depicts the value of  $p$  depending on the arc angle  $\alpha$  along the ellipse in Fig. 6.3. The ellipse intersects the FRC twice, because  $p$  reaches the target value  $p^*$  twice.

The continuation procedure is detailed in Algorithm 6.1. Thanks to the online CBC experiment developed in Section 4.4.1, the higher harmonics in the excitation are canceled automatically. The continuation process only involves choosing the input parameters. We only need to know two responses on the FRC to identify a third one; the current one is denoted  $(\Omega_c, X_c^*)$ , and the previous one  $(\Omega_p, X_p^*)$ . An ellipse with semi-major axes  $\Delta\Omega$  and  $\Delta X_1^*$  is centered at the current point. The slope angle  $\beta$  between the current and previous points approximates the FRC slope. The input parameters  $(\Omega, X_1^*)$  are set on the ellipse with an arc angle  $\alpha$  from the previous point. The arc angle  $\alpha$  is increased progressively from an initial angle

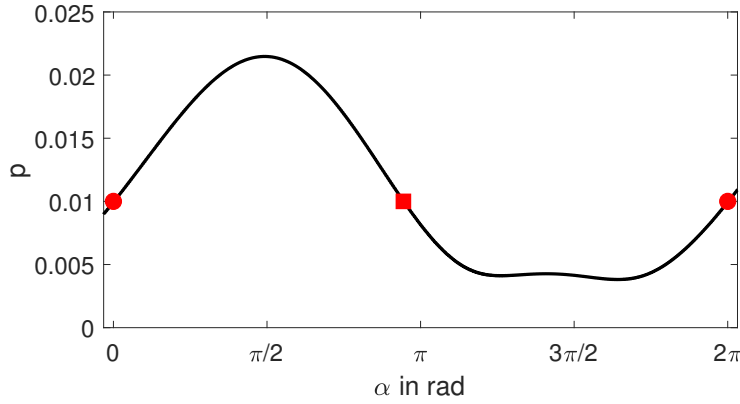


Figure 6.4: Force amplitude  $p$  during the CBC experiment (Table 6.2) along the arc centered at  $X^* = 0.02$ ,  $\Omega = 40.8$  with the continuation parameters in Table 6.3 and excitation amplitude target  $p^* = 0.01$ . Previously-identified response: circles, and next response: square.

$\alpha_0$  sufficiently far away from the previous point until  $p$  reaches  $p^*$ , up to a certain tolerance  $\text{tol}_p$ .

---

**Algorithm 6.1** Arclength continuation for CBC experiment

---

- 1:  $(\Omega_p, X_p^*)$  and  $(\Omega_c, X_c^*)$  defined by user
  - 2: **loop**
  - 3:    $\alpha \leftarrow \alpha_0$
  - 4:    $\beta \leftarrow \text{atan2}(X_c^* - X_p^*, \Omega_c - \Omega_p)$
  - 5:    $(\Omega, X_1^*) = (\Omega_c + \Delta\Omega \cos(\beta + \pi - \alpha), X_c^* + \Delta X^* \sin(\beta + \pi - \alpha))$
  - 6:   Wait a duration  $t_{\text{wait}}$  for steady state
  - 7:   **while**  $|p - p^*| > \text{tol}_p$  **do**
  - 8:     Modify  $\alpha$  with chosen method (see Section 6.4.1) while maintaining the equality in step 5 continuously
  - 9:   **end while**
  - 10:    $(\Omega_p, X_p^*) \leftarrow (\Omega_c, X_c^*)$
  - 11:    $(\Omega_c, X_c^*) \leftarrow (\Omega, X_1^*)$
  - 12: **end loop**
- 

In practice, we advise to identify the backbone curve before using the arclength continuation method to identify an FRC. In doing so, the experimenter can estimate the intervals in which the frequency and amplitude vary, and, in turn, adimensionalize the input parameter space  $(\Omega, X_1^*)$  such that the eccentricity of the ellipse is close to unity, i.e.,  $\Delta\Omega \approx \Delta X_1^*$ . Ad-

ditionally, knowing the backbone allows to decrease the rate of change of the arclength when approaching the resonance peak, the region where transients can have the greatest effect on accuracy. The resonance peak can also be localized by looking at the evolution of the phase lag. An arc angle margin  $\alpha_0$  is chosen to ensure a sufficient distance with previously identified responses on the FRC. Finally, a cooldown time  $t_{\text{wait}}$  is needed for damping the transients resulting from sudden changes in input parameters.

During the arclength continuation process, the responses identified along the continuation arcs are not part of the useful exported data. The method is therefore similar to members of the “mapping-based” continuation family, and in particular to the method used in [41, 71] that creates a local map of the response surface near branches of interest. The main conceptual difference is that no interpolation or extrapolation is made during the arclength process.

It is possible to implement an offline arclength continuation process such that the derivative of the excitation amplitude along the continuation arc is evaluated by finite differences. Finding the next point on the frequency response curve can then be done in an iterative way using e.g. the Newton method on the arc length. Such an implementation would be integrated in the “derivative-based” method family. One difference with existing methods is that the root-finding problem would be one-dimensional instead of two- or multi-dimensional.

## 6.4 Numerical examples

In this Section, the arclength continuation method is first demonstrated numerically using the cubic oscillator in Table 6.1 with the parameters in Tables 6.2 and 6.3.

During a CBC experiment, the reference derivative  $\dot{x}^*$  appears in the differential controller. It is usually equivalent to define the reference signal  $x^*$ , then differentiate it to obtain  $\dot{x}^*$ , or to define  $\dot{x}^*$  directly. However, for arclength continuation, because the reference amplitude follows an ellipse in the input parameter space, the path is different if the fundamental amplitude of  $x^*$ ,  $X_1^*$ , or the fundamental amplitude of  $\dot{x}^*$ ,  $\Omega X_1^*$ , is considered, especially when the frequency  $\Omega$  changes significantly during the experiment. In this Section, we implement the CBC experiment by defining  $\dot{x}^*$  directly. The reference amplitudes are therefore displayed as  $\Omega X_1^*$ .

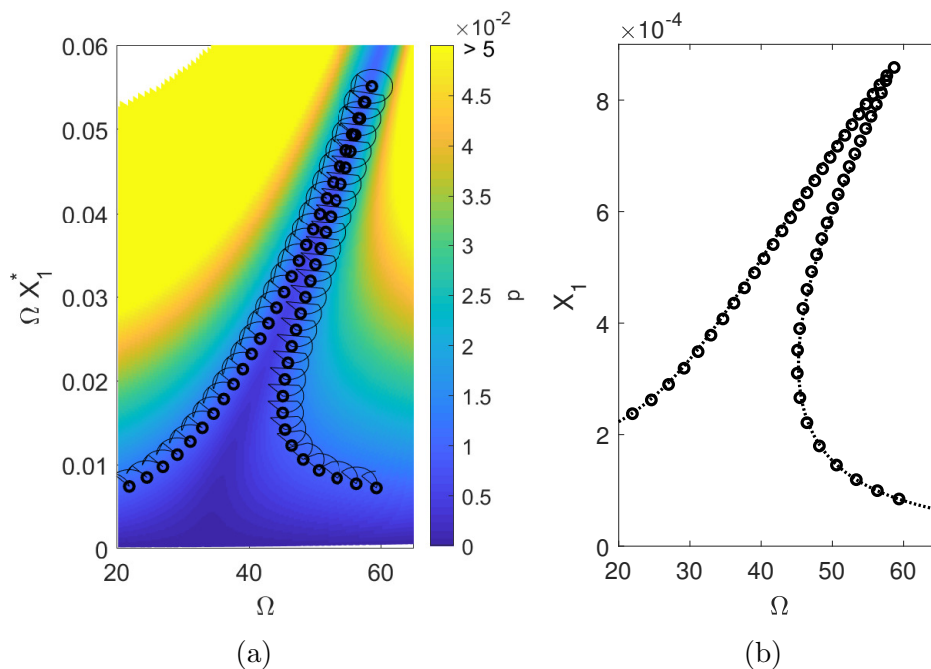


Figure 6.5: Arclength continuation of a cubic oscillator with arclength sweep. The accepted points are marked by circles. (a) Input parameter space, and (b) FRC at  $p = 0.01$  (harmonic balance in dotted curve).

Table 6.2: Simulation parameters of the CBC experiment (cubic oscillator).

$N$	$f_s$ in kHz	$\mu$	$k_d$
5	5	0.001	2

### 6.4.1 Arclength strategy

In this Section, three strategies for moving along the ellipse and reaching the force target  $p^*$  are introduced.

The first method is to sweep at a constant rate  $\dot{\alpha} = \eta_\alpha$  until the excitation amplitude tolerance  $\text{tol}_p$  is reached. The path followed in the input parameter space is represented in Fig. 6.5a. Fig. 6.6 shows that the system is not in steady state when  $p^*$  is reached. Transients both in the system response and in the adaptive filters thus decrease the accuracy of the identified FRC, which is slightly shifted compared to the harmonic balance reference in Fig. 6.5b.

The impact of changes in the sweep rate  $\eta_\alpha$  or the semi-major axes

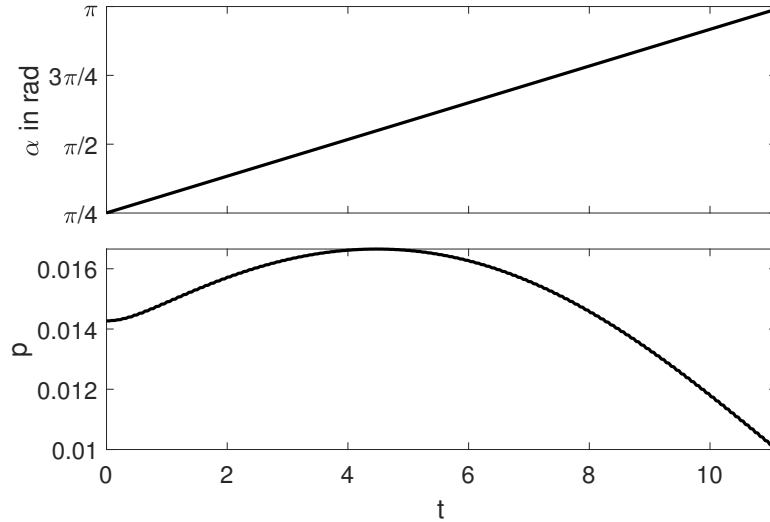


Figure 6.6: Time series of the arc angle  $\alpha$  (arc sweep) and force amplitude  $p$  along an arc centered at  $\Omega X^* = 0.02$ ,  $\Omega = 6.5$ .

Table 6.3: CBC continuation parameters (cubic oscillator).

$\text{tol}_p$	$\alpha_0$	$\eta_\alpha$	$k_i$	$\Delta\Omega$	$\Delta X^*$	$t_{\text{wait}}$
$p^*/100$	$\pi/4$	$\pi/15$	75	0.5	0.002	2

$(\Delta\Omega, \Delta X^*)$  is plotted in Fig. 6.7. As expected, decreasing the sweep rate reduces the transients, which, in turn, increases the accuracy. However, this comes at the cost of a longer testing time (Table 6.4). When increasing the sweep rate, the more important transients may prevent the estimated force amplitude from reaching  $p^*$ . In this case, the continuation procedure is looping indefinitely and fails to go across the fold bifurcation. Reducing the size of the arc allows the experimenter to identify more points on the FRC, as confirmed in Fig. 6.7. Additionally, smaller arcs reduce the magnitude of the transients. Eventually, the accuracy is improved whereas testing time is increased (Table 6.4).

The second arclength strategy is to use an integral controller acting on the arc angle  $\alpha$  with the excitation amplitude error as the input, i.e.,  $\dot{\alpha} = k_i(p - p^*)$ . The path followed in Fig. 6.8a is similar to that in Fig. 6.5a, because the arcs have the same dimensions. The effects of the transients are, however, diminished as the arc angle gently converges toward its target, as displayed in Fig. 6.9. The identified FRC in Fig. 6.8b is thus more accurate.

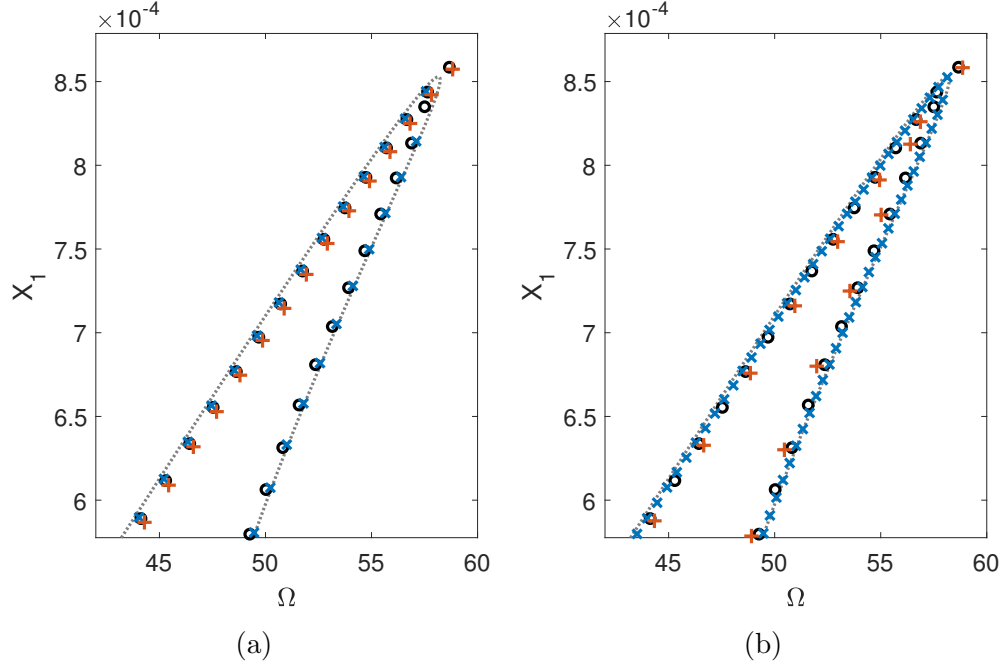


Figure 6.7: Parametric study varying (a) the sweep rate  $\eta_\alpha = \pi/30$  (blue  $\times$ ),  $\pi/15$  (black  $\circ$ ), and  $2\pi/15$  (orange  $+$ ) or (b) the semi-major axes  $(\Delta\Omega, \Delta X^*) = (0.25, 0.001)$  (blue  $\times$ ),  $(0.5, 0.002)$  (black  $\circ$ ), and  $(1, 0.004)$  (orange  $+$ ). The dotted curve represents harmonic balance results.

Table 6.4: Time (s) to reach the amplitude peak of the cubic oscillator. The reference parameters are  $(\Delta\Omega, \Delta X^*) = (0.5, 0.002)$ ,  $\eta_\alpha = \pi/30$ , and  $k_i = 75$ . The slower and faster runs correspond to  $\eta_\alpha/2 - k_i/2$  and  $2\eta_\alpha - 2k_i$ , respectively. Smaller and larger arcs correspond to half and twice the reference semi-major axes. An asterisk means CBC failed to go across the fold bifurcation.

	Arc sweep	Arc control
Reference	365	259
Slower	650	500
Faster	*210	*153
Smaller arc	908	1486
Larger arc	180	*73

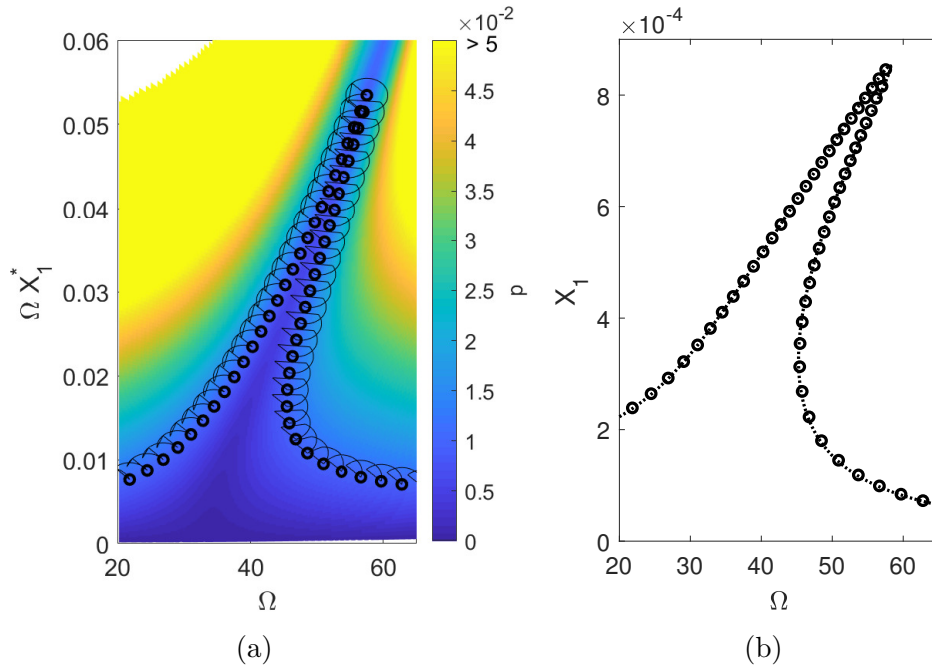


Figure 6.8: Arclength continuation of a cubic oscillator with arclength integral control. The accepted points are marked by circles. (a) Input parameter space, and (b) FRC at  $p = 0.01$  (harmonic balance in dotted curve).

The influence of the integral gain  $k_i$  is similar to that of the sweep rate  $\eta_\alpha$ . For instance, decreasing  $k_i$  leads to a longer (Table 6.4) but more accurate experiment (Fig. 6.10a). Fig. 6.10b evidences one drawback of the integral controller, namely the arclength evolution depends on the force amplitude error. Input parameters further away from the desired values means a greater force amplitude error and therefore faster evolution of the arclength. Decreasing the semi-major axes cause the experiment to last much longer (Table 6.4), but leads to excellent accuracy (Fig. 6.10b). We note that a PID controller could also be considered. In theory, the proportional and differential gains could decrease the settling time and the overshoot. However, we think that a single control law cannot be optimal for the identification of the complete FRC, because the settling time would increase far away from resonance whereas the overshoot would increase close to resonance.

The third arclength strategy combines both arc sweep and integral control. The arc is first swept at a constant rate  $\eta_\alpha$ . This has the advantage

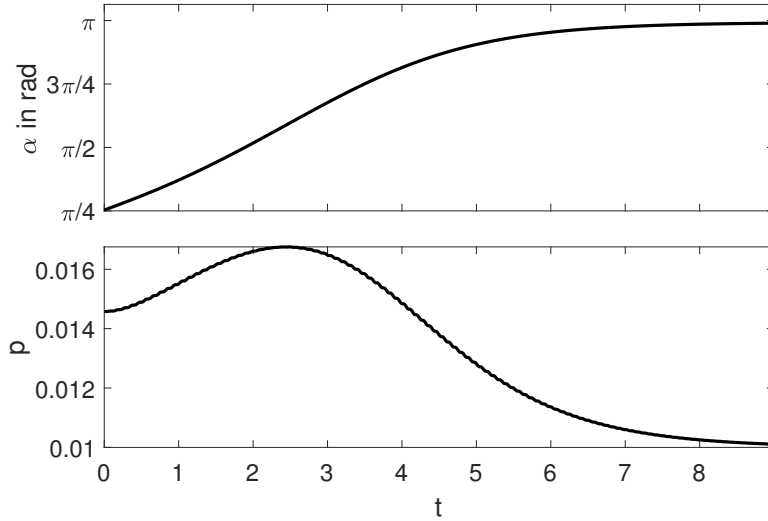


Figure 6.9: Time series of the arc angle  $\alpha$  (integral control) and force amplitude  $p$  along an arc centered at  $\Omega X^* = 0.02$ ,  $\Omega = 6.5$ .

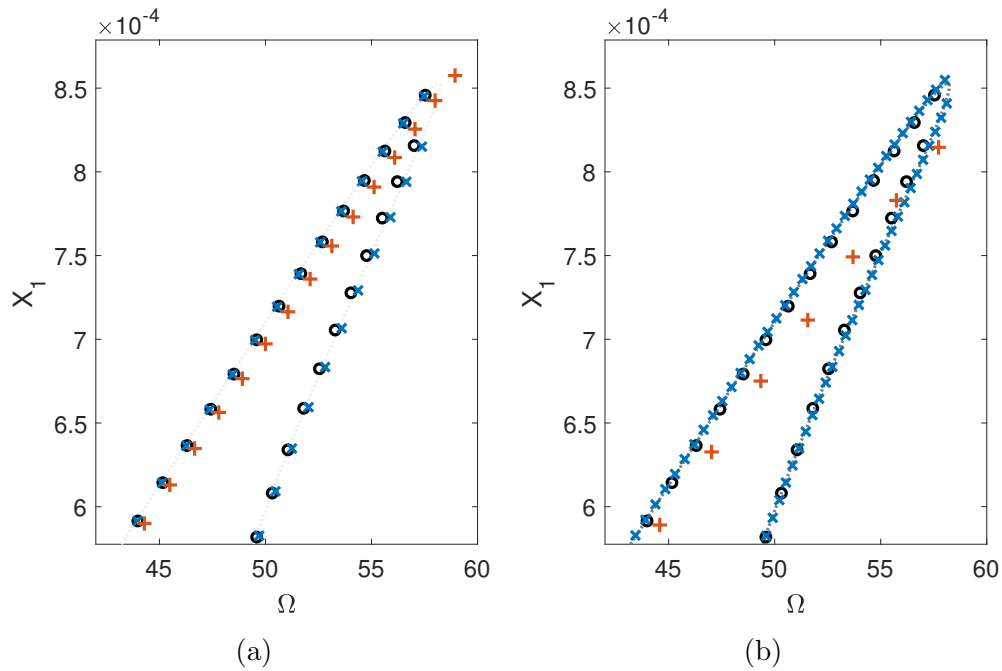


Figure 6.10: Parametric study varying (a) the integral gain  $k_i = 40$  (blue  $\times$ ), 75 (black  $\circ$ ), and 150 (orange  $+$ ) or (b) the semi-major axes  $(\Delta\Omega, \Delta X^*) = (0.25, 0.001)$  (blue  $\times$ ),  $(0.5, 0.002)$  (black  $\circ$ ), and  $(1, 0.004)$  (orange  $+$ ). The dotted curve represents harmonic balance results.

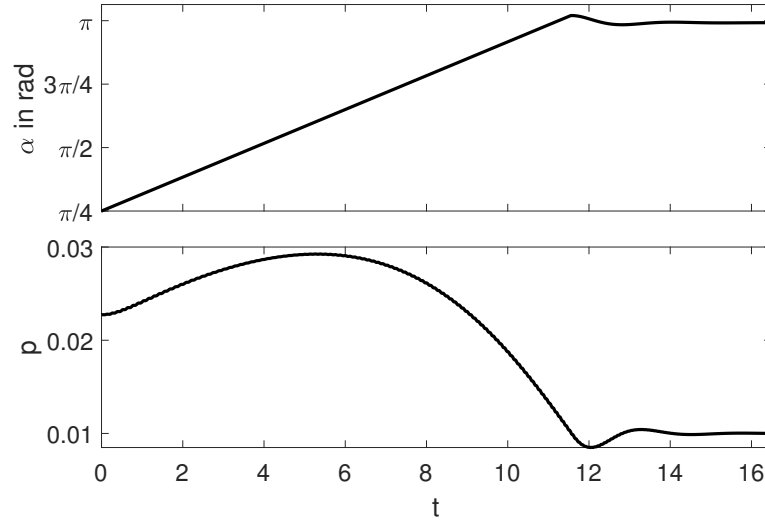


Figure 6.11: Time series of the arc angle  $\alpha$  (arc sweep+integral control) and force amplitude  $p$  along an arc centered at  $\Omega X^* = 0.02$ ,  $\Omega = 6.5$ .

that the arc's semi-major axes are decoupled from the rate at which the arclength evolves. When  $p^*$  is reached, the sweep is interrupted, and an integral controller is activated, allowing a gentle convergence toward  $p^*$ . Fig. 6.11 plots the results for this strategy.

### 6.4.2 Softening-hardening and piecewise linear oscillators

The versatility of the arclength continuation method is demonstrated using two additional systems possessing either a softening-hardening nonlinearity  $f_{\text{nl}}(x) = k_{\text{soft}}x^2 + k_{\text{hard}}x^3$  or a piecewise-linear stiffness

$$f_{\text{nl}}(x) = \begin{cases} k_{\text{pwl}}(x + x_{\text{lim}}) & \text{for } x \leq -x_{\text{lim}}, \\ 0 & \text{for } -x_{\text{lim}} < x < x_{\text{lim}}, \\ k_{\text{pwl}}(x - x_{\text{lim}}) & \text{for } x \geq x_{\text{lim}}. \end{cases} \quad (6.8)$$

The respective system parameters are listed in Tables 6.5 and 6.8. The parameters used for the simulation are given in Tables 6.6 and 6.9, respectively. The piecewise-linear stiffness generates high harmonic content in the response. To ensure that CBC identifies the same responses as the open-loop experiment, a high number of harmonics  $N$  must be evaluated in the Fourier decomposition for this nonsmooth nonlinearity.

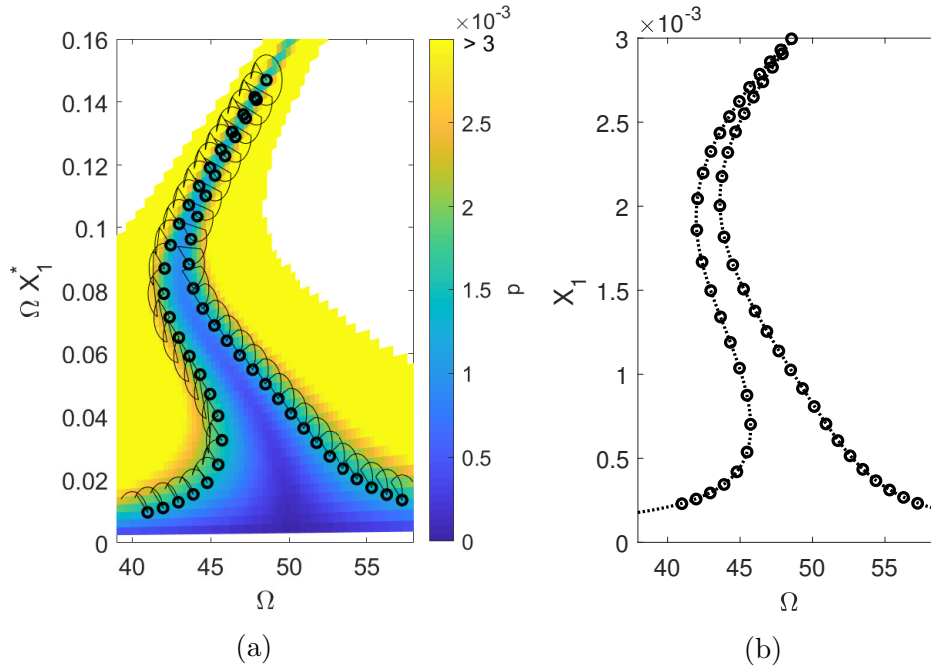


Figure 6.12: Arclength continuation of a softening-hardening oscillator with arclength sweep and integral control. The accepted points are marked by circles. (a) Input parameter space, and (b) FRC at  $p = 0.0015$  (harmonic balance in dotted curve).

Table 6.5: Parameters of the softening-hardening oscillator.

$m$	$c$	$k$	$k_{\text{hard}}$	$k_{\text{soft}}$
0.008	0.01	20	$2 \times 10^6$	$10^4$

Table 6.6: Simulation parameters (softening-hardening oscillator).

$N$	$f_s$ in kHz	$\mu$	$k_d$
5	5	0.002	1

The CBC experiment for the softening-hardening oscillator is designed with the parameters in Table 6.7. It combines a phase arclength sweep with integral control. The path followed in the input parameter space is plotted in Fig. 6.12a, and the identified FRC is represented in Fig. 6.12b. The accuracy is excellent, and the arclength continuation scheme is capable of going through four successive fold bifurcations, including those around the acute resonance peak.

Table 6.7: CBC continuation parameters (softening-hardening oscillator).

$\text{tol}_p$	$\alpha_0$	$\eta_\alpha$	$k_i$	$\Delta\Omega$	$\Delta X^*$	$t_{\text{wait}}$
$p^*/100$	$\pi/4$	$\pi/15$	200	1	0.008	2

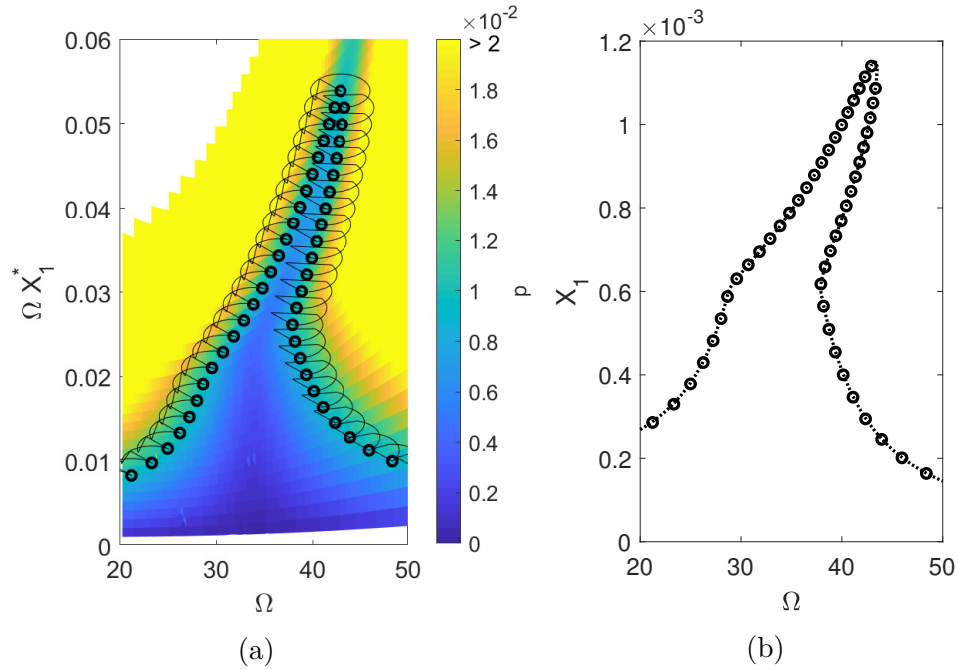


Figure 6.13: Arclength continuation with arclength sweep of an oscillator with piece-linear stiffness. The accepted points are marked by circles. (a) Input parameter space, and (b) FRC at  $p = 0.01$  (harmonic balance in dotted curve).

Table 6.8: Parameters of the oscillator with piecewise-linear stiffness.

$m$	$c$	$k$	$k_{\text{pwl}}$	$x_{\text{lim}}$
0.05	0.2	57	100	$6 \times 10^{-4}$

The parameters of the arclength continuation for the piecewise-linear stiffness are listed in Table 6.10. The path followed in the input parameter space is displayed in Fig. 6.13a. The identified FRC in Fig. 6.13b confirms the effectiveness of the proposed method.

Table 6.9: Simulation parameters (piecewise-linear stiffness).

$N$	$f_s$ in kHz	$\mu$	$k_d$
11	5	0.001	2

Table 6.10: CBC continuation parameters (piecewise linear stiffness).

$\text{tol}_p$	$\alpha_0$	$\eta_\alpha$	$k_i$	$\Delta\Omega$	$\Delta X^*$	$t_{\text{wait}}$
$p^*/100$	$\pi/4$	$\pi/15$	75	2	0.003	1

Table 6.11: Parameters of the experimental set-up.

$N$	$f_s$ in kHz	$\mu$	$k_d$ in $\text{V s m}^{-1}$
10	10	0.01	5

## 6.5 Experimental demonstration

An experimental setup featuring an isolated response branch was introduced in Section 4.3.2 and in Fig. 4.13. The experiment was designed according to the parameters in Tables 6.11 and 6.12. The differential gain leading to an unfolded experiment was found by trial and error during a preliminary run, i.e., it was increased each time a jump occurred.

A response was considered to belong to the FRC if the excitation amplitude was within one percent of the targeted value  $p^*$ . An integral controller drove the arc angle  $\alpha$  with gain  $k_i$ . The input parameter space was adimensionalized, such that  $\Delta\Omega$  and  $\Delta X_1^*$  have the same order of magnitude. Specifically, frequencies were converted to units of 10 rad/s and reference amplitudes to units of 1 mm. Before starting the control of the arc angle, the experiment was allowed to settle for a duration  $t_{\text{wait}}$ .

The FRC identified for  $p = 0.17$  N is shown in Fig. 6.14a. Two continuation runs were necessary, namely one for the main branch and another one for the isola. Initial coordinates on the isola were determined in a prelimi-

Table 6.12: CBC continuation parameters of the experimental set-up.

$\text{tol}_p$ in N	$\alpha_0$ in rad	$k_i$ in $\text{rad (N s)}^{-1}$
$p^*/100$	$\pi/4$	30
$\Delta\Omega$ in rad/s	$\Delta X_1^*$ in m	$t_{\text{wait}}$ in s
0.3	$3 \times 10^{-4}$	1

Table 6.13: Simulation parameters of the CBC experiment (3DOF system).

$N$	$f_s$ in kHz	$\mu$	$k_d$
5	1	0.005	5

nary run by following the backbone curve until 22 Hz. Fig. 6.14b highlights that multiple responses can possess the same phase lag, e.g. there are three responses with phase quadrature. Furthermore, there are five responses coexisting at  $\phi_1 \approx -\pi/4$ , indicating that the isola might result from the merging of two smaller isolas existing at lower excitation amplitudes.

Fig. 6.15 depicts the FRC at  $p = 0.2$  N. It turns out that the isola has grown and merged with the main branch. The merging point is not highest peak on the main branch, leaving a complicated topology with multiple inflection points handled successfully by the arclength continuation method.

## 6.6 Multi-degree-of-freedom systems

As discussed in Chapter 1, the identification of the FRCs of multi-degree-of-freedom systems using a phase-locked loop (PLL) is challenging, because the phase lag does not vary monotonically across the different resonances and antiresonances. Conversely, CBC arclength continuation can handle multiple modes without difficulty, because it relies on the monotonicity of S-curves rather than of phase lags. To illustrate this, a three-degree-of-freedom (3DOF) system with the structural matrices and nonlinear vector

$$\mathbf{M} = \begin{bmatrix} 0.1 & 0 & 0 \\ 0 & 0.1 & 0 \\ 0 & 0 & 0.1 \end{bmatrix}, \quad \mathbf{C} = \begin{bmatrix} 0.2 & -0.1 & 0 \\ -0.1 & 0.2 & -0.1 \\ 0 & -0.1 & 0.2 \end{bmatrix},$$

$$\mathbf{K} = \begin{bmatrix} 200 & -100 & 0 \\ -100 & 200 & -100 \\ 0 & -100 & 200 \end{bmatrix}, \quad \mathbf{f}_{nl}(\mathbf{x}, \dot{\mathbf{x}}) = \begin{bmatrix} 2 \times 10^7 x_1^3 \\ 0 \\ 0 \end{bmatrix} \quad (6.9)$$

is considered. The different parameters for CBC arclength continuation are listed in Tables 6.13 and 6.14.

The results of the different steps of the continuation algorithm are given in Fig. 6.16. The resulting FRC in Fig. 6.17 is found to be in excellent agreement with the harmonic balance method. The first harmonic phase lag depicted in Fig. 6.18 features numerous changes of its slope, which invalidates the use of PLL.

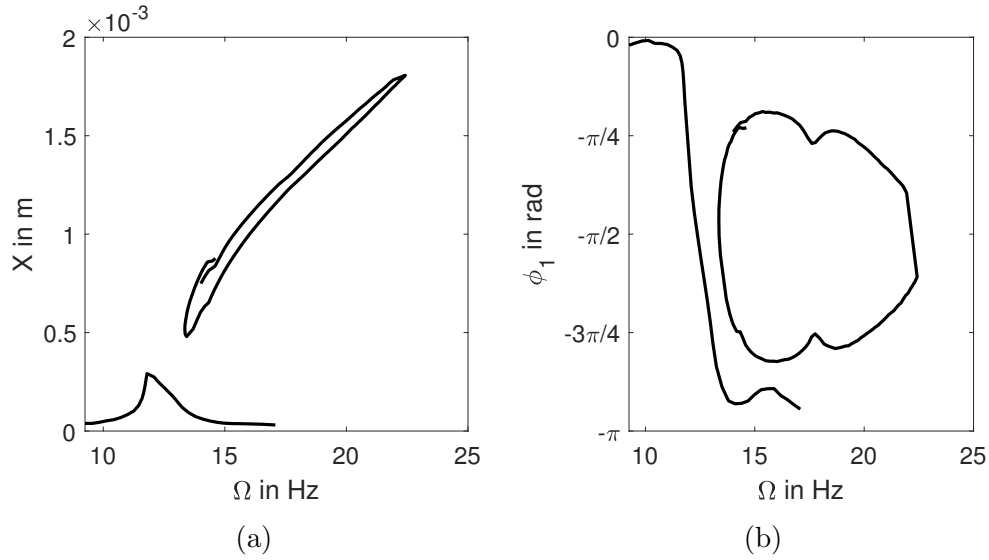


Figure 6.14: (a) Total amplitude  $X$  and (b) phase lag  $\phi_1$  of the fundamental harmonic of the FRC ( $p^* = 0.17$  N, doubly clamped thin beam).

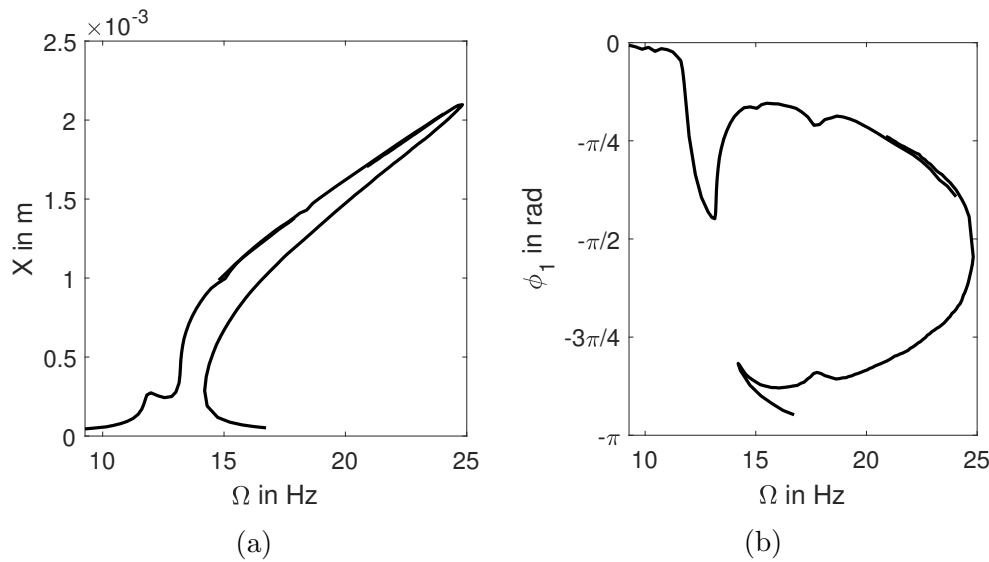


Figure 6.15: (a) Total amplitude  $X$  and (b) phase lag  $\phi_1$  of the fundamental harmonic of the FRC ( $p^* = 0.2$  N, doubly clamped thin beam).

Table 6.14: CBC continuation parameters (3DOF system).

$\text{tol}_p$	$\alpha_0$	$k_i$
$p^*/100$	$\pi/4$	2
$\Delta\Omega$	$\Delta X_1^*$	$t_{\text{wait}}$
1.3	$8 \times 10^{-3}$	2

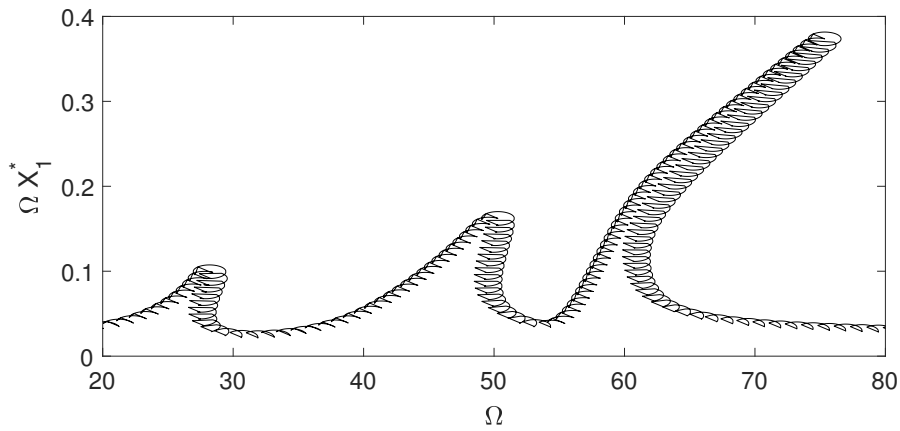


Figure 6.16: Successive input parameters of CBC (3DOF system).

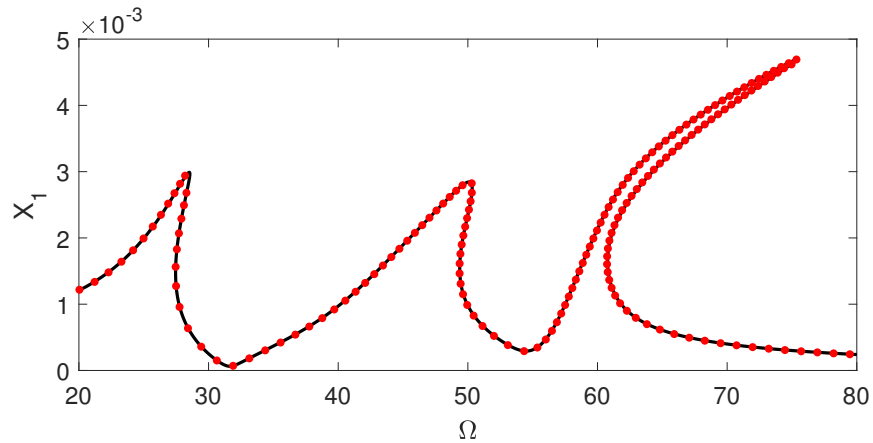


Figure 6.17: FRC of the 3DOF system. Red dots: CBC, black: harmonic balance with 5 harmonics.

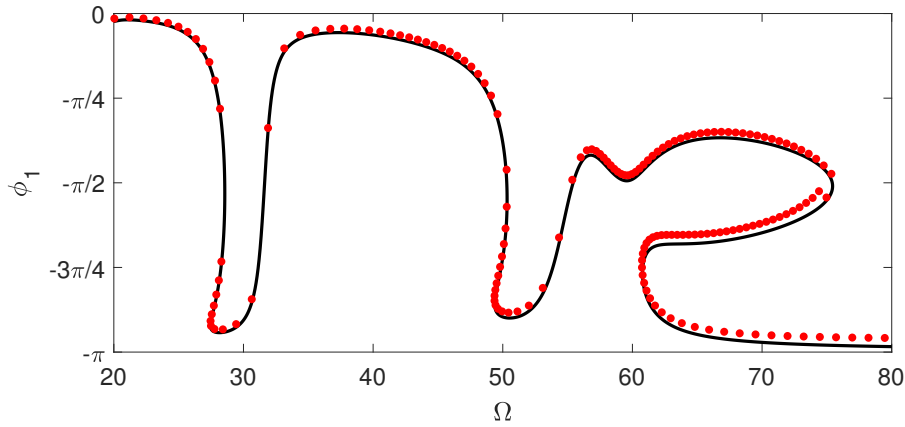


Figure 6.18: Phase lag of the 3DOF system. Red dots: CBC, black: harmonic balance with 5 harmonics.

Fig. 6.17 illustrates that the continuation steps decrease when the frequency increases. This can be explained by the use of a reference signal in velocity whose amplitude increases faster with frequency than that of the displacement (compare Figs. 6.16 and 6.17). A higher resonance peak implies more continuation arcs and, therefore, more continuation points. Additionally, Fig. 6.16 shows that the elliptic arcs are wider along frequency than amplitude. This causes the continuation steps to be finer vertically, close to resonance and bifurcations, than horizontally. An adaptive step size based on the local slope of the phase lag could be imagined. Indeed, Fig. 6.18 highlights that the phase lag slope is greater near resonances and antiresonances and flatter far away. Resonances and antiresonances could then be differentiated by the sign of the phase lag slope.

## 6.7 Conclusion

This Chapter has introduced a novel experimental continuation method for FRCs requiring neither the estimation of derivatives nor the approximation of the response surface. One underlying assumption is that the input parameter space has no more than two dimensions. At the root of the method is an arclength continuation process during which the experiment follows an elliptic arc (centered on a previously-identified response on the FRC) until it intersects the FRC again. Thanks to adaptive filtering, the continuation does not need to be halted, rendering the complete process fully online.

The arclength continuation procedure was validated numerically using

one- and multi-degree-of-freedom oscillators with various nonlinear stiffnesses and experimentally using a beam exhibiting an isolated response branch. In all cases, a successful identification of the sought FRC was achieved.

# Chapter 7

## Identification of folded backbone curves

### Abstract

A backbone curve can be defined as the collection of the resonant responses of a harmonically-forced oscillator. They relate the resonance frequency, excitation amplitude and response amplitude. They can be easily identified during a phase-locked loop experiment, because the excitation amplitude is an input parameter and the frequency is modified until the oscillator features phase quadrature. However, in some cases, backbone curves can be folded when varying the excitation amplitude, causing jumps during experiments. This Chapter proposes a new control-based method, termed control-based phase-locked loop experiment, which combines control-based continuation and a phase-locked loop. This method allows to identify folded backbone curves without jumps and with the improved stability offered by control-based continuation. The method is first demonstrated numerically, then experimentally using a system featuring an isolated frequency response curve and a superharmonic resonance interacting with another mode.

## 7.1 Introduction

The backbones considered so far were never folded. They could be regarded as a collection of resonant responses for which each response corresponds to a unique set of input parameters. Specifically,

- during an open-loop experiment, each response on the backbone had a different force amplitude and excitation frequency;
- during a control-based continuation (CBC), two responses never corresponded to the same reference signal;
- during a phase-locked loop experiment (PLL), each response of the backbone resulted from the same phase lag target (quadrature).

In this Chapter, backbone curves containing multiple responses at the same force amplitude are considered, which may happen for isolated frequency response branches and modal interactions. The origin of the folding is explained in Section 7.2, and its consequences on control-based methods are detailed in Section 7.3. In particular, Section 7.3.1 discusses that a folded PLL experiment can lead to instabilities similar to those observed in [102]. Then, a new control-based method combining a PLL with CBC, termed control-based phase-locked loop (CBPLL), is introduced in Section 7.4. This method can identify backbones which are folded when varying the excitation amplitude. CBPLL is demonstrated experimentally in Section 7.5 for a system with an isolated frequency response and with a superharmonic resonance interacting with the fundamental resonance. Conclusions are drawn in Section 7.6.

## 7.2 Examples of folded backbone curves

### 7.2.1 Isolated frequency response branch

Frequency response curves (FRCs) are one-dimensional curves in the excitation frequency-response amplitude plane. There can, however, exist branches which are completely disconnected from the main branch, i.e., isolated branches or isolas [89]. For illustration, the numerical example from [103] is considered herein, see Fig. 7.1. Two masses sliding on a rail are connected by a spring. The left mass is connected to ground by transverse springs causing a geometrical nonlinearity and is excited by a

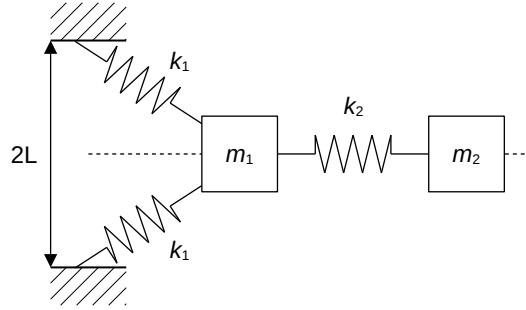


Figure 7.1: System composed of two masses constrained in a horizontal motion with nonlinear stiffness due to transverse springs [103]

Table 7.1: Parameters of the system with transverse springs

$m_1$	$m_2$	$k_1$	$k_2$	$L$	$\lambda$	$c_1$	$c_2$
1	0.2	60	35	0.1	0.9	0.25	0.15

harmonic force:

$$\begin{cases} m_1 \ddot{x}_1 + c_1 \dot{x}_1 + c_2 (\dot{x}_1 - \dot{x}_2) + f_{\text{nl}}(x_1) + k_2 (x_1 - x_2) = p \sin(\Omega t) \\ m_2 \ddot{x}_2 + c_2 (\dot{x}_2 - \dot{x}_1) + k_2 (x_2 - x_1) = 0 \end{cases} \quad (7.1)$$

with the nonlinear force

$$f_{\text{nl}}(x_1) = 2k_1 \left( 1 - \frac{\lambda}{\sqrt{1 + (x_1/L)^2}} \right) x_1. \quad (7.2)$$

The system parameters are listed in Table. 7.1.

At low amplitudes, the system behaves almost linearly. Above a certain force amplitude, the isola depicted in Fig. 7.2 is created. As discussed in Chapter 1, multiple responses exist at the same frequency  $\Omega$ , leading to a fold in the open-loop experiment. However, Fig. 7.2b presents a new behavior, i.e., multiple responses co-exist for the same phase lag. At higher amplitudes, the isola grows until it merges with the main branch, as illustrated in Fig. 7.3. Fig. 7.3b shows that responses sharing the same phase lag value can still co-exist.

Fig. 7.4 displays the input parameter space of a PLL experiment applied to the same system. Each point in the plane corresponds to a pair of input parameters that the experimenter is free to choose. It is seen that

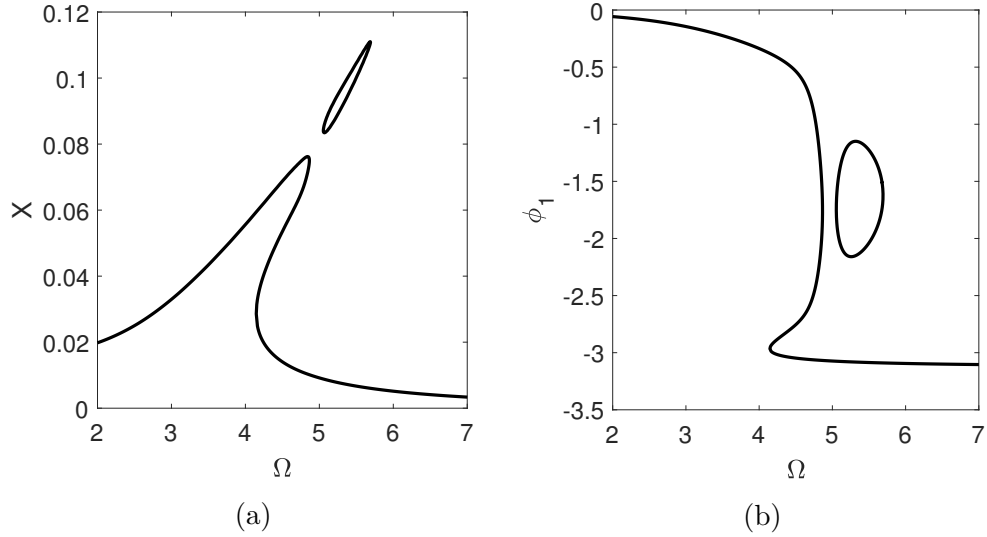


Figure 7.2: (a) Total amplitude  $X$  and (b) phase lag  $\phi_1$  of the fundamental harmonic of the FRC of the system with transverse springs ( $p = 0.17$ , harmonic balance method with three harmonics).

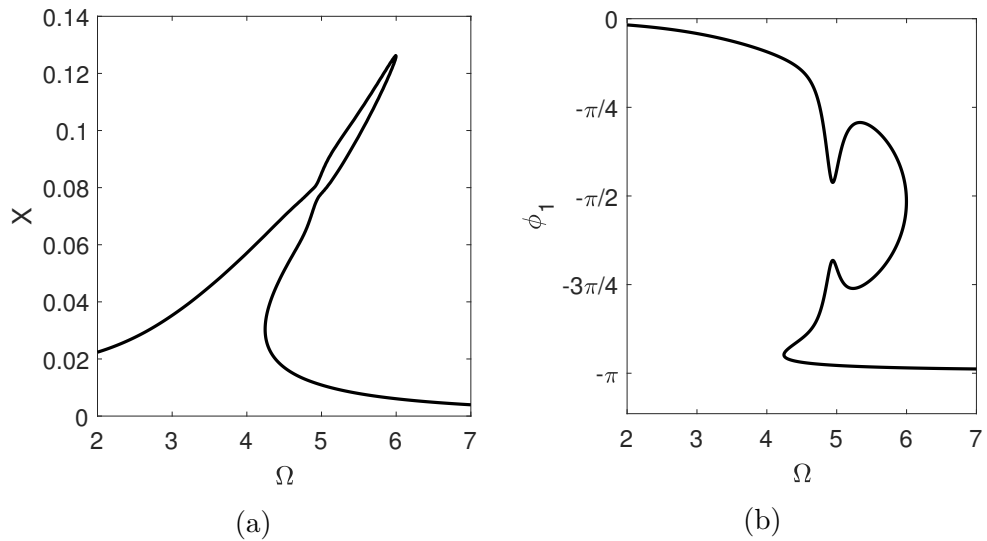


Figure 7.3: (a) Total amplitude  $X$  and (b) phase lag  $\phi_1$  of the fundamental harmonic of the FRC of the system with transverse springs ( $p = 0.2$ ).

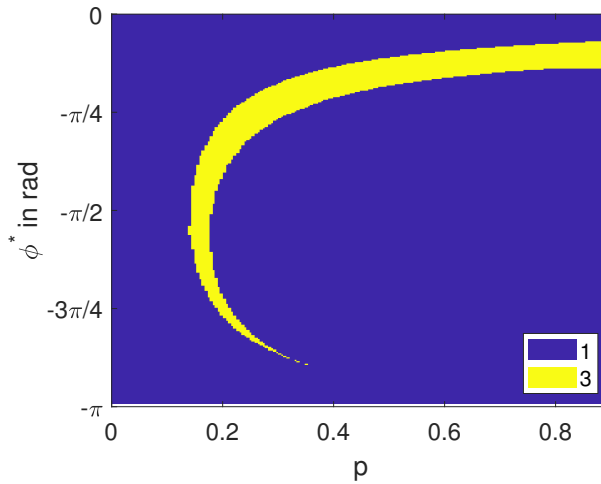


Figure 7.4: Number of different responses of a PLL experiment applied to the transverse springs system.

some input parameter pairs can correspond to three different responses, confirming that the PLL experiment is folded. Fig. 7.5 illustrates what happens with PLL if the FRC in Fig. 7.3 is identified by stepping through the phase lag target. Regardless of the step direction, a fold bifurcation is eventually reached, and the system jumps to another response at higher or lower frequency. As a result, two FRC branches are left unidentified.

Moving now to the backbone of the system in Fig. 7.6, we see that, at low excitation frequencies, the resonance frequency  $\omega$  increases alongside the excitation amplitude  $p$ , as a result of the hardening behavior. However, around  $\omega \approx 5$ ,  $p$  decreases locally, and three different responses featuring phase quadrature co-exist in the range  $p \in (0.15, 0.19)$ . The link between the FRC and the backbone is shown in Fig. 7.7. The backbone is seen to connect the resonance peak on the main FRC to the extremities of the isola. Specifically, when  $p$  reaches a minimum along the backbone, the isola is created; the isola then merges with the main branch when  $p$  reaches a local maximum.

## 7.2.2 Modal interaction

Modal interactions happen when multiple resonances happen near or at the same frequency. If the modes are not well-separated, a modal interaction between fundamental modes can also take place [49].

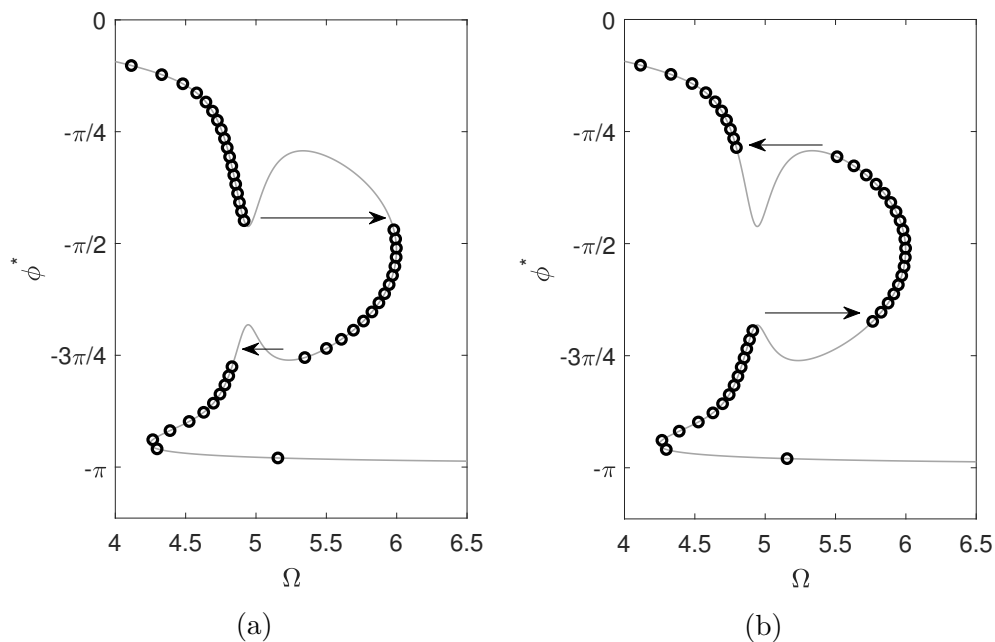


Figure 7.5: Jumps during a PLL experiment applied to the system with transverse springs at  $p = 0.2$  when stepping the phase lag target (a) down or (b) up

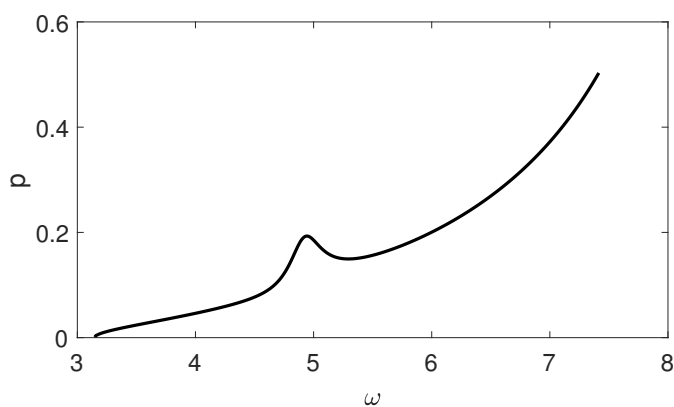


Figure 7.6: Backbone curve of the system with transverse springs (Eq. (7.1))

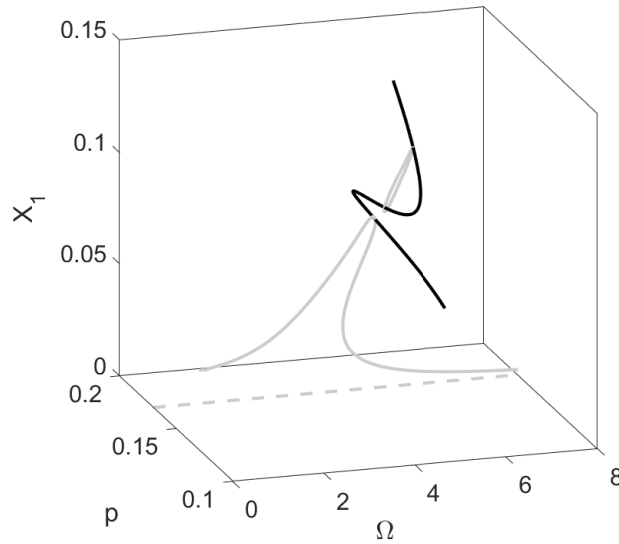


Figure 7.7: Backbone curve of the system with transverse springs (black) and corresponding FRC at  $p = 0.17$  with an isolated response curve (gray) computed using harmonic balance and pseudo-arclength continuation [59]

A modal interaction for a cantilever beam with artificial cubic nonlinearity was already discussed in Chapter 5. For the H5M4 resonance, the fifth harmonic of the response was resonating with the fourth bending mode of the beam. The excitation frequency, i.e., the natural frequency of the fourth mode divided by five, happened to be slightly larger than H1M2, the fundamental resonance of the second bending mode. Due to the hardening effect of the cubic nonlinearity, the H1M2 resonance peak crossed the frequency of H5M4, as it was shown in Fig. 5.15.

The H5M4 backbone of the numerical model of the beam made in Section 4.4.2 is shown in Fig. 7.8. This figure confirms that modal interactions can create a folded backbone curve for which multiple resonant responses share the same force amplitude.

## 7.3 Backbone identification

### 7.3.1 Phase-locked loop experiment

Figs. 7.9a and 7.9b present the results of a PLL experiment which tries to identify the backbone of the system with transverse springs and of the

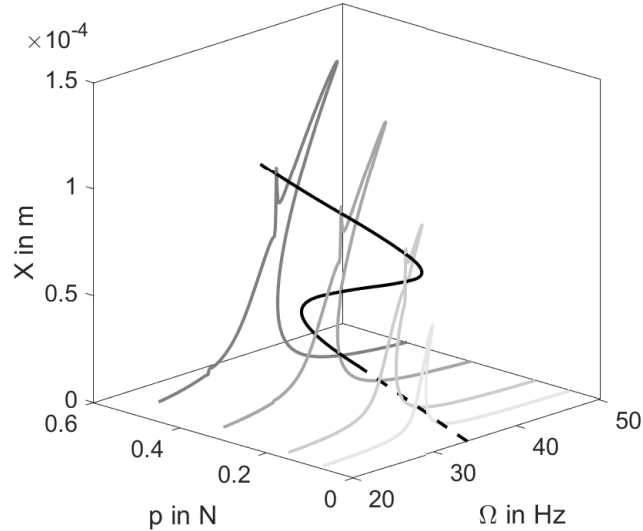


Figure 7.8: H5M4 backbone curve (black) of the cantilever beam and FRCs at  $p = 0.07, 0.15, 0.3,$  and  $0.45$  N (from light to dark gray) computed using harmonic balance. The backbone could not be evaluated at lower amplitudes because the fifth harmonic amplitude becomes as low as the numerical errors, rendering the fifth harmonic phase lag very noisy. A linear extrapolation is shown as a dashed line.

cantilever beam, respectively. The phase lag target is  $\phi^* = -\pi/2$  rad, and the excitation amplitude is increased or decreased sequentially. In both examples, two fold bifurcations occur along the backbone at excitation amplitudes  $p_1$  and  $p_2$ . When  $p < p_1$ , PLL behaves nominally by tracking the resonance frequency  $\omega$ . Once  $p$  reaches  $p_1$ , two additional resonant responses appear at higher response amplitudes, but the PLL experiment has no knowledge about them. Once  $p_2$  is reached, the branch of tracked responses suddenly disappears with the result that the PLL corrects the excitation frequency until the resonant response at higher amplitude is attained. A similar behavior happens when starting at high excitation amplitude and decreasing it sequentially. Eventually, a portion of the backbone is left unidentified for both examples.

### 7.3.2 Control-based continuation experiment

The folded backbones in Fig. 7.9 have an appealing property, namely the response amplitude varies monotonically. As a consequence, Fig. 7.10 demon-

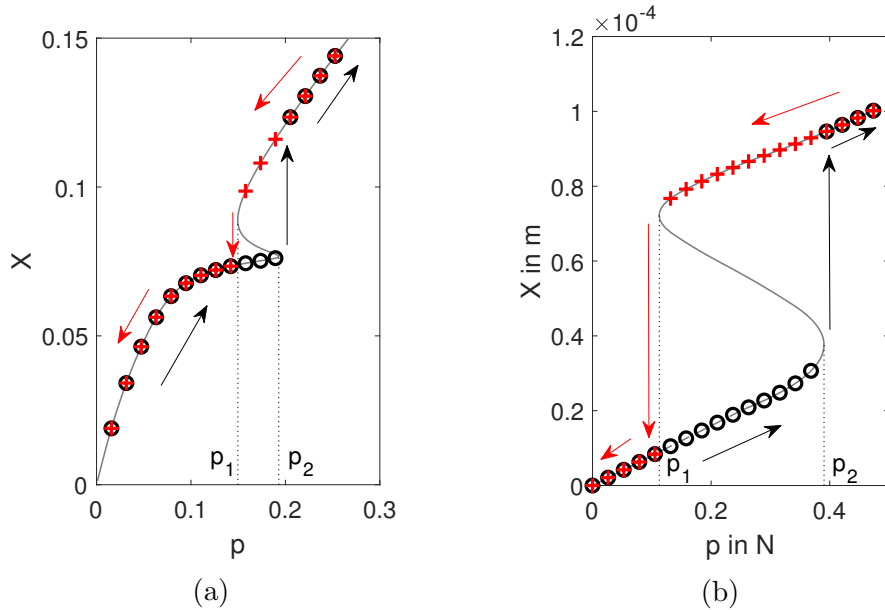


Figure 7.9: PLL experiments for backbone identification of (a) the fundamental resonance of the system with transverse springs ( $\phi_1 = -\pi/2$ , numerical) and (b) the H5M4 superharmonic resonance of the cantilever beam ( $\Delta_{3,5} = -\pi/2$ , experimental).

states that the backbone can be unfolded during a CBC experiment using a sufficiently high differential gain. A CBC experiment is therefore able to carry out a complete identification of the folded backbone curves presented in this Chapter. However, the second input parameter of the experiment, the reference frequency  $\Omega$  corresponding to the resonance frequency  $\omega$ , is not known in advance. A method to correct the reference frequency until the response is at phase quadrature is needed (see Algorithm 3.3).

## 7.4 Control-based phase-locked loop experiment

A novel control-based method combining CBC with PLL, termed control-based phase-locked loop (CBPLL), is proposed in this Section for the identification of backbone curves. In essence, it is a CBC experiment in which the PLL corrects the frequency of the CBC reference signal (rather than the excitation frequency) to reach a specific phase lag target  $\phi^*$ . CBPLL has the same key feature as CBC in that it is able to unfold and stabilize

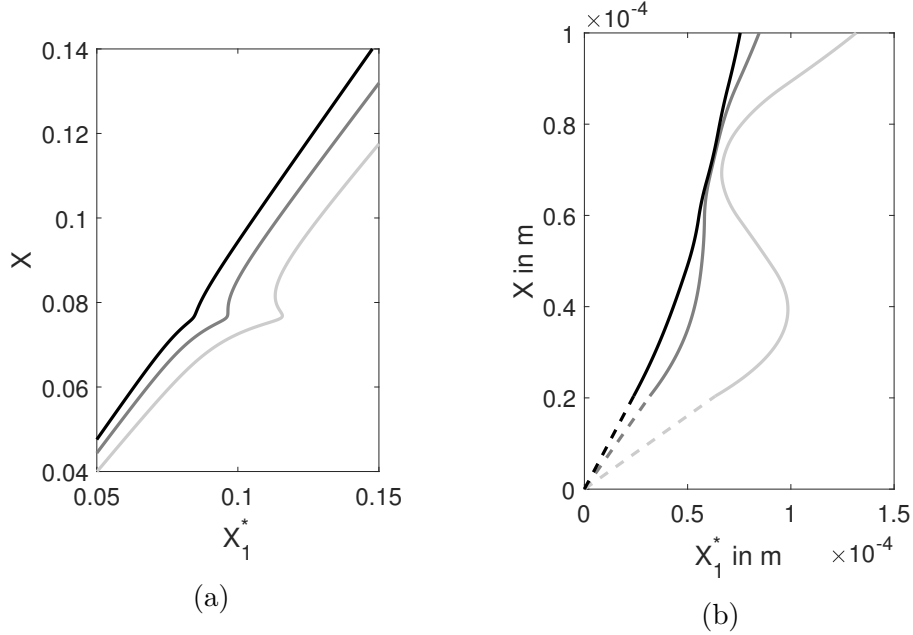
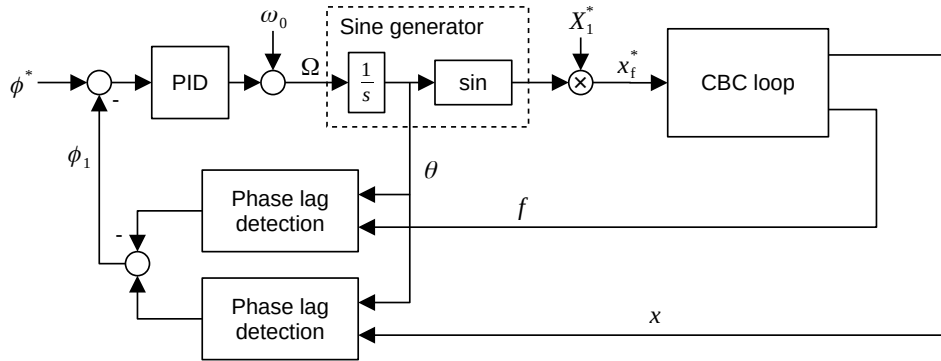


Figure 7.10: Amplitude of backbone curves vs. the reference signal amplitude of a CBC experiment. (a) System with transverse springs ( $k_d = 1$ : light gray; 2: dark gray; and 5: black); (b) cantilever beam ( $k_d = 20$ : light gray; 50: dark gray; and 100: black).

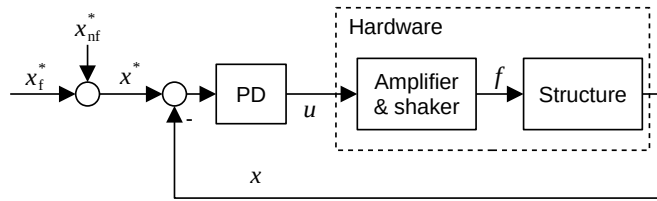
any system whose fundamental response amplitude increases monotonically. In addition, because CBPLL utilizes the stabilization provided by a CBC feedback loop, the stability constraints of the PLL control gains discussed in Chapter 2 do not apply. The PLL behaves more like a traditional control loop that the experimenter can tune to reach the target phase as fast as possible.

As schematized in Fig. 7.11, a CBPLL experiment has two input parameters, namely the phase lag target  $\phi^*$  and the fundamental amplitude of the reference  $X_1^*$ . The voltage sent to the shaker is a combination of Eqs. (3.1), (3.2), and (3.3):

$$\begin{cases} u(t) = k_{p,CBC}(x^*(t) - x(t)) + k_{d,CBC}\frac{d}{dt}(x^*(t) - x(t)) \\ x^*(t) = x_f^*(t) + x_{nf}^*(t) \\ x_f^*(t) = X_1^* \sin\left(\int_0^t \Omega(\tau) d\tau\right) \\ \Omega(t) = \omega_0 + k_{p,PLL}(\phi^* - \phi_1(t)) + k_{i,PLL} \int_0^t (\phi^* - \phi_1(\tau)) d\tau - k_{d,PLL} \frac{d\phi_1}{dt}(t). \end{cases} \quad (7.3)$$



(a)



(b)

Figure 7.11: CBPLL algorithm. (a) Phase-locked loop correcting the frequency of the reference signal, and (b) control-based continuation loop.

In this Chapter, CBPLL is implemented as an online scheme based on adaptive filtering. However, the non-fundamental component of the reference signal  $x_{nf}^*$  can also be defined offline as in Chapter 3, and the estimation of the fundamental phase lag  $\phi_1$  can be achieved using synchronous demodulation as in Chapter 4.

For illustration, the Duffing oscillator in Eq. (1.1) is considered again with the parameters in Table 7.2. The backbones identified using PLL (Table 7.3) and CBPLL (Table 7.4) are in very close agreement in Fig. 7.12. Fig. 7.13 compares the outcomes of PLL and CBPLL when the excitation amplitude is suddenly increased by 10%. PLL takes around 4 seconds to return to the phase lag target, while CBPLL takes about half the time. It shows that the CBC loop in the CBPLL experiment reduces the transients through damping increase.

PLL and CBPLL are now applied to the system with transverse springs.

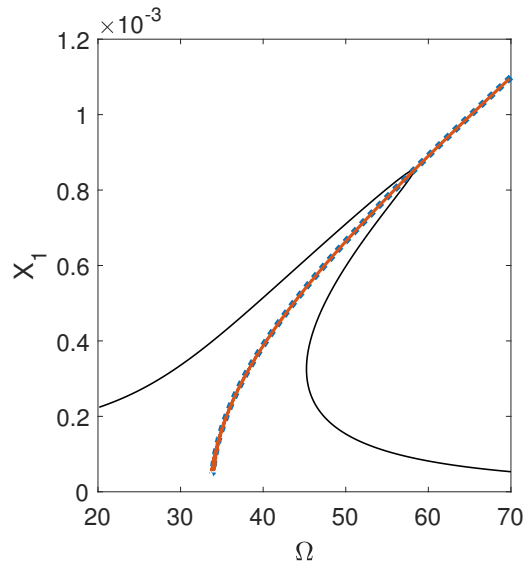


Figure 7.12: Backbone curve of the Duffing oscillator. PLL: dashed blue; CBPLL: orange; and harmonic balance: black.

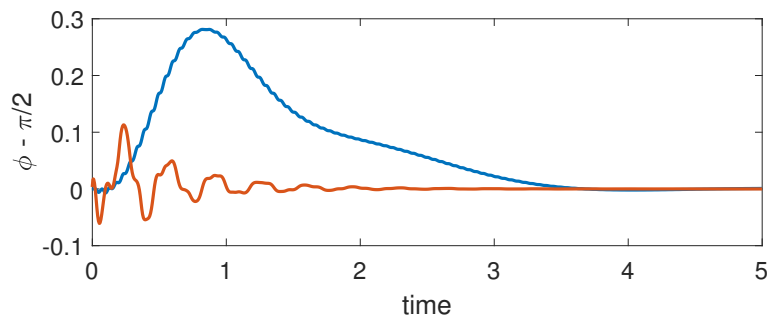


Figure 7.13: Phase lag of the Duffing oscillator when  $p$  is suddenly increased from 0.01 to 0.011 ( $\phi^* = -\pi/2$  rad). PLL: blue; CBPLL: orange.

Table 7.2: Parameters of the Duffing oscillator.

$m$	$c$	$k$	$f_{nl}(x)$
0.05	0.2	57	$2 \times 10^8 x^3$

Table 7.3: Parameters of the virtual PLL experiment.

System	$N$	$f_s$ in kHz	$\mu$	$k_i$	$k_p$
Cubic stiffness	5	10	0.001	1	0.3
Transverse springs	5	1	0.001	0.1	0.5

Table 7.4: Parameters of the virtual CBPLL experiment.

System	$N$	$f_s$ in kHz	$\mu$	$k_{d,CBC}$	$k_{i,PLL}$	$k_{p,PLL}$
Cubic stiffness	5	10	0.001	2	1	2
Transverse springs	5	1	0.0005	5	0.05	0.05

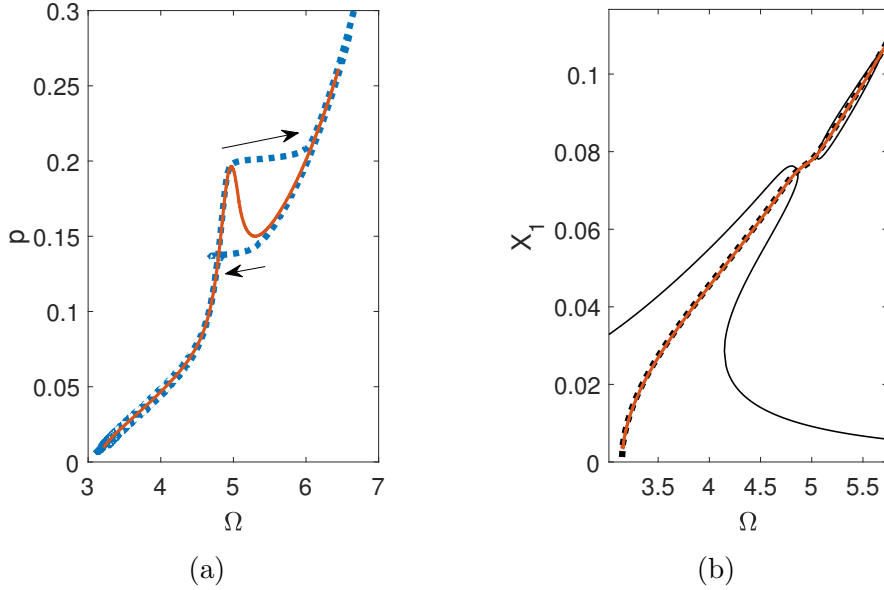


Figure 7.14: Backbone curve of the system with transverse springs. CBPLL: orange; PLL: blue; and harmonic balance with 3 harmonics: black.

The corresponding parameters are listed in Tables 7.3 and 7.4, respectively. As discussed before, Fig. 7.14a confirms that jumps are present during the identification with PLL. Conversely, CBPLL has not trouble to identify the full backbone curve because the fundamental amplitude increases monotonically along it, as shown in Fig. 7.14b. The same figure displays that the CBPLL backbone is in excellent agreement with the one computed using harmonic balance.

## 7.5 Experimental demonstration of control-based phase-locked loop

Both PLL and CBPLL are exploited to identify the folded backbones of the physical experiments of the previous Chapters. The first test case is the clamped-clamped thin beam introduced in Section 4.3.2 which possesses an

Table 7.5: PLL and CBPLL parameters for the clamped-clamped thin beam.

$k_{d,CBC}$ in $V\ s\ m^{-1}$	$k_{p,PLL}$ in $Hz\ rad^{-1}$	$k_{i,PLL}$ in $Hz\ (rad\ s)^{-1}$
5	1	0.3
$\mu$	$f_s$ in kHz	$N$
$10^{-2}$	10	5

Table 7.6: PLL and CBPLL parameters for the cantilever beam.

$k_{d,CBC}$ in $V\ s\ m^{-1}$	$k_{p,PLL}$ in $Hz\ rad^{-1}$	$k_{i,PLL}$ in $Hz\ (rad\ s)^{-1}$
100	0.02	0.1
$\mu$	$f_s$ in kHz	$N$
$10^{-3}$	10	10

isola and whose FRC was identified in Chapter 6. The second test case is the cantilever beam with the artificial cubic stiffness introduced in Section 4.4.2 whose superharmonic resonances were characterized in Chapter 5.

The PLL and CBPLL parameters are given in Tables 7.5 and 7.6. The differential gain of the CBC loop was selected by trial and error such that the experiment is not folded. The higher harmonics in the voltage signal were canceled using adaptive filtering and the online process proposed in Section 4.4. The phase lag detection in the PLL is carried out by the same adaptive filter whose internal parameter  $\mu$  was chosen slightly lower than critical to ensure the filter's stability. There is more freedom for the PLL gains because the CBPLL experiment's stability is ensured by the CBC loop. The controller was tuned manually to ensure a fast convergence while limiting the overshoot of the phase lag target. A greater number of harmonics  $N$  was considered for the cantilever beam to include harmonics higher than the fifth harmonic.

The backbone curve of the first mode of the clamped-clamped beam identified using CBPLL is plotted in Fig. 7.15. Without the knowledge of the excitation amplitude, there is no way to deduce the existence of an isola from the backbone. Fig. 7.16a represents the backbones identified during PLL and CBPLL experiments. At the highest and lowest amplitudes, both experiments output similar results. However, when approaching the bifurcation points at  $p \approx 0.07\ N$  and  $0.15\ N$ , the PLL experiment is unable to go around the fold and jumps either to lower or higher amplitudes, respectively. Conversely, CBPLL goes across the folds without any problem.

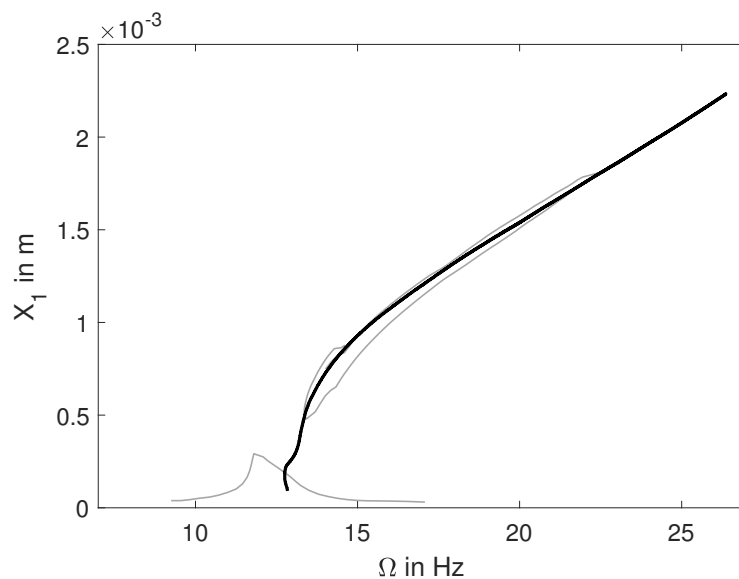


Figure 7.15: Backbone curve (black) of the clamped-clamped beam identified using CBPLL. The FRC (gray) is identified using CBC with arclength continuation ( $p = 0.17$  N).

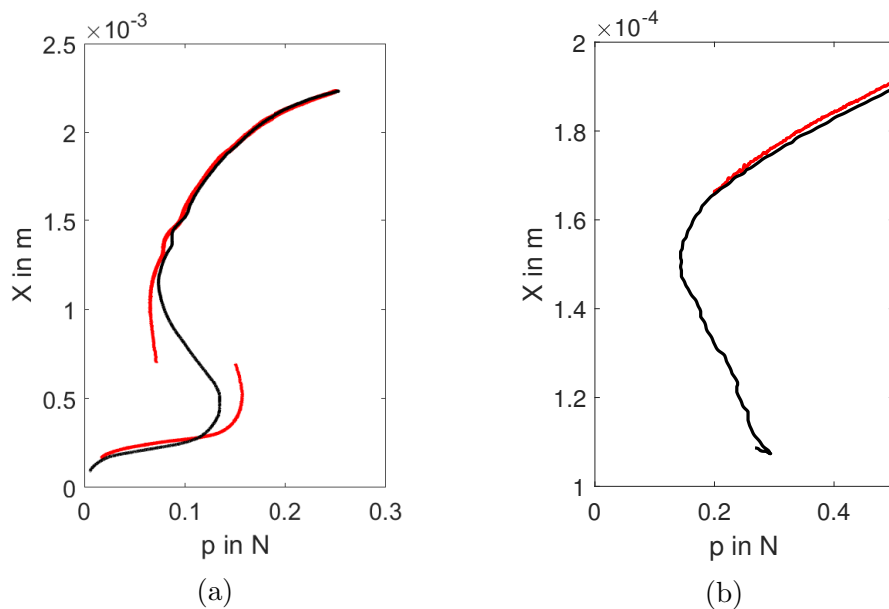


Figure 7.16: Backbone curves of (a) the fundamental resonance of the clamped-clamped beam with an isola and (b) the H5M4 resonance of the cantilever beam. PLL: red; CBPLL: black.

We note that the slight discrepancy in the location of the lower bifurcation point could result from a slight change in testing conditions between experimental runs.

The backbone curve of the fifth superharmonic resonance of the fourth bending mode of the cantilever beam is plotted in Fig. 7.16b. The lower bifurcation point and the lowest branch could not be identified because the fifth harmonic amplitude is too low ( $X_5 < 1 \times 10^{-6}$  m). Unlike CBPLL, the PLL backbone cannot go across the higher fold bifurcation at  $p \approx 0.14$  N, but, more importantly, the PLL loses stability in its vicinity.

## 7.6 Conclusion

This chapter has examined the performance of control-based continuation methods in the presence of folded backbones. Because the excitation amplitude is an input parameter of a PLL experiment, this method is unable to go across fold bifurcations present on the backbones, which eventually results in jumps in amplitude and frequency. This was exemplified in the presence of isolas and superharmonic resonances. For a CBC experiment, it was shown that the experiment may not be folded provided a large enough differential gain is adopted. However, both input parameters, namely the excitation frequency and the reference amplitude, change along the backbone. An offline method must be thus used to correct the frequency until phase quadrature is reached.

To address this limitation, a novel online experiment, termed control-based phase-locked loop (CBPLL), has been proposed. An online PLL corrects the CBC reference amplitude rather than the excitation amplitude. The key advantage is that the stability constraints imposed on the PLL control gains do not apply to a CBPLL experiment because stability is eventually ensured by the CBC loop. CBPLL was successfully demonstrated experimentally using a clamped-clamped beam featuring an isola and a cantilever beam with artificial cubic nonlinearity exhibiting a folded superharmonic backbone curve.

We note that CBPLL is not well-suited for the identification of FRCs because the excitation amplitude is not an input of the experiment, and the relation between the reference and excitation amplitudes is not trivial.

# Conclusions

This thesis work pursued a twofold research objective. On the one hand, the main thrust of Chapters 1-3 was to build a deeper and more complete understanding of control-based methods for the identification of nonlinear structures. These chapters highlighted the inherent strengths and weaknesses of control-based continuation (CBC) and phase-locked loop (PLL) testing. On the other hand, both CBC and PLL experiments were improved in Chapters 4-7 with a particular effort to render the algorithms fully on-line. Eventually, the proposed improvements rendered CBC and PLL more efficient and amenable to identify more dynamical features than before.

In this final Chapter, we first come back to the important questions that have been addressed. A discussion of our personal contributions followed by the remaining limitations is then proposed. This thesis manuscript ends with possible future research directions.

## Answers to research questions

The Introduction raised several questions about control-based methods, namely:

- How can control-based methods ensure that experiments are unfolded?
- Can we always tune the control gains to ensure stability?
- How do CBC and PLL compare to each other, what features can they identify, and how?

These questions were answered in Chapters 1-3. Chapter 1 revealed that the feedback loop of control-based methods transforms one input parameter of the open-loop experiment into another. For CBC, the response amplitude

is transformed indirectly into an input parameter. Except in specific situations (e.g., in Chapter 5), responses under the same excitation frequency have different amplitudes, which removes fold bifurcations. Similarly, for PLL, the phase lag is used as an input parameter. Again, except in specific cases (e.g., in Chapter 7), responses under constant excitation amplitude have different phase lags, ensuring that there is no bifurcation.

A crucial aspect of control-based methods is how they are able to identify unstable responses in the open-loop experiment. Chapter 2 demonstrated analytically that a CBC experiment including a PD controller acts like an oscillator with its own stiffness and damping directly affected by the controller gains, making the link with experimental studies [34]. An analytical study generalizing the work in [49] proved that the stability of a PLL experiment results from a complex interaction between the controller, the oscillator and the phase lag estimator.

When methods pursuing the same objective exist in the literature, it is certainly useful to discuss their similarities and differences. This was achieved in Chapter 3, adapted from the journal article [51]. Although CBC and PLL differ in their architecture and continuation procedures, they were both able to identify backbone curves, frequency response curves and nonlinear modal parameters to a comparable degree of accuracy.

## Contributions

Although significant work remains to be done, we believe that our advancements have pushed the envelope in the area of control-based methods and have helped close the gap between an academic and an industrial use of these techniques.

Chapter 2 indicated that, under certain simplifications, hypotheses, and limitations brought by real life implementation, a CBC loop could significantly improve the stability of a nonlinear oscillator. When confronted to unstable responses, experimenters will have the opportunity to couple their experiment with a CBC loop, just like PLL was coupled with CBC in Chapter 7.

In addition to analytical developments to better understand control-based methods, direct improvements were proposed both for CBC and PLL experiments. First and foremost, performing Fourier decomposition through adaptive filtering was shown to be very valuable throughout this

thesis. For CBC, adaptive filtering allows to perform the experiment in a fully online manner, as in Chapter 4. This change in architecture removes the need to interrupt the experiment regularly to perform offline computations. This not only accelerates testing time, but input parameters of the CBC experiment can now be swept continuously. Adaptive filtering also leads to simpler continuation procedures such as the arclength continuation proposed in Chapter 6. For PLL, adaptive filters were found to be more accurate and robust than synchronous demodulation for phase lag estimation.

Chapters 5-7 identified features that were difficult, not to say impossible, to consider using existing control-based techniques. Specifically, Chapter 5 highlighted that CBC was not adequate to characterize superharmonic resonances. For the first time, superharmonic resonances were characterized experimentally using a PLL-based algorithm. Chapter 5 also proved analytically that the influence of lower order resonances must be taken into account when considering the resonant phase lags of superharmonic resonances. The resonance therefore happens when the combination of multiple phase lags reaches a specific value. This is especially important for multi-degree-of-freedom systems and for modal interactions.

Chapter 6 proposed a novel arclength continuation procedure for CBC experiments. This method requires neither the estimation of derivatives during the experiment nor the mapping of the response surface. Rather, the arclength is swept or controlled until the next point on the branch is identified. This greatly simplifies the identification of topologically complex branches of responses such as frequency response curves.

Finally, a new online experiment coupling CBC and PLL, termed CB-PLL, was introduced in Chapter 7. This method is especially relevant for identifying backbones which cannot be handled by PLL alone, such as folded backbones. Furthermore, CBPLL simplifies the continuation process to obtain backbones while offering the more robust CBC stabilization.

## Limitations

The analytical developments in Chapter 2 did not result in a predictive method which can determine the PLL control gains robustly. Because the stability of a PLL experiment depends heavily on the system's dynamics, in the absence of knowledge about the nonlinearity, we systematically used trial and error to tune the gains. However, this work has confirmed the

result from [49] that a fast phase lag estimation has a positive effect on the stability, and that a large integral gain has a destabilizing effect.

Along the same lines, the precise impact of adaptive filters in the CBC and PLL experiments has not been derived analytically. However, we know from Section B.2.3 that the stability of an adaptive filter is conditional when implemented in a feedback loop. Reducing the internal parameter of the LMS algorithm improves stability but slows down the filter.

In the theoretical sections of this thesis, it is assumed that the control-based methods output a force signal; a stark contrast with experimental sections where the output is a voltage signal. A discrepancy between these two signals is due to shaker-structure interaction, mentioned in Section 3.2.5. This open problematic in structural engineering may defy one stated objective of the experiments: ensure harmonic forcing, whether in open- or closed-loop.

The resonant phase lags for superharmonic resonances derived in Chapter 5 change according to the nonlinearity at end (e.g., odd, even, or none of the two). Without any knowledge of the nonlinearity, the experimental resonant phase lag should be determined by trial and error.

Finally, in this thesis, the methods were not implemented with time performance in mind. Therefore, they could not be compared under that umbrella.

## Further research and development

One of the most important developments which is currently lacking in the domain of control-based methods is a robust and general method for control gain tuning. We have, however, shown that increasing the differential gain of a CBC experiment improves its stability. Estimating the stability during the experiment as in [36, 37] could be sufficient to know whether the gain must be increased or decreased. Adaptive controllers with gains automatically corrected during experiments [78] are certainly a path to investigate.

To increase the maturity of control-based methods in view of an industrial application, an all-in-one experimental continuation package switching between methods and controllers depending on the dynamics of interest would be also a meaningful contribution.

Finally, dynamical features not considered in this thesis could be identified using control-based methods. For instance, even superharmonic resonances behave differently than superharmonic resonances, i.e., they emerge from branch point bifurcations on the main frequency response branch [86]. But the resonant phase lags for such resonances are still unknown. Other secondary resonances exist as well, such as subharmonic and ultrasubharmonic resonances [86]. Identifying quasiperiodic branches experimentally could also be an important future development for control-based methods.



# Appendix A

## Derivation of slowflow dynamics

Let us consider an experiment during which a general single-degree-of-freedom nonlinear oscillator is excited by harmonic forcing following the equation of motion

$$\ddot{x} + \delta\dot{x} + \omega_0^2 x + f_{\text{nl}}(x, \dot{x}) = p \sin(\Omega t). \quad (\text{A.1})$$

Such an experiment will be referred by “open-loop” due to the absence of a feedback. Under the right assumptions, the dynamics of the system can be separated in “fast” and “slow” parts whose time constants differ by an order of magnitude.

The objective of this Appendix is first to use the Van der Pol transformation in Section A.1 to derive the slowflow dynamics of the open-loop experiment in Section A.1.1 and of control-based continuation (CBC) in Section A.1.2. Secondly, a phase Van der Pol transformation is proposed in Section A.2 to derive the slowflow dynamics of the same open-loop experiment in Section A.2.1 and of phase-locked loop (PLL) testing in Section A.2.2.

### A.1 Van der Pol transformation

The Van der Pol (VdP) transformation is defined

$$\begin{cases} u = x \cos(\Omega t) - \frac{\dot{x}}{\Omega} \sin(\Omega t) \\ v = -x \sin(\Omega t) - \frac{\dot{x}}{\Omega} \cos(\Omega t) \end{cases} \quad (\text{A.2})$$

whose inverse is

$$\begin{cases} x = u \cos(\Omega t) - v \sin(\Omega t) \\ \dot{x} = -\Omega[u \sin(\Omega t) + v \cos(\Omega t)]. \end{cases} \quad (\text{A.3})$$

Eq. (A.3) looks very similar to the Fourier decomposition of a monoharmonic signal. In reality, the coordinates vary through time, i.e.  $u = u(t)$ ,  $v = v(t)$ . In that way, any trajectory  $(x, \dot{x})$  can be transformed into VdP coordinates  $(u, v)$ , whether monoharmonic or not, periodic or not. If the  $(x, \dot{x})$  trajectory is indeed monoharmonic with frequency  $\Omega$ , the trajectory  $(u, v)$  is constant through time. This is the key to the VdP transformation: It transforms monoharmonic orbits into limit points whose stability is much easier to characterize.

### A.1.1 Open-loop experiment

Differentiating the VdP coordinates defined in Eq. (A.2) leads to

$$\begin{cases} \dot{u} = \frac{1}{\Omega} (-x\Omega^2 - \ddot{x}) \sin(\Omega t) \\ \dot{v} = \frac{1}{\Omega} (-x\Omega^2 - \ddot{x}) \cos(\Omega t). \end{cases} \quad (\text{A.4})$$

For convenience, let us define a new parameter  $\psi = \Omega^2 - \omega_0^2$  showing how close the excitation frequency is from the natural frequency. Replacing the system's state  $(x, \dot{x})$  by the VdP coordinates (Eq. (A.2)) into the equation of motion of the open-loop experiment (Eq. (A.1)) leads to

$$\begin{aligned} & -x\Omega^2 - \ddot{x} \\ &= -\psi[u \cos(\Omega t) - v \sin(\Omega t)] - \Omega\delta[u \sin(\Omega t) + v \cos(\Omega t)] + g(u, v, \Omega t) - p \sin(\Omega t) \end{aligned} \quad (\text{A.5})$$

with the reparametrized nonlinear force

$$g(u, v, \Omega t) = f_{\text{nl}}(u \cos(\Omega t) - v \sin(\Omega t), -\Omega[u \sin(\Omega t) + v \cos(\Omega t)]). \quad (\text{A.6})$$

Substituting Eq. (A.5) into Eq. (A.4) removes every  $(x, \dot{x})$ , leaving only  $(u, v)$ .

We are now going to make a strong set of assumptions that we will call the VdP assumptions. A parameter  $\epsilon$  is introduced highlighting parameters with small order of magnitude. We assume that the system is weakly nonlinear ( $f_{\text{nl}} \rightarrow \epsilon f_{\text{nl}}$ ), lightly damped ( $\delta \rightarrow \epsilon\delta$ ), the excitation is small in amplitude ( $p \rightarrow \epsilon p$ ), and the difference  $y$  between excitation and natural

frequency is small ( $\Omega - \omega_0 \rightarrow \epsilon y$ ). The last assumption implies that the parameter  $\psi$  is also of order  $\epsilon$ :

$$\begin{aligned} \psi &= \Omega^2 - \omega_0^2 = \epsilon y(\epsilon y + 2\omega_0) \\ &\rightarrow \epsilon \psi. \end{aligned} \quad (\text{A.7})$$

Both sides of Eq. (A.5) are consequently of order  $\epsilon$ . As a consequence, we deduce from Eq. (A.4) that  $\dot{u}$  and  $\dot{v}$  are small, i.e.,  $u$  and  $v$  vary slowly through time. More specifically, they vary in time scales larger than the excitation period  $2\pi/\Omega$  during which they can be considered constant:

$$\int_t^{t+\frac{2\pi}{\Omega}} u(\tau) d\tau = \frac{2\pi}{\Omega} u(t) + O(\epsilon), \quad (\text{A.8})$$

$$\int_t^{t+\frac{2\pi}{\Omega}} v(\tau) d\tau = \frac{2\pi}{\Omega} v(t) + O(\epsilon). \quad (\text{A.9})$$

Averaging the right-hand side of Eq. (A.4) over one period therefore leads to the autonomous dynamic system

$$\begin{cases} \dot{u} = \frac{1}{2\Omega} (\psi v - \Omega \delta u + g_s(u, v) - p) \\ \dot{v} = \frac{1}{2\Omega} (-\psi u - \Omega \delta v + g_c(u, v)). \end{cases} \quad (\text{A.10})$$

with the harmonic components of the internal nonlinear force

$$g_s(u, v) = \frac{\Omega}{\pi} \int_t^{t+\frac{2\pi}{\Omega}} g(u, v, \Omega\tau) \sin(\Omega\tau) d\tau, \quad (\text{A.11})$$

$$g_c(u, v) = \frac{\Omega}{\pi} \int_t^{t+\frac{2\pi}{\Omega}} g(u, v, \Omega\tau) \cos(\Omega\tau) d\tau. \quad (\text{A.12})$$

### A.1.2 Control-based continuation

Let us consider that the general nonlinear system from the open-loop experiment in Eq. (A.1) is subjected to CBC:

$$\ddot{x} + \delta \dot{x} + \omega_0^2 x + f_{\text{nl}}(x, \dot{x}) = y. \quad (\text{A.13})$$

The excitation  $y$  is the output of a controller  $C$  whose input is the difference between the displacement  $x$  and a user-defined reference displacement  $x^* = u^* \cos(\Omega t) - v^* \sin(\Omega t)$ . In the Laplace domain,

$$Y(s) = C(s)(X^*(s) - X(s)). \quad (\text{A.14})$$

Let us consider an LTI controller whose transfer function is the fraction between two polynomials  $A(s)$  and  $B(s)$  of respective degrees  $m$  and  $n$ :

$$C(s) = \frac{A(s)}{B(s)} = \frac{\sum_{k=0}^m a_k s^k}{\sum_{k=0}^n b_k s^k}, \quad (\text{A.15})$$

with  $m \leq n+1$ .  $C(s)$  is in general an improper transfer function because the derivative of the input, i.e. the velocity of the system, is available for use. Writing Eq. (A.14) in the time domain leads to the differential equation

$$\sum_{k=0}^n b_k \frac{d^k}{dt^k} z = \sum_{k=0}^m a_k \frac{d^k}{dt^k} (x^* - x). \quad (\text{A.16})$$

Let us apply a complex VdP transformation on  $x$  to derive the excitation  $y$ :

$$x = w \exp(i\Omega t) + \bar{w} \exp(-i\Omega t). \quad (\text{A.17})$$

This transformation is analogous to Eq. (A.2) with  $w(t) = [u(t) + iv(t)]/2$ . The complex Fourier transformation of  $x^*$ , a monoharmonic reference signal, is

$$x^* = w^* \exp(i\Omega t) + \bar{w}^* \exp(-i\Omega t) \quad (\text{A.18})$$

with constant coefficients  $w^* = (u^* + iv^*)/2$ . Under the VdP assumption, the ‘‘low excitation’’ assumption now implies that every coefficient  $a_k$  is small. The assumption ensure that  $w$  varies slowly through time. The time derivative  $\dot{w}$  is therefore small compared to the other terms and Eq. (A.16) can be rewritten

$$\begin{aligned} & \sum_{k=0}^n b_k \frac{d^k}{dt^k} y \\ &= (w^* - w) \sum_{k=0}^m a_k (i\Omega)^k \exp(i\Omega t) + (\bar{w}^* - \bar{w}) \sum_{k=0}^m a_k (-i\Omega)^k \exp(-i\Omega t). \end{aligned} \quad (\text{A.19})$$

The solution to this ODE is directly

$$y = C(i\Omega)(w^* - w) \exp(i\Omega t) + C(-i\Omega)(\bar{w}^* - \bar{w}) \exp(-i\Omega t). \quad (\text{A.20})$$

Separating the controller’s transfer function in its real and imaginary parts, i.e.,  $C(i\Omega) = c(\Omega) + id(\Omega)$ , leads to

$$\begin{aligned} y = & [c(\Omega)(u^* - u) - d(\Omega)(v^* - v)] \cos(\Omega t) \\ & - [d(\Omega)(u^* - u) + c(\Omega)(v^* - v)] \sin(\Omega t). \end{aligned} \quad (\text{A.21})$$

To describe the controlled system dynamics, we will perform a development similar to the one done in Sect. A.1 for the open-loop system. Substituting Eq. (A.21) into Eq. (A.13) leads to

$$\begin{aligned} & -x\Omega^2 - \ddot{x} \\ & = -(\psi - c)(u \cos(\Omega t) - v \sin(\Omega t)) - (\Omega\delta + d)(u \sin(\Omega t) + v \cos(\Omega t)) \\ & \quad + g(u, v, t) - (cu^* - dv^*) \cos(\Omega t) + (du^* + cv^*) \sin(\Omega t). \end{aligned} \quad (\text{A.22})$$

Substituting Eq. (A.22) into the VdP coordinates derivatives (Eq. (A.4)) and averaging over one period leads to the autonomous dynamic system

$$\begin{cases} \dot{u} = \frac{1}{2\Omega}((\psi - c)v - (\Omega\delta + d)u + g_s(u, v) + du^* + cv^*) \\ \dot{v} = \frac{1}{2\Omega}(-(\psi - c)u - (\Omega\delta + d)v + g_c(u, v) - cu^* + dv^*). \end{cases} \quad (\text{A.23})$$

## A.2 Phase Van der Pol transformation

Let us consider the phase VdP transformation defined by the coordinates

$$\begin{cases} r = \sqrt{x^2 + \frac{1}{\Omega^2}\dot{x}^2} \\ \phi = \text{atan2}\left(x, \frac{1}{\Omega}\dot{x}\right) - \Omega t \pmod{2\pi} \end{cases} \quad (\text{A.24})$$

whose inverse is

$$\begin{cases} x = r \sin(\Omega t + \phi) \\ \dot{x} = r\Omega \cos(\Omega t + \phi) \end{cases} \quad (\text{A.25})$$

It is equivalent to the VdP transformation from Eq. (A.2) with  $u = r \sin \phi$  and  $v = -r \cos \phi$ , or  $r = \sqrt{u^2 + v^2}$  and  $\tan \phi = -u/v$ . Similarly to VdP coordinates  $(u, v)$ , phase VdP coordinates  $(r, \phi)$  are time-varying. The transformation can therefore correspond to any response of system (A.1). Under the transformation, monoharmonic orbits of the system become limit points that are easier to study.

### A.2.1 Open-loop experiment

Differentiating  $r$  leads to

$$\dot{r} = \frac{1}{\Omega}(\Omega^2 x + \ddot{x}) \cos(\Omega t + \phi). \quad (\text{A.26})$$

Substituting Eq. (A.25) into Eq. (A.1) leads to

$$\Omega^2 x + \ddot{x} = \psi r \sin(\Omega t + \phi) - \Omega\delta r \cos(\Omega t + \phi) - h(r, \Omega t + \phi) + p \sin(\Omega t) \quad (\text{A.27})$$

with  $\psi = \Omega^2 - \omega_0^2$  and the parametrized nonlinear force

$$h(r, \Omega t + \phi) = f_{\text{nl}}(r \sin(\Omega t + \phi), r\Omega \cos(\Omega t + \phi)). \quad (\text{A.28})$$

Differentiating  $\phi$  leads to

$$\dot{\phi} = -\frac{1}{\Omega r}(\Omega^2 x + \ddot{x}) \sin(\Omega t + \phi). \quad (\text{A.29})$$

Let us now make the VdP assumption from Section A.1. As a consequence, the right-hand sides of Eqs. (A.26) and (A.29) are of order  $\epsilon$  and so are  $\dot{r}$  and  $\dot{\phi}$  on the left-hand side. The consequence of the assumptions are that  $r$  and  $\phi$  vary in time scales much larger than one period of the system. Therefore, they can be considered constant when integrating over a period. Under this assumption, averaging Eqs. (A.26) and (A.29) over one period lead to the system

$$\begin{cases} \dot{r} = -\frac{1}{2}(\delta r + \frac{1}{\Omega}(h_c(r) + p \sin \phi)) \\ \dot{\phi} = -\frac{1}{2}(\frac{\psi}{\Omega} - \frac{1}{\Omega r}(h_s(r) - p \cos \phi)), \end{cases} \quad (\text{A.30})$$

with

$$h_s(r) = \frac{\Omega}{\pi} \int_t^{t+\frac{2\pi}{\Omega}} h(r, \Omega\tau + \phi) \sin(\Omega\tau + \phi) d\tau \quad (\text{A.31})$$

$$h_c(r) = \frac{\Omega}{\pi} \int_t^{t+\frac{2\pi}{\Omega}} h(r, \Omega\tau + \phi) \cos(\Omega\tau + \phi) d\tau \quad (\text{A.32})$$

independent of  $\phi$  because  $h$  is periodic with frequency  $\Omega$ .

### A.2.2 Phase-locked loop testing

Let us consider a variation of the nonlinear system from Eq. (A.1) once again

$$\ddot{x} + \delta\dot{x} + \omega_0^2 x + f_{\text{nl}}(x, \dot{x}) = p \sin \theta. \quad (\text{A.33})$$

A phase-locked loop targets a phase lag  $\phi^*$  with a PI controller that it compares to the phase lag  $\phi$ :

$$\dot{\theta} = \omega_0 + y + k_p(\phi - \phi^*), \quad (\text{A.34})$$

$$\dot{z} = k_i(\phi - \phi^*). \quad (\text{A.35})$$

Eqs. (A.33) to (A.35) form a dynamic system describing Eq. (A.1) controlled by a phase-locked loop.

Until now,  $\Omega$  represented the user-defined excitation frequency. Let now us consider a constant parameter  $\Omega$  that does not correspond in general to the excitation frequency  $\dot{\theta}(t)$ , as the latter is time-varying. A practical application of a phase-locked loop does not require the user to define  $\Omega$ . It is an analytical parameter whose purpose is to reparametrize the response to study the effect of the phase-locked loop. A phase VdP transformation similar to Eq. (A.24) is defined with coordinates

$$\begin{cases} r = \sqrt{x^2 + \frac{1}{\Omega^2}\dot{x}^2} \\ \phi = \text{atan2}\left(x, \frac{1}{\Omega}\dot{x}\right) - \theta \pmod{2\pi} \end{cases} \quad (\text{A.36})$$

whose inverse is

$$\begin{cases} x = r \sin(\theta + \phi) \\ \dot{x} = r\Omega \cos(\theta + \phi) \end{cases} \quad (\text{A.37})$$

Like in Section A.2.1, the parameter space  $(r, \phi)$  is time-varying. The transformation can therefore correspond to any response of system (A.33). Under the transformation, monoharmonic orbits of the system become limit points that are easier to study.

Firstly, let us make the VdP assumption from Section A.1. In this setting, the difference between excitation and natural frequency  $\dot{\theta} - \omega_0$  is of order  $\epsilon$ . Secondly, let us assume that the gains of the controller are order  $\epsilon$  as well ( $k_i \rightarrow \epsilon k_i$ ,  $k_p \rightarrow \epsilon k_p$ ). Consequently from Eq. (A.34),

$$\ddot{\theta} = \epsilon \left( k_i (\phi - \phi^*) + k_p \dot{\phi} \right), \quad (\text{A.38})$$

i.e. the excitation frequency  $\dot{\theta}$  varies slowly through time. We can therefore choose a parameter  $\Omega$  arbitrarily close to  $\dot{\theta}$  at some point in time, at which point  $\psi = \Omega\dot{\theta} - \omega_0^2$  is also order  $\epsilon$ . The same development done in Section A.2.1 concludes that  $r$  and  $\phi$  vary in time scales much larger than one period of the system: They can be considered constant when integrating over a period. Finally, combining with Eqs. (A.34) to (A.35) lead to the time-invariant dynamic system

$$\begin{cases} \dot{r} = -\frac{1}{2} \left( \delta r + \frac{1}{\Omega} (h_c(r) + p \sin \phi) \right) \\ \dot{\phi} = -\frac{1}{2} \left( \omega_0 \left( 1 - \frac{\omega_0}{\Omega} \right) + z + k_p (\phi - \phi^*) - \frac{1}{r\Omega} (h_s(r) - p \cos \phi) \right) \\ \dot{z} = k_i (\phi - \phi^*). \end{cases} \quad (\text{A.39})$$



# Appendix B

## Dynamics of online Fourier decomposition methods

This Appendix analyzes the online Fourier decomposition methods as dynamical systems. The accuracy and convergence speed of synchronous demodulation and adaptive filtering are derived in order to build a performance comparison in Chapter 4.

### B.1 Synchronous demodulation

Let us evaluate the Fourier coefficient  $a$  of a signal  $x(t) = a \sin(\Omega t)$  through synchronous demodulation. Let us only consider a demodulation by a sine wave, such that the product

$$x'(t) = x(t) \sin(\Omega t) \quad (\text{B.1})$$

$$= a \sin^2(\Omega t) \quad (\text{B.2})$$

$$= \frac{a}{2}(1 - \cos(2\Omega t)) \quad (\text{B.3})$$

has a constant term proportional to  $a$ . In the Laplace domain,

$$X'(s) = \frac{a}{2} L\{1 - \cos(2\Omega t)\} \quad (\text{B.4})$$

$$= \frac{a}{2} \left( \frac{1}{s} - \frac{s}{s^2 + 4\Omega^2} \right) \quad (\text{B.5})$$

$$= \frac{2a\Omega^2}{s(s^2 + 4\Omega^2)}. \quad (\text{B.6})$$

Let us now extract the Fourier coefficient by applying a low-pass (LP) filter with cut-off frequency  $\omega_p$  to  $x'(t)$ . The LP filter has the transfer

function

$$F(s) = \frac{\omega_{lp}}{s + \omega_{lp}}. \quad (\text{B.7})$$

The output of the filter is

$$Y(s) = F(s)X'(s) = \frac{2a\Omega^2}{s(s^2 + 4\Omega^2)} \cdot \frac{\omega_{lp}}{s + \omega_{lp}} \quad (\text{B.8})$$

$$= \frac{2a\Omega^2\omega_{lp}}{s(s + 2i\Omega)(s - 2i\Omega)(s + \omega_{lp})} \quad (\text{B.9})$$

$$= \frac{ar_0}{s} + \frac{ar_1}{s + 2i\Omega} + \frac{a\bar{r}_1}{s - 2i\Omega} + \frac{ar_2}{s + \omega_{lp}} \quad (\text{B.10})$$

with a bar marking the conjugate operator. The residues are

$$r_0 = \frac{1}{2} \quad (\text{B.11})$$

$$r_1 = -\frac{1}{4} \cdot \frac{\omega_{lp}}{\omega_{lp} - 2i\Omega} \quad (\text{B.12})$$

$$r_2 = -\frac{2\Omega^2}{\omega_{lp}^2 + 4\Omega^2}. \quad (\text{B.13})$$

To derive the output of the LP filter in the time domain, we apply the inverse Laplace transform:

$$y(t) = L^{-1}\{Y(s)\} = \frac{a}{2} + ar_1 \exp(-2i\Omega t) + a\bar{r}_1 \exp(2i\Omega t) + ar_2 \exp(-\omega_{lp}t). \quad (\text{B.14})$$

The output has three terms: the constant term is still  $a/2$ , the oscillatory error is

$$y_e(t) = -\frac{a}{2} \cdot \frac{\omega_{lp}}{\omega_{lp}^2 + 4\Omega^2} (\omega_{lp} \cos(2\Omega t) + 2\Omega \sin(2\Omega t)), \quad (\text{B.15})$$

and the transient is

$$y_t = -2a \frac{\Omega^2}{\omega_{lp}^2 + 4\Omega^2} \exp(-\omega_{lp}t). \quad (\text{B.16})$$

Fig. B.1 shows an example of output  $y$ .

Two performance factors are defined: the relative amplitude of the oscillatory error in the Fourier coefficient

$$e = \frac{2\|y_e\|}{a} = \frac{\omega_{lp}}{\sqrt{\omega_{lp}^2 + 4\Omega^2}}, \quad (\text{B.17})$$

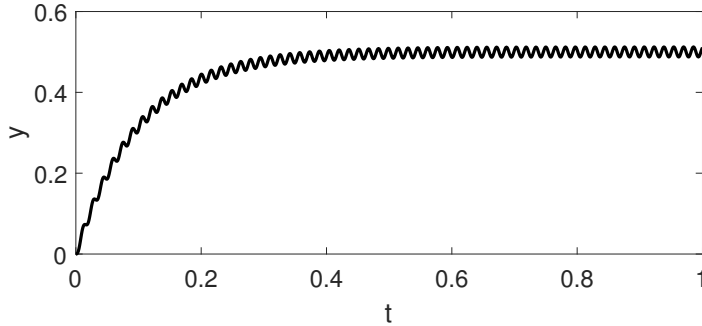


Figure B.1: Time series of the LP filter output  $y$  from Eq. B.15 with  $a = 1$ ,  $\Omega = 200$ , and  $\omega_{lp} = 10$

and the settling time until reaching a convergence margin  $\epsilon$

$$\tau_{lp}(\epsilon) = -\frac{1}{\omega_{lp}} \log \left( \epsilon \frac{\omega_{lp}^2 + 4\Omega^2}{2\Omega^2} \right). \quad (\text{B.18})$$

An non-dimensional alternative for  $\tau_{lp}$  is the number of periods needed to settle within the margin  $\epsilon$

$$N_{lp}(\epsilon) = \frac{\Omega \tau_{lp}(\epsilon)}{2\pi}. \quad (\text{B.19})$$

If we assume that the cut-off frequency is much lower than the frequency of the signal to demodulate, i.e.  $\omega_{lp} \ll \Omega$ , the expression of the error amplitude ratio and settling time can be simplified

$$e \approx \frac{\omega_{lp}}{2\Omega}, \quad (\text{B.20})$$

$$N_{lp}(\epsilon) \approx -\frac{\Omega}{2\pi\omega_{lp}} \log(2\epsilon). \quad (\text{B.21})$$

## B.2 Adaptive filtering

The objective of an adaptive filter is to replicate a reference signal using a number of basis signals. In this work however, the goal is to estimate the Fourier coefficients of a signal  $x$  at a reference frequency  $\omega_f$ . We use an adaptive notch filter that was introduced in [Widrow, 1975]. The adaptive filter synthesizes the signal  $y$  by performing a time-varying linear combination of the basis  $\mathbf{q}$ :

$$y(t) = \mathbf{w}^T(t)\mathbf{q}(t). \quad (\text{B.22})$$

The basis  $\mathbf{q}$  is composed of harmonic signals

$$\mathbf{q}(t) = \begin{bmatrix} q_s(t) \\ q_c(t) \end{bmatrix} = \begin{bmatrix} \sin(\omega_f t) \\ \cos(\omega_f t) \end{bmatrix} \quad (\text{B.23})$$

and the combination coefficients are the weights

$$\mathbf{w}(t) = \begin{bmatrix} w_s(t) \\ w_c(t) \end{bmatrix}. \quad (\text{B.24})$$

There exist several algorithms to define appropriate weights  $\mathbf{w}$ . A simple and inexpensive one is the Least Mean Square (LMS) algorithm [88], which updates  $\mathbf{w}$  discretely through time. At time  $t$ , the synthesis error is estimated

$$e(t) = x(t) - y(t) \quad (\text{B.25})$$

$$= x(t) - \mathbf{w}^T(t)\mathbf{q}(t) \quad (\text{B.26})$$

The weights are updated after a step time  $t_s$

$$\mathbf{w}(t + t_s) = \mathbf{w}(t) + \mu\mathbf{q}(t)e(t) \quad (\text{B.27})$$

with  $\mu$  the step size factor, which is an internal parameter of the LMS algorithm and therefore of the adaptive filter. For further information about adaptive filters, the reader is invited to consult reference books, such as [88].

Traditionally, the output of interest is  $y$  when the purpose is filtering, or  $e$  when the purpose is noise cancellation. In this application, we notice that if  $e$  has a very low frequency content at  $\omega_f$ , the weights  $w_s$  and  $w_c$  are very close to the Fourier coefficients of  $y$  at frequency  $\omega_f$ . An adaptive filter can therefore be used to perform a Fourier decomposition at each time step  $t_s$ .

### B.2.1 Transfer function

The transfer function between the z-transform of the synthesized harmonic signal  $Y$  and the adaptive filter error  $E$  is has been shown [87] to equal

$$A(z) = \frac{Y}{E} = \mu \frac{z \cos(\omega_f t_s) - 1}{z^2 - 2z \cos(\omega_f t_s) + 1} \quad (\text{B.28})$$

with  $t_s$  the sampling time,  $\mu$  the LMS parameter. There is a zero at  $z = 1/\cos(\omega_f t_s)$  and poles at  $z = \exp(\pm i\omega_f t_s)$ , i.e. at a frequency  $\Omega = \omega_f$ .

The error signal is expressed

$$E = X - Y \quad (\text{B.29})$$

$$= X - A(z)E \quad (\text{B.30})$$

$$= \frac{1}{A(z) + 1}X = B(z)X. \quad (\text{B.31})$$

The corresponding Bode diagram is shown in Fig. B.2. It corresponds to a notch filter at frequency  $\omega_f$ . The value of  $\mu$  determines the sharpness of the peak: values closer to 0 lead to a sharper peak but a longer convergence time. The synthesized signal is expressed

$$Y = X - E \quad (\text{B.32})$$

$$= X - \frac{1}{A(z)}Y \quad (\text{B.33})$$

$$= \frac{A(z)}{A(z) + 1}X = C(z)X. \quad (\text{B.34})$$

The corresponding Bode diagram is shown in Fig. B.3. It corresponds to a filter reproducing the signal  $x$  at frequency  $\omega_f$  and cancelling everything else. Increasing parameter  $\mu$  still sharpens the filter while increasing the convergence time.

## B.2.2 Performance

Like in Section B.1, the performance is evaluated when applying the filter to a sine wave of amplitude  $a$ . The frequency of the basis is chosen identical to the discrete reference signal  $x[n] = a \sin(\Omega n t_s)$ , i.e.  $\omega_f = \Omega$ . In the  $z$  domain,

$$X(z) = Z\{a \sin(\Omega t_s n)\} \quad (\text{B.35})$$

$$= \frac{az \sin(\Omega t_s)}{z^2 - 2z \cos(\Omega t_s) + 1}. \quad (\text{B.36})$$

Interestingly, the denominator of  $X$  is identical to the numerator of  $B(z)$  from Eq. (B.31). Therefore, the error is easily expressed

$$E(z) = B(z)X(z) = \frac{az \sin(\Omega t_s)}{z^2 + (\mu - 2)z \cos(\Omega t_s) + 1 - \mu}. \quad (\text{B.37})$$

The performance of the filter depends on the dynamics of the error  $e[n]$ . Its poles in the  $z$  domain depend on the value of  $\mu$ . The discriminant of the denominator is

$$\Delta = (\mu - 2)^2 \cos^2(\Omega t_s) - 4(1 - \mu). \quad (\text{B.38})$$

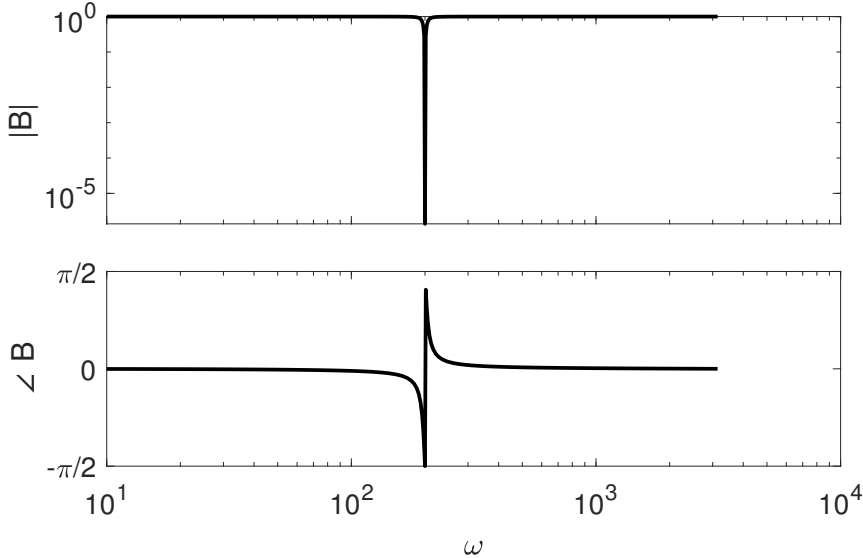


Figure B.2: Bode diagram of  $B(\exp(i\Omega t_s))$  for  $t_s = 10^{-3}$  s,  $\mu = 0.01$ , and  $\omega_f = 200$  rad/s

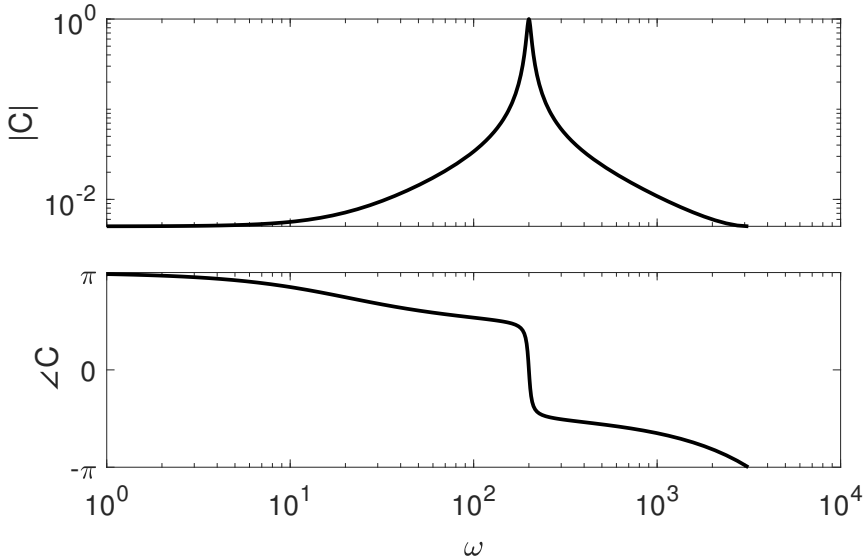


Figure B.3: Bode diagram of  $C(\exp(i\Omega t_s))$  for  $t_s = 10^{-3}$  s,  $\mu = 0.01$ , and  $\omega_f = 200$  rad/s

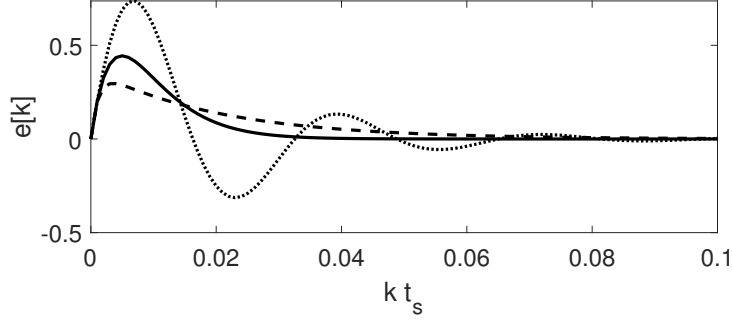


Figure B.4: Time series of the error signal  $e$  with step size  $t_s = 10^{-3}$ , a reference signal with  $a = 1$ ,  $\Omega = 200$ , and an adaptive filter coefficient  $\mu = 0.2$  (dotted curve),  $\mu = \mu_c \approx 0.33$  (plain curve), and  $\mu = 0.6$  (dashed curve)

Let us define a critical coefficient

$$\mu_c = 2 \sin(\Omega t_s) \frac{1 - \sin(\Omega t_s)}{\cos^2(\Omega t_s)}. \quad (\text{B.39})$$

**Subcritical coefficient** With a subcritical  $\mu \in [0, \mu_c)$ ,  $\Delta < 0$ . The error has two complex conjugate poles in the  $z$  domain:

$$p = \frac{1}{2} \left( (2 - \mu) \cos(\Omega t_s) + i\sqrt{-\Delta} \right) \quad (\text{B.40})$$

and  $\bar{p}$ . The error is expressed

$$E(z) = \frac{arz}{z-p} + \frac{a\bar{r}z}{z-\bar{p}} \quad (\text{B.41})$$

with the residual

$$r = \frac{\sin(\Omega t_s)}{i\sqrt{-\Delta}}. \quad (\text{B.42})$$

In the time domain,

$$e[k] = Z^{-1}\{E(z)\} = arp^k + a\bar{r}\bar{p}^k. \quad (\text{B.43})$$

An example is shown in Fig. B.4 with a dotted curve. The error is said to be underdamped with oscillation envelope

$$\|e\| [k] = 2a|r| \exp(k\Re(\log p)). \quad (\text{B.44})$$

The settling time to reach an amplitude ratio  $\|e\|/a = \epsilon$  in the underdamped case is therefore

$$\tau_{ud}(\epsilon) = \frac{\log \frac{\epsilon}{2|r|}}{\Re(\log p)} t_s. \quad (\text{B.45})$$

**Critical coefficient** In the critical case,  $\mu = \mu_c$  and  $\Delta = 0$ . The error has a pole with double multiplicity in the  $z$  domain:

$$p = \frac{1}{2}(2 - \mu_c) \cos(\Omega t_s). \quad (\text{B.46})$$

The error is expressed

$$E(z) = \frac{ar z}{(z - p)^2} \quad (\text{B.47})$$

with the coefficient

$$r = \sin(\Omega t_s). \quad (\text{B.48})$$

In the time domain,

$$e[k] = Z^{-1}\{E(z)\} = arkp^{k-1}. \quad (\text{B.49})$$

An example is shown in Fig. B.4 with a plain curve. The error is said to be critically damped. The settling time to reach an amplitude ratio  $e/a = \epsilon$  is

$$\tau_c(\epsilon) = \frac{W_{-1}\left(\epsilon \frac{p \log p}{r}\right)}{\log p} t_s \quad (\text{B.50})$$

with  $W_{-1}$  a Lambert W function.

**Supercritical coefficient** Finally for a supercritical  $\mu \in (\mu_c, 1]$ ,  $\Delta > 0$ . The error has two real poles in the  $z$  domain:

$$p_{1,2} = \frac{1}{2} \left( (2 - \mu) \cos(\Omega t_s) \pm \sqrt{\Delta} \right). \quad (\text{B.51})$$

The error is expressed

$$E(z) = \frac{ar z}{z - p_1} - \frac{ar z}{z - p_2} \quad (\text{B.52})$$

with the residual

$$r = \frac{\sin(\Omega t_s)}{\sqrt{\Delta}}. \quad (\text{B.53})$$

In the time domain,

$$e[k] = Z^{-1}\{E(z)\} = arp_1^k - arp_2^k. \quad (\text{B.54})$$

An example is shown in Fig. B.4 with a dashed curve. The error is said to be overdamped. The time constant of the first term  $ar_1 p_1^n$  is greater

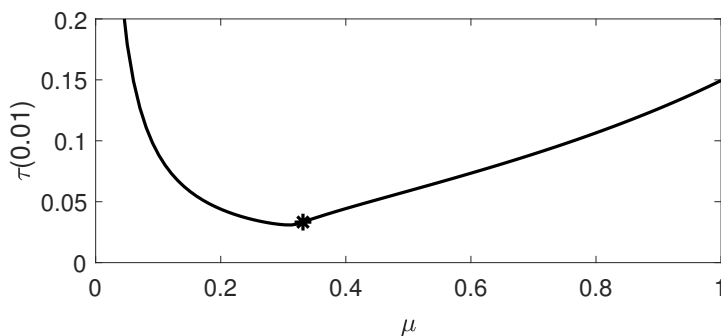


Figure B.5: Settling time to reach an error amplitude ratio of 1% for  $\Omega = 200$ ,  $t_s = 10^{-3}$ ; the critical coefficient  $\mu_c$  is shown with an asterisk

than the second because  $p_1 > p_2$ . Therefore, the settling time to reach an amplitude ratio  $e/a = \epsilon$  is approximated

$$\tau_{\text{od}}(\epsilon) \approx \frac{\log \frac{\epsilon}{r}}{\log p_1} t_s. \quad (\text{B.55})$$

Fig. B.5 compares the settling time depending on the adaptive coefficient  $\mu$ . The three regimes are visible: underdamped, critically damped, then overdamped. It can be proven that the optimal value of the adaptive coefficient  $\mu$  is  $\mu_c$ .

Let us consider a critical coefficient  $\mu_c$  from Eq. (B.39) with corresponding values  $p$  and  $r$  from Eqs. (B.46) and (B.48) respectively. Let us assume a small time step compared to the reference signal's frequency:  $\Omega t_s \ll 1$  implies  $\mu_c \approx 2\Omega t_s$ . Taking the limit

$$\lim_{t_s \rightarrow 0} \frac{\log(p)}{t_s} \approx \lim_{t_s \rightarrow 0} \frac{\log(1 - \Omega t_s)}{t_s} = -\Omega. \quad (\text{B.56})$$

Therefore, Eq. (B.50) can be approximated

$$\tau_c(\epsilon) \approx -\frac{1}{\Omega} W_{-1}(-\epsilon). \quad (\text{B.57})$$

### B.2.3 Stability

Let us consider that the adaptive filter is in a positive feedback loop with a linear oscillator, as shown in Fig. B.6. The oscillator's transfer function is

$$O(s) = \frac{1}{s^2 + \delta s + \omega_0^2}. \quad (\text{B.58})$$

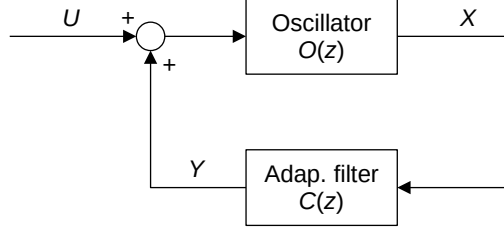


Figure B.6: Positive feedback loop between the oscillator  $O(z)$  and the adaptive filter  $C(z)$

The corresponding discrete system is

$$O(z) = \frac{1}{\omega_0^2} \frac{(1 - \exp(s_1 t_s))(1 - \exp(s_2 t_s))}{(z - \exp(s_1 t_s))(z - \exp(s_2 t_s))}. \quad (\text{B.59})$$

with

$$s_{1,2} = -\frac{1}{2} \left( \delta \pm i\sqrt{\delta^2 - 4\omega_0^2} \right), \quad (\text{B.60})$$

the poles of  $O(s)$ .

Let us take the transfer function of the adaptive filter from the input  $X$  to the output  $Y$ ,  $C(z)$  (Eq. (B.34)), and put it in a positive closed loop with  $O(z)$ , as shown in Fig. B.6. We will not focus on the feedback input  $U$ . Rather, we will discuss the stability of the feedback itself.

An easy way of knowing whether the system  $O(z)C(z)$  is stable in closed loop is to look at a Bode plot in open loop. If the gain is larger than one while the phase lag is  $0^\circ$ , the feedback system is unstable. Fig. B.7 shows that an adaptive filter at frequency  $\omega_f$  lower than the resonance frequency  $\omega_0$  of the oscillator will always lead to a stable feedback. The frequency at which the phase lag equals  $0^\circ$  is always  $\omega_f$  and the amplitude is  $|O(i\omega_f)|$ , very small if  $\omega_f \ll \omega_0$ . The story is not the same if  $\omega_f > \omega_0$ . Fig. B.8 shows that the phase lag can be equal or very near zero at the resonance peak, whose amplitude can be higher than 1 due to resonance. In this case, the feedback loop can be unstable. The solution is to reduce  $\mu$ , i.e. make the adaptive filter slower.

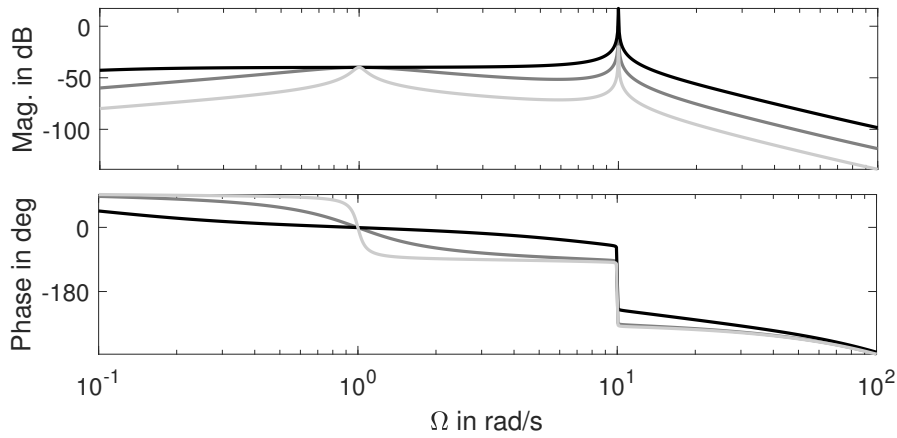


Figure B.7: Bode plot of the positive feedback between an oscillator resonating at  $\omega_0 = 10$  rad/s and an adaptive filter targeting  $\omega_f = 1$  rad/s with  $\mu = 0.001$  (light gray),  $0.01$  (dark gray), and  $0.1$  (black);  $t_s = 0.01$  s

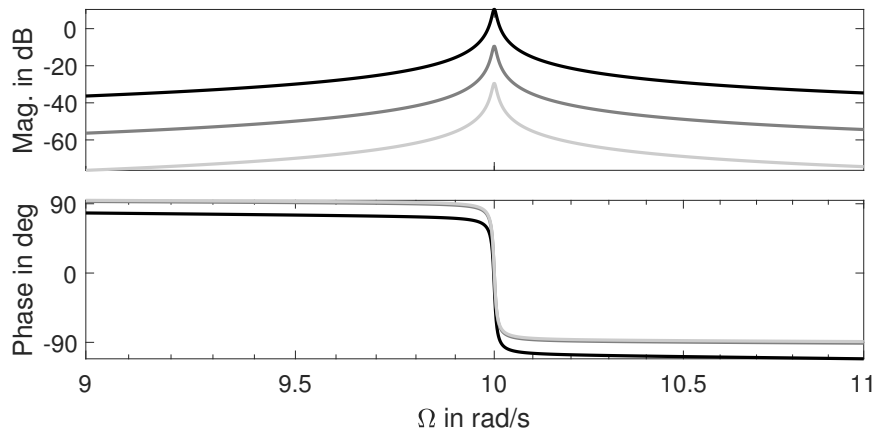


Figure B.8: Bode plot of the positive feedback between an oscillator resonating at  $\omega_0 = 10$  rad/s and an adaptive filter targeting  $\omega_f = 20$  rad/s with  $\mu = 0.001$  (light gray),  $0.01$  (dark gray), and  $0.1$  (black);  $t_s = 0.01$  s



# Bibliography

- [1] D. J. Ewins. *Modal Testing: Theory, Practice and Application*. Research Studies Press, Hertfordshire, U.K., 2nd edition, 2000.
- [2] Rik Pintelon and Johan Schoukens. *System Identification: A Frequency Domain Approach*. John Wiley & Sons, 2010.
- [3] Kenneth A Ramsey. Effective measurements for structural dynamics testing. *Sound and Vibration*, 9(11):24–34, 1975.
- [4] Nuno Manuel Mendes Maia and Júlio Martins Montalvao e Silva. *Theoretical and experimental modal analysis*. Research Studies Press, 1997.
- [5] Zhi-Fang Fu and Jimin He. *Modal analysis*. Elsevier, 2001.
- [6] Gaëtan Kerschen, Keith Worden, Alexander F Vakakis, and Jean-Claude Golinval. Past, present and future of nonlinear system identification in structural dynamics. *Mechanical Systems and Signal Processing*, 20(3):505–592, 2006.
- [7] Ondrej Rubes, Martin Brablec, and Zdenek Hadas. Nonlinear vibration energy harvester: Design and oscillating stability analyses. *Mechanical Systems and Signal Processing*, 125:170–184, 2019.
- [8] Chiara Gastaldi, Johann Gross, Maren Scheel, Teresa M Berruti, and Malte Krack. Modeling complex contact conditions and their effect on blade dynamics. *Journal of Engineering for Gas Turbines and Power*, 143(1):011007, 2021.
- [9] Alexander F. Vakakis, Leonid I. Manevitch, Yurl V. Mikhlin, Valery N. Pilipchuk, and Alexandr A. Zevin. *Normal Modes and Localization in Nonlinear Systems*. Springer Netherlands, 1 edition, 2008.

- [10] Ali H Nayfeh and Dean T Mook. *Nonlinear oscillations*. John Wiley & Sons, 2008.
- [11] Gaetan Kerschen, Young Sup Lee, Alexander F. Vakakis, D. Michael McFarland, and Lawrence A. Bergman. Irreversible passive energy transfer in coupled oscillators with essential nonlinearity. *SIAM Journal on Applied Mathematics*, 66(2):648–679, 2006.
- [12] Dieter Grass, Jonathan P Caulkins, Gustav Feichtinger, Gernot Tragler, Doris A Behrens, et al. Optimal control of nonlinear processes. *Berlino: Springer*, 2008.
- [13] Keith Worden and Geoffrey R Tomlinson. *Nonlinearity in structural dynamics: detection, identification and modelling*. CRC Press, 2019.
- [14] Jean-Philippe Noël and Gaëtan Kerschen. A new subspace-based approach to identify nonlinear mechanical structures in the frequency domain. *IFAC Proceedings Volumes (IFAC-PapersOnline)*, 45(16 PART 1):650–655, 2012.
- [15] Jean Philippe Noël, L. Renson, C. Grappasonni, and G. Kerschen. Identification of nonlinear normal modes of engineering structures under broadband forcing. *Mechanical Systems and Signal Processing*, 74:95–110, 2016.
- [16] H. B. Keller. Numerical solution of bifurcation and nonlinear eigenvalue problems. In P. Rabinowitz, editor, *Applications of Bifurcation Theory*, pages 359–384. Academic Press, New York, 1977.
- [17] R Seydel. A continuation algorithm with step control. In *Numerical methods for bifurcation problems*, pages 480–494. Springer, 1984.
- [18] E Doedel and J Kernévez. Auto: Software for continuation problems in ordinary differential equations with applications. *Applied Mathematics, California Institute of Technology, Pasadena, CA*, 1986.
- [19] Malte Krack and Johann Gross. *Harmonic Balance for Nonlinear Vibration Problems*. Mathematical Engineering. Springer International Publishing, Cham, 2019.
- [20] M. R.W. Brake, C. W. Schwingshackl, and P. Reuß. Observations of variability and repeatability in jointed structures. *Mechanical Systems and Signal Processing*, 129:282–307, 2019.

- [21] Mehmet Kurt, Melih Eriten, D. Michael McFarland, Lawrence A. Bergman, and Alexander F. Vakakis. Methodology for model updating of mechanical components with local nonlinearities. *Journal of Sound and Vibration*, 357:331–348, 2015.
- [22] K. Nandakumar and Anindya Chatterjee. Resonance, parameter estimation, and modal interactions in a strongly nonlinear benchtop oscillator. *Nonlinear Dynamics*, 40(2):149–167, 2005.
- [23] Maren Scheel, Simon Peter, Remco I. Leine, and Malte Krack. A phase resonance approach for modal testing of structures with nonlinear dissipation. *Journal of Sound and Vibration*, 435:56–73, 2018.
- [24] Young S. Lee, Alexander F. Vakakis, Lawrence A. Bergman, D. Michael McFarland, and Gaëtan Kerschen. Suppressing aeroelastic instability using broadband passive targeted energy transfers, part 1: Theory. *AIAA Journal*, 45(3):693–711, 2007.
- [25] G. Zhao, A. Paknejad, G. Raze, A. Deraemaeker, G. Kerschen, and C. Collette. Nonlinear positive position feedback control for mitigation of nonlinear vibrations. *Mechanical Systems and Signal Processing*, 132:457–470, 2019.
- [26] K. Pyragas. Continuous control of chaos by self-controlling feedback. *Physics Letters A*, 170(6):421–428, 1992.
- [27] Jan Sieber and Bernd Krauskopf. Control-based continuation of periodic orbits with a time-delayed difference scheme. *International Journal of Bifurcation and Chaos*, 17(8):2576–2593, 2007.
- [28] Bernd Krauskopf, Hinke M Osinga, and Jorge Galán-Vioque. *Numerical continuation methods for dynamical systems*, volume 2. Springer, 2007.
- [29] Jan Sieber and Bernd Krauskopf. Control based bifurcation analysis for experiments. *Nonlinear Dynamics*, 51:356–377, 2008.
- [30] Jan Sieber, A. Gonzalez-Buelga, S. A. Neild, D J Wagg, and Bernd Krauskopf. Experimental continuation of periodic orbits through a fold. *Physical Review Letters*, 100(24):244101, 2008.
- [31] Jan Sieber, Bernd Krauskopf, David Wagg, Simon Neild, and Alicia Gonzalez-Buelga. Control-based continuation of unstable periodic orbits. *Journal of Computational and Nonlinear Dynamics*, 6(1), 2011.

- [32] David A.W. Barton and Stephen G. Burrow. Numerical continuation in a physical experiment: Investigation of a nonlinear energy harvester. *Journal of Computational and Nonlinear Dynamics*, 6(1):011010, 2011.
- [33] Emil Bureau, Frank Schilder, Ilmar Santos, Jon Juel Thomsen, and Jens Starke. Experimental bifurcation analysis for a driven nonlinear flexible pendulum using control-based continuation. In *7th European Nonlinear Dynamics Conference*, pages 24–29, July 2011.
- [34] Emil Bureau, Frank Schilder, Ilmar Ferreira Santos, Jon Juel Thomsen, and Jens Starke. Experimental bifurcation analysis of an impact oscillator - Tuning a non-invasive control scheme. *Journal of Sound and Vibration*, 332(22):5883–5897, 2013.
- [35] David A.W. Barton, Brian P. Mann, and Stephen G. Burrow. Control-based continuation for investigating nonlinear experiments. *JVC/Journal of Vibration and Control*, 18(4):509–520, 2012.
- [36] Emil Bureau, Frank Schilder, Michael Elmegård, Ilmar F Santos, Jon J Thomsen, and Jens Starke. Experimental bifurcation analysis of an impact oscillator—determining stability. *Journal of Sound and Vibration*, 333(21):5464–5474, 2014.
- [37] David A.W. Barton. Control-based continuation: Bifurcation and stability analysis for physical experiments. *Mechanical Systems and Signal Processing*, 84(B):54–64, 2017.
- [38] Ludovic Renson, A. Gonzalez-Buelga, David A.W. Barton, and S. A. Neild. Robust identification of backbone curves using control-based continuation. *Journal of Sound and Vibration*, 367:145–158, 2016.
- [39] Ludovic Renson, David A.W. Barton, and Simon A. Neild. Experimental tracking of limit-point bifurcations and backbone curves using control-based continuation. *International Journal of Bifurcation and Chaos*, 27(1), 2017.
- [40] Ludovic Renson, A. D. Shaw, David A.W. Barton, and S. A. Neild. Application of control-based continuation to a nonlinear structure with harmonically coupled modes. *Mechanical Systems and Signal Processing*, 120:449–464, 2019.

- [41] L. Renson, J. Sieber, David A.W. Barton, A. D. Shaw, and S. A. Neild. Numerical continuation in nonlinear experiments using local Gaussian process regression. *Nonlinear Dynamics*, 98:2811–2826, 2019.
- [42] Gleb Kleyman, Martin Paehr, and Sebastian Tatzko. Application of control-based-continuation for characterization of dynamic systems with stiffness and friction nonlinearities. *Mechanics Research Communications*, 106:103520, 2020.
- [43] Brandon Gomes, Irene de Cesare, Agostino Guarino, Mario di Bernardo, Ludovic Renson, and Lucia Marucci. Exploring the dynamics of nonlinear biochemical systems using control-based continuation. *bioRxiv*, page 695866, 2019.
- [44] Irene de Cesare, Davide Salzano, Mario di Bernardo, Ludovic Renson, and Lucia Marucci. Control-based continuation: a new approach to prototype synthetic gene networks. *ACS Synthetic Biology*, 11(7):2300–2313, 2022.
- [45] Ilias Panagiotopoulos and Jens Starke. Control-based continuation of unstable pedestrian flows. *Simulation*, 2(3):4.
- [46] I. J. Sokolov and V. I. Babitsky. Phase control of self-sustained vibration. *Journal of Sound and Vibration*, 248(4):725–744, 2001.
- [47] Sebastian Mojrzisch, Jörg Wallaschek, and Jan Bremer. An experimental method for the phase controlled frequency response measurement of nonlinear vibration systems. *PAMM*, 12(1):253–254, 2012.
- [48] Simon Peter and Remco I. Leine. Excitation power quantities in phase resonance testing of nonlinear systems with phase-locked-loop excitation. *Mechanical Systems and Signal Processing*, 96:139–158, 2017.
- [49] V. Denis, M. Jossic, C. Giraud-Audine, B. Chomette, A. Renault, and O. Thomas. Identification of nonlinear modes using phase-locked-loop experimental continuation and normal form. *Mechanical Systems and Signal Processing*, 106:430–452, 2018.
- [50] Maren Scheel, Tobias Weigele, and Malte Krack. Challenging an experimental nonlinear modal analysis method with a new strongly friction-damped structure. *Journal of Sound and Vibration*, 485:115580, 2020.

- [51] G. Abeloos, F. Müller, E. Ferhatoglu, M. Scheel, C. Collette, G. Kerschen, M.R.W. Brake, P. Tiso, L. Renson, and M. Krack. A consistency analysis of phase-locked-loop testing and control-based continuation for a geometrically nonlinear frictional system. *Mechanical Systems and Signal Processing*, 170:108820, 2022.
- [52] M. Link, M. Böswald, S. Laborde, M. Weiland, and A. Calvi. Non-linear experimental modal analysis and application to satellite test data. In *Proceedings of COMPDYN 2011 - 3rd International Conference on Computational Methods in Structural Dynamics & Earthquake Engineering*, pages 26–28, 2011.
- [53] Taylan Karaağaçlı and H. Nevzat Özgüven. Experimental Identification of Backbone Curves of Strongly Nonlinear Systems by Using Response-Controlled Stepped-Sine Testing (RCT). *Vibration*, 3(3):266–280, 2020.
- [54] Taylan Karaağaçlı and H. Nevzat Özgüven. Experimental modal analysis of nonlinear systems by using response-controlled stepped-sine testing. *Mechanical Systems and Signal Processing*, 146, 2021.
- [55] Shinpachiro Urasaki and Hiroshi Yabuno. Identification method for backbone curve of cantilever beam using van der pol-type self-excited oscillation. *Nonlinear Dynamics*, 103(4):3429–3442, 2021.
- [56] Maren Scheel. Nonlinear modal testing of damped structures: Velocity feedback vs. phase resonance. *Mechanical Systems and Signal Processing*, 165:108305, 2022.
- [57] David A.W. Barton and Jan Sieber. Systematic experimental exploration of bifurcations with noninvasive control. *Physical Review E*, 87:052916, 2013.
- [58] Simon Peter and Remco I. Leine. Experimental nonlinear modal analysis using a Phase-Locked-Loop. *6th International Conference on Nonlinear Vibrations, Localization and Energy Transfer*, pages 1–2, 2016.
- [59] Thibaut Detroux, Ludovic Renson, L. Masset, and Gaëtan Kerschen. The harmonic balance method for bifurcation analysis of nonlinear mechanical systems. *Conference Proceedings of the Society for Experimental Mechanics Series*, 1:65–82, 2016.

- [60] Herbert B Keller. Lectures on numerical methods in bifurcation problems. *Applied Mathematics*, 217:50, 1987.
- [61] Yuri A Kuznetsov, Iu A Kuznetsov, and Y Kuznetsov. *Elements of applied bifurcation theory*, volume 112. Springer, 1998.
- [62] Rüdiger Seydel. *Practical bifurcation and stability analysis*, volume 5. Springer Science & Business Media, 2009.
- [63] PJ Holmes and DA Rand. The bifurcations of duffing's equation: An application of catastrophe theory. *Journal of Sound and Vibration*, 44(2):237–253, 1976.
- [64] Xiaotian Sun, Roberto Horowitz, and K Komvopoulos. Stability and resolution analysis of a phase-locked loop natural frequency tracking system for mems fatigue testing. *J. Dyn. Sys., Meas., Control*, 124(4):599–605, 2002.
- [65] Mingxuan Fan, Matthew Clark, and ZC Feng. Implementation and stability study of phase-locked-loop nonlinear dynamic measurement systems. *Communications in Nonlinear Science and Numerical Simulation*, 12(7):1302–1315, 2007.
- [66] C.S. Koukourlis, V.K. Trigonidis, and John N. Sahalos. Differential synchronous demodulation for small signal amplitude estimation. *IEEE Transactions on Instrumentation and Measurement*, 1993.
- [67] Sebastian Mojrzisch, Jörg Wallaschek, and Jan Bremer. An experimental method for the phase controlled frequency response measurement of nonlinear vibration systems. *PAMM*, 12(1):253–254, 2012.
- [68] Simon Peter, Maren Scheel, Malte Krack, and Remco I. Leine. Synthesis of nonlinear frequency responses with experimentally extracted nonlinear modes. *Mechanical Systems and Signal Processing*, 101:498–515, 2018.
- [69] Gaëtan Abeloos, Ludovic Renson, Christophe Collette, and Gaëtan Kersche. Stepped and Swept Control-Based Continuation using Adaptive Filtering. *Nonlinear Dynamics*, 2021.
- [70] R. J. Kuether, L. Renson, T. Detroux, C. Grappasonni, G. Kerschen, and M. S. Allen. Nonlinear normal modes, modal interactions and isolated resonance curves. *Journal of Sound and Vibration*, 351:299–310, 2015.

- [71] Ludovic Renson. Identification of backbone curves and nonlinear frequency responses using control-based continuation and local gaussian process regression. In Gaetan Kerschen, Matthew R.W. Brake, and Ludovic Renson, editors, *Nonlinear Structures & Systems, Volume 1*, pages 83–85, Cham, 2021. Springer International Publishing.
- [72] S. Peter, F. Schreyer, P. Reuss, and L. Gaul. Consideration of local stiffening and clearance nonlinearities in coupled systems using a generalized Harmonic Balance Method. *Proceedings of ISMA 2014 - International Conference on Noise and Vibration Engineering and USD 2014 - International Conference on Uncertainty in Structural Dynamics*, pages 3097–3110, 2014.
- [73] M.I. McEwan, J.R. Wright, J.E. Cooper, and A.Y.T. Leung. A Combined Modal/Finite Element Analysis Technique for The Dynamic Response of a Non-linear Beam to Harmonic Excitation. *Journal of Sound and Vibration*, 243(4):601–624, jun 2001.
- [74] F. Müller et al. Experimental validation of a model for a self-adaptive beam-slider system. Under review in *Mechanical Systems and Signal Processing*, 2022.
- [75] Florian Müller. Self-adaptive beam slider system, v1 edition. DaRUS dataset, 2022. Available at <https://doi.org/10.18419/darus-2462>.
- [76] Mrdjan Jankovic. Control lyapunov-razumikhin functions and robust stabilization of time delay systems. *IEEE Transactions on Automatic Control*, 46(7):1048–1060, 2001.
- [77] Yang Li and Harry Dankowicz. Adaptive control designs for control-based continuation in a class of uncertain discrete-time dynamical systems. *JVC/Journal of Vibration and Control*, 0(February):1–18, 2020.
- [78] Yang Li and Harry Dankowicz. Adaptive control designs for control-based continuation of periodic orbits in a class of uncertain linear systems. *Nonlinear Dynamics*, 103(3):2563–2579, 2021.
- [79] Kiam Heong Ang, Gregory Chong, and Yun Li. PID control system analysis, design, and technology. *IEEE Transactions on Control Systems Technology*, 13(4):559–576, 2005.
- [80] Jacopo Marconi, Paolo Tiso, Davide E. Quadrelli, and Francesco Braghin. A higher-order parametric nonlinear reduced-order model

- for imperfect structures using Neumann expansion. *Nonlinear Dynamics*, 2021.
- [81] Malte Krack. Nonlinear modal analysis of nonconservative systems: Extension of the periodic motion concept. *Computers and Structures*, 154:59–71, 2015.
- [82] Sebastian Mojrzisch and Jens Twiefel. Phase-controlled frequency response measurement of a piezoelectric ring at high vibration amplitude. *Archive of Applied Mechanics*, 86(10):1763–1769, 2016.
- [83] Stefan Schwarz, Lukas Kohlmann, Andreas Hartung, Johann Gross, Maren Scheel, and Malte Krack. Validation of a Turbine Blade Component Test With Frictional Contacts by Phase-Locked-Loop and Force-Controlled Measurements. *Journal of Engineering for Gas Turbines and Power*, 142(5):051006, 2020.
- [84] G Matheron. Principles of geostatistics. *Economic Geology*, 58:1246–1266, 1963.
- [85] Gregory E Fasshauer. *Meshfree approximation methods with MATLAB*, volume 6. World Scientific, 2007.
- [86] Martin Volvert and Gaetan Kerschen. Phase resonance nonlinear modes of mechanical systems. *Journal of Sound and Vibration*, 511, 2021.
- [87] Bernard Widrow, Charles S. Williams, John R. Glover, John M. McCool, Robert H. Hearn, James R. Zeidler, John Kaunitz, Eugene Dong, and Robert C. Goodlin. Adaptive Noise Cancelling: Principles and Applications. *Proceedings of the IEEE*, 63(12):1692–1716, 1975.
- [88] Simon Haykin. *Adaptive filter theory*. Prentice Hall, New Jersey, 3rd edition, 1996.
- [89] Thibaut Detroux, Jean-Philippe Noël, Lawrence N. Virgin, and Gaëtan Kerschen. Experimental study of isolas in nonlinear systems featuring modal interactions. *PLOS ONE*, 13:e0194452, 3 2018.
- [90] Patrick Guillaume, Peter Verboven, Steve Vanlanduit, Herman Van Der Auweraer, and Bart Peeters. A poly-reference implementation of the least-squares complex frequency-domain estimator. *Proceedings of IMAC*, 21:183–192, 2003.

- [91] Martin Volvert and Gaëtan Kerschen. Characterizing fundamental, superharmonic, and subharmonic resonances using phase resonance nonlinear modes, 2022.
- [92] Eric Pesheck, Nicolas Boivin, Christophe Pierre, and Steven W Shaw. Nonlinear modal analysis of structural systems using multi-mode invariant manifolds. *Nonlinear Dynamics*, 25(1):183–205, 2001.
- [93] Robert S MacKay and James D Meiss. *Hamiltonian Dynamical Systems: a reprint selection*. CRC Press, 2020.
- [94] Nikolai Mitrofanovich Krylov and Nikolai Nikolaevich Bogoliubov. *Introduction to non-linear mechanics*. Number 11. Princeton university press, 1950.
- [95] James A Murdock. *Perturbations: theory and methods*. SIAM, 1999.
- [96] Gaetan Kerschen, Young Sup Lee, Alexander F. Vakakis, D. Michael McFarland, and Lawrence A. Bergman. Irreversible passive energy transfer in coupled oscillators with essential nonlinearity. *SIAM Journal on Applied Mathematics*, 66:648–679, 1 2005.
- [97] V. Eyert. A comparative study on methods for convergence acceleration of iterative vector sequences. *Journal of Computational Physics*, 124:271–285, 3 1996.
- [98] Rüdiger Seydel. *Practical Bifurcation and Stability Analysis*. Springer, 3rd edition, 2010.
- [99] Eusebius Doedel, Herbert B. Keller, and Jean Pierre Kernevez. Numerical analysis and control of bifurcation problems (i): Bifurcation in finite dimensions. *International Journal of Bifurcation and Chaos*, 01:493–520, 9 1991.
- [100] E. Riks. An incremental approach to the solution of snapping and buckling problems. *International Journal of Solids and Structures*, 15:529–551, 1979.
- [101] M.A. Crisfield. A fast incremental/iterative solution procedure that handles “snap-through”, 1981.
- [102] Arthur Givois, Jin-Jack Tan, Cyril Touzé, and Olivier Thomas. Backbone curves of coupled cubic oscillators in one-to-one internal resonance: bifurcation scenario, measurements and parameter identification. *Meccanica*, 55(3):481–503, 2020.

- [103] J. P. Noël, T. Detroux, L. Masset, G. Kerschen, and L. N. Virgin. Isolated response curves in a base-excited, two-degree-of-freedom, nonlinear system. American Society of Mechanical Engineers, 8 2015.

